Generation and implementation of optogenetic tools for cNMP generation and cell de- and hyperpolarization in *Caenorhabditis elegans*

Dissertation

zur Erlangung des Doktorgrades

der Naturwissenschaften

vorgelegt beim Fachbereich Biochemie, Chemie und Pharmazie

der Johann Wolfgang Goethe-Universität

in Frankfurt am Main

von Thilo Henß

aus Bad Soden, Hessen

Frankfurt am Main, 2023

(D 30)

Vom Fachbereich Biochemie, Chemie und Pharmazie der

Johann Wolfgang Goethe-Universität als Dissertation angenommen.

Dekan: Prof. Dr. Clemens Glaubitz

Gutachter: Prof. Dr. Alexander Gottschalk

Prof. Dr. Clemens Glaubitz

Datum der Disputation: ……..

Eidesstattliche Erklärung

Ich erkläre hiermit, dass ich die vorgelegte Dissertation mit dem Titel „Generation and implementation of optogenetic tools for cNMP generation and cell de- and hyperpolarization in *Caenorhabditis elegans*" selbstständig angefertigt und mich anderer Hilfsmittel als der in der angegebenen Arbeit nicht bedient habe, insbesondere, dass alle Entlehnungen aus anderen Schriften mit Angabe der betreffenden Schrift gekennzeichnet sind.

Ich erkläre hiermit, dass ich mich bisher keiner Doktorprüfung im mathematisch-naturwissenschaftlichen Bereich unterzogen habe.

Declaration

This thesis consists solely of work generated by the doctoral candidate and supervision of his/her advisors.

Except where stated otherwise by reference or acknowledgment, the work presented was generated by myself under the supervision of my advisors during my doctoral studies.

Whenever a figure, table or text is identical to a previous publication, it is stated explicitly in the thesis that copyright permission and/or co-author agreement has been obtained.

Frankfurt am Main, den ……

_____

(Thilo Henß)

Contents

Zusammenfassung

In den letzten zehn Jahren wurde der optogenetische Werkzeugkasten für die Manipulation von Ionenströmen und cNMP-Spiegeln in *Caenorhabditis elegans* (*C. elegans*) erweitert. Bei den eingesetzten Werkzeugen für die cAMP-Erzeugung handelte es sich jedoch um lösliche Enzyme (euPAC, bPAC, IlaC22 k27 und PaaC), so dass sie die physiologische cAMP-Signalgebung, die in Mikrodomänen in unmittelbarer Nähe der Plasmamembran stattfindet, nicht genau nachahmen. Hier wird cAMP vorwiegend von membrangebundenen Adenylylzyklasen erzeugt, die sich in Mikrodomänen zusammen mit G-Protein-gekoppelten Rezeptoren (GPCRs), Proteinkinase A (PKA) und ihren Substraten befinden, was eine räumliche und zeitliche Regulierung der cAMP-Signalgebung ermöglicht. Ein Ziel dieser Studie war es daher, membrangebundene photoaktivierbare Adenylylzyklasen für die Manipulation der cAMP-vermittelten Signalübertragung in unmittelbarer Nähe der Plasmamembran zu entwickeln und zu implementieren. Zu diesem Zweck wurden die Guanylylzyklase Domänen der *Blastocladiella*- und *Catenaria*- Cyclase Opsine (CyclOps) entweder durch die Einführung der Mutationen E497K und C566D (abgekürzt als (A-2x)) oder durch die Mutationen E497K, H564D und C566T (abgekürzt als (A-3x)) zu Adenylylzyklasen mutiert.

Um den Nukleotid-Spezifitätswechsel von GTP zu ATP und das Ausmaß der lichtabhängigen cAMP-Erzeugung zu bestimmen, wurden die generierten Enzyme in Körperwandmuskelzellen von *C. elegans* exprimiert und *in vitro* cNMP-Messungen mit *C. elegans* Extrakten durchgeführt. Dabei wurden die höchsten Werte der lichtinduzierten cAMP-Erzeugung während konstanter Stimulation (0,5 mW/mm^2; 470 nm, 15 min) für die Varianten BeCyclOp(A-2x), YFP-BeCyclOp(A-2x) und YFP-CaCyclOp(A-2x) festgestellt (39, 57 bzw. 40 nM), obwohl sie nicht das Ausmaß erreichten, welche durch das lösliche bPAC (142 nM) erzeugt wurde. Im Gegensatz dazu wurden für die Versionen BeCyclOp(A-3x) und CaCyclOp(A-2x) geringe Mengen an erzeugtem cAMP gemessen (8 bzw. 7 nM). Darüber hinaus wurde für keines der generierten Enzyme eine übriggebliebene cGMP-Erzeugung und keine basale cAMP-Erzeugung festgestellt.

Um ihr Potenzial zur Auslösung und Modulation von cAMP-vermittelter cholinerger Neurotransmission zu beurteilen und den Einfluss der zytosolischen und membrannahen optogenetischen cAMP-Erzeugung zu bewerten, wurden die Enzyme in cholinergen Motoneuronen exprimiert und mit dem implementierten löslichen bPAC durch Analyse des Fortbewegungsverhaltens in festen und flüssigen Medien verglichen. Die Photoaktivierung von BeCyclOp(A-2x), YFP-BeCyclOp(A-2x) und YFP-CaCyclOp(A-2x) führte zu ähnlich verstärkten oder sogar stärkeren Verhaltensänderungen (Schwimmen und Kriechen) wie bPAC, während bei den durch bPAC hervorgerufenen Effekten eine schnellere abklingende Reaktion beobachtet wurde. Darüber hinaus wurde bei der zytosolischen cAMP-Produktion durch bPAC eine größere Vielfalt der Verhaltensänderungen festgestellt, d. h. erhöhte Biegewinkel und eine verringerte Körperlänge.

Mit Hilfe der konfokalen Fluoreszenzmikroskopie wurde das Expressionsniveau der YFP-markierten Enzyme in cholinergen Neuronen untersucht, wobei beide YFP-CyclOp(A-2x)s in ähnlichem Ausmaß exprimiert wurden, jedoch ~1,4-fach geringer als das lösliche bPAC-YFP. Um die Menge der lichtabhängigen cAMP-Produktion von bPAC und BeCyclOp(A-2x) unter Lichtbedingungen zu vergleichen, die den Bedingungen der Verhaltensexperimente (30 s) entsprechen, wurden cAMP-Messungen mit *C. elegans* Extrakten durchgeführt, wobei BeCyclOp(A-2x) eine viermal geringere Menge an optogenetischer cAMP-Produktion zeigte als das lösliche bPAC.

Zusammenfassend lässt sich sagen, dass die lokale (membranproximale) cAMP-Erzeugung durch die membrangebundenen photoaktivierbaren Adenylylzyklasen die cAMP-abhängige Neurotransmission cholinerger Motoneuronen möglicherweise spezifischer aktiviert als die zytosolische cAMP-Erzeugung, d.h. eine verstärkte Mobilisierung und Priming/Docking von synaptischen Vesikeln und eine verstärkte Füllung der synaptischen Vesikel mit dem Neurotransmitter Acetylcholin und damit eine Steigerung des Fortbewegungsverhaltens.

Der optogenetische Werkzeugkasten für die Manipulation der cGMP-vermittelten Signalübertragung in *C. elegans* bestand aus dem natürlichen membrangebundenen BeCyclOp und dem synthetischen löslichen bPGC. Letzterer erzeugt cGMP mit geringer Effizienz und langsamer Kinetik (~0,2 cGMP s^{-1}), während BeCyclOp die Produktion viel größerer Mengen von cGMP (L/D = 5000) bei hoher Umsatzrate (~17

cGMP s^{-1}) ermöglicht. Ein Ziel dieser Arbeit war es daher, ein Werkzeug zu entwickeln, dessen Eigenschaften zwischen denen von BeCyclOp und bPGC liegen. Mehrere orthologe CyclOps wurden von Gao et al. (2015) im Hinblick auf die lichtregulierte cGMP-Produktion durch *in vitro* Assays bewertet, die auf der Messung des cNMP-Gehalts von CyclOp-haltigen Oozyten Membranen basieren. Hier zeigte CaCyclOp nach BeCyclOp das höchste Verhältnis von Licht- zu Dunkelaktivität (L/D = 230) und wurde daher für die Charakterisierung in *C. elegans* ausgewählt. Die Photoaktivierung von CaCyclOp; TAX-2/-4 in Körperwandmuskelzellen verursachte im Vergleich zu BeCyclOp; TAX-2/-4 langsamere und weniger ausgeprägte Körperkontraktionen (~3,5 % Maximalkontraktion mit einer Kontraktionsrate von ~0,88 s für CaCyclOp gegenüber ~9 % Maximalkontraktion und einer Kontraktionsrate von ~0,23 s für BeCyclOp), während die Photoaktivierung von bPGC; TAX-2/-4 die geringste Körperkontraktion verursachte, d. h. ~2,5 % Maximalkontraktion mit einer Kontraktionsrate von ~1,78 s. Um die Nukleotidspezifität und das Ausmaß der lichtabhängigen cGMP-Erzeugung zu bestimmen, wurden *in vitro* cNMP-Messungen mit *C. elegans* Extrakten durchgeführt, wobei bPGC und CaCyclOp vergleichbare cGMP-Konzentrationen (18 bzw. 13 nM) erzeugten, während die höchste cGMP-Konzentration für BeCyclOp (74 nM) ermittelt wurde. Für alle untersuchten photoaktivierbaren Guanylylzyklasen wurden die Lichtsättigungsbedingungen in *C. elegans* bei Intensitäten von ≥ 0,2 mW/mm^2 erreicht, was mit den für die Channelrhodopsin-2 (ChR2) Aktivierung verwendeten Intensitäten vergleichbar ist. Zusammenfassend lässt sich sagen, dass BeCyclOp das leistungsfähigste Werkzeug zur Erzeugung von cGMP ist und CaCyclOp eine nützliche, membrangebundene Alternative zum löslichen bPGC darstellt.

Neben ihrer primären Anwendung als optogenetische Werkzeuge für die cNMP-Erzeugung können die photoaktivierbaren Nukleotidylzyklasen mit zyklischen Nukleotid-gesteuerten Kanälen (CNGCs) gekoppelt werden, um das Membranpotenzial erregbarer Zellen zu manipulieren. Der Vorteil dieser Systeme besteht darin, dass sie weniger Licht benötigen, da die Erzeugung des Second Messenger mit einer Verstärkung des Primärsignals einhergeht. Der TAX-2/-4-Kanal wird hauptsächlich durch cGMP, bei hohen Konzentrationen aber auch durch cAMP aktiviert (EC_{50}^{cGMP} = 8,4 µM; EC_{50}^{cAMP} = 300 µM). Der TAX-2/-4 CNGC wurde in Körperwandmuskelzellen entweder mit dem Wildtyp CaCyclOp oder den generierten membrangebundenen photoaktivierbaren Adenylylzyklasen kombiniert und mittels

Körperlängenanalyse mit den etablierten Systemen TAX-2/-4; BeCyclOp, TAX-2/-4; bPAC und TAX-2/-4; bPGC verglichen. Keines der untersuchten Systeme war in der Lage, vergleichbar starke und schnelle Depolarisationseffekte hervorzurufen wie das TAX-2/-4; BeCyclOp-System. Allerdings waren die induzierten Muskeldepolarisationen durch unterschiedliche Größenordnungen und kurz- und langanhaltende Effekte gekennzeichnet. Darüber hinaus wurde bei TAX-2/-4, welches an CaCyclOp, bPGC oder BeCyclOp(A-2x) gekoppelt ist, keine Desensibilisierung festgestellt, wie dies bei dem System TAX-2/-4; BeCyclOp der Fall war. Insgesamt wurde ein umfassender optogenetischer Mehrkomponenten-Werkzeugkasten für die Zelldepolarisation etabliert, wobei sich die Systeme in ihrer Effizienz, ihren enzymatischen Eigenschaften, ihrer Kinetik sowie ihren kurz- und lang anhaltenden Wirkungen unterscheiden.

Bisher wurden die Protonenpumpe Archaerhodopsin-3 (Arch), die Chloridpumpe Halorhodopsin (NpHR) und das Anionenrhodopsin (GtACR) als hyperpolarisierende optogenetische Werkzeuge in *C. elegans* etabliert. Ihre Anwendung geht jedoch mit unerwünschten Veränderungen der Ionenverteilung in der Membran einher und erfordert eine kontinuierliche Lichtstimulation. Aus diesem Grund war ein Ziel dieser Arbeit, optogenetische Zweikomponenten-Silencing-Systeme zur Manipulation von K^+-Strömen zu entwickeln und zu implementieren. Der cGMP-gesteuerte K^+-Kanal BeCNG1 stammt aus dem aquatischen Pilz *Blastocladiella emersonii*, bei dem der Kanal und BeCyclOp für die phototaktische Reaktion der Zoospore verantwortlich sind. Dieser Mechanismus wurde adaptiert und nach seiner Funktionalität in Körperwandmuskelzellen von *C. elegans* durch Körperlängenmessungen bewertet, wobei das System in der Lage war, die Zellen leicht zu hyperpolarisieren (~1 % Körperverlängerung innerhalb von ~3 s), ein Effekt, der auch nach Ausschalten des Lichts bestehen blieb. Ein zweiter Ansatz koppelt den cAMP-gesteuerten K^+-Kanal SthK aus *Spirochaeta thermophila* entweder mit einer der generierten membrangebundenen photoaktivierbaren Adenylylzyklasen oder dem löslichen bPAC. Unter den untersuchten Systemen stechen die Kombinationen SthK; bPAC und SthK; BeCyclOp(A-2x) durch ihre starken und langanhaltenden Hyperpolarisationseffekte hervor. In den Körperwandmuskelzellen bewirkten sie eine Verlängerung der Körperlänge von ~4 bzw. ~3 %. Bemerkenswert ist, dass bei SthK; bPAC die induzierte Muskelhyperpolarisation bis zu etwa 10 Minuten nach der Lichtapplikation anhielt. In cholinergen Neuronen verringerten sie die

Schwimmfrequenzen um etwa 84,4 bzw. 72,3 %. Darüber hinaus wurde der Kanal mit BeCyclOp(A-3x) kombiniert, einem Enzym, das sich durch die Erzeugung geringer Mengen von cAMP auszeichnet. In den Muskelzellen der Körperwand löste das System die stärkste Muskelhyperpolarisation unter den untersuchten Systemen aus (~5 %), wobei die Wirkung einige Sekunden nach dem Ausschalten des Lichts nachließ. Die Expression von SthK reduzierte jedoch die basale Schwimmfrequenz der Tiere, unabhängig vom Zelltyp (Körperwandmuskelzellen oder cholinerge Neuronen). Die basale Schwimmfrequenz wurde durch die Koexpression des Kanals mit den photoaktivierbaren Adenylylzyklasen weiter reduziert (mit Ausnahme von BeCyclOp(A-3x) in Körperwandmuskelzellen). Für das System SthK; bPAC war die Voraktivierung bereits im Dunkeln beträchtlich, weshalb diese Kombination in *C. elegans* nur von begrenztem Nutzen zu sein scheint, es sei denn, eine dauerhafte K^+-basierte Hemmung des gewünschten Zelltyps wird angestrebt. Außerdem zeigten die Systeme SthK; BeCyclOp(A-2x) und SthK; BeCyclOp(A-3x) eine erhebliche Voraktivierung im Dunkeln in cholinergen Motoneuronen. Die Expression von YFP-BeCyclOp(A-2x) und geringen Mengen von SthK in cholinergen Motoneuronen stellte die basale Schwimmfrequenz wieder her, es wurde jedoch keine lichtabhängige Hemmung beobachtet. Nichtsdestotrotz würde das System ein leistungsfähiges Silencing-System für cholinerge Motoneuronen darstellen, da YFP-BeCyclOp(A-2x) durch die Erzeugung hoher Amplituden von cAMP gekennzeichnet ist und im Vergleich zu BeCyclOp(A-2x) weniger oder keine Dunkelaktivität zeigt. Somit kann die relative Expression weiter titriert werden, um ein Optimum für dieses System zu erreichen.

Ein weiterer Teil dieser Arbeit zielte auf die Identifizierung möglicher cAMP-Effektoren ab, die an der cAMP-induzierten Hyperpolarisation der Körperwandmuskelzellen von *C. elegans* beteiligt sind. J. Nagpal, ein ehemaliger Doktorand im Gottschalk-Labor, fand heraus, dass die optogenetische cAMP-Erzeugung durch bPAC in *C. elegans* Körperwandmuskelzellen eine Muskelrelaxation bewirkt, d. h. eine Zunahme der Körperlänge um etwa 2 %. Um einen möglichen Mechanismus für die cAMP-induzierte Muskelrelaxation zu untersuchen, wurde ein cAMP-modulierter Ionenkanal in der Plasmamembran vermutet. Um Ionenkanäle mit einer cAMP-Bindungsdomäne zu identifizieren, wurde ein Sequenz-Alignment der regulatorischen Untereinheit Riα der PKA gegen das *C. elegans* Genom durchgeführt, wobei vier zyklische Nukleotid-gesteuerte Ionenkanäle

(CNG-1, CNG-2, CNG-3 und CHE-6) und zwei spannungsgesteuerte Kaliumkanäle (EGL-2, UNC-103) identifiziert wurden. Mit Hilfe von S. Zhou und A. Pieragnolo wurden Stämme erzeugt, die bPAC in Muskelzellen mit doppeltem Mutationshintergrund (Funktionsverlust des Kanals und *lite-1(ce314)*) und mit Funktionsverlust des Kanals exprimieren. Die Untersuchung der optogenetisch ausgelösten Muskelrelaxation in doppeltem Mutanten Hintergrund wurde von S. Zhou in ihrer BSc Thesis durchgeführt. Die optogenetische cAMP-Erzeugung führte bei allen doppelten Mutationshintergründen zu keinen oder sehr schwachen Körperdehnungen (+1 %). Bei der Analyse des Schwimmverhaltens stellte sie fest, dass die cAMP-Erzeugung durch bPAC bei den meisten Mutanten Stämmen die Schwimmgeschwindigkeit der Tiere stark verringerte (~52 - 72 % nach 60 s Lichtapplikation; 470 nm; 0,2 mW/mm^2), wenn auch nicht in dem Maße wie bei der *lite-1(ce314)* Kontrolle und der Mutante *egl-2(rg4); lite-1(ce314)* (~77 %). Bemerkenswert ist, dass die bPAC-Aktivierung im *unc-103(n1213); lite-1(ce314)* Hintergrund eine verzögerte und geringere Abnahme der Schwimmfrequenz (21 %) bewirkte. Bei den Kanalverlustmutanten reduzierte die optogenetische cAMP-Generierung die Schwimmzyklen bei allen Stämmen stark (~64 - 89 % nach 60 s Lichtapplikation; 470 nm; 0,2 mW/mm^2), wobei bei den Mutanten *che-6(e1126)IV* (60 %), *unc-103(n1213)* (64 %), *egl-2(rg4)* (64 %) und *cng-3(jh113)* (67 %) die Reduktionen nicht das Ausmaß der Wildtypkontrolle (75 %) erreichten. Im Gegensatz dazu wurden bei den Mutanten *cng-2(tm4267)* (82 %) und *cng-1(jh111)* (89 %) stärkere Reduzierungen des Schwimmzyklus festgestellt. Zusammenfassend lässt sich sagen, dass die bPAC-Aktivierung hinsichtlich der Kanäle CNG-3, CHE-6 und UNC-103 eine geringfügigere Verringerung der Schwimmgeschwindigkeit in den doppelten Mutationshintergründen und Kanalverlustmutanten im Vergleich zu den Kontrollen *lite-1(ce314)* und Wildtyp verursachte, was auf eine mögliche Rolle der Kanäle bei der cAMP-induzierten Muskelhyperpolarisation hindeutet.

Abstract

In the past decade, the optogenetic toolbox for the manipulation of ion currents and cNMP levels in *Caenorhabditis elegans* (*C. elegans*) expanded. However, the implemented tools for cAMP generation were soluble enzymes (euPAC, bPAC, IlaC22 k27 and PaaC) and thus they do not precisely mimic physiological cAMP signalling occurring in microdomains in close proximity to the plasma membrane. Here, cAMP is predominantly generated by membrane-bound adenylyl cyclases, that are located in microdomains together with G protein-coupled receptors (GPCRs), protein kinase A (PKA) and their targets, enabling spatially and temporal regulation of cAMP signalling. For this reason, one aim of this study was to develop and implement membrane bound photoactivatable adenylyl cyclases for the manipulation of cAMP mediated signalling in close proximity to the plasma membrane. For this purpose, the guanylyl cyclase domains of the *Blastocladiella* and *Catenaria* Cyclase Opsins (CyclOps) were mutated to adenylyl cyclases either by introducing the mutations E497K and C566D (abbreviated as (A-2x)) or by the mutations E497K, H564D, and C566T (abbreviated as (A-3x)).

To determine the nucleotide specificity switch from GTP to ATP and the extent of light-dependent cAMP generation, the engineered enzymes were expressed in body wall muscle cells of *C. elegans* and *in vitro* cNMP measurements using *C. elegans* extracts were performed. Here, the highest levels of light induced cAMP generation during sustained stimulation (0.5 mW/mm^2; 470 nm, 15 min) were detected for the variants BeCyclOp(A-2x), YFP-BeCyclOp(A-2x), and YFP-CaCyclOp(A-2x) (39, 57, 40 nM, respectively), though they did not reach the extent produced by the soluble bPAC (142 nM). In contrast, low magnitudes of generated cAMP were measured for the versions BeCyclOp(A-3x) and CaCyclOp(A-2x) (8 and 7 nM, respectively). Importantly, no obvious residual cGMP and basal activity was ascertained for any of the engineered enzymes.

To assess their potential to trigger and modulate cAMP mediated cholinergic neurotransmission, and to evaluate the influence of cytosolic and membrane proximal optogenetic cAMP generation, the enzymes were expressed in cholinergic motor neurons and compared to the implemented soluble bPAC via locomotion behaviour

analysis on solid and in liquid media. Photoactivation of BeCyclOp(A-2x), YFP-BeCyclOp(A-2x), and YFP-CaCyclOp(A-2x) caused similarly enhanced or even more potent behavioural changes (swimming and crawling) as bPAC, whereas a more rapidly decaying response was observed for the bPAC evoked effects. Moreover, an increased diversity of the behavioural output was detected for cytosolic cAMP production by bPAC, i.e. increased bending angles and a decreased body length.

Confocal fluorescence microscopy was performed to examine the expression levels of YFP-tagged enzymes in cholinergic neurons, whereas both YFP-CyclOp(A-2x)s were expressed at similar levels, but ~1.4-fold lower relative to the soluble bPAC-YFP. To compare the amount of light-dependent cAMP generation bPAC and BeCyclOp(A-2x) at light conditions that match the conditions of the behavioural experiments (30 s), cAMP measurements using *C. elegans* extracts were performed, whereas BeCyclOp(A-2x) depicted a 4-fold lower amount of optogenetic cAMP production than the soluble bPAC.

In sum, local (membrane proximal) cAMP generation by the membrane-bound photoactivatable adenylyl cyclases may more specifically activate cAMP dependent neurotransmission of cholinergic motor neurons than cytosolic cAMP generation, i.e. an increased mobilization and priming/docking of synaptic vesicles and an increased filling of the synaptic vesicles with the neurotransmitter acetylcholine and thus an increase in locomotion behaviour.

The optogenetic toolbox for the manipulation of cGMP mediated signalling in *C. elegans* consisted of the natural membrane-bound BeCyclOp and the artificial soluble bPGC. The latter generates cGMP with low efficiency and slow kinetics (~0.2 cGMP s^{-1}), whereas BeCyclOp enables the production of much larger amounts of cGMP (L/D = 5000) at a high turnover rate (~17 cGMP s^{-1}). Thus, one aim of this thesis was to implement a tool with features in between those of BeCyclOp and bPGC. Several orthologous CyclOps were assessed by Gao et al., 2015 for light-regulated cGMP production by *in vitro* assays based on the measurement of the cNMP content from CyclOp containing oocyte membranes. Here, CaCyclOp showed the highest ratio of light versus dark activity (L/D = 230) after BeCyclOp, and thus was selected for characterization in *C. elegans*. Photoactivation of CaCyclOp; TAX-2/-4 in body wall muscle cells caused slower and less pronounced body contractions compared to BeCyclOp; TAX-2/-4 (~3.5 % peak contraction with a contraction on rate of ~0.88 s

for CaCyclOp vs ~9 % peak contraction and a contraction on rate of ~0.23 s for BeCyclOp), whereas photoactivation of bPGC; TAX-2/-4 caused the slightest body contraction, i.e. ~2.5 % peak contraction with a contraction on rate of ~1.78 s. To determine the nucleotide specificity and the extent of light-dependent cGMP generation, *in vitro* cNMP measurements using *C. elegans* extracts were performed, whereas bPGC and CaCyclOp produced comparable cGMP levels (18, 13 nM, respectively), and highest cGMP level was determined for BeCyclOp (74 nM). For all analysed photoactivatable guanylyl cyclases, light saturation conditions in *C. elegans* were reached at intensities of ≥ 0.2 mW/mm^2, that is comparable to applied intensities for channelrhodopsin-2 (ChR2) activation. In sum, BeCyclOp is the most potent tool for cGMP generation, and CaCyclOp is a useful, membrane-bound alternative to the soluble bPGC.

Beyond their primary application as optogenetic tools for cNMP generation, the photoactivatable nucleotidyl cyclases can be coupled to cyclic nucleotide-gated channels (CNGCs) to manipulate the membrane potential of excitable cells. The benefit of these systems is their reduce need for light, since second messenger generation is accompanied by amplification of the primary signal. The TAX-2/-4 channel is mainly gated by cGMP, but also by cAMP at high concentrations (EC_{50}^{cGMP} = 8.4 µM; EC_{50}^{cAMP} = 300 µM). The TAX-2/-4 CNGC was combined in body wall muscle cells with either wild type CaCyclOp or the engineered membrane-bound photoactivatable adenylyl cyclases and evaluated and compared via body length analysis to the established systems TAX-2/-4; BeCyclOp, TAX-2/-4; bPAC and TAX-2/-4; bPGC. None of the investigated systems were able to evoke comparably strong and fast depolarization effects as the TAX-2/-4; BeCyclOp system. However, the provoked muscle depolarizations are characterized by different orders of magnitudes and short- and long-lasting effects. Moreover, no desensitization was detected for TAX-2/-4 coupled to CaCyclOp, bPGC or BeCyclOp(A-2x), as it was observed for the system TAX-2/-4; BeCyclOp. In sum, a comprehensive multicomponent optogenetic toolbox for cell depolarization was established, whereas the systems differ in their efficiency, enzymatic properties, kinetics and short- and long-lasting effects.

So far, the proton pump archaerhodopsin-3 (Arch), the chloride pump halorhodopsin (NpHR), and the anion rhodopsin (GtACR) have been established as hyperpolarizing optogenetic tools in *C. elegans*. However, their application is accompanied by

undesired changes in ion distribution across the membrane and requires continuous light stimulation. For this reason, one aim of this study was to develop and implement two-component optogenetic silencing systems for the manipulation of K^+-currents. The cGMP-gated K^+-channel BeCNG1 channel originates from the aquatic fungus *Blastocladiella emersonii*, in which the channel and BeCyclOp are responsible for the phototactic response of the zoospore. This mechanism was adapted and assessed after its functionality in *C. elegans* body wall muscle cells via body length measurements, where the system was able to slightly hyperpolarize the cells (~1 % body elongation within ~3 s), an effect that remained even after turning off light. A second approach couples the cAMP-gated K^+-channel SthK from *Spirochaeta thermophila* with either one of the generated membrane-bound photoactivatable adenylyl cyclases or the soluble bPAC. Amongst the analysed systems, the combinations SthK; bPAC and SthK; BeCyclOp(A-2x) protruded due to their strong and long-lasting hyperpolarization effects. In body wall muscle cells, they evoked body length elongations of ~4 and ~3 %, respectively. Noteworthy, for SthK; bPAC the induced muscle hyperpolarization lasted up to about 10 min after light application. In cholinergic neurons, they decreased the swimming frequencies by about 84.4 and 72.3 %, respectively. In addition, the channel was combined with BeCyclOp(A-3x), an enzyme that is characterized by the generation of low levels of cAMP. In body wall muscle cells, the system provoked the strongest muscle hyperpolarization amongst the analysed systems (~5 %), whereas the effect decayed a few seconds after turning off light. However, expression of SthK alone reduced the basal swimming frequency of the animals, independent of the cell type (body wall muscle cells or cholinergic neurons). The basal swimming rate was further reduced by co-expression of the channel with the photoactivatable adenylyl cyclases (with exception of BeCyclOp(A-3x) in body wall muscle cells). The pre-activation was already substantial in dark for the system SthK; bPAC, wherefor this combination appears of limited use in *C. elegans* unless researchers aimed on permanent K^+-based inhibition of the desired cell type. Also, the systems SthK; BeCyclOp(A-2x) and SthK; BeCyclOp(A-3x) exhibited substantial pre-activation in dark in cholinergic motor neurons. Expression of YFP-BeCyclOp(A-2x) and low levels of SthK in cholinergic motor neurons restored the basal swimming frequency, however, no light dependent inhibition was observed. Nevertheless, the system would represent a powerful silencing system for cholinergic motor neurons, as YFP-BeCyclOp(A-2x) is

characterized by the generation of high amplitudes of cAMP, and in relation to BeCyclOp(A-2x) depicts less or no dark activity. Thus, the relative expression can be further titrated to achieve an optimum for this system.

Another part of this work aimed on the identification of possible cAMP effectors involved in cAMP-induced hyperpolarization of *C. elegans* body wall muscle cells. J. Nagpal, a former PhD student in the Gottschalk lab, found that optogenetic cAMP generation by bPAC in *C. elegans* muscle cells caused muscle relaxation, i.e. evoked an increase in the body length of about 2 %. To investigate a possible mechanism for cAMP induced muscle relaxation, a cAMP modulated ion channel in the plasma membrane was assumed. To identify ion channels with a cAMP binding domain, a sequence alignment of PKA´s regulatory subunit Riα against the *C. elegans* genome was executed, identifying four cyclic nucleotide-gated ion channels (CNG-1, CNG-2, CNG-3 and CHE-6) and two voltage-gated potassium channels (EGL-2, UNC-103). With the help of S. Zhou and A. Pieragnolo, strains expressing bPAC in muscle cells of double mutant background (channel loss of function and *lite-1(ce314)*), and in channel loss of function background were generated. Investigation of optogenetically triggered muscle relaxation in double mutant background was performed by S. Zhou in her BSc thesis. Optogenetic cAMP generation in all channel loss of function *lite-1(ce314)* mutants evoked no or very weak body elongations (+1 %). For swimming behaviour analysis, she found that cAMP generation by bPAC in most mutant strains strongly decreased the swimming rates of the animals (~52 - 72 % after 60 s light application; 470 nm; 0.2 mW/mm^2), though they did not reach the extent as detected for the *lite-1(ce314)* control and the mutant *egl-2(rg4); lite-1(ce314)* (~77 %). Noteworthy, bPAC activation in *unc-103(n1213); lite-1(ce314)* background caused a delayed and smaller decrease of the swimming frequency (21 %). In channel loss of function mutants, optogenetic cAMP generation strongly reduced the swimming cycles for all strains (~64 - 89 % after 60 s light application; 470 nm; 0.2 mW/mm^2), whereby for the mutants *che-6(e1126)IV* (60 %), unc-103(n1213) (64 %), *egl-2(rg4)* (64 %) and *cng-3(jh113)* (67 %) the reductions reached not the extend as the wild type control (75 %). In contrast, stronger swimming cycle reductions were detected for the mutants *cng-2(tm4267)* (82 %) and *cng-1(jh111)* (89 %). In sum, for CNG-3, CHE-6, and UNC-103, bPAC activation caused minor swimming rate reductions in channel loss of function; *lite-1(ce314)* and channel loss of function backgrounds

compared to the controls *lite-1(ce314)* and wild type, suggesting a potential role for the channels in cAMP induced muscle hyperpolarization.

1. Introduction

1.1. Optogenetics

Optogenetics combines genetic and optical techniques to control and monitor cellular activities in a spatiotemporally highly defined manner within biological systems as complex as freely moving mammals (wormDeisseroth, 2015; Knöpfel *et al.*, 2010). For this purpose, photosensitive proteins are genetically targeted to particular cell types, whereas fluorescent reporters are used to monitor and optogenetic actuators to modulate cellular activities (Rost *et al.*, 2017). In neuroscience, optogenetics is a well-established technique because optogenetic modulation matches the speed of electrical neuronal activity, allows experimental intervention limited to specific time periods, and it enables genetically targeted and cell-type specific expression of photosensitive proteins (Rost *et al.*, 2017). Application of optogenetics facilitates new insights into a broad range of scientific questions e.g. in behaviour, physiology and pathology (Deisseroth, 2015). In the past decades, several optogenetic tools were developed and implemented for distinct applications in various model organisms, including tools for e.g. neuronal activation (e.g. channelrhodopsin-2 (ChR2)) and silencing (e.g. *Natronomonas pharaonis* halorhodopsin (NpHR)), G-protein activation (e.g. OptoXR), second messenger manipulation (e.g. *Blastocladiella emersonii* guanylyl cyclase rhodopsin (BeCyclOp)), monitoring of ion concentrations (e.g. GCaMP), and membrane voltage reporters (e.g. QuasAr) (Azimi Hashemi *et al.*, 2019; Boyden *et al.*, 2005; Gao *et al.*, 2015; Husson *et al.*, 2012; Kim *et al.*, 2005; Nagel *et al.*, 2005; Rost *et al.*, 2017; Scheib *et al.*, 2015).

1.2. Sensory photoreceptors

Sensory photoreceptors are light-sensitive proteins that are responsible for the adjustment of the cellular activity to ambient light conditions and are involved in processes such as photosynthesis, bioluminescence, vision, and biological rhythms of organisms (Rost *et al.*, 2017). They could be found in all kingdoms of life and include seven main protein classes: rhodopsins, blue light receptors using flavine adenine dinucleotide (BLUF), light-oxygen-voltage (LOV) sensors, photoactive yellow

proteins (or xanthopsins), cryptochromes, phytochromes, and UV-B receptors (UVR8) (Ahmad *et al.*, 1993; Gomelsky *et al.*, 2002; Hoff *et al.*, 1997; Huala *et al.*, 1997; Kort *et al.*, 1996; Quail, 1998; Rost *et al.*, 2017; Spudich *et al.*, 2000; van der Horst *et al.*, 2004). In contrast to UVR8 receptors that utilizes intrinsic tryptophan clusters, the photoreceptors bind exogenous cofactors, termed chromophores, that absorb light and transfer energy to the protein scaffolds. The chromophores comprise conjugated π- systems that allows the delocalization of electrons and, depending on the size of the system, the absorption of light in a range between 300 – 800 nm (Rost *et al.*, 2017). Photon absorption evokes photochemical transformations (i.e. cis-trans isomerization, photoelectron transfer, rearrangement of hydrogen bonds, or flavin mononucleotide (FMN)–cysteinyl adduct formation) in the chromophores that usually cause conformational changes in the protein backbone, which are finally transmitted to the respective effector domains, leading to receptor activation and signal propagation (Shcherbakova *et al.*, 2015). Depending on the light-sensitive protein, three types of signal transmission are distinguished: Transduction within a photoreceptor that combine sensory and receptor functions (e.g. ChR2), transmission from the sensory to the effector domain (e.g. BLUF proteins), and propagation to distinct interacting protein partners (e.g. visual rhodopsins). Complementary to the natural sensory photoreceptors, synthetic photoreceptors were engineered via modification and recombination of existing photoreceptors (Figure 1) (Rost *et al.*, 2017). The families of the rhodopsins and BLUF and their application as optogenetic tools are described in more detail in the following subsections.

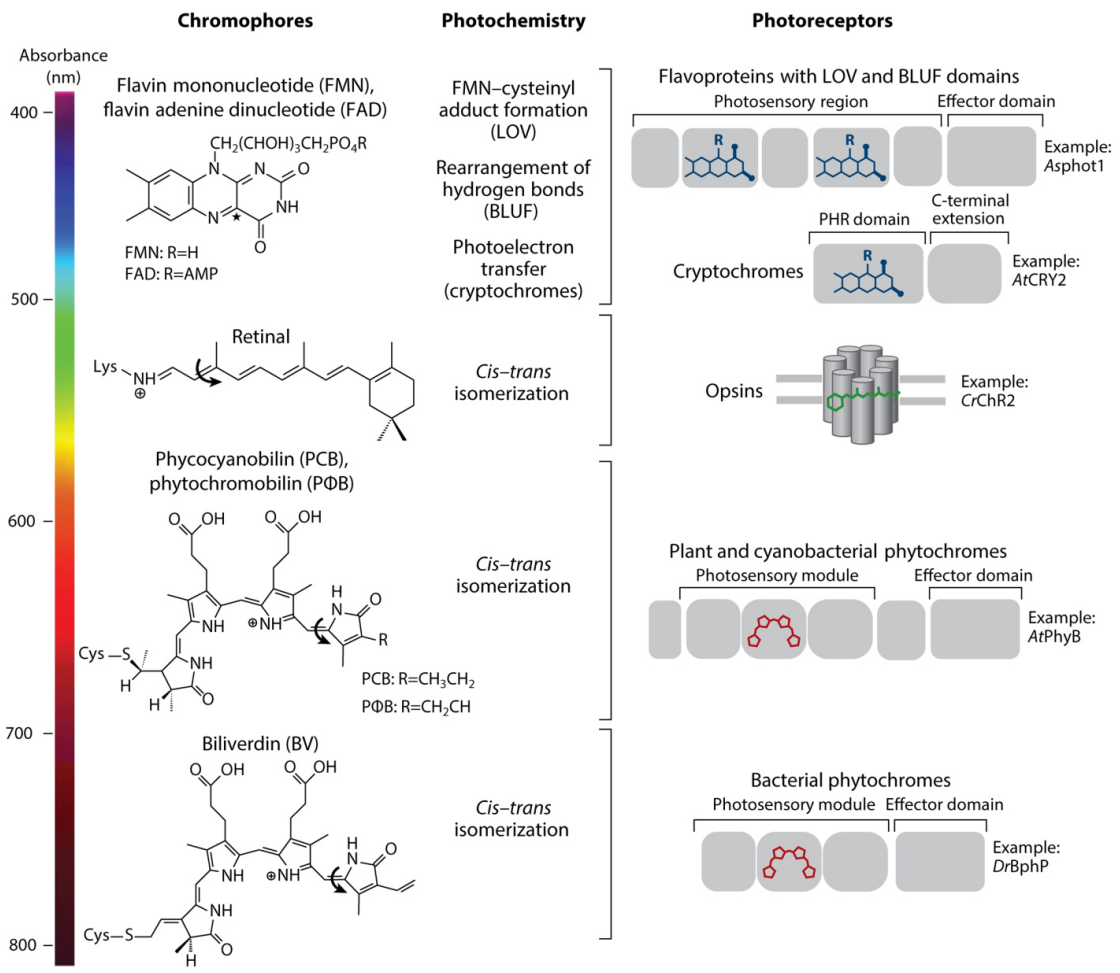

Figure 1: Overview of particular sensory photoreceptor classes and their associated chromophores and primary photochemical reactions. *Left) Illustrated are the chemical structures of flavin mononucleotide (FMN), flavin adenine dinucleotide (FAD), retinal, phycocyanobilin (PCB), phytochromobilin (PΦB), and biliverdin (BV), and their primary photochemistry. The colour-scale bar depicts their absorption maximum wavelength in their natural photoreceptor. Right) Schematic domain architecture of following natural photoreceptor classes: flavoproteins with light-oxygen-voltage (LOV) and flavine adenine dinucleotide (BLUF) domains, cryptochromes, opsins, plant and cyanobacterial phytochromes, and bacterial phytochromes. Shown are the domain architectures for an example of each receptor class. Abbreviations: Asphot1, Avena sativa phototropin 1; AtCRY2, Arabidopsis thaliana cryptochrome 2; AtPhyB, A. thaliana phytochrome B; CrChR2, Chlamydomonas reinhardtii channelrhodopsin-2; DrBphP, Deinococcus radiodurans bacterial phytochrome; LOV, light-oxygen voltage-sensing. Image adapted from (Shcherbakova et al., 2015).*

1.2.1. Rhodopsins

Rhodopsins are integral membrane proteins which can be found in all domains of live - *Archea*, *Bacteria* and *Eukaryotes*, where they are responsible for light sensation and responses. Rhodopsins consist out of an opsin apoprotein moiety and a linked retinal as chromophore (aldehyde of vitamin A). The retinal chromophore is responsible for photon absorption, which causes an isomerization of the polyene

backbone of retinal at different positions (depending on the class of rhodopsin) and which is further transmitted to the opsin moiety and triggers the initiation of intra- or intercellular signalling. Rhodopsins are classified into two subfamilies – type I rhodopsins (microbial rhodopsins) and type II rhodopsins (animal rhodopsins) (Spudich *et al.*, 2000). Microbial rhodopsins are utilized by lower organisms (prokaryotes, algae, fungi), whereas animal rhodopsins are used by higher eukaryotes (Palczewski, 2006; Spudich, 2006). Though the sequence homology between both types is extremely low, they share a common structural architecture - the opsin domain consists of seven transmembrane (TM) α-helices with an extracellular N- and cytosolic C-terminus (Figure 2) (Man *et al.*, 2003; Soppa, 1994; Spudich *et al.*, 2000). The retinal chromophore is attached to the opsin protein via a Schiff base (RSB) linkage to the ε-amino group of a conserved lysine residue in TM7. In most cases, the retinal Schiff base is protonated ($RSBH^+$) and stabilized by conserved counterion residues containing carboxylate side chains, and changes in the protonation state are crucial for its function (Ernst *et al.*, 2014). Microbial rhodopsins bind retinal in the all-*trans* configuration in dark state, which isomerizes to the 13-*cis* configuration upon photon absorption. In contrast to this, animal rhodopsins bind 11-*cis* retinal in dark state, that photo-isomerizes to all-*trans* retinal (ATR) (Nakanishi, 1991; Spudich *et al.*, 2000). In microbial rhodopsins, the activated retinal chromophore remains covalently attached to the opsin partner and thermally reverts to the all-*trans* configuration, whereas in animal rhodopsins retinal dissociates after isomerization and a novel 11-*cis* retinal has to be recruited (Zhang *et al.*, 2011). While animal rhodopsins are specialized G-protein-coupled receptors (GPCR), microbial rhodopsins act as light-driven ion pumps, light-gated ion channels or light sensors which couple to transducer proteins (Klare *et al.*, 2008).

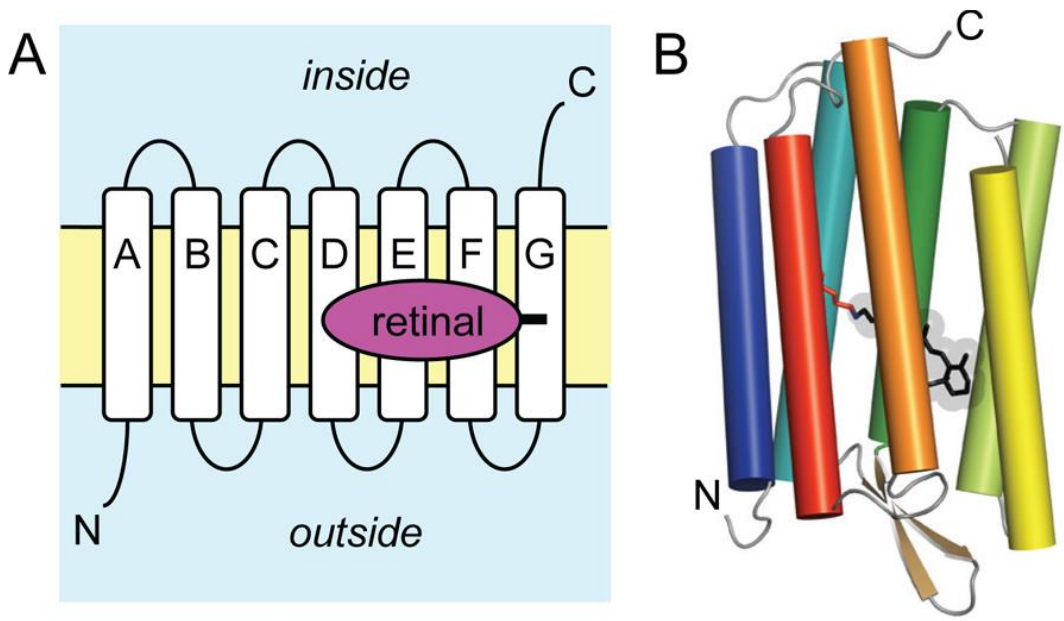

Figure 2: Schematic representation of the architecture of rhodopsins. *A) The opsin protein consists of seven transmembrane (TM) α-helices with an extracellular N- and cytosolic C-terminus. The retinal chromophore is bound to the ε-amino group of a conserved lysine residue in helix G (TM7) via a Schiff base bond (RSB). The TM helices in microbial rhodopsins are referred to as helix A-G and TM1-7 in animal rhodopsins. B) Representation of the bacteriorhodopsin structure (PDB ID: 1C3W). Image adapted from (Ernst et al., 2014).*

In microbial rhodopsins, photon absorption by the retinal chromophore and the accompanying isomerization from the all-*trans* to the 13-*cis* configuration triggers a cyclic reaction of the retinal/opsin ensemble, termed as `photocycle`. A typical photocycle for microbial rhodopsins, exemplified for bacteriorhodopsin (BR) is illustrated in figure 3 (Balashov *et al.*, 2001; Haupts *et al.*, 1999; Herzfeld *et al.*, 2002; Lanyi, 2004; Mathies *et al.*, 1991). Here, spectrally distinct intermediates sequentially termed `K`, `L`, `M`, `N`, and `O`, are formed until the ground (dark) state is recovered. The spectroscopic features of the individual intermediates are dependent on the isomeric configuration, planarity, and the protonation state of the retinal, ion changes, water molecules, and the position of the surrounding protein. The red-shifted K intermediate is followed by the blue-shifted L intermediate, which serves as precursor of the proton transfer reaction from the $RSBH^+$ to its primary carboxyl proton acceptor. This transfer leads to the formation of the blue-shifted M intermediate (Braiman *et al.*, 1980; Lozier *et al.*, 1975). Regarding microbial chloride pumps, no deprotonation of the $RSBH^+$ occurs, and the L intermediate is directly converted into the N intermediate (Varo *et al.*, 1995). In contrast, the N intermediate in microbial proton-pumps is formed due to reprotonation of the RSB. The N

intermediate is characterized by the largest influence on the conformation of the protein moiety (Klare *et al.*, 2004). The photocycle ends with the formation of the red-shifted O intermediate and the recovery of the ground state.

In general, the de- and reprotonation of the RSB evoke conformational changes of the protein moiety, leading to functionally relevant events such as opening or closing of a pore, changes of the surface accessibility or the activation of transducers (Govorunova *et al.*, 2017). Further, the molecular dynamics of the photocycle are linked to the protein function, i.e. for ion-pumping rhodopsins, one ion is actively transported per photocycle, and fast kinetics determine the pump efficacy at high light intensities, whereas sensory rhodopsins depict slow kinetics for proper signal-propagation from the signalling state of the sensor to the effector (Mukherjee *et al.*, 2019).

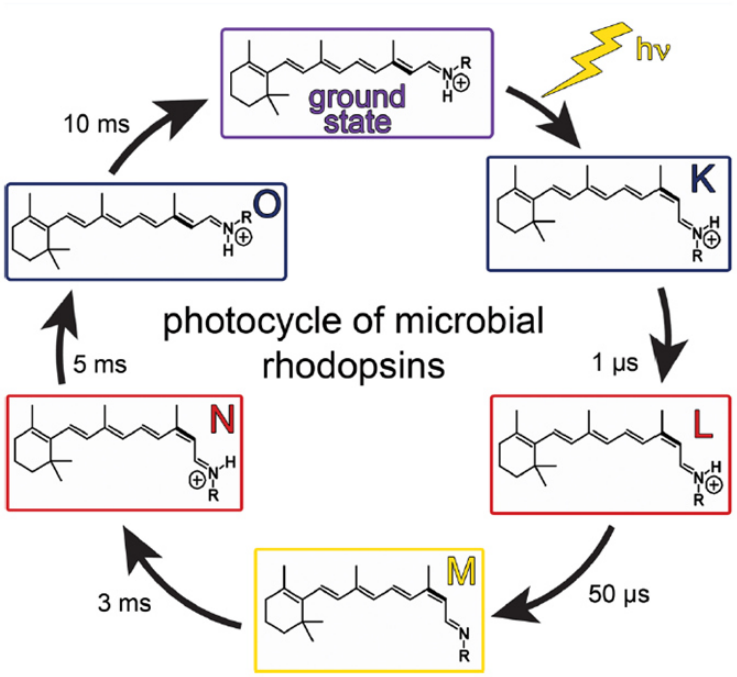

Figure 3: Overview of the photocycle of microbial rhodopsins. *The photocycle is initiated by photon absorption and accompanying isomerization from the all-trans to the 13-cis configuration of the retinal. A proton transfer reaction from the RSBH+ of the L intermediate to its primary carboxyl proton acceptor leads to the formation of the M state, followed by reprotonation of the RSB and formation of the N intermediate. Thermal reisomerization of retinal leads to formation of the O intermediate and return to the ground state. The photocycle intermediates and their properties are derived from bacteriorhodopsin, where K and O are red-shifted states, whereas L, M, and N are blue-shifted intermediates. Image adapted from (Ernst et al., 2014).*

1.2.1.1. Cyclase Opsins

The Cyclase Opsins (CyclOps), also termed as rhodopsin guanylyl cyclases (RhGCs), belong to the recently identified class of enzymerhodopsins. This family is characterized by the combination of an N-terminal type-1 rhodopsin domain and a C-terminal enzyme domain, and besides to the CyclOps, it encompasses the histidine kinase rhodopsins (HKRs) and rhodopsin phosphodiesterases (RhoPDEs) (Mukherjee *et al.*, 2019). Several orthologous CyclOps were found in the genomes of related fungi and assessed in *Xenopus* oocytes with respect to light-regulated 3`,5`-cyclic guanosine monophosphate (cGMP) production. Whereas the *Blastocladiella emersonii* (Be) and *Catenaria anguillulae* (Ca) CyclOps produced cGMP upon activation, the other CyclOps had no or little light-dependent enzymatic activity (Gao *et al.*, 2015). BeCyclOp and CaCyclOp depict 77% sequence similarity, with the largest differences occurring within the N-terminal domain and the TM helices four and five, including the helix 4/5-loop (Scheib *et al.*, 2018). Both CyclOps were characterized and implemented as membrane-bound optogenetic tools for cGMP generation in various cells and organisms. Both proteins depict a high substrate specificity towards GTP, no detectable dark activity and light versus dark activities of L/D = 230 (CaCyclOp) and L/D = 5000 (BeCyclOp) (Gao *et al.*, 2015; Scheib *et al.*, 2015). Furthermore, both proteins were converted into adenylyl cyclases by mutating two to three key amino acids in the active site, generating membrane-bound optogenetic tools for 3`,5`-cyclic adenosine monophosphate (cAMP) production. They are characterized by the production of cAMP with high specificity and by light versus dark activities of L/D = 220 (YFP-BeCyclOp(A-2x)) and L/D = 280 (YFP-CaCyclOp(A-2x)) in *Xenopus* oocyte membranes, and of L/D ratios of 12 (BeCyclOp(A2x)), 30 (YFP-BeCyclOp(A-2x)), and 13 (YFP-CaCyclOp(A-2x)) in *Caenorhabditis elegans* (*C. elegans*) extracts (Henss *et al.*, 2021; Scheib *et al.*, 2018).

CyclOps are particular proteins because they combine a microbial type-I rhodopsin domain and a C-terminal guanylyl cyclase domain. In contrast to microbial rhodopsins, they have an additional TM helix (helix 0) and an intracellularly located N-terminus that includes an extra helix (helix -1) (Figure 4) (Gao *et al.*, 2015; Mukherjee *et al.*, 2019; Scheib *et al.*, 2018; Scheib *et al.*, 2015). The guanylyl cyclase domain is connected to the rhodopsin moiety via 50 amino acids with pronounced heptad repeats which is typical for coiled-coil structures. Interestingly, mutations

affecting the coiled-coil structure cause the loss of photoregulation (Mukherjee *et al.*, 2019). Further, the linker includes a conserved stretch of 19 amino acids, the cyclase transducing element, which is also present in class III nucleotidyl cyclases (Govorunova *et al.*, 2017; Mukherjee *et al.*, 2019). Truncation of the N-terminal domain affects the enzymatic activity of the guanylyl cyclase moiety, thus indicating its functional relevance for the regulation and activation of the activity of the guanylyl cyclase domain (Fischer *et al.*, 2021; Gao *et al.*, 2015; Scheib *et al.*, 2015).

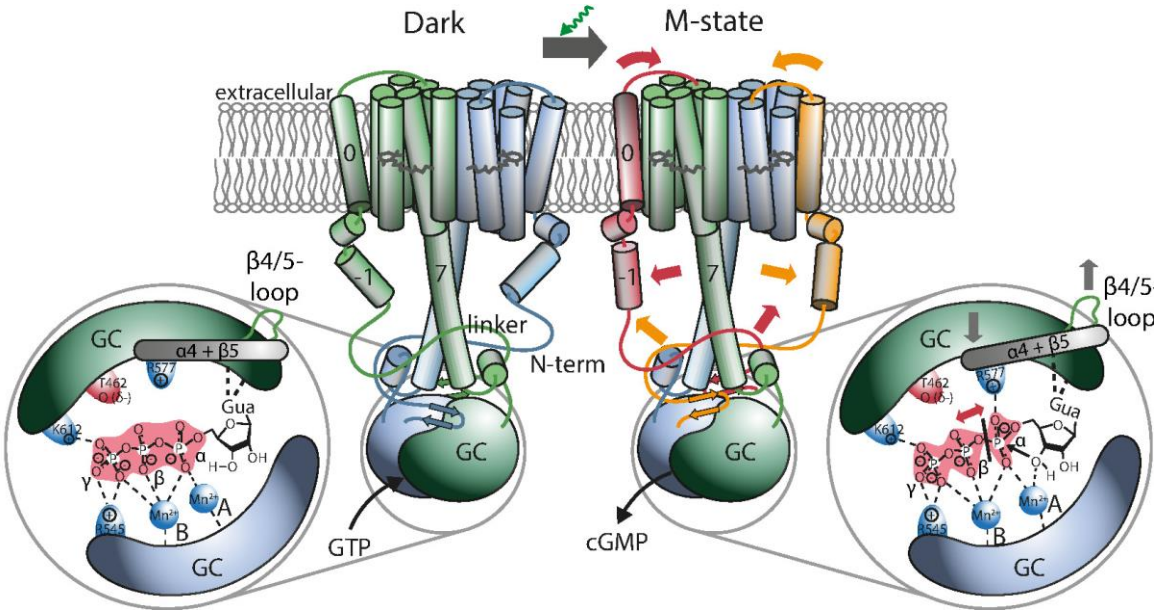

Figure 4: Schematic illustration of the CyclOp domain architecture and proposed model for light-induced activation of the guanylyl cyclase domain of CyclOps. *CyclOps are composed out of a microbial type-1 rhodopsin domain, an additional transmembrane helix (helix 0), an intracellularly located N-terminus including a further helix (helix -1), and a cytosolic guanylyl cyclase domain (GC), which is connected to the rhodopsin domain via a linker domain. Upon green light activation, the proteins generate the formation of cGMP out of GTP. The substrate GTP is bound by the guanylyl cyclase domain in dark state. The formation of cGMP is initiated by the absorption of a photon by the retinal chromophore and the consequent isomerization leading to the transition of the rhodopsin moiety into the M intermediate, where the N-terminus either interacts with the linker or is pulled off the β4/5-loop at the guanylyl cyclase moiety, causing the conversion of the guanylyl cyclase domain to an active state. The interaction between the positively charged residue R577 and the α-phosphate enables the nucleophilic attack of the ribose-3`-OH group and the cleavage of the α-β bond. Image adapted from (Fischer et al., 2021).*

The rhodopsin moiety of the CyclOps contains the hydrophobic retinal binding pocket and shares conserved photochemically active residues with other microbial rhodopsins, i.e. lysine for retinal binding and an aspartate-cysteine pair, disruption of which decelerates the photocycle kinetics (Figure 5) (Fischer *et al.*, 2021; Gao *et al.*, 2015; Scheib *et al.*, 2015). Recently, photocycle kinetics for the wild type BeCyclOp and CaCyclOp rhodopsin domain were determined via UV/Vis spectroscopy and

laser flash photolysis (Scheib *et al.*, 2018; Scheib *et al.*, 2015). The CaCyclOp rhodopsin moiety maximally absorbs light at 540 nm and converts to an early red shifted K-intermediate after photon absorption. In contrast to BeCyclOp rhodopsin, two blue-shifted L1 and L2 intermediates are formed in CaCyclOp rhodopsin before the RSB deprotonates to build the M-intermediate (active state), which recovers back to the initial ground state. While in CaCyclOp rhodopsin the M-state evolves within 31.4 ms and decays within 571 ms, in BeCyclOp rhodopsin the formation and decay are significantly faster (8 ms and 93 ms, respectively) (Fischer *et al.*, 2021; Penzkofer *et al.*, 2017; Scheib *et al.*, 2018; Scheib *et al.*, 2015).

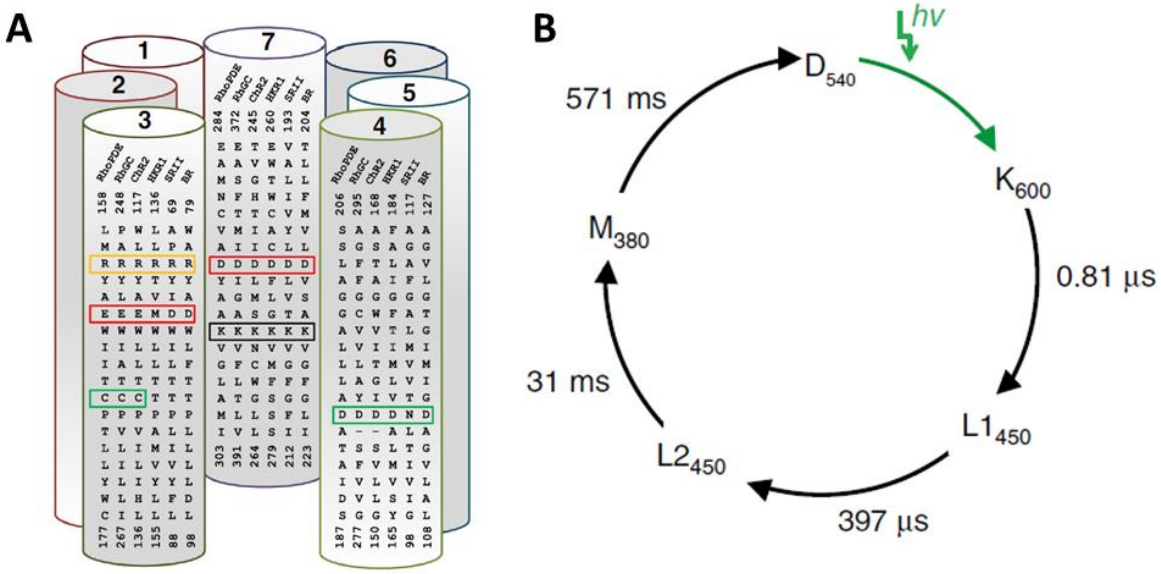

Figure 5: Schematic overview of the conserved photochemically active residues of microbial rhodopsins and the CaCyclOp rhodopsin domain photocycle. *A) Sequence alignment of rhodopsin sequences from RhoPDE (S. rosetta), RhoGC (C. anguillulae), ChR-2 and HKR1 (C. reinhardtii), sensory rhodopsin II (SRII, N. pharaonis) and BR (H. salinarum). Conserved photochemically active residues are highlighted in black (retinal-binding lysine), red (counterion/proton acceptor of RSB), orange (proton-release complex), and green (aspartate-cysteine gate). B) Photocycle model of CaCyclOp rhodopsin domain. Photocycle intermediates (K, L1, L2, and M) and life times were determined via spectroscopic analysis (evolutionary-associated difference spectra) of purified CaCyclOp rhodopsin domain. Images adapted and modified from (Mukherjee et al., 2019; Scheib et al., 2018).*

The CyclOps guanylyl cyclase domain belongs to the class III cyclic nucleoside-3`,5`-monophosphate (cNMP) cyclases which can be found in prokaryotes to mammalians (Figure 6). Recently, the crystal structure of the adenylyl cyclase domain (co-crystallized in the presence of the inhibitor adenosine triphosphate (ATPαS) of the mutated CaCyclOp was solved (Scheib *et al.*, 2018). The adenylyl cyclase domain showed the classical class III cyclase fold characterized by a central 7 stranded β-sheet which is shielded by 3 helices and depicts the functional homodimeric head-to-

tail arrangement (Scheib *et al.*, 2018; Zhang *et al.*, 1997). The inhibitor is bound by two symmetric active sites at the dimer interface, and residues anchoring the adenine and phosphate moiety belong to distinct monomers, thus supporting a cyclization mechanism which involves the movement of the monomers to enable substrate alignment, formation of the transition state, and catalytic turnover (Scheib *et al.*, 2018). The cyclization of nucleoside triphosphate (NTP) is executed via an intramolecular nucleophilic substitution (SN2), which is initiated by the attack of the ribose-3`-OH oxygen at Pα (Gerlt *et al.*, 1980; Sinha *et al.*, 2006; Steegborn, 2014). Two metal ions (A and B) participate in catalysis - one binds the NTP substrate (via triphosphate) and one facilitates the deprotonation of the ribose-3`-OH (Steegborn *et al.*, 2005; Tesmer *et al.*, 1999).

Interestingly, the guanylyl cyclase domain depicts a constitutive activity in *Escherichia coli* (*E. coli*) cells, thus implicating a strong suppression of its activity in darkness to enable light-regulation of the full-length protein. Besides to this, the full-length CyclOps are ~3 – 5-fold more active during light application compared to the isolated guanylyl cyclase domains. Thus, the activated rhodopsin domain stabilizes an enzyme conformation which promotes guanylyl cyclase activity (Fischer *et al.*, 2021; Scheib *et al.*, 2018).

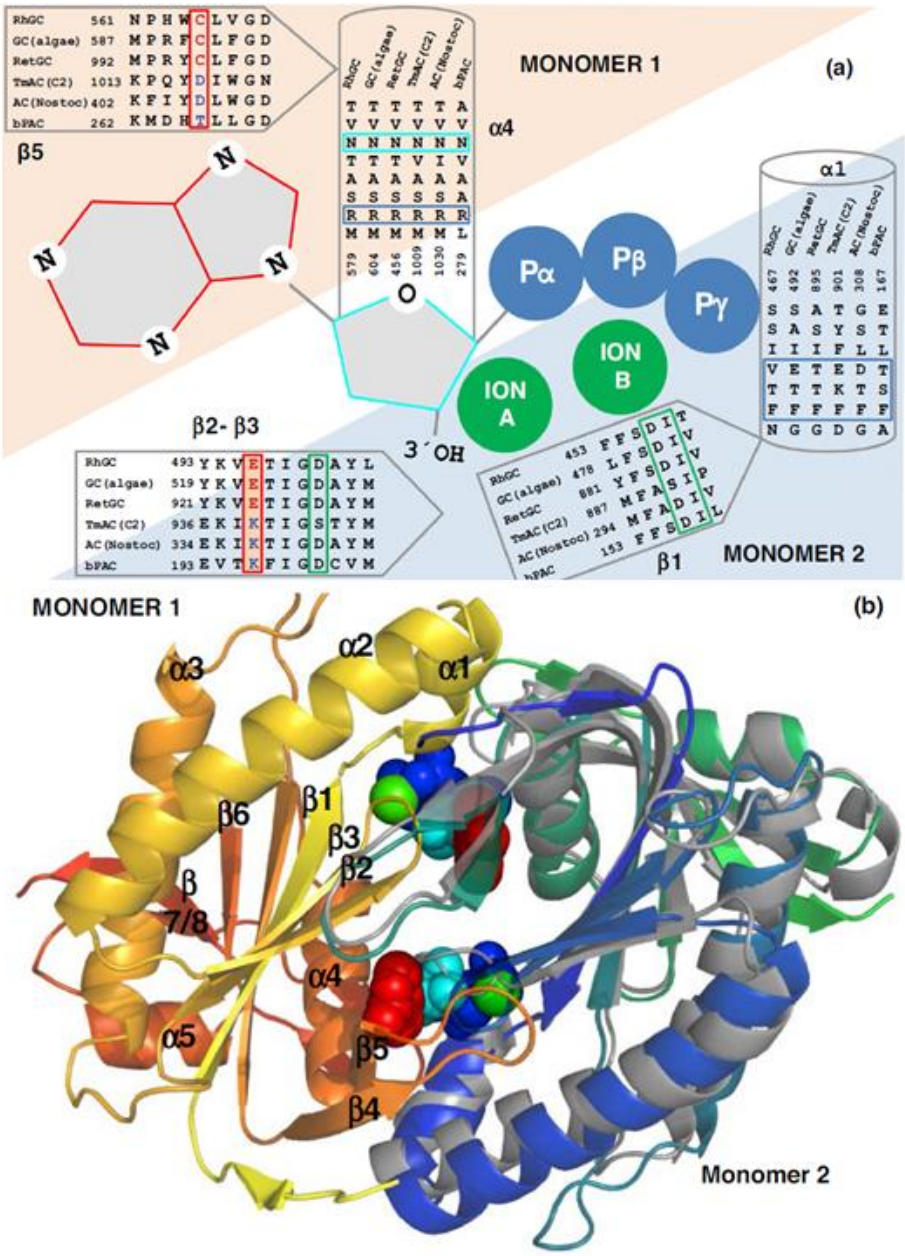

Figure 6: Schematic overview of the nucleotide binding pocket of class III cyclases and the structure of the CaCyclOp adenylyl cyclase domain. *A) Representation of nucleotide binding by the nucleotide binding pocket and conserved residues for substrate binding. Illustrated are the secondary structure elements of the cyclases as cylinder (α-helix) or arrow (β-sheet), and conserved residues participating in sugar binding (cyan), phosphate binding (blue), metal ion binding (green), and base-selectivity (red and blue) are emphasized. Sequence alignment of RhGC (C. anguillulae), GC (C. reinhardtii), RetGC (Retinal guanylyl cyclase, human), tmAC C2 (transmembrane adenylyl cyclase, rat), AC (Nostoc sp.), and from bPAC. B) Structure of the homodimeric cyclase domain of CaCyclOp with converted nucleotide specificity (PDB entry 5OYH). One monomer is coloured in red/yellow and one in blue/green. In grey the eukaryotic GC from C. reinhardtii (PDB entry 3ET6) is superimposed to monomer 2. The applied inhibitor ATP$_{\alpha}$S is shown in red (adenine), cyan (ribose) and blue (phosphate), and the Ca^{2+} ions as spheres (green). Image adapted and modified from (Mukherjee et al., 2019).*

1.2.1.2. Microbial rhodopsins as optogenetic actuators

Depending on the organism they originate from, microbial rhodopsins are responsible for the generation of membrane ion gradients for energy production or for photosensory purposes i.e. phototactic and photophobic responses (Rost *et al.*, 2017). Due to their simple structure (combining sensory and receptor functions within a single gene) and fast kinetics, microbial rhodopsins are well suited for optogenetic applications (Zhang *et al.*, 2011). As mentioned, microbial rhodopsins can act as light-driven ion pumps, light-gated ion channels or as light sensors (Figure 7).

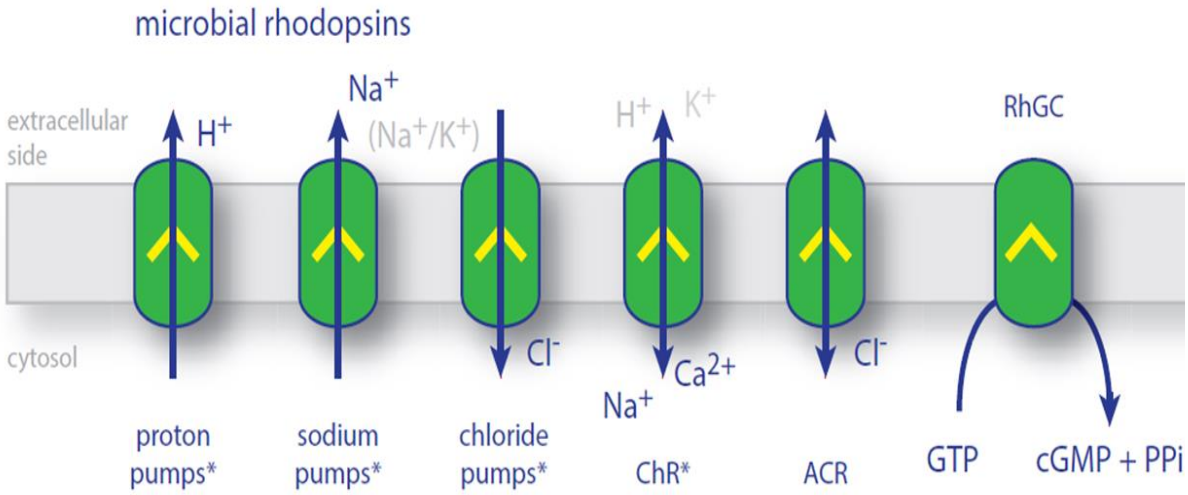

Figure 7: Overview of microbial rhodopsins acting as optogenetic actuators. *Microbial rhodopsins can act as proton, sodium, or chloride pumps, or as cation (ChR) or chloride (ACR) conducting ion channels. Light sensors like RhGC catalyse the generation of the second messenger cGMP. Abbreviations: ChR, Channelrhodopsin; ACR, anion channel rhodopsin; RhGC, rhodopsin guanylyl cyclases. Image adapted and modified from (Rost et al., 2017).*

In optogenetics, microbial pumps and channels are used to modulate the membrane potential of target cells, whereas microbial sensors are applied for the generation of the second messengers cAMP and cGMP. Upon photon absorption, microbial pumps transport H^+ or Na^+ from the cytosol into the extracellular space or transport Cl^- in the opposite direction, and thus are applied to hyperpolarize the plasma membrane of neuronal cells. This can be applied to increase the electrical threshold necessary to evoke action potentials, and to supress the release of neurotransmitters (Chow *et al.*, 2010; El-Gaby *et al.*, 2016; Han *et al.*, 2007; Inoue *et al.*, 2013; Kato *et al.*, 2015; Mahn *et al.*, 2016; Zhang *et al.*, 2007b). However, only one ion per absorbed photon is transported within the photocycle, and thus high light intensities together with high protein expression levels are necessary for an effective hyperpolarization of the target cell. For optogenetic silencing of neuronal cells, the microbial proton pumps

archaerhodopsin-3 (Arch) from *Halorubrum sodomense* or the related archaerhodopsin from the *Halorubrum* strain TP009 (ArchT) are most commonly used, however, their application is accompanied by changes of the intra- or extracellular pH (Chow *et al.*, 2010; Han *et al.*, 2011; Ihara *et al.*, 1999). A similar efficiency in evoked neuronal hyperpolarization is achieved by chloride pumping halorhodopsins, whereas NpHR has been applied *in vitro* and *in vivo* (*C. elegans*, zebrafish, rodents, and non-human primates) and is a favourite tool for optogenetic silencing due to its superior protein expression level in neurons (Arrenberg *et al.*, 2009; Diester *et al.*, 2011; Gradinaru *et al.*, 2008; Han *et al.*, 2007; Zhang *et al.*, 2007b). Further, the light driven Na^+ pump from *Krokinobacter eikastus* rhodopsin 2 (KR2) was utilized for the hyperpolarization of cultured rat cortical neurons as well as for the inhibition of *C. elegans* locomotion during pan-neuronal activation (Inoue *et al.*, 2013; Kato *et al.*, 2015). Since KR2 induces hyperpolarization without altering proton and chloride concentrations, it would be an interesting inhibitory tool, but its efficacy remains to be tested in various model organisms.

In contrast to microbial pumps, Channelrhodopsins (ChRs) are light-gated cation channels which passively conduct ions along the electrochemical gradients, and thus could be applied to depolarize the plasma membrane of excitable cells (Nagel *et al.*, 2002; Nagel *et al.*, 2003). The ChR prototype is the ChR2 from the green alga *Chlamydomonas reinhardtii*, which was applied for the investigation of numerous neuroscientific questions in different model organisms (Arenkiel *et al.*, 2007; Li *et al.*, 2005; Nagel *et al.*, 2005; Schroll *et al.*, 2006). In recent years, a number of ChR variants were established by engineering approaches and genome mining, establishing an optogenetic toolbox for a broad range of optogenetic applications (Bergs *et al.*, 2018; Schneider *et al.*, 2015). Particularly ChR2 serves as template for protein engineering, whereas the protein was modified by mutations affecting the photocycle kinetics, spectral properties, ion selectivity or conductivity. For example, the introduction of the mutations H134R and T159C leads to an increase of the photocurrents by an improved folding and retinal binding of ChR2, whereas the mutations C128 and/or D156 (termed as step-function opsins (SFOs)) decelerate the photocycle kinetics and generate variants with long-lived open states (Bamann *et al.*, 2010; Berndt *et al.*, 2011; Berndt *et al.*, 2009; Dawydow *et al.*, 2014; Nagel *et al.*, 2005; Schultheis *et al.*, 2011; Yizhar *et al.*, 2011). An advantage of SFOs is that they could be activated by a short light pulse of one wavelength (e.g. blue light) and

closed by the application of light of another wavelength (e.g. red light). In contrast to this, the fast cycling ChRs ChR2-E123T (ChETA), ChR2-E123T/T159C ($ChETA_{TC}$) or the ChR from *Stigeoclonium helveticum* (Chronos) enable the generation of action potentials at frequencies of up to 200 Hz due to their fast photocycle kinetics (Berndt *et al.*, 2011; Gunaydin *et al.*, 2010; Klapoetke *et al.*, 2014). In addition, ChRs with discrete spectral properties were designed which enable the independent control of two neural populations by light application of different wavelengths, e.g. the blue-shifted ChR from *Platymonias subcordiformus* (PsChR) and *Tetraselmis striata* (TsChR), the green to orange activated C1V1, ReaChR, and Chrimson (Erbguth *et al.*, 2012; Govorunova *et al.*, 2013; Klapoetke *et al.*, 2014; Lin *et al.*, 2013; Prigge *et al.*, 2012; Rajasethupathy *et al.*, 2015; Yizhar *et al.*, 2011). Besides, ChRs with variations in the ion selectivity exist, encompassing the H^+ selective ChR from *Dunaliella salina* (DChR1) or the ChR2 L132C (CatCh) variant with an increased Ca^{2+} and Mg^{2+} conductance and weak inactivation (Kleinlogel *et al.*, 2011; Schneider *et al.*, 2013). In contrast, the engineered ChRs ChloC and iC1C2 are Cl--selective variants which are applied to inhibit action potentials by clamping the membrane potential to the reversal potential of Cl^- (Berndt *et al.*, 2014; Wietek *et al.*, 2014). Further, Cl^- conducting ChRs with increased protein expression levels and Cl^- conductance such as improved ChloC (iChloC) and the chimeric channels iC++ and SwiChR+++ were engineered (Berndt *et al.*, 2016; Wietek *et al.*, 2015). The Cl^- conducting ChRs are complemented by the natural anion-selective rhodopsins (ACRs) from *Guillardia theta* and *Proteomonas sulcata*, which are characterized by a large conductance upon light stimulation (Govorunova *et al.*, 2015; Wietek *et al.*, 2016).

In conclusion, in recent years a large optogenetic toolbox of microbial rhodopsin pumps and channels was established to modulate the neuronal membrane potential in diverse ways. Due to the small size of their protein-encoding genes, their activation and inactivation kinetics in the millisecond timescale, microbial rhodopsins are the most commonly used optogenetic tools.

1.2.2. Blue light receptors using FAD as optogenetic actuators

The BLUF photoreceptor family is found in prokaryotes and eukaryotes, in which they are responsible for photoprotective reactions (e.g. phototaxis) or the regulation of lifestyle decisions (e.g. biofilm formation) (Gomelsky *et al.*, 2011; Iseki *et al.*, 2002). BLUF photoreceptors have a variety of architectures and oligomeric forms, but the BLUF receptor module has a well-preserved structure and mechanism. They have a modular architecture composed from an about 100 amino acid long receptor module, C-terminally connected to either effector domains (`group I`) or secondary structural elements (`group II`) (Park *et al.*, 2017). The receptor domain forms a ferredoxin-like βαββαβ fold and binds flavins -FAD/FMN/RF non-covalently as chromophores (Kennis *et al.*, 2013). The effector domain of `group I` receptors has mainly enzymatic activity (e.g. second messenger synthesis and breakdown) or other properties (e.g. transcriptional effector for gene expression), and its activity is modulated by the BLUF module in response to light (Barends *et al.*, 2009; Masuda *et al.*, 2002; Ryu *et al.*, 2010; Stierl *et al.*, 2011).

The BLUF modules contain conserved tyrosine, glutamine and methionine residues, which are essential for their function (Park *et al.*, 2017). After photon absorption, a rearrangement of hydrogen bonds around the flavin chromophore takes place, whereas a red-shifted intermediate is formed and the signal is transmitted to the respective effector domain (Figure 8) (Kennis *et al.*, 2013).

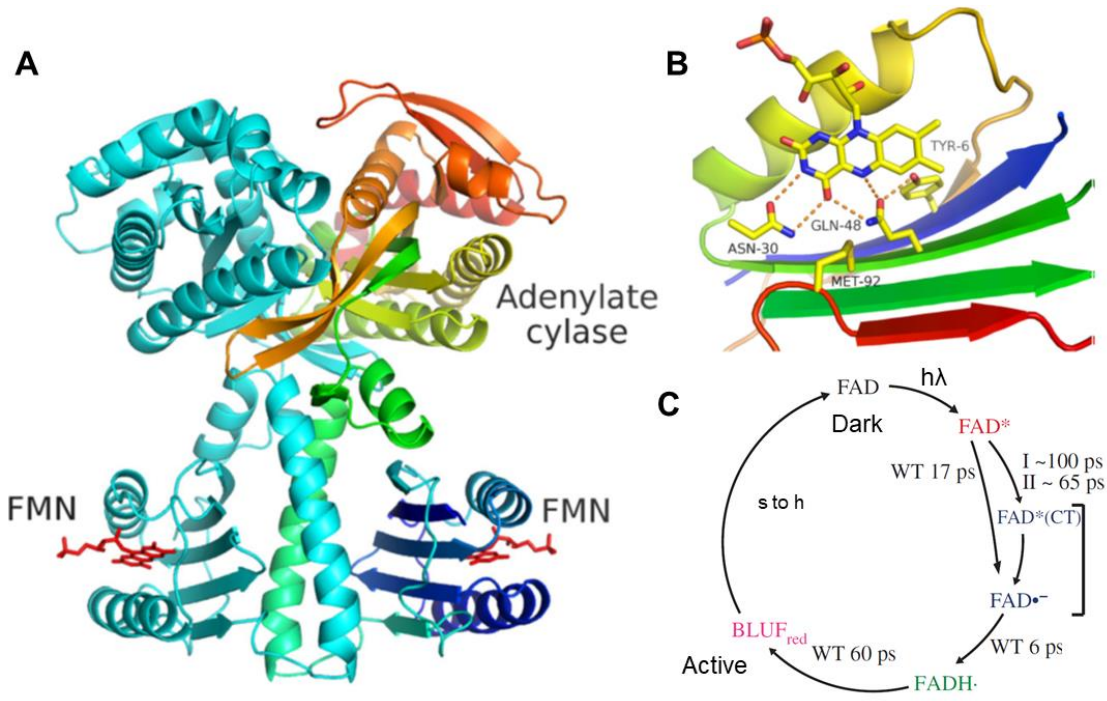

Figure 8: Schematic overview of BLUF proteins and light induced signal transduction. *A) Structure of the OaPAC homodimer, wherein the subunits comprise a BLUF domain fused to a C-terminal adenylyl cyclase domain via a helical region. Photon absorption by the flavin mononucleotide (FMN) chromophore is transmitted via the helical linker to the adenylyl cyclase domain. B) Representation of the BLUF domain of OaPAC. The FMN chromophore is bound via hydrogen bonds with the conserved residues Asn-30 and Gln-48 in the BLUF domain. C) Photocycle of BLUF domains. Photon absorption by the chromophore (FAD) causes a tautomerisation of a conserved glutamine side chain. The adjacent conserved tyrosine residue modulates the β-sheet structure of the BLUF domain, transmitting the energy to the effector domain of the protein. The photocycle includes a sub nanosecond proton transfer and a photoreceptor dependent relaxation constant (s to h). Images adapted and modified from (Kennis et al., 2013; Park et al., 2017).*

For optogenetic purposes, BLUF photoreceptors are applied to control the level of the cNMP second messengers. Here, the euPAC from *Euglena gracilis*, bPAC from *Beggiatoa*, and OaPAC from *Oscillatora acuminate*, which are composed out of a BLUF domain which is fused to an adenylyl cyclase domain, are established for the generation of the second messenger cAMP. The first applied photoactivatable adenylyl cyclase was the PACα subunit from euPAC that was used to modulate the cAMP concentrations in sensory neurons of *Aplysia*, neuronal populations of *Drosophila melanogaster* and in cholinergic neurons of *C. elegans (Bellmann et al., 2010; Nagahama et al., 2007; Schröder-Lang et al., 2007; Weissenberger et al., 2011)*. In contrast to PACα, bPAC is about 60% smaller, more soluble and has a lower dark activity (Ryu *et al.*, 2010; Stierl *et al.*, 2011). Further, BLUF based tools for the production of the second messenger cGMP were engineered by mutating key

substrate-specific residues, e.g. bPAC was converted into bPGC (also termed BlgC) (Ryu *et al.*, 2010; Tanwar *et al.*, 2018). However, photoreceptors using flavin as cofactor showed significant dark activity which could influence the cell physiology and the animals' behaviour prior to the experiment.

1.3. Cyclic nucleotide-gated channels

"Cyclic nucleotide-gated channels (CNGCs) are cation-permeable ion channels activated by direct binding of the second messengers cAMP or cGMP. Thus, they translate changes in intracellular second messenger concentrations into changes in membrane potential and Ca^{2+} concentration" (Biel *et al.*, 2009). CNGCs play a crucial role in sensory signalling (vision and olfaction), but also have several other physiological functions. For example, they have been shown to be expressed in multiple tissues, where they contribute to e.g. the alveolar liquid reabsorption in the lung or inhibition of inflammatory pain hypersensitivity in the spinal cord (Fesenko *et al.*, 1985; Heine *et al.*, 2011; Lancet, 1986; Wilkinson *et al.*, 2011). CNGCs are members of the voltage-gated ion channel superfamily which also comprises hyperpolarization-activated cyclic nucleotide-gated (HCN), voltage-gated potassium (K_V), sodium (Na_V), calcium (Ca_V), and the transient receptor potential channels (Dhallan *et al.*, 1990; Kaupp *et al.*, 1989; Kaupp *et al.*, 2002; Varnum *et al.*, 2015; Zagotta, 1996). In mammals, two CNGC subfamilies were identified, comprising four distinct A subunits (CNGA1-4) and two B subunits (CNGB1 and CNGB3), which form homo- or heteromeric assemblies (Bradley *et al.*, 2001). Here, the subunits CNGA1-3 are able to form functional channels when expressed as homomultimers, which was not observed for the other subtypes and thus they are described as modulatory subunits. The diversity of CNGCs in mammalians is further increased via alternative splicing of precursor mRNAs and/or alternative transcriptional start sites (Varnum *et al.*, 2015). CNGC subunit homologous genes have also been identified in lower organisms, e.g. *Caenorhabditis elegans* (TAX-2 and TAX-4), *Drosophila melanogaster* (Or22a and Or83b), or bacteria *Mesorhizobium loti* (MloK), *Spirochaeta thermophila* (SthK) and *Leptospira licerasiae* (LliK) (James *et al.*, 2017; Komatsu *et al.*, 1999; Nimigean *et al.*, 2004; Rheinberger *et al.*, 2018; Wicher *et al.*, 2008). The CNGC subunits are composed out of six transmembrane segments (S1-S6), a pore-

loop between S5 and S6 and intracellularly located N- and C-termini (Figure 9). The cyclic nucleotide-binding domain (CNBD) is in the C-terminus and connected to the S6 fragment in the pore region via a C-linker domain. CNGCs are tetramers, whereas the subunits are circularly symmetric and the ion conducting pore is formed by the segments S5, the pore-loop and S6 (Craven *et al.*, 2006; Flynn *et al.*, 2001; Rehmann *et al.*, 2007; Zagotta, 1996). Though including a voltage-sensor-like domain consisting of S1-S4 and the S4-S5 linker, their activity is only slightly modulated by depolarizing voltages (Benndorf *et al.*, 1999; Clayton *et al.*, 2004; Kaupp *et al.*, 1989; Nache *et al.*, 2006). In contrast to other voltage-gated ion channels, the voltage-sensor-like domain interacts with the pore domain of the same subunit in a non-domain-swapped configuration via hydrophobic and hydrogen-bonding interactions (James *et al.*, 2017; Li *et al.*, 2017).

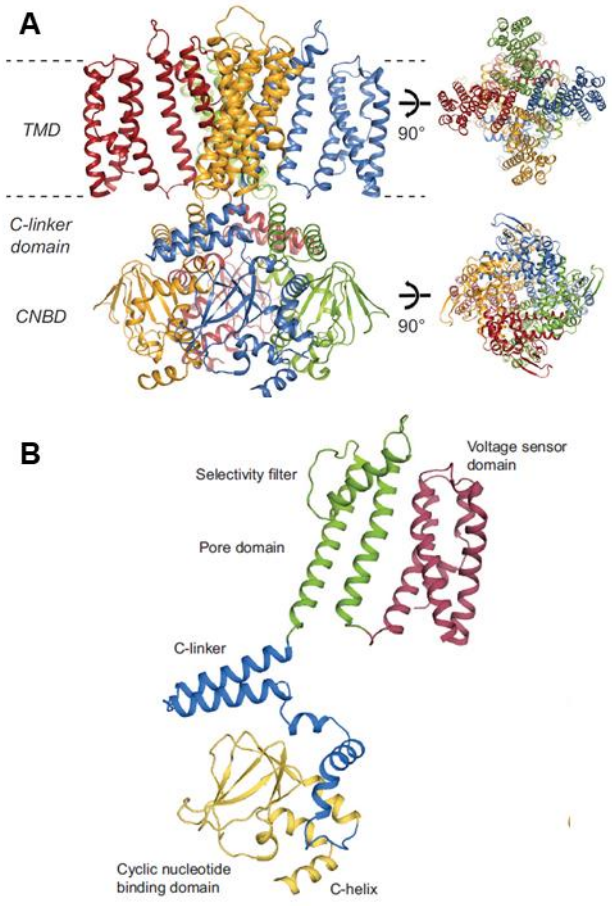

Figure 9: Schematic overview of CNGC domain structure. *A) Representation of the Spirochaeta thermophila cAMP-gated K^+ channel (SthK) in the resting state. B) Illustration of a SthK subunit, consisting of voltage sensor domain (red), pore domain (green), C-linker (blue), and the CNBD (yellow). Abbreviations: TMD, transmembrane domain; CNBD, cyclic nucleotide binding domain. Image adapted and modified from (Rheinberger et al., 2018).*

Each subunit of the CNGCs contain a cytoplasmatic CNBD, and the ligand affinity and efficacy for each channel vary depending on the subunit composition. In general, CNGCs are more sensitive to cGMP than for cAMP (Varnum *et al.*, 2015). The CNBD consists of three α-helices (A-, B-, and C-helix) and a β-roll domain with eight β-strands, and is homologous to the CNBD of other proteins such as protein kinase A (PKA) regulatory subunit or protein kinase G (PKG) (Flynn *et al.*, 2007; McKay *et al.*, 1981; Su *et al.*, 1995; Zagotta *et al.*, 2003). Initial ligand docking is mediated between interactions of the ribose phosphate of the cyclic nucleotide and a short α-helical structure between the β-6 and β-7 strands of the β-roll, termed the phosphate-binding cassette (PBC), which contains a conserved GE sequence, as well as an interaction between a conserved arginine in the β-7 strand and the cyclic phosphate of the cyclic nucleotide (Tibbs *et al.*, 1998; Varnum *et al.*, 2015). Further, a threonine residue adjacent to arginine within the β-7 strand participates in ligand binding, and has been shown to contribute to selectivity for cGMP over cAMP (Altenhofen *et al.*, 1991; Flynn *et al.*, 2007; Varnum *et al.*, 1995; Zagotta *et al.*, 2003; Zhou *et al.*, 2007).

After initial ligand-docking, the C-helix moves and interact with the purine ring of the ligand, which triggers further conformational changes in the CNGC and ultimately channel opening (Flynn *et al.*, 2007; Varnum *et al.*, 1995). Due to the orientation of the purine moiety to the ribose of the cyclic nucleotide, cAMP and cGMP are bound by the CNBD in two possible conformations – *syn* (cGMP) and *anti* (cAMP) (Flynn *et al.*, 2007; Zagotta *et al.*, 2003; Zhou *et al.*, 2007). Though the conserved threonine residue in the β-7 strand is proposed to interact with the purine ring of cGMP in the *syn* configuration, it is not sufficient for the high selectivity for cGMP over cAMP. The high cGMP selectivity is mainly dependent on the residues aspartic acid (CNGA1 and CNGA3) or a glutamic acid (CNGA2) near the C-terminal end of helix C. Here, the negatively charged residues form advantageous electrostatic interactions with cGMP, i.e. two hydrogen bonds with N1 and N2 of the guanine ring (Flynn *et al.*, 2007; Zhou *et al.*, 2007). Mutating the aspartic acid to methionine reversed the ligand selectivity (Varnum *et al.*, 1995). In CNGB1 subunits, the equivalent residue is an asparagine which leads to an enhanced cAMP efficiency for heteromeric rod CNGCs (He *et al.*, 2001; Pages *et al.*, 2000). Regarding CNGA4, the residue is a methionine which leads to a high selectivity for cAMP for heteromeric olfactory CNGC (Bradley *et al.*, 1994; Shapiro *et al.*, 2000). Nevertheless, also other regions of the CNBD domain contribute to ligand selectivity, e.g. the β-roll (Young *et al.*, 2004).

The C-linker is composed out of six α-helices (A`-F`) and has been shown to be critical for the coupling of ligand binding to the opening of cone, olfactory and rod CNGCs (Brown *et al.*, 1998; Gordon *et al.*, 1995; Zhou *et al.*, 2004; Zong *et al.*, 1998). The C-linker is thought to support intersubunit interactions in the tetrameric channel which are crucial for channel gating and assembly. These interactions include an elbow on the shoulder contact (A`-B` helices (elbow) of one subunit and C`-D` helices (shoulder) of the adjacent subunit), Ni^{2+} coordination sites in the A´-helix and interacting histidines in adjacent subunits, disulfide-bond formations, a conserved tripeptide in helix A´, and salt bridges. Further, the C-linker could interact with the N-terminal domain between and within subunits in e.g. CNGA1 to adjust the gating properties of CNGCs (Rosenbaum *et al.*, 2002).

Recently, full-length structures of SthK (closed state), TAX-4 (open state) and LliK (closed state) were solved using cryoEM (James *et al.*, 2017; Li *et al.*, 2017; Rheinberger *et al.*, 2018), allowing the construction of a model for cyclic nucleotide-induced channel opening. Here, cyclic nucleotide mediated gating is exemplified on the model for SthK channel gating (Figure 10). Upon cNMP binding, the B and C helices of the CNBD are pushed as a single unit, bringing the C helix close to the ligand (Rheinberger *et al.*, 2018). In addition, siphon loop (loop that connects the C-linker with the CNBD is shifted vertically towards the membrane (Kowal *et al.*, 2018; Rheinberger *et al.*, 2018). The C-linker of the neighbouring subunit performs a translational and rotational movement, generating space for the displaced siphon loop. Because the C-linker is directly linked to the S6 segment, the entryway is enlarged. This movement is transferred to the selectivity filter and leads to the opening of the channel. Besides to this, movements of the C-linker can also be propagated to the S4-S5 linker of the adjacent subunit, where displacement of the S5 helix is perceived by the pore helix and the selectivity filter and promotes opening of the channel (Rheinberger *et al.*, 2018).

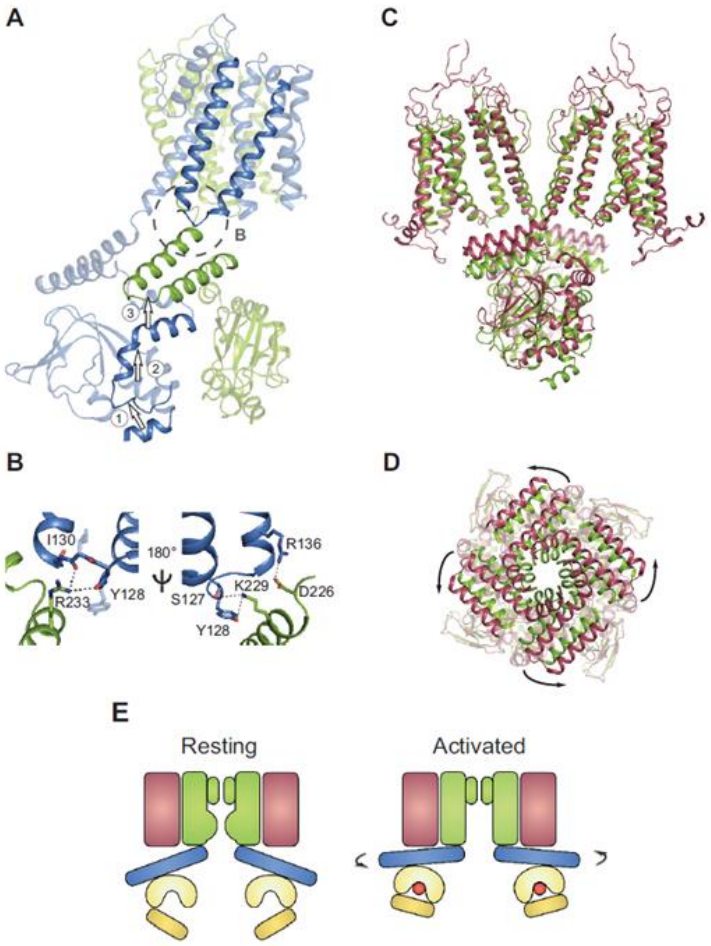

Figure 10: Proposed gating mechanism of CNGCs. *The model is based on the gating mechanism for SthK channels established by Rheinberger et al. (2018). A) Two neighbouring subunits and the ligand induced intra- and intermolecular motions are illustrated. B) Molecular interactions between the C-linker of one subunit and the S4-S5 linker of the adjacent subunit. C) Superposition of the structures of SthK (green) and TAX-4 (red). The SthK structure is in the closed state, while the TAX-4 structure is in the open state, highlighting the movement of the C-linker and CNBD. D) Extracellular side view of structures in C, showing additional counter clockwise rotation of the C-linker pulling on the ends of S6 and causing enlargement of the entrance channel. E) Schematic model of* CNGC *gating. Illustrated are the domain movements between closed (resting) and open (activated) state. Image adapted and modified from (Rheinberger et al., 2018).*

1.4. cAMP signalling pathways

cAMP is a ubiquitous second messenger that relays the information of an extracellular signal to the intracellular environment, triggering a cascade of biochemical events that finally results in the appropriate cellular response to the respective extracellular stimulus (Sutherland *et al.*, 1958). In general, cAMP is involved in a myriad of signalling pathways and thus the regulation of a multitude of biological processes (Musheshe *et al.*, 2018). cAMP signalling is initiated by the

binding of an extracellular ligand, i.e. catecholamine hormones such as adrenaline or noradrenaline, neurotransmitters or other extracellular cues to a GPCR at the plasma membrane (Figure 11) (Levitzki, 1988; Selbie *et al.*, 1998). Ligand binding triggers conformational changes within the receptor and allows the receptor to act as guanine nucleotide exchange factor (GEF), thus causing the exchange of GDP for GTP within the Gα subunit (*C. elegans* ortholog GSA-1) of the trimeric αβγ G protein which further results in the dissociation of Gα-GTP from the Gβγ dimer and the receptor (Willoughby *et al.*, 2007). The Gα-GTP subunit can either stimulate ($G\alpha_s$) or inhibit ($G\alpha_i$) plasma membrane bound adenylyl cyclases (*C. elegans* ortholog ACY-1), that catalyse the conversion of ATP to cAMP and pyrophosphate, and thus increase or decrease the intracellular cAMP level (Rodbell *et al.*, 1971; Ross *et al.*, 1978). Depending on the extracellular ligand and the respective cell type, cAMP can bind to several effector proteins, that are PKA, exchange protein directly activated by cAMP (EPAC), multiple families of channel proteins (CNGCs, HCNCs or voltage gated potassium channels) or Popeye domain-containing (POPDC) proteins, whereas each of these effectors is responsible for a distinct cellular response (Musheshe *et al.*, 2018). PKA is the most-extensively investigated cAMP effector, a tetrameric enzyme consisting of two regulatory subunits (R) and two catalytic subunits (C), whereas cAMP binding to the R subunits releases their inhibitory effect on the C subunits and thus could phosphorylate a multitude of different targets within the same cell, e.g. metabolic enzymes, receptors, channels or transcription factors (Taylor *et al.*, 2013). EPAC proteins function as GEFs that directly activate Ras-like small GTPases (Rap1 and Rap2) upon cAMP binding and thus participate in the control of Rap-mediated biological functions – e.g. inflammation or pain sensing (de Rooji *et al.*, 1998; Kawasaki *et al.*, 1998). POPDC proteins are a novel class of membrane-bound cAMP effector proteins that are abundantly expressed in cardiac and skeletal muscle and have so far been linked to the regulation of cell-cell adhesion, vesicular transport and interaction with ion channels such as TREK-1 (Froese *et al.*, 2012; Hager *et al.*, 2010; Osler *et al.*, 2005). Finally, the signal is terminated by receptor desensitization and the action of phosphodiesterases (PDEs), which are a large superfamily of metallohydrolases and are responsible for the degradation of cAMP to adenosine monophosphate (Conti *et al.*, 2007). To achieve a high signal fidelity and an accurate coordination of the different functional outcomes, cAMP signalling is compartmentalized in subcellular nanodomains, whereas the participating proteins

are organized in multiprotein signalosomes and cAMP diffusion affecting other pathways is hampered through PDE-mediated degradation (Anton *et al.*, 2022; Brescia *et al.*, 2016).

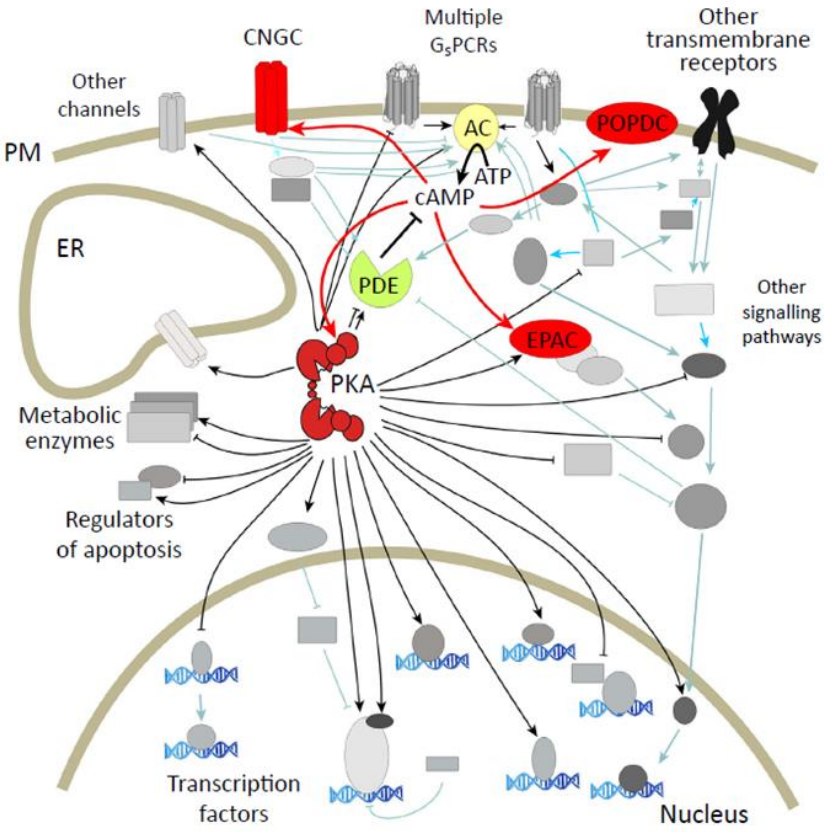

Figure 11: Schematic illustration of the cAMP signalling pathways. *The cAMP effectors PKA, EPAC, POPDC and CNGC are highlighted in red. For simplicity, only a minor fraction of PKA targets and possible crosstalk interactions are depicted, and multiple names of PKA targets are omitted. Arrows indicate activation, blunted lines inhibition and blue lines depict crosstalk between the cAMP signalling pathway and other signalling pathways. Abbreviations: AC, adenylyl cyclase; EPAC, exchange protein directly activated by cAMP; ER, endoplasmic reticulum; GsPCR, Gs-protein-coupled receptor; PDE, phosphodiesterase; PM, plasma membrane; POPDC, Popeye domain-containing protein. Image adapted from (Musheshe et al., 2018).*

1.5. The nematode *Caenorhabditis elegans* as a model organism

The nematode *C. elegans* is a popular animal model because it combines many advantages, including its small size, transparency, simple cultivation, fast and efficient transgenesis, extensive collection of gene expression data and a small and well-defined nervous system.

C. elegans as was implemented as a model system around 1974 by Sidney Brenner to answer developmental biological questions, and until now, the nematode has been

extensively applied as model organism to many diverse areas such as neuroscience, cell biology, aging or genomics (Corsi *et al.*, 2015). Using *C. elegans*, many seminal discoveries could be achieved: the first complete metazoan cell lineage (Kimble *et al.*, 1979; Sulston *et al.*, 1975; Sulston *et al.*, 1983), the first complete wiring diagram of a nervous system (Jarrell *et al.*, 2012; White, 2013; White *et al.*, 1986), the first description of microRNA and its mRNA target (Lee *et al.*, 1993; Vella *et al.*, 2005; Wightman *et al.*, 1993), the implementation of green fluorescent protein (GFP) as fluorescence reporter (Boulin *et al.*, 2006; Chalfie *et al.*, 1994), the first metazoan genome sequenced (Consortium, 1998; Schwarz, 2005), the discovery of RNA interference (Fire *et al.*, 1998), the first full genome-wide profiling of gene function (Fraser *et al.*, 2000; Kamath *et al.*, 2001), and the first application of microbial rhodopsin based optogenetics in an intact animal (Nagel *et al.*, 2005). Consequently, Sidney Brenner, Robert Horvitz, and John Sulston were awarded 2002 with the Nobel prize in physiology and medicine for their work on the deciphering of the cell lineage.

1.5.1. *C. elegans* anatomy and life cycle

C. elegans is a free-living roundworm that grows to about 1 mm in length and can be found within naturally decaying vegetable matter which supplies the necessary bacterial food source (Barrière *et al.*, 2005). In the laboratory, the animals are cultivated on agar dishes supplemented with the bacterium *E. coli*, whereas the strain OP-50 (auxotrophic for uracil) is mainly used (Brenner, 1974). The nematode occurs in two sexes - predominantly as self-fertilizing hermaphrodite, or as male at a frequency of < 0.2 % by spontaneous non-disjunction in the hermaphrodite germ line (Zarkower, 2006). Through mating, males arise at higher frequencies (≤ 50 %). Self-fertilization of homozygous hermaphrodites enables the generation of genetically identical progenies, whereas mating between hermaphrodites and males allows the isolation or transfer of mutations between strains.

The nematode consists of an invariant number of somatic cells, i.e. 959 in hermaphrodites and 1031 in males, and both sexes have the same general anatomy (Figure 12). They have an unsegmented, cylindrical body shape which is tapered at the ends (hermaphrodites), or blunt-ended at the tail (males). Similar to other nematodes, the body consists of an outer (body wall) and inner tube (alimentary

system, gonads), separated by the pseudocoelomic space. The outer tube includes the cuticle, hypodermis, excretory system, neurons, and muscle, while the inner tube contains the pharynx, intestine and the gonads. The excretory system is composed out of four distinct cell types (pore, conduct, excretory and a fused pair of gland cells), and participates in osmoregulation and waste disposal (Altun *et al.*, 2009a). The coelomocyte system is located in the pseudocoelomic space and is composed of three pairs of coelomocytes, that act as scavenger cells by endocytosing fluid from the pseudocoelomic cavity. Thus, they are suggested to serve as primitive immune system in *C. elegans* (Grant *et al.*, 2006). The alimentary system is segmented into the foregut (buccal cavity, pharynx), the midgut (intestine) and the hindgut (rectum, anus in hermaphrodites; cloaca in males). After ingestion of bacteria by the buccal cavity, the cells are crushed and transported to the intestine via the pharynx, which acts like a tube-like muscular pump and is composed out of muscle, nervous, gland and structural cells. The intestine consists of 20 cells, forming a tube with a central lumen, whereas the apical surface of the cells carries numerous microvilli for nutrient absorption. The remaining intestinal content is finally excreted to the outside via the rectal valve, rectum and anus (Altun *et al.*, 2009a). The reproductive system is built of the somatic gonad, the germ line and the egg-laying apparatus. Somatic gonad and germ line build two symmetrical U-shaped tubes, connected through a common uterus and egg-laying apparatus via the two spermathecae. Here, the germ cells develop in an assembly-line fashion from mitotic divisions at the distal part to ovulation and fertilization at the proximal end, and finally their release by the vulva. Hermaphrodites are able to self-fertilize up to 300 embryos, whereas mating with males could produce about 1000 progeny (Altun *et al.*, 2009a).

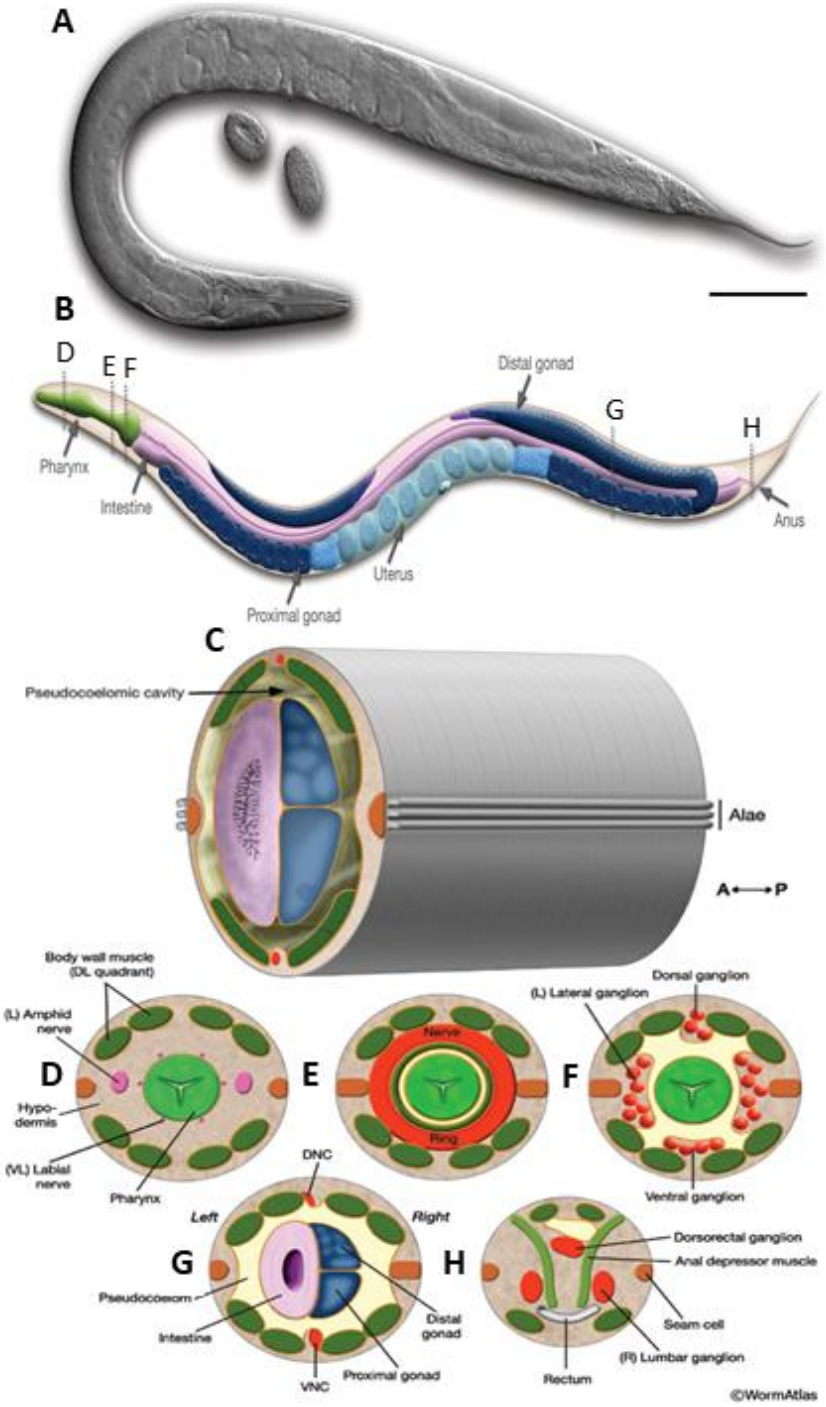

Figure 12: C. elegans anatomy. *A) Differential interference contrast (DIC) image of an adult hermaphrodite. Scale bar is 100 µm. B) Schematic illustration of the adult hermaphrodite morphology. C) Cross section of the posterior body region showing the body wall (outer tube), which is separated from the alimentary system and the gonads (inner tube) via a pseudocoelom. Cross sections of D) the anterior head, E) the middle of the head, F) the posterior head, G) the posterior body, and F) the tail. Abbreviations: DNC, dorsal nerve cord; VNC, ventral nerve cord. Image adapted and modified from* (Altun *et al.*, 2009a).

C. elegans has a rapid life cycle, i.e. a fertilized oocyte develops to a young adult animal capable to lay eggs within 2.5 to 3 days at 25 °C. During its life cycle the

nematode passes through four larval stages, termed as L1, L2, L3, and L4, each separated by a period of sleep-like inactivity (called lethargus) followed by molting of the old cuticle (Figure 13) (Raizen *et al.*, 2008). Beyond that, unfavourable life conditions such as insufficient food or crowding, that are sensed by the chemosensory systems, initiate an alternative life cycle, the `dauer` larval stage which is formed at the L2 to L3 molt. These larvae are unable to feed and arrest their development, allowing them to survive for several months until the life conditions become favourable again (Hu, 2007).

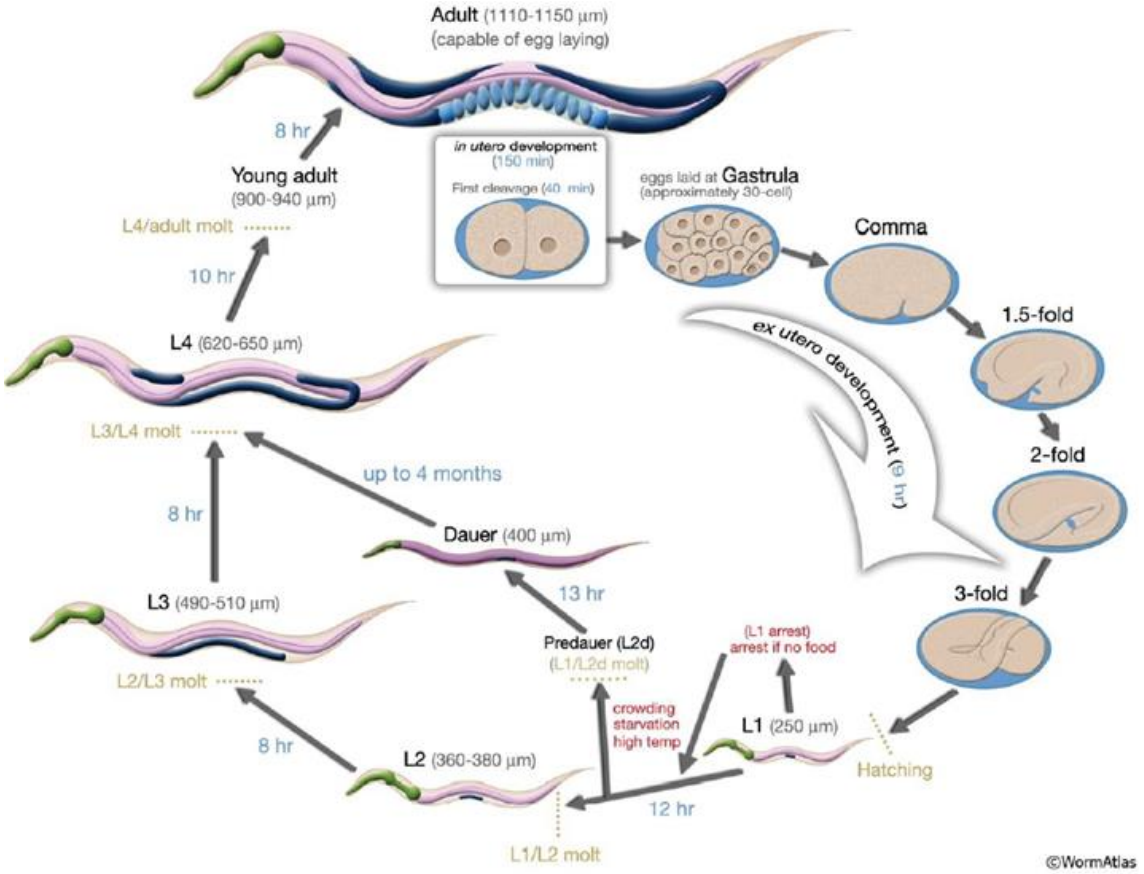

Figure 13: C. elegans life cycle at 22 °C. *The animal develops from fertilized egg through the larvae stages L1, L2, L3, and L4 into an adult hermaphrodite that is capable to lay eggs. Under unfavourable conditions, an alternative life cycle is adapted, whereas a resistant `dauer` larvae stage is formed. Numbers in blue depict the time period the animal spends at the respective larvae stage, and numbers in black indicate the length of the animals. Image adapted from* (Altun *et al.*, 2009a).

1.5.2. *C. elegans* muscle and neuromuscular junction

The nematode contains two muscle types - the striated (multiple sarcomere) and the nonstriated (single sarcomere) muscles. The striated muscle is the most abundant

type and encompasses 95 body wall muscles. In hermaphrodites, the nonstriated muscle type consists of 20 pharyngeal, 2 stomato-intestinal, 1 anal sphincter and anal depressor, 8 vulval and uterine muscle, and a contractile gonadal sheath. Instead of the vulval and uterine muscles and the gonadal sheath, males contain 41 specialized mating muscles. The muscle cells are mostly mononucleated, excluding the pharyngeal muscle cells pm1-5 that are multinucleated syncytia. Body wall muscles are organized in four quadrants that run along the ventral and dorsal side of the animal, and each quadrant contains 2 muscle rows that are innervated with the closest nerve cord (Figure 14). Thus, each nerve cord innervates the muscles of two quadrants, which causes dorsal and ventral body bending of the animal. In contrast, head muscles are regulated by motor neurons of only the nerve ring, or the nerve ring and the closest nerve cord which results in lateral and dorsal ventral movements. Unlike other organisms, neuromuscular junctions are created by extending arms from the muscle cells towards the motor neurons (Dixon *et al.*, 2006; Dixon *et al.*, 2005; Stretton, 1976; Sulston *et al.*, 1977; Sulston *et al.*, 1983; White *et al.*, 1986).

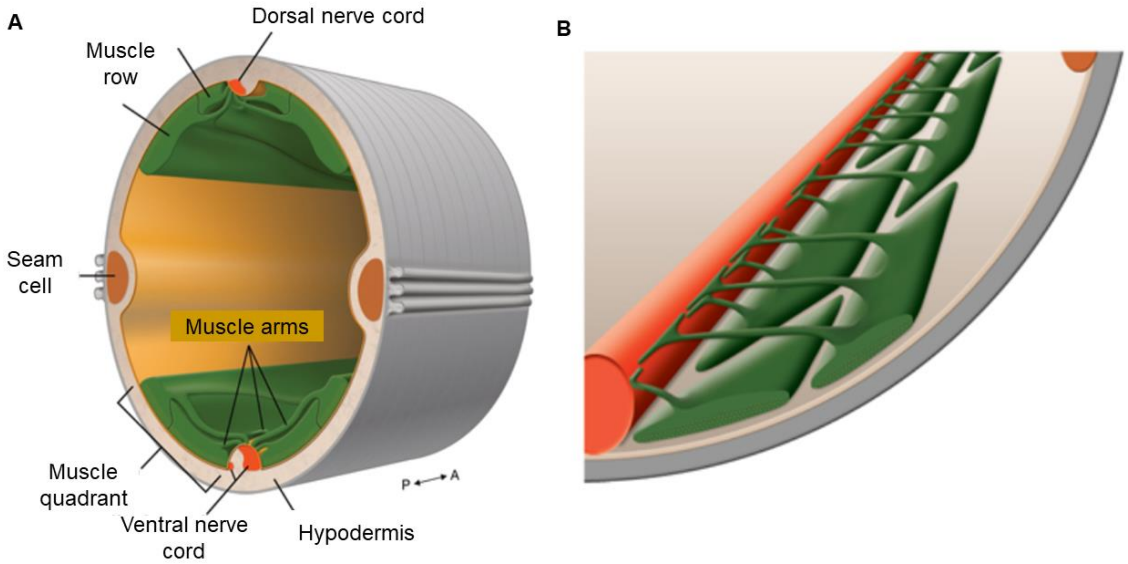

Figure 14: Schematic overview of C. elegans body wall muscle organization*. A) Body wall muscles are organized in four quadrants, each containing two muscle rows that are innervated by the nearest nerve cord via muscle arms. B) Schematic illustration of the connectivity between muscle cells and the nearest nerve cord via muscle arms. In adult animals, each muscle cell comprises three to six muscle arms. Image adapted and modified from* (Altun *et al.*, 2009b)*.*

Muscle contraction is mostly triggered by neurotransmission using the transmitter acetylcholine, with the exception of defecation cycles, which are stimulated by the transmitter γ-aminobutyric acid (GABA) released by AVL and DVB, and contractions

of the gonadal sheath, which are stimulated by calcium signals and RHO-1/Rho (Jorgensen, 2005; Kelley *et al.*, 2019). Acetylcholine induced muscle contraction is initiated by the release of the transmitter from cholinergic motor neurons at the neuromuscular junction and the activation of acetylcholine receptors on the postsynaptic muscle membrane. The acetylcholine receptors evoke bursts of action potentials which converge in graded potentials and propagate to the contractile machinery of the muscle cell (Jospin *et al.*, 2002; Richmond *et al.*, 1999; Schafer, 2002). *C. elegans* does not express Na^+ channels, and thus the potential is thought to be propagated via voltage-gated calcium channels (L-type channels; *C. elegans* ortholog EGL-19), causing the influx of Ca^{2+} ions from the extracellular space and muscle contraction. Synchronisation of action potentials through the muscle takes place via gap junctions (Lee *et al.*, 1997; Maryon *et al.*, 1996).

Muscle relaxation is evoked by the release of the transmitter GABA into the neuromuscular junction and the activation of $GABA_A$ receptors at the presynaptic muscle membrane, triggering the influx of Cl^- ions that causes muscle hyperpolarization and relaxation (Schuske *et al.*, 2004).

1.5.3. Overview of the *C. elegans* nervous system

The nervous system consists of 302 neurons in adult hermaphrodites and 385 neurons in adult males, whereas the majority of the male-specific neurons are located in the tail and participate in mating behaviour (Jarrell *et al.*, 2012; White *et al.*, 1986). It is divided into two distinct and independent systems – a somatic nervous system (282 neurons) and a pharyngeal nervous system (20 neurons) that differ in their topologies. The somatic neurons and their processes share a common basal lamina with the hypodermis and are separated from the body wall muscle cells. In contrast to this, the pharyngeal neurons are not separated from the pharyngeal muscles by a basal lamina. The hermaphrodite neurons are grouped into 118 neuronal classes depending on their topology and synaptic connectivity, and are clustered in several ganglia in the head, tail and along the ventral cord (Figure 15) (White *et al.*, 1986). Complementary to neurons, *C. elegans* has 56 glia-like supporting cells which are primarily associated with the somatic nervous system (Oikonomou *et al.*, 2011).

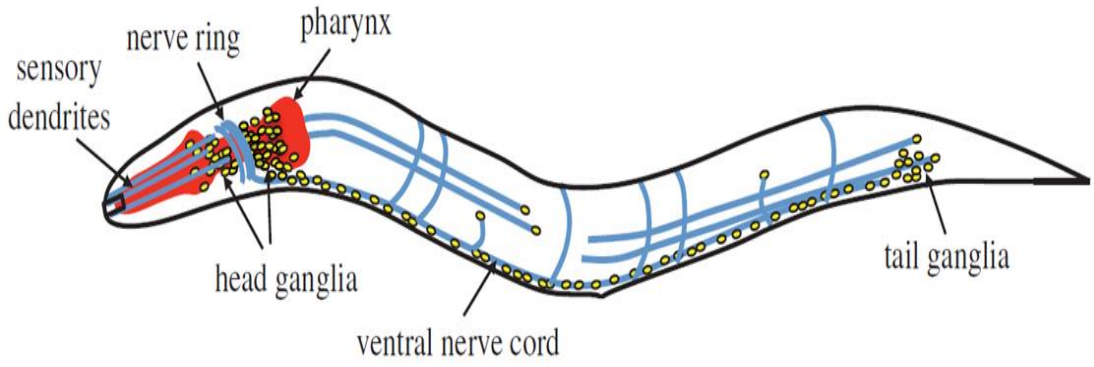

Figure 15: Illustration of the C. elegans nervous system. *Most of the neurons are clustered in the head, along the ventral nerve cord, and in the tail. Image adapted from (Fang-Yen et al., 2015).*

Communication between the neurons is performed via 6400 chemical synapses, 900 gap junctions and 1500 neuromuscular junctions (Altun *et al.*, 2011). Most of the neurons have one or two neurites proceeding from the cell body. Only a few cells such as the mechanosensory neurons FLP and PVD have complex branched neurites (Dong *et al.*, 2013). The neurites form synapses with each other in four main areas: the nerve ring, the ventral and dorsal nerve cord, and the neuropil in the tail. Most synapses are made *en passant*, i.e. side by side as neurites pass each other. Instead of sending cellular projections from motor neurons to muscles, the muscles send specialized cellular projections to motor neurons to receive synapses (Corsi *et al.*, 2015).

The neuron names consist of two to three letters, indicating the neuronal class and in certain cases a number indicating the neuron number within one class. If the neurons are radially symmetrical, the letter name is followed by L (left), R (right), D (dorsal), or V (ventral) to specify the anatomical position. Depending on their circuit function, the neurons are classified into sensory neurons, interneurons, motor neurons and polymodal neurons. Sensory neurons sense a variety of environmental cues such as temperature, touch, chemicals, oxygen and UV-light. Interneurons integrate the receiving sensory inputs and transmit the signal to motor neurons that trigger the respective behavioural output via the musculature. Polymodal neurons exert more than one circuit function (motor and sensory functions; interneuron- motor neuron; interneuron and sensory function) (Altun *et al.*, 2011). Despite the small number of neurons, *C. elegans* is able to regulate a variety of behaviours such as locomotion,

feeding, chemo- and mechanosensation, thermotaxis, male mating, learning and memory (Ardiel *et al.*, 2010; Bargmann, 2006; de Bono *et al.*, 2005).

1.5.4. Cholinergic neurotransmission

Acetylcholine was the first substance identified to act as a neurotransmitter (Loewi, 1921). It is released by more than a third of the *C. elegans* neurons and represents the major excitatory neurotransmitter at the neuromuscular junction and is involved directly or indirectly in many *C. elegans* behaviours such as locomotion, feeding or male mating.

Acetylcholine is synthesized in cholinergic neurons by the transfer of an acetyl group from acetyl-CoA to choline which is catalysed by the choline acetyltransferase (*C. elegans* ortholog CHA-1). Subsequently, it is transferred from the cytoplasm into synaptic vesicles via the vesicular acetylcholine transporter (vAChT; *C. elegans* ortholog UNC-17), an antiporter that exchanges one molecule acetylcholine for two protons. The driving force for this exchange is a proton gradient between the cytoplasm and the lumen of the synaptic vesicles, which is acidified by the action of the vacuolar-type H^+-adenosine triphosphatase. After docking, priming and calcium-stimulated fusion of the synaptic vesicles with the plasma membrane, acetylcholine is released into the synaptic cleft and activates acetylcholine receptors located at the postsynaptic neurons or at muscle arms in case of neuromuscular junctions. Synaptic transmission is terminated by the hydrolysis of acetylcholine by the acetylcholinesterase (in *C. elegans* encoded by the *ace* genes) into acetate and choline. The latter is transported back into the presynaptic neuron via a high affinity vesicular transporter (*C. elegans* ortholog CHO-1) and is used for new synthesis of acetylcholine (Rand, 2007).

C. elegans muscles contain two types of pentameric acetylcholine receptors - levamisole-sensitive receptors (L-AChR) and nicotine-sensitive receptors (N-AChR) (Richmond *et al.*, 1999). L-AChRs are pentameric channels composed out of three essential α subunits UNC-63, UNC-38 and LEV-8 and two non-essential β subunits UNC-29 and LEV-1 (Boulin *et al.*, 2008; Culetto *et al.*, 2004; Fleming *et al.*, 1997; Gottschalk *et al.*, 2005; Towers *et al.*, 2005). In contrast to this, N-AChRs are

homomeric channels that are composed out of the essential α subunit ACR-16 (Francis *et al.*, 2005; Touroutine *et al.*, 2005).

1.5.5. Motor neurons and motor circuit

The nematode can move in two main behavioural patterns – crawling on solid media and swimming (thrashing) in liquid media. Here, the animal propagates sinusoidal waves along the entire body in the direction opposing that of locomotion, driven by reciprocal dorsoventral body contractions (Gray *et al.*, 1964). On solid media, the animal crawls in a S-wave fashion, and in liquid media it swims through C-shaped bends. Besides the control of the swimming and crawling behaviours, motor neurons are also responsible for the motility of the alimentary and reproductive systems (Altun *et al.*, 2011). The locomotion of the animal during sensory and exploratory behaviours includes forward and backward (reversal) movements, omega turns (180° change in the direction) and shallow turns (Altun *et al.*, 2011; Kim *et al.*, 2011).

C. elegans contains 113 motor neurons that are mainly distributed along the ventral nerve cord and that form excitatory or inhibitory neuromuscular junctions with one or more muscle cells (Aamodt *et al.*, 2005). The excitatory and inhibitory signals are transmitted via acetylcholine and GABA, respectively. The motor neurons of the ventral nerve cord are categorized in the classes A (21 neurons), B (18), D (19), VC (6), and AS (11), while the classes A, B, and D are further subdivided into DA (9), VA (12), DB (7), VB (11), DD (6) and VD (13), depending on the innervation of ventral or dorsal muscle cells (Von Stetina *et al.*, 2005). A and B-type neurons are cholinergic and responsible for backward and forward movement, respectively. D-type neurons are GABAergic and are postsynaptic to A and B-type neurons that innervate the contralateral muscle group. Although *C. elegans* is anatomically not segmented, the motor circuit could be separated into six repeating units consisting of ~12 motor neurons and ~12 muscle cells (Figure 16).

B-type motor neurons are postsynaptic to the premotor interneurons AVB and PVC, whereas AVB signals via gap junctions and PVC via chemical synapses. The interneurons AVA and AVD are presynaptic to A-type motor neurons and signal chemically and electrically. Further, in the anterior half of the animal the A-type neurons receive their input from AVE (Altun *et al.*, 2011). Motor neurons of the same

neuronal class are connected to their neighbouring cell by gap junctions. Communication between motor neurons and muscle cells is accomplished via acetylcholine and GABA and the ionotropic receptors $GABA_A$ and acetylcholine receptors. Motor neurons also contain a third class of acetylcholine receptors, the neuronal ionotropic acetylcholine receptors (nAChRs) that are similar to L-AChRs in their composition, but that are insensitive to levamisole and contain neuron specific subunits. These receptors are postsynaptic in GABAergic neurons, and dendritic in the remaining motor neuron classes, and they are required for the regulation of excitatory and inhibitory inputs at the neuromuscular system (Barbagallo *et al.*, 2010; Jospin *et al.*, 2009). Besides to this, *C. elegans* contains three muscarinic acetylcholine receptors (mAChRs) and two $GABA_B$ receptor subunits participating in feedback inhibition (Bargmann, 1998; Dittman *et al.*, 2008; Schultheis *et al.*, 2011). The mAChR GAR2 is expressed in cholinergic and GABAergic neurons and regulates the activity of cholinergic neurons at elevated acetylcholine levels. The heterodimeric GBB-1/GBB-2 $GABA_B$ receptors are expressed in cholinergic neurons and regulate their activity after activation of GABAergic neurons and the release of (spillover) GABA (Dittman *et al.*, 2008; Schultheis *et al.*, 2011). In addition to neurotransmitters, the excitation-inhibition balance in the neuromuscular system is regulated by neuropeptides such as the FMRFamides FLP-1 and FLP-18 that are released from AVK and cholinergic neurons, respectively, and the receptors NPR-1 (in neurons), NPR-5 (in muscle), and the FLP-1 receptors NPR-6 and FRPR-7 (Oranth *et al.*, 2018; Stawicki *et al.*, 2013). Several monoamines and neuropeptides have been shown to modulate specific behavioural outputs, e.g. the release of NLP-12 by the mechanosensory/proprioceptive neuron DVA that potentiates cholinergic neuron activity to regulate the bending amplitude during locomotion (Hu *et al.*, 2011; Li *et al.*, 2006; Oranth *et al.*, 2018).

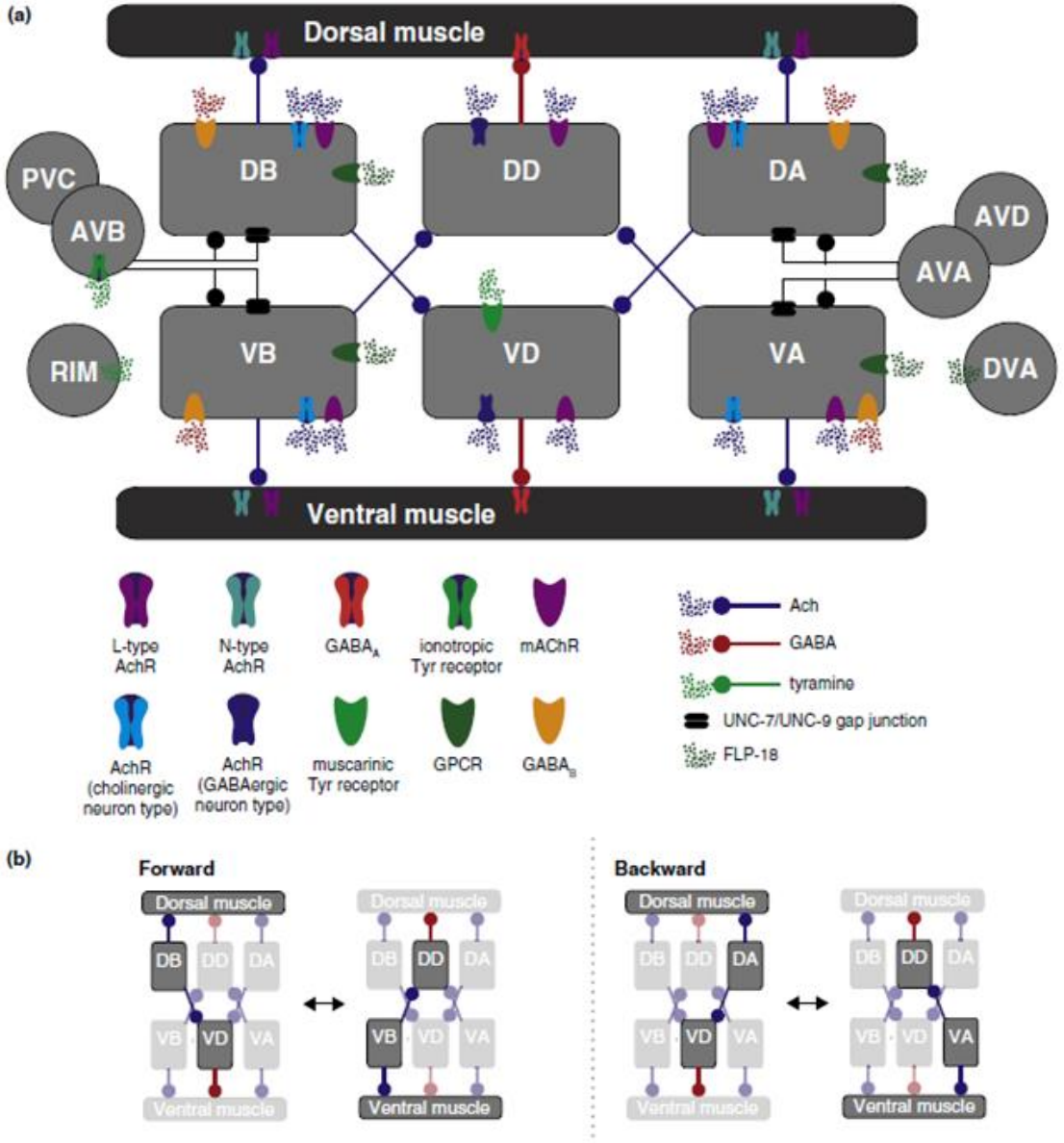

Figure 16: Schematic overview of the C. elegans motor circuit. *A) A structural unit includes A- and B-type cholinergic neurons, D-type GABAergic neurons, ventral and dorsal muscles, and interneurons (AVA, AVD, AVB, and PVC). Receptors and gap junctions involved in intercellular communication are also shown. B) Mediation of forward and backward movement of an adult animal. The forward movement is triggered by B- and D-type neurons, the backward movement by A- and D-type neurons. Image adapted from (Zhen et al., 2015).*

1.5.6. cAMP modulation of neurotransmission

Neurotransmission describes the transmission of a signal from one neuron to an adjacent neuron or cell by the release of a neurotransmitter via synaptic vesicles into the synaptic cleft. Synaptic vesicles are stored in the readily releasable pool, the reserve pool and the recycling pool. In the reserve pool, they are immobilized by

tethering to the cytoskeleton and to each other via synapsin, and are mobilized via PKA- and Ca^{2+}-calmodulin kinase II dependent synapsin phosphorylation to promote high rates of transmitter release (Cesca *et al.*, 2010; Menegon *et al.*, 2006). Afterwards, the synaptic vesicles translocate to the plasma membrane and are docked and primed at the active zone membrane scaffold, termed dense projection, and form the readily releasable pool (Siksou *et al.*, 2007; Stigloher *et al.*, 2011). After depolarization and the accompanying Ca^{2+} entry into the neuronal terminal via voltage-dependent calcium channels, the primed synaptic vesicles fuse with the plasma membrane and release their content into the synaptic cleft. The added synaptic vesicle membrane and proteins are endocytosed and synaptic vesicles are recovered from endosomal compartments and filled with neurotransmitters (Jahne *et al.*, 2015; Kittelmann *et al.*, 2013; Kononenko *et al.*, 2015; Rizzoli, 2014; Watanabe *et al.*, 2014).

In addition to the communication via classical neurotransmission, neurons signal via the release of neuropeptides from dense core vesicles. In contrast to the fast synaptic transmission via neurotransmitters that act at short distances (nm), neuropeptides diffuse from their point of release and act at long distances (nm to mm) and at low concentrations, which is referred to as volume transmission (Russo, 2017). They bind mainly to GPCRs and evoke second messenger cascades to modulate neural activity on long-time scales (second to minutes), and thus are important for the regulation of various neuronal functions and behaviours such as learning and memory or social behaviours (Dominguez *et al.*, 2018; Russo, 2017). Neuropeptides are synthesised as precursor proteins on ribosomes of the endoplasmic reticulum and are packaged in dense core vesicle precursors which bud from the trans Golgi apparatus. The dense core vesicle is further compacted by membrane budding, and during axonal transport, the neuropeptide precursors are proteolytically cleaved and post-translationally modified to obtain the active peptides (Russo, 2017). They traffic antero- and retrogradely between synapses, and are captured for their release from synaptic and extrasynaptic regions on axons and dendrites (van de Bospoort *et al.*, 2012; Wong *et al.*, 2012). The release of dense core vesicles is triggered by elevated cytosolic Ca^{2+} levels via protein kinase C (PKC), but also via increased cAMP levels and PKA phosphorylation of synaptic targets, e.g. synapsin (SNN-1) (Park *et al.*, 2006; Sieburth *et al.*, 2006; Yu *et al.*, 2021). Further, priming and docking of dense core vesicles require the calcium-

activated protein for secretion (CAPS/UNC-31) (Charlie *et al.*, 2006; Rupnik *et al.*, 2000). Neuropeptide signalling is terminated by peptide inactivation via extracellular proteases.

Recently, Steuer Costa et al. 2017 showed that optogenetic cAMP production in cholinergic motor neurons via bPAC induced an increase in neurotransmission and motor neuron-evoked behaviours. Here, elevated cAMP levels caused an enhanced mobilization of synaptic vesicles from the reserve pool and increased docking and priming events. Further, cAMP triggered the release of neuropeptides from dense core vesicles, which activate auto-receptors leading to an increased filling of synaptic vesicles with acetylcholine via the vAChT (Figure 17) (Steuer Costa *et al.*, 2017).

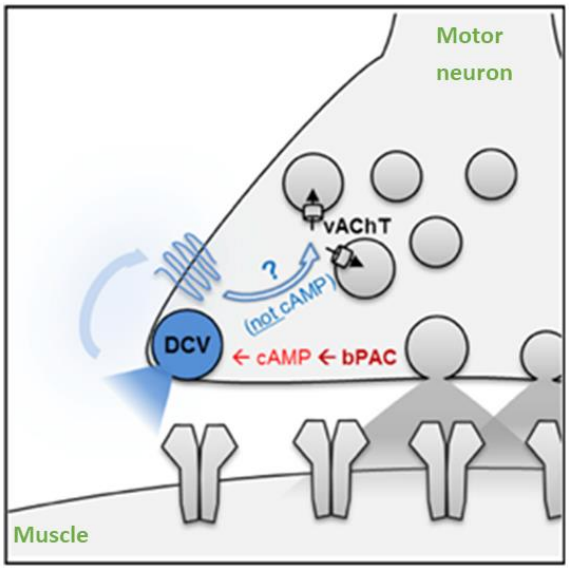

Figure 17: Schematic overview of cAMP modulation of cholinergic neurotransmission via neuropeptide signalling and synaptic vesicle loading. *In C.* elegans cholinergic neurons, optogenetic increase of cAMP levels (triggered by bPAC) caused an enhanced neurotransmission and behaviours by the release of dense core vesicles and acetylcholine release. cAMP promotes the mobilization of synaptic vesicles from the reserve pool and the release of neuropeptides from dense core vesicles, that act in an autocrine manner to trigger filling of synaptic vesicles with acetylcholine *via the vAChT and to a synaptic vesicle size increase. Image adapted and modified from (Steuer Costa et al., 2017).*

The cAMP dependent increase in neurotransmission caused profound changes in the behaviour of the animal. On solid media, photoactivation of bPAC enhanced the crawling speed and the body bending of the nematode, and in liquid media it increased the swimming frequency (Figure 18).

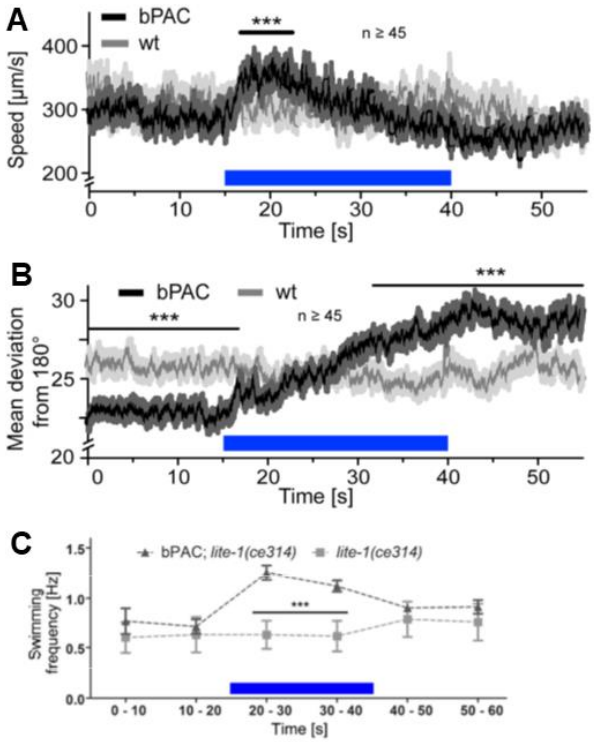

Figure 18: Optogenetic activation of cholinergic motor neurons via bPAC has profound effects on locomotion behaviour. *Photoactivation of bPAC caused an increased A) crawling speed and B) body bending on solid substrate, and an enhanced C) swimming rate in liquid media. Image adapted and modified from (Steuer Costa et al., 2017).*

1.5.7. Optogenetic tools in *C. elegans*

Due to its transparency, amenability for genetic manipulation and small and well-defined nervous system that controls a multitude of quantifiable behavioural outputs, the nematode *C. elegans* is an ideal model organism for the development and application of optogenetic tools and methods. In the past decade, a wide range of optogenetic tools were implemented in *C. elegans*, including optogenetic actuators for de- and hyperpolarization (e.g. ChR2, *Guillardia theta* ACR2, respectively) of excitable cells, for the generation of the second messengers cAMP (e.g. bPAC) and cGMP (e.g. BeCyclOp), as well as for protein-protein interaction (e.g. photoactivatable botulinum neurotoxin (PA-BoNT)) (Bergs *et al.*, 2018; Gao *et al.*, 2015; Liu *et al.*, 2019; Nagel *et al.*, 2005; Steuer Costa *et al.*, 2017). Beyond that, fluorescent sensors to monitor the cellular activity of a specific cell type are established, encompassing sensors to visualize changes in the concentration of the second messengers Ca^{2+} (GCaMP) or cGMP (e.g. WincG2), of the energy carrier

ATP (ATeam), and also changes in membrane voltage (QuasAr) (Azimi Hashemi *et al.*, 2019; Nakai *et al.*, 2001; Wang *et al.*, 2019; Woldemariam *et al.*, 2019).

Predominantly, microbial rhodopsins such as ChR2, NpHR, Mac or Arch are applied to specifically activate or inhibit a desired neuronal cell type, causing quantifiable behavioural changes in e.g. the crawling speed, swimming frequency or the body length (Husson *et al.*, 2012; Liewald *et al.*, 2008). Further, genetically encoded calcium indicators (GECIs) such as GCaMP or RCaMP are employed to monitor neuronal activity in immobilized or even moving animals (Oranth *et al.*, 2018; Steuer Costa *et al.*, 2019; Tolstenkov *et al.*, 2018). The resulting behavioural and fluorescence changes are measured using established tracking systems (Akerboom *et al.*, 2013; Stirman *et al.*, 2011; Swierczek *et al.*, 2011). Moreover, optogenetic actuators and reporters are combined for simultaneous neuronal activation or inhibition and monitoring of the neuronal activity (Husson *et al.*, 2012). Last, multi component optogenetic systems for excitable cell activation and silencing are established, consisting of a photoactivatable nucleotidyl cyclase coupled to a CNGC (Gao *et al.*, 2015; Henss *et al.*, 2021).

For the development and implementation of novel optogenetic tools, the proteins are commonly expressed in body wall muscle cells (*myo-3* promoter), because depolarization or hyperpolarization of the muscle causes macroscopic behavioural changes (body reduction or elongation, respectively) (Erbguth *et al.*, 2012; Husson *et al.*, 2012; Nagel *et al.*, 2005; Zhang *et al.*, 2007a). Further, the performance of the new proteins could be assessed by their expression in cholinergic motor neurons (*unc-17* promoter) or in GABAergic motor neurons (*unc-47* promoter), whereas neuronal activation or silencing caused quantifiable changes in the locomotion behaviour and in the body length (Erbguth *et al.*, 2012; Husson *et al.*, 2012; Liewald *et al.*, 2008). Since microbial rhodopsins require retinal as chromophore, and the nematode does not synthesize retinal, it has to be supplied exogenously with the bacterial food to obtain functional microbial rhodopsins. This provides an ideal internal control for optogenetic experiments in *C. elegans* using microbial rhodopsins.

Recently, the optogenetic toolbox for excitable cell activation and inhibition in *C. elegans* was expanded by protein engineering and implementation of novel microbial rhodopsins (Figure 19). Here, the GtACR2 was established as new hyperpolarizer that offers high effectiveness and fast kinetics. Further, ChR2 variants were

established enabling long-term depolarization (Bergs *et al.*, 2018). Beyond that, light-activatable cyclases like the microbial photoactivatable adenylyl cyclases from *Euglena* (euPAC) and *Beggiatoa* (bPAC), as well as the synthetic phytochrome-linked cyclases PaaC and IlaC22 k27 were implemented as optogenetic tools for cAMP production (Etzl *et al.*, 2018; Ryu *et al.*, 2014; Steuer Costa *et al.*, 2017; Weissenberger *et al.*, 2011)

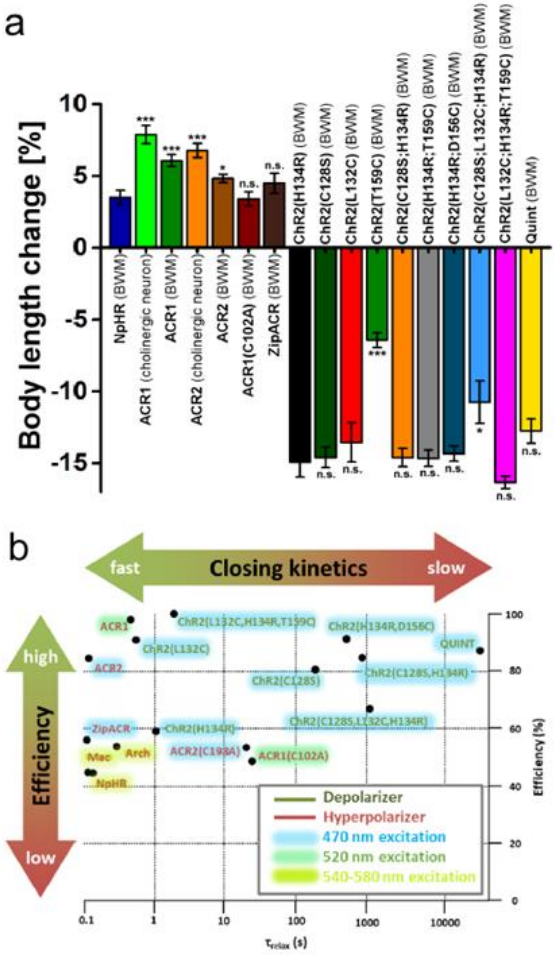

Figure 19: Evaluation of novel and engineered de- and hyperpolarizers in C. elegans. *A) Increase or decrease in body length evoked by novel and engineered de- and hyperpolarizers, which were expressed either in body wall muscle cells or in cholinergic motor neurons, respectively. Illustrated is the mean normalized body length change (± SEM) relative to the initial body length of the animal before light application. Statistically significant differences were calculated in comparison to ChR2(H134R) (depolarizer) and NpHR (hyperpolarizer). B) Schematic representation of de- and hyperpolarizers expressed in body wall muscle cells of C. elegans. The tools are categorized according to their closure kinetics and efficiency, which was estimated by comparing the body length reduction (depolarizer) or increase (hyperpolarizer) induced by the respective protein relative to the maximum body contraction or elongation. Image adopted from (Bergs et al., 2018).*

1.6. Objectives of the thesis

Three major objectives were followed during the course of this thesis. First, novel optogenetic tools should be engineered and implemented in *C. elegans* that mimic more the physiological conditions of cAMP signalling and hyperpolarization of excitable cells. Membrane-bound photoactivatable adenylyl cyclases should be generated by mutating two to three key amino acids in the active site of the guanylyl cyclase domains from the *Blastocladiella* and *Catenaria* CyclOps. To characterize the mutated versions after optogenetic cAMP production, they should be expressed in cholinergic motor neurons and light evoked changes in *C. elegans* locomotion behaviour should be compared to bPAC induced effects. Further, the membrane-bound photoactivatable adenylyl cyclases should be expressed in body wall muscle cells and *in vitro* cNMP measurements should be performed to assess the amount of generated cAMP and to evaluate the nucleotide specificity switch. To implement hyperpolarizers on the basis of K^+-currents, two component optogenetic systems should be established and evaluated via behavioural experiments. Here, the engineered membrane-bound photoactivatable adenylyl cyclases or the soluble bPAC were co-expressed with the cAMP-gated K^+-channel SthK in body wall muscle cells and cholinergic motor neurons. Another approach should be to combine BeCyclOp and the cGMP-gated K^+-channel BeCNG1.

Second, BeCyclOp should be purified for molecular characterization and structural analysis. For this purpose, BeCyclOp monomers as well as a dimer-concatamer should be overexpressed with a C-terminal TAP-tag in *C. elegans* muscle cells and purified via tandem affinity purification. To enable purification of both proteins, stable expression strains with genome integrated transgene arrays should be generated and detergent screening for high solubilization of BeCyclOp should be executed. To assess the functionality of the BeCyclOp concatamer, the protein should be co-expressed with the cationic TAX-2/-4 CNGC in body wall muscle cells and analysed via body length measurements.

Third, cAMP effectors in *C. elegans* body wall muscle cells should be identified that participate in cAMP dependent muscle hyperpolarization. To this end, a sequence alignment of PKA´s regulatory subunit Riα against the *C. elegans* genome should be performed to identify ion channels that contain a cAMP binding domain. To evaluate

the identified channels with respect to a possible participation in cAMP-induced muscle relaxation, bPAC expressing strains (*myo-3* promoter) in the respective channel loss of function background and in double mutant background (channel loss of function; *lite-1(ce314)*) should be generated by crossing and assessed by behavioural analyses.

2. MATERIALS AND METHODS

2.1. Materials

2.1.1. Chemical substances

Table 1: Used chemical substances.

Substance	Manufacturer
2-Mercaptoethanol	Carl Roth
3-isobutyl-1-methylxanthine (IBMX)	Carl Roth
Acetic acid	Carl Roth
Acetone	Carl Roth
Agar	AppliChem
Agarose	Invitrogen
All-trans retinal	Merck
Ammonium persulfate (APS)	Carl Roth
Ampicillin sodium salt	AppliChem
Bromophenol blue	Sigma Aldrich
Bovine serum albumin (BSA)	Carl Roth
Calcium chloride	Carl Roth
Cholesterol	Merck
cOmplete Protease Inhibitor Cocktail tablets	Roche
Deoxyribonucleoside triphosphates (dNTP)	Invitrogen
Detergent Screening Set Classic	Biozym
Dimethyl sulfoxide (DMSO)	Carl Roth
Dipotassium phosphate	Carl Roth
Disodium phosphate	Carl Roth
Dithiotreitol (DTT)	Carl Roth
Ethanol 94 %	Carl Roth
Ethanol 99 % (AR grade)	Carl Roth
Ethidium bromide 5 %	Carl Roth

Substance	Manufacturer
Ethylene-diamine-tetra-acetic acid (EDTA)	Carl Roth
Ethylenglycol-bis(aminoethylether)-N, N, N′, N′-tetraessigsäure (EGTA)	Carl Roth
Formaldehyde (37%)	Sigma Aldrich
GeneRuler 100bp DNA Ladder	Thermo Fisher Scientific
GeneRuler 1 kb Plus DNA Ladder	Thermo Fisher Scientific
GE Healthcare Amersham™ ECL Prime Western-Blot-Detection Reagent	Cytivia
Glass Beads (0.25- to 0.5-mm)	Carl Roth
Glycerin	Carl Roth
Halocarbon oil	Halocarbon
Hydrochloric acid (37 %)	AppliChem
Imidazole	Carl Roth
Isopropanol	Carl Roth
Kobe Agar	Carl Roth
Magnesium acetate	Carl Roth
Magnesium chloride	Carl Roth
Magnesium sulfate	Carl Roth
Milk powder	Carl Roth
Monopotassium phosphate	Carl Roth
Nα-p-Tosyl-L-arginine methyl ester hydrochloride (TAME)	Carl Roth
Nitrogen	Linde
Nystatin	Merck
Rotiphorese Gel 30	Carl Roth
Oligonucleotides	Eurofins MWG/Microsynth AG
PageRuler™ Prestained Protein Ladder, 10 to 180 kDa	Thermo Fisher Scientific
PageRuler™ Plus Prestained Protein Ladder, 10 to 250 kDa	Thermo Fisher Scientific
Phenylmethane sulfonyl fluoride (PMSF)	Carl Roth

Substance	Manufacturer
Pierce Coomassie Plus (Bradford) Assay Reagent	Thermo Fisher Scientific
Potassium acetate	Carl Roth
Potassium chloride	Carl Roth
Potassium citrate	Potassium citrate
Polyethylen glycol (PEG) 6000	Carl Roth
Polyethylene glycol sorbitan monolaurate (Tween-20)	Carl Roth
Polyvinylidene fluoride (PVDF) membrane	Carl Roth
Roti®-NC transfer membrane	Carl Roth
Silver nitrate	Carl Roth
Sodium acetate	Carl Roth
Sodium azide	Carl Roth
Sodium carbonate	Carl Roth
Sodium chloride	Carl Roth
Sodium dodecyl sulfate (SDS)	Carl Roth
Sodium hydroxide	Carl Roth
Sodium hypochlorite 12 %	Carl Roth
Sodium thiosulfate	Carl Roth
Streptomycin sulfate	AppliChem
Tetramethylethylenediamine (TEMED)	Carl Roth
Trichloroacetic acid (TCA) (6.1 N)	Sigma Aldrich
Tripotassium phosphate	Carl Roth
Tris-(hydroxymethyl)-aminomethane (TRIS)	Carl Roth
Triton X-100	Carl Roth/Sigma Aldrich
Tryptone/Peptone from Casein	Carl Roth
Yeast extract	Carl Roth
Zellutrans Roth dialysis tube	Carl Roth

2.1.2. Devices and equipment

Table 2: Used devices and equipment.

Description	Type	Manufacturer
Autoclave	5075 ELVC	Tuttnauser
	Serie FVS	Fedgari
Bunsen burner	Labogaz 470	Campingaz
Cameras	AVT Guppy F-033	Edmund Optics
	Falcon 4M30	DALSA
	EM-C2	Rolera
	ORCA-Flash 2.8	Hamamatsu
	ORCA-Flash 4.0	Hamamatsu
	Powershot G9	Canon
Centrifuges	Centrifuge 5810R	Eppendorf
	Microcentrifuge	Carl Roth
	Mikro 200R	Hettich
	OptimaTM L-90 Ultracentrifuge	Beckman Coulter
	Pico 17	Heraeus
Chemilumineszenz und Fluoreszenz/ECL Westernblotting	ChemoCam	Intas
Compressor	BT-AC 200/24 OF	Einhell
ddH_2O equipment	Milli-Q Plus	Millipore
Electrophoresis chamber, horizontal	Varia 1	Carl Roth
Electrophoresis chamber, vertical	SDS-PAGE apparatus	Phase
Filter sets	F37-525 (eGFP)	AHF Analysentechnik
	F37-580 (NpHR)	AHF Analysentechnik
	F41-007 (mCherry)	AHF Analysentechnik
	530 ± 50 nm bandpass	AHF Analysentechnik
	675 ± 50 nm bandpass	AHF Analysentechnik
	HC BS 605 beam splitter	AHF Analysentechnik

Description	Type	Manufacturer
Gel documentation system	Dark Hood DH-40	Biostep
	EOS 500D	Canon
Head-over tail rotor		VWR
Heat block	AccuBlockTM Digital Dry Bath	Labnet
	Rotilabo- Block Heater H 250	Carl Roth
Incubator	DF8528GL Slimvip (-80 °C)	Skadi
	Ectron (37 °C)	INFORS HT
	FKS 3600 Index 20B (20 °C)	Liebherr
	INB 400 basic convection 53L (37 °C)	Memmert
	Vinothek (16 °C)	Liebherr
Lamps	HBO 50	Osram
	UVT-20 M/W	Herolab
LED	Blue 3 W 30°	Ledxon
	infrared (850 nm) 3 W 120°	Winger Electronics
Magnetic stirrer	Stuart CB162	Bibby Scientific
Micromanipulator	MMJ	Märzhäuser
Micropipette puller	Model P-97	Sutter Instrument
Microscopes	Axiovert 35	Carl Zeiss
	Axiovert 40 CFL	Carl Zeiss
	Axiovert Observer Z1	Carl Zeiss
	Axio Scope.A1	Carl Zeiss
	Leica MZ 16F	Leica
	SMZ 645	Nikon
	Zeiss Cell Observer SD Spinning Disc Confocal microscope	Carl Zeiss
Microwave oven	MM 41580	Micromaxx
Multi-Plate Reader	CLARIOstar PLUS	BMG Labtech
Optical power meter	PM 100	Thorlabs
	S120UV	Thorlabs
Pipets	Gilson PIPETMAN	Gilson

Description	Type	Manufacturer
	P1000, P100N, P10N, P2	
pH meter	Cyberscan pH 510	Eutech
Photometer	Genova	Jenway
Pipet controller	Pipetus	Hirschmann
Rotor	70 Ti	Beckman Coulter
Shutter	Shutter	Sutter Instrument Company
Thermal cycler	MyCycler Personal Thermal Cycler	Bio-Rad
UV crosslinker	UV Stratalinker® 2400	Stratagene
Vortexer	Vortex Genie 2	Scientific Industries
Weighing machines	EMB 600-2 Analysewaage 770	Kern Kern
Western blot	Semi-Dry Blotter `Pegasus`	Phase

2.1.3. Buffers and Media

Buffer and media were prepared using sterile ddH_2O as solvent (if not noted otherwise).

Table 3: Used buffer and media.

Buffer/medium	Ingredients/manufacturer
Acetone stock (Pretreat 1)	50 % (v/v) Acetone
Antarctic phosphatase (AP) Reaction Buffer (10x)	New England Biolabs (NEB)
Bleach solution	0.5 M Sodium hydroxide 2.5 % (w/v) Sodium hypochlorite (12%)
Blocking buffer	1x TBS-T 5 % Milk powder
Buffer D	20 mM Tris-HCl (pH 8) 10 % (v/v) Glycerol

Buffer/medium	Ingredients/manufacturer
	150 mM NaCl +“goodies“: 0.5 mM DTT 0.5 mM PMSF (in ethanol) 1 mM EDTA 1 µg/ml TAME (in DMSO) cOmplete Protease Inhibitor Cocktail tablets
Develop	0.02 % (w/v) Sodium carbonate 0.05 % (v/v) Formaldehyde (37%) 0.05 % (v/v) Sodium thiosulfate stock
DNA loading dye (6x), blue	10 % (v/v) Glycerol 0.25 % (w/v) Bromophenol blue in 6x TAE-buffer
DNA loading dye, purple (6x)	NEB
dNTP Mix	10 mM dATP 10 mM dCTP 10 mM dGTP 10 mM dTTP
ESB	2 % (w/v) SDS 80 mM Tris-HCl (pH 6.8) 10 % (v/v) Glycerol 1.5 % (w/v) DTT 0.1 mg/ml Bromophenol blue
Fixation	97.5 % (v/v) Acetone stock 2.4 % (v/v) TCA stock 0.04 % (v/v) Formaldehyde (37%)
Impregnate	1.3 % (v/v) Silver nitrate stock 1 % (v/v) Formaldehyde (37%)
Injection buffer (10x)	20 % (w/v) PEG 200 mM Potassium phosphate 0.33 mM Calcium chloride

Buffer/medium	Ingredients/manufacturer
	0.33 mM Magnesium sulfate
IPP150	10 mM Tris-Cl pH 8
	150 mM Sodium chloride
	0.05% Triton X-100
IPP150 Calmodulin binding buffer	10 mM 2-Mercaptoethanol
	10 mM Tris-Cl pH 8
	150 mM Sodium chloride
	1 mM Magnesium acetate
	1 mM Imidazole
	2 mM Calcium chloride
	0.05% Triton X-100
IPP150 Calmodulin elution buffer	10 mM 2-Mercaptoethanol
	10 mM Tris-Cl pH 8
	150 mM Sodium chloride
	1 mM Magnesium acetate
	1 mM Imidazole
	2 mM EGTA
	0.05% Triton X-100
Laemmli B (pH 8.8)	1.5 M Tris
	0.4 % (w/v) SDS
Laemmli C (pH 6.8)	0.5 M Tris
	0.4 % (w/v) SDS
	1 mg Bromophenol blue
Lysogeny broth (LB) medium	0.5 % (w/v) Yeast extract
	1 % (w/v) Tryptone/Peptone
	1 % Sodium chloride
	Optional 1.5 % (w/v) Agar
	Optional after autoclaved:
	100 µg/µL Ampicillin
	200 µg/µL Streptomycin
M9 buffer	1 mM Magnesium sulfate
	20 mM Monopotassium phosphate

Buffer/medium	Ingredients/manufacturer
	40 mM Disodium phosphate
	85 mM Sodium chloride
Nematode growth medium (NGM)	0.25 % (w/v) Tryptone/Peptone
	0.3 % (w/v) Sodium chloride
	1.7 % (w/v) Agar
	1 mM Calcium chloride
	1 mM Magnesium sulfate
	25 mM Potassium phosphate buffer
	0.0005 % (w/v) Cholesterol (in ethanol)
	0.001 % (w/v) Nystatin (in ethanol)
PBS (10x, pH 7.4)	Carl Roth
Phusion HF buffer (5x)	NEB
Potassium phosphate buffer (1 M, pH 7.5)	1 M Monopotassium phosphate
	1 M Dipotassium phosphate
Pretreat 2	0.2 % (v/v) Sodium thiosulfate stock
Restriction Enzyme Buffers (10x)	NEB
SDS Running buffer (10x, pH 8.3)	0.25 M Tris
	2 M Glycine
	1 % (w/v) SDS
SDS Sample buffer (4x)	12.5 ml Laemmli C
	5 ml Glycerol
	5 ml 20% SDS
	2.5 ml 2-Mercaptoethanol
	0.5 g Bromophenol blue
Silver nitrate stock	20 % (w/v) Silver nitrate
Single egg/worm lysis buffer (SEWLB)	2.5 mM Magnesium chloride
	10 mM Tris-HCl (pH 8.3)
	50 mM Potassium chloride
	0.05 % (w/v) Gelatine
	0.45 % (v/v) Tween-20
Sodium thiosulfate stock	20 % (w/v) Sodium thiosulfate
Stop	1 % (v/v) Acetic acid (99%)

Buffer/medium	Ingredients/manufacturer
Super Optimal broth with Catabolite repression (SOC)	Clontech
S buffer (pH 6)	6.5 mM Monopotassium phosphate 43.5 mM Dipotassium phosphate 100 mM Sodium chloride
T4 DNA ligase buffer (10x)	NEB
TCA stock	50 % (v/v) TCA (6.1 N)
Tobacco etch virus (TEV) cleavage buffer	10 mM Tris-Cl pH 8 150 mM Sodium chloride 0.5 mM EDTA 1 mM DTT 0.05% Triton X-100
ThermoPol Reaction Buffer (10x)	NEB
Transfer buffer (10x)	1.9 M Glycine 250 mM Tris
TRIS acetate EDTA (TAE) buffer (50x, pH 8.5)	40 mM TRIS/Acetic acid 2 mM EDTA
Tris-buffered saline (TBS) (10x, pH 7.6)	200 mM Tris 1.5 M Sodium chloride
Tris-buffered saline with Tween-20 (TBS-T)	1X TBS 0.05% Tween-20

2.1.4. Kits and beads

Table 4: Used kits and beads.

Kit/Beads	Application	Manufacturer
AlphaScreen cAMP Detection Kit	*In vitro* cAMP measurement	PerkinElmer
Calmodulin-Agarose	Protein purification	Sigma Aldrich
cGMP Direct Chemiluminescent ELISA Kit	*In vitro* cGMP measurement	Arbor Assays

Kit/Beads	Application	Manufacturer
Gibson Assembly Cloning Kit	Gibson assembly	NEB
Human IgG-Agarose	Protein purification	Sigma Aldrich
NucleoBond PC 100	Plasmid DNA purification (Midi)	Macherey-Nagel
QIAquick Gel Extraction Kit	Gel extraction	Qiagen
QIAquick PCR Purification Kit	PCR purification	Qiagen
Roti-Prep Plasmid Mini	Plasmid DNA purification (Mini)	Carl Roth

2.1.5. Enzymes

Table 5: Used enzymes.

Enzyme	Manufacturer	Buffer
Antarctic Phosphatase	NEB	Antarctic Phosphatase Reaction Buffer
Phusion High-Fidelity DNA polymerase	NEB	Phusion HF-Buffer
Proteinase K	Thermo Fisher Scientific	-
Restriction Enzymes	NEB	Respective Buffers
T4 DNA ligase	NEB	T4 DNA Ligase Buffer
Taq DNA Polymerase	NEB	ThermoPol Reaction Buffer
TEV Protease	Sigma Aldrich	TEV cleavage buffer

2.1.6. Antibodies

Table 6: Used antibodies

Name	Epitope	Working concentration	Host	Manufacturer
anti-α-tubulin	15S complex dynein subunits from axonemes	1:50	Mouse	Piperno and Fuller Cat# 4A1, RRID:AB_2732839
anti-mCherry	mCherry	1:10000	Rabbit	OriGene
anti-mouse-HRP	Mouse IgG	1:100	Goat	Thermo Fisher Scientific
anti-rabbit-HRP	rabbit	1:1000 - 1:3000	Goat	Carl Roth
anti-rabbit-HRP	rabbit	1:50000	Goat	Bethyl Laboratories
Anti-Strep Tag II	NWSHPQFEK	1:40	Rabbit	Antibodies-online
anti-TAP	C-terminus of the TAP construct after TEV cleavage	1:1000	Rabbit	Thermo Fisher Scientific
Peroxidase-Anti-Peroxidase (PAP)	horseradish peroxidase	1:1000	Rabbit	Sigma Aldrich

2.1.7. Oligonucleotides

Table 7: Used oligonucleotides.

Name	Sequence (5`-> 3`)	Description
oCS131	CACGGGAGACGAAGAGC	*lite-1(ce314)* genotyping; reverse
oCS131	GCCTTAGAACATTGACGC	*lite-1(ce314)* genotyping; forward

Name	Sequence (5`-> 3`)	Description
oTH01	GCCGTCTAGAATGAAGGACAAGGACAAC AACC	*BeCyclOp* amplification; forward XbaI
oTH03	GATCTAGAATGGAGCAAGCCCAAAACC	*BeCyclOp(aa397-626)* amplification; forward XbaI
oTH04	AGCCGGTACCTTACTTACGTCCGAGGAC CC	*BeCyclOp* amplification; reverse KpnI
oTH12	GACAAGCAGTTAACTAGGTG	Insert amplification from *SL2*; reverse
oTH13	GATTCTTTGCTTGTCAAC	Insert sequencing from *pmyo-3*; forward
oTH14	ACTTGTAAGCTTCTAGG	Insert sequencing from *SL2*; reverse
oTH25	CCCACGACCACTAGATCCATC	Concatamer; *BeCyclOp*1 amplification; forward
oTH26	CCGCCACCAGAACCGCCACCGCCCGAT CCTCCTCCTCCCTTACGTCCGAGGACCC AGT	Concatamer; *BeCyclOp*1 amplification reverse with GGGS linker
oTH27	GCGGTTCTGGTGGCGGTGGCTCAGGCG GCGGCGGCTCCATGAAGGACAAGGACA ACAAC	Concatamer; *BeCyclOp*2 amplification; forward with GGGS linker
oTH28	GTAGGATGAGACAGCGGTACC	Concatamer; *BeCyclOp*2 amplification; reverse KpnI
oTH38	CAACCCACACTGGGACCTCGTCGGAGA CAC	*BeCyclOp(C566D)* site-directed mutagenesis; forward
oTH39	GTGTCTCCGACGAGGTCCCAGTGTGGG TTG	*BeCyclOp(C566D)* site-directed mutagenesis; reverse
oTH46	AGTCTAGAATGGGATGTATCAAATC	*2xLyn11-Eex-Y-b/biPAC* amplification; forward XbaI

Name	Sequence (5`-> 3`)	Description
oTH47	TCCTCAGCCTACTTTATTTGTGGTT	*2xLyn11-Eex-Y-biPAC* amplification; reverse BbvCI
oTH49	TCCTCAGCTTACTTGTCGTTTTC	*2xLyn11-Eex-Y-bPAC* amplification; reverse BbvCI
oTH50	CCATCTAGAATGAAAAGCTCCGCC	*SthK* amplification; forward XbaI
oTH52	ATGGTACCTTATCCCCGCCGTGATG	*SthK* amplification; reverse KpnI
oTH56	ATGAAGGACAAGGACAACAAC	*BeCyclOp* amplification; forward
oTH69	ACGACCACTAGATCCATCTAGAATGGTG AGCAAGGGCGAGGAG	*YFP* amplification; forward with *pmyo-3* overlap
oTH70	GTTGTCCTTGTCCTTCATTGATCCCTTGT ACAGCTCGTCCATG	*YFP* amplification; reverse with BeCyclOp overlap
oTH71	CTTTATCTTTCATAGACATTGATCCCTTG TACAGCTCGTCCATGCC	*YFP* amplification; reverse with *CaCyclOp* overlap
oTH72	GGACGAGCTGTACAAGGGATCAATGTCT ATGAAAGATAAAG	*CaCyclOp* amplification; forward with *YFP* overlap
oTH81	CGGCTAGCATGGTGAGCAAGGG	*YFP* amplification; forward NheI
oTH94	CTACTACTTCTACGTAACCG	*cng-2(tm4267)* genotyping; forward
oTH95	TCCAGCCGCTTGACAAGGTC	*cng-2(tm4267)* genotyping; reverse
oTH96	CTGCAAACCTCCACATGG	*che-6(e1126)* genotyping; forward
oTH97	GCCCGTCAAAGTCCTATAATATAC	*che-6(e1126)* genotyping; reverse
oTH98	GCAAATCTTGCAATTCGCTTC	*cng-1(jh111)* genotyping; forward

Name	Sequence (5`-> 3`)	Description
oTH99	CTGCACTGACTCTGGTGACAC	*cng-1(jh111)* genotyping; reverse
oTH100	GATCACCAGCTTTTCAGAAACTTGG	*cng-3(jh113)* genotyping; forward
oTH101	GTCTCTTCTGCCATTTCATATTCAC	*cng-3(jh113)* genotyping; reverse
oTH102	CCTCTGCCAATGTGGTTGATG	*egl-2(rg-4)* genotyping; forward
oTH103	GCGCTAGTCCGCCTTTAACTC	*egl-2(rg-4)* genotyping; reverse
oTH108	GGTTCTATCACTTGGCGCCGATGTTCTGCCAGAGTAC	*unc-103(n1213)* genotyping; forward
oTH109	CGCTGACGATATGTAGTTGTTCGGACGGTAACGGGC	*unc-103(n1213)* genotyping; reverse
oTH114	ACCGTCGAGCAAGCCGGTGCGGCCGCAATGCTCGAGATGGTG	*BeCyclOp(aa171-399)* amplification; forward
oTH115	GGCTTGGCGCTCGTGCATTCTAGATGGATC	*BeCyclOp(aa171-399)* amplification; reverse
oTH116	GATCCATCTAGAATGCACGAGCGCCAAGCC	*BeCyclOp(aa171-399)* amplification; forward
oTH117	CACCATCTCGAGCATTGCGGCCGCACCGGCTTGCTCGACGGTGG	*BeCyclOp(aa171-399)* amplification; reverse
oTH118	ACCATCTAGAATGCTCTCCACCCCATC	*BeCyclOp(TM0)* amplification; forward
oTH119	ATTGCGGCCGCGGCTTGCTCGACGGTG	*BeCyclOp(TM7)* amplification; reverse
oTH121	CAGCGGTACCTTAGGCTTGCTCGACGGTG	*BeCyclOp(aa171-399)* amplification; reverse KpnI
oTH123	AATGCGGCCGCGGCTTGTCCGTTCTTG	*BeCyclOp(aa442)* amplification; reverse NotI

Name	Sequence (5`-> 3`)	Description
oTH124	ATCCATCTAGAATGGCCACCGAGGCCAAG	*BeCyclOp(aa423)* amplification; forward XbaI
oTH125	ATGCGGCCGCTCCACGGTTGTAGGC	*BeCyclOp(aa178)* amplification; reverse NotI
oTH126	CAGCGGTACCTTATCCACGGTTGTAGGC	*BeCyclOp(aa1-178)* amplification; reverse KpnI
oTH127	TCCATCTAGAATGGGAGAGACCCAGTGCAACG	*BeCyclOp(aa230)* amplification; forward XbaI
oTH128	GCGGTACCTTAGGCTTGTCCGTTCTTG	*BeCyclOp(aa139-442)* amplification; reverse KpnI

2.1.8. Plasmids

Table 8: Used plasmids.

Name	Description	Source
-	*2xLyn11-Eex-Y-biPAC*	Prof. G. Nagel
-	*2xLyn11-Eex-Y-bPAC*	Prof. G. Nagel
-	*2xLyn11-Eex-Y-bPAC(F198Y)*	Prof. G. Nagel
-	*L1_CMV_SthK-mCherry*	Dr. F. Schneider-Warme
-	*pMA-T_PaaC+7*	Ass.Prof. A. Winkler
-	*pmyo-3::BKT0::SthK(T378V) ::YFP::bPAC(K29E)*	Prof. G. Nagel
-	*pGEM_CaCyclOp*	Prof. P. Hegemann
-	*pGEM_CaCyclOp(A-2x)*	Prof. P. Hegemann
pASH3	*pmyo-3::BeCNG1-YFP*	A. Hirschhäuser

Name	Description	Source
pCS175	*pflp-1(trc 332bp)::FLP-1::bicisGFP*	Dr. C. Schultheis
pMS04	*pmyo-3::bPGC::SL2::mCherry*	M. Schneider
pMS05	*pmyo-3::bPAC::SL2::mCherry*	M. Schneider
pNHO1	*pmyo-3::PaaC+7::SL2::mCherry*	N. Ho
pJN55	*pmyo-3::tax-2::GFP*	Dr. J. Nagpal
pJN58	*pmyo-3::tax-4::GFP*	Dr. J. Nagpal
pJN63	*pmyo-3::BeCyclOp::SL2::mCherry*	Dr. J. Nagpal
pJN67	*punc-17::BeCyclOp::SL2::mCherry*	Dr. J. Nagpal
pJN68	*punc-17::BeCyclOp(E497K,H564D,C566T)::SL2::mCherry*	Dr. J. Nagpal
pJN69	*pmyo-3::BeCyclOp(E497K,H564D,C566T)::SL2::mCherry*	Dr. J. Nagpal
pTH01	*pmyo-3::CaCyclOp(E497K,C566D)::SL2::mCherry*	My MSc Thesis
pTH02	*pmyo-3::CaCyclOp::SL2::mCherry*	My MSc Thesis
pTH03	*punc-17::CaCyclOp::SL2::mCherry*	My MSc Thesis
pTH04	*punc-17::CaCyclOp(E497K,C566D)::SL2::mCherry*	My MSc Thesis
pTH05	*pmyo-3::BeCyclOp::TAP::SL2::mCherry*	My MSc Thesis
pTH06	*pmyo-3::BeCyclOp(aa1-146)::SL2::mCherry*	My MSc Thesis
pTH07	*pmyo-3::BeCyclOp(aa397-626)::SL2::mCherry*	My MSc Thesis
pTH08	*pmyo-3::BeCyclOp(aa397-626)::SL2::GFP*	My MSc Thesis
pTH09	*pmyo-3::BeCyclOp::(GGGS)4::BeCyclOp::TAP::SL2::mCherry*	This work
pTH10	*pmyo-3::BeCyclOp(aa1-146)::SL2::GFP*	This work
pTH11	*punc-17::BeCyclOp(E497K,C566D)::SL2::mCherry*	This work
pTH12	*pmyo-3::BeCyclOp(E497K,C566D)::SL2::mCherry*	This work
pTH15	*pmyo-3::2xLyn::YFP::biPAC*	This work
pTH16	*pmyo-3::2xLyn::YFP::bPAC*	This work
pTH17	*pmyo-3::2xLyn::YFP::bPAC(F198Y)*	This work
pTH18	*pmyo-3::SthK::mCherry*	This work
pTH19	*pmyo-3::SthK::SL2::mCherry*	This work

Name	Description	Source
pTH20	*pmyo-3::SthK::SL2::GFP*	This work
pTH21	*punc-17::SthK::mCherry*	This work
pTH23	*punc-17::SthK::SL2::GFP*	This work
pTH32	*pmyo-3::YFP::CaCyclOp(E497K,C566D)::SL2::mCherry*	This work
pTH33	*pmyo-3::YFP::BeCyclOp(E497K,C566D)::SL2::mCherry*	This work
pTH41	*punc-17::YFP::BeCyclOp(E497K,C566D)::SL2::mCherry*	This work
pTH42	*punc-17::YFP::CaCyclOp(E497K,C566D)::SL2::mCherry*	This work
pTH44	*pET-29::BeCyclOp::Strep*	This work
pTH45	*pmyo-3::BeCyclOp(aa1-178)::SL2::mCherry*	This work
pTH46	*pmyo-3::BeCyclOp(aa171-399)::mCherry*	This work
pTH47	*pmyo-3::BeCyclOp(aa139-399)::mCherry*	This work
pTH48	*pmyo-3::BeCyclOp(aa139-626)::mCherry*	This work
pTH49	*pmyo-3::BeCyclOp(aa1-399)::mCherry*	This work
pTH50	*pmyo-3::BeCyclOp(aa171-399)::SL2::GFP*	This work
pTH52	*pmyo-3::BeCyclOp(aa139-626)::SL2::GFP*	This work
pTH55	*pmyo-3::BeCyclOp(aa397-626)::mCherry*	This work
pTH57	*pmyo-3::BeCyclOp(aa139-442)::mCherry*	This work
pTH58	*pmyo-3::BeCyclOp(aa1-442)::mCherry*	This work
pTH59	*pmyo-3::BeCyclOp(aa442-626)::mCherry*	This work
pTH60	*pmyo-3::BeCyclOp(aa139-442)::SL2::GFP*	This work
pTH61	*pmyo-3::BeCyclOp(aa1-442)::Sl2::GFP*	This work
pTH62	*pmyo-3::BeCyclOp(aa442-626)::SL2::GFP*	This work
pTH63	*pmyo-3::BeCyclOp(aa1-178)::mCherry*	This work
pTH65	*pmyo-3::BeCyclOp(aa230-626)::mCherry*	This work
pTH66	*pmyo-3::BeCyclOp(aa230-626)::SL2::GFP*	This work

2.1.9. Organisms

Table 9: Used organisms.

Species	Strain	Source
Caenorhabditis elegans	Bristol N2 (wild type)	*Caenorhabditis* Genetics Center (CGC)
Escherichia coli	DH5a	Invitrogen
Escherichia coli	HB101	Bio-Rad
Escherichia coli	OP50-1	CGC

2.1.10. Transgenic *C.elegans* strains

Table 10: Used C. elegans strains.

Strain	Genotype	Transgene	Source
CB1126	*che-6(e1126)IV*	-	CGC
CG197	*egl-2(rg4); him-5(e1490)*	-	CGC
KG1180	*lite-1(ce314)*	-	CGC
KJ461	*cng-1(jh111)*	-	CGC
KJ462	*cng-3(jh113)*	-	CGC
ZX1569	*lite-1(ce314)*	*zxIs53[punc-17::bPAC::YFP; pmyo-2::mCherry]*	Dr. W. Steuer Costa
ZX1741	*lite-1(ce314)*	*zxEx889[pmyo-3::tax-2::GFP, pmyo-3::tax-4::GFP, pmyo-2::mCherry]*	Dr. J. Nagpal
ZX1742	*lite-1(ce314)*	*zxEx851[pmyo-3::BeCyclOp::SL2::mCherry, pmyo-3::tax-2::GFP, pmyo-3::tax-4::GFP]*	Dr. J. Nagpal
ZX1940	*lite-1(ce314)*	*zxEx960[punc-17::BeCyclOp::SL2::mCherry, pelt-2::GFP]*	Dr. J. Nagpal
ZX1941	*lite-1(ce314)*	*zxEx961[punc-17::BeCyclOp(E497K,H564D,C566T)::SL2::mCherry, pelt-2::GFP]*	Dr. J. Nagpal

Strain	Genotype	Transgene	Source
ZX2154	*lite-1(ce314)*	*zxEx1043[punc-17::CaCyclOp(E497K,C566D)::SL2::mCherry]*	My MSc Thesis
ZX2165	*lite-1(ce314)*	*zxEx1054[pmyo-3::BeCyclOp(397-626)::SL2::GFP]*	My MSc Thesis
ZX2166	*lite-1(ce314)*	*zxEx1055[pmyo-3::BeCyclOp(397-626)::SL2::mCherry]; ZxEx889[pmyo-3::tax-2::GFP, pmyo-3::tax-4::GFP,pmyo-2::mCherry]*	My MSc Thesis
ZX2168	*lite-1(ce314)*	*zxEx1057[pmyo-3::BeCyclOp(1-146)::SL2::mCherry; pmyo-3::BeCyclOp(397-626)::SL2::GFP]*	My MSc Thesis
ZX2169	*lite-1(ce314)*	*zxEx1058[pmyo-3::BeCyclOp(1-146)::SL2::mCherry; pmyo-3::BeCyclOp(397-626)::SL2::GFP]; ZxEx889[pmyo-3::tax-2::GFP, pmyo-3::tax-4::GFP,pmyo-2::mCherry]*	My MSc Thesis
ZX2316	*lite-1(ce314)*	*zxEx889; zxEx1088[pmyo-3::BeCyclOp(E497K,H564D,C566T)::SL2::mCherry]*	This work
ZX2317	*lite-1(ce314)*	*zxEx1089[pmyo-3::BeCyclOp::BeCyclOp::TAP::SL2::mCherry]*	This work
ZX2318	*lite-1(ce314)*	*zxEx889; zxEx1089*	This work
ZX2326	*lite-1(ce314)*	*zxEx1091[pmyo-3::BeCyclOp::SL2::mCherry; pmyo-3::BeCNG1::YFP]*	This work
ZX2327	*lite-1(ce314)*	*zxIs117[pmyo-3::BeCyclOp::TAP::SL2::mCherry]*	This work
ZX2391	*lite-1(ce314)*	*zxEx1117[punc-17::BeCyclOp(E497K,C566D)::Sl2::mCherry]*	This work
ZX2393	*lite-1(ce314)*	*zxEx1119[pmyo-3::SthK::SL2::GFP; pmyo-2::mCherry]*	This work
ZX2394	*lite-1(ce314)*	*zxEx1119; zxEx1120[pmyo-3::bPAC::SL2::mCherry]*	This work
ZX2395	*lite-1(ce314)*	*zxEx1121 [punc-17::SthK::SL2::GFP; pmyo-3::mCherry]*	This work

Strain	Genotype	Transgene	Source
ZX2396	*lite-1(ce314)*	*zxEx1121; zxIs53*	This work
ZX2397	wild type	*zxEx1121*	This work
ZX2398	*lite-1(ce314)*	*zxEx1122[pmyo-3::SthK::mCherry; pmyo-2::CFP]*	This work
ZX2399	*lite-1(ce314)*	*zxEx1123[punc-17::SthK::mCherry; pmyo-2::CFP]*	This work
ZX2400	*lite-1(ce314)*	*zxEx889; zxEx1124[pmyo-3::BeCyclOp::SL2::mCherry]*	This work
ZX2401	*lite-1(ce314)*	*zxEx889; zxEx1125[pmyo-3::bPGC::SL2::mCherry]*	This work
ZX2402	*lite-1(ce314)*	*zxEx889; zxEx1126[pmyo-3::CaCyclOp::SL2::mCherry]*	This work
ZX2403	*lite-1(ce314)*	*zxEx889; zxEx1127[pmyo-3::BeCyclOp(E497K,C566D)::SL2::mCherry]*	This work
ZX2404	*lite-1(ce314)*	*zxEx889; zxEx1128[pmyo-3::YFP::BeCyclOp(E497K,C566D)::SL2::mCherry]*	This work
ZX2405	*lite-1(ce314)*	*zxEx889; zxEx1129[pmyo-3::CaCyclOp(E497K,C566D)::SL2::mCherry]*	This work
ZX2406	*lite-1(ce314)*	*zxEx889; zxEx1130[pmyo-3::YFP::CaCyclOp(E497K,C566D)::SL2::mCherry]*	This work
ZX2408	*lite-1(ce314)*	*zxEx889; zxEx1132[pmyo-3::bPAC::SL2::mCherry]*	This work
ZX2504	*lite-1(ce314)*	*zxEx1119; zxEx1219[pmyo-3::BeCyclOp::SL2::mCherry]*	This work
ZX2505	*lite-1(ce314)*	*zxEx1119; zxEx1220[pmyo-3::BeCyclOp(E497K,C566D)::SL2::mCherry]*	This work
ZX2506	*lite-1(ce314)*	*zxEx1119; zxEx1221[pmyo-3::BeCyclOp(E497K,H564D,C566T)::SL2::mCherry]*	This work

Strain	Genotype	Transgene	Source
ZX2507	*lite-1(ce314)*	*zxEx1119; zxEx1222[pmyo-3::CaCyclOp(E497K,C566D)::SL2::mCherry]*	This work
ZX2508	*lite-1(ce314)*	*zxEx1119; zxEX1176[pmyo-3::2xLyn11::Eex::YFP::biPAC; pmyo-3::mCherry]*	This work
ZX2509	*lite-1(ce314)*	*zxEx1119; zxEX1177[pmyo-3::2xLyn11::Eex::YFP::bPAC(F198Y); pmyo-3::mCherry]*	This work
ZX2510	*lite-1(ce314)*	*zxEx1121; zxIs112[punc-17::mPAC::YFP; pmyo-2::mCherry]*	This work
ZX2511	*lite-1(ce314)*	*zxEx1121; zxEX1178[punc-17::mPAC::YFP; pmyo-2::mCherry]*	This work
ZX2512	*lite-1(ce314)*	*zxEx1179[pmyo-3::BKT0::SthK(T378V)::YFP::bPAC; pmyo-2::mCherry]*	This work
ZX2514	*lite-1(ce314)*	*zxEx1181[pmyo-3::2xLyn11::Eex::YFP::bPAC; pmyo-2::CFP]*	This work
ZX2516	*lite-1(ce314)*	*ZxEx889; zxEX1177[pmyo-3::2xLyn11::Eex::YFP::bPAC(F198Y); pmyo-3::mCherry]*	This work
ZX2523	*lite-1(ce314)*	*zxEx1198[pmyo-3::BKT0::SthK(T378V)::YFP::bPAC; pmyo-2::mCherry]*	N. Ho
ZX2525	*lite-1(ce314)*	*zxEx1210 [pmyo-3::PaaC+7::SL2::mCherry; pmyo-3::SthK::Sl2::mCherry]*	N. Ho
ZX2526	*lite-1(ce314)*	*zxEx1211 [pmyo-3::PaaC+7::SL2::mCherry]*	N. Ho
ZX2530	*lite-1(ce314)*	*zxEx1119; zxEx1230[pmyo-3::BeCyclOp(E497K,H564D,C566T)::SL2::mCherry]*	This work
ZX2606	*lite-1(ce314)*	*zxEx1231[punc-17::SthK::SL2::GFP; punc-17::BeCyclOp(E497K,H564D,C566T)::SL2::mCherry; pmyo-2::mCherry]*	This work

Strain	Genotype	Transgene	Source
ZX2607	*lite-1(ce314)*	*zxEx1232[punc-17::SthK::SL2::GFP; punc-17::BeCyclOp(E497K,H564D,C566T)::SL2::mCherry; pmyo-2::mCherry]*	This work
ZX2608	*lite-1(ce314)*	*zxEx1233[punc-17::SthK::SL2::GFP; punc-17::BeCyclOp(E497K,C566D)::SL2::mCherry]*	This work
ZX2609	*lite-1(ce314)*	*zxEx1124[pmyo-3::BeCyclOp::SL2::mCherry]*	This work
ZX2610	*lite-1(ce314)*	*zxEx1125[pmyo-3::bPGC::SL2::mCherry]*	This work
ZX2611	*lite-1(ce314)*	*zxEx1126[pmyo-3::CaCyclOp::SL2::mCherry]*	This work
ZX2612	*lite-1(ce314)*	*zxEx1088[pmyo-3::BeCyclOp(E497K,H564D,C566T)::SL2::mCherry]*	This work
ZX2613	*lite-1(ce314)*	*zxEx1127[pmyo-3::BeCyclOp(E497K,C566D)::SL2::mCherry]*	This work
ZX2614	*lite-1(ce314)*	*zxEx1128[pmyo-3::YFP::BeCyclOp(E497K,C566D)::SL2::mCherry]*	This work
ZX2615	*lite-1(ce314)*	*zxEx1129[pmyo-3::BeCyclOp(E497K,C566D)::SL2::mCherry]*	This work
ZX2616	*lite-1(ce314)*	*zxEx1130[pmyo-3::YFP::BeCyclOp(E497K,C566D)::SL2::mCherry]*	This work
ZX2617	*lite-1(ce314)*	*zxEx1132[pmyo-3::bPAC::SL2::mCherry]*	This work
ZX2657		*zxIs128[pmyo-3::BeCyclOp::BeCyclOp::TAP::SL2::mCherry]*	This work
ZX2659	*lite-1(ce314)*	*zxEx1255[punc-17::YFP::BeCyclOp(E497K,C566D)::SL2::mCherry; pmyo-2::mCherry]*	This work
ZX2660	*lite-1(ce314)*	*zxEx1256[punc-17::YFP::CaCyclOp(E497K,C566D)::SL2::mCherry; pmyo-2::mCherry]*	This work
ZX2662	*egl-2(rg4); lite-1(ce314)*	-	A. Pieragnolo and this work

Strain	Genotype	Transgene	Source
ZX2663	*unc-103(n1213)*	-	A. Pieragnolo and this work
ZX2664	*egl-2(rg4); lite-1(ce314)*	*zxEx1132*	A. Pieragnolo and this work
ZX2665	*che-6(e1126)IV; lite-1(ce314)*	*zxEx1132*	S. Zhou and this work
ZX2666	*che-6(e1126)IV; lite-1(ce314)*	-	S. Zhou and this work
ZX2667	*unc-103(n1213); lite-1(ce314); pha-1(e2123)III; him-5(e1490)*	-	A. Pieragnolo and this work
ZX2730	*cng-2(tm4261*	-	Dennis H. Kim (HMS, Boston)
ZX2782	*unc-103(n1213); lite-1(ce314); pha-1(e2123)III; him-5(e1490)*	*zxEx1132*	A. Pieragnolo and this work
ZX2783	*cng-3(jh113); lite-1(ce314)*	*zxEx1132*	S. Zhou and this work
ZX2784	*cng-3(jh113); lite-1(ce314)*	-	S. Zhou and this work
ZX2785	*cng-1(jh111); lite-1(ce314)*	*zxEx1132*	S. Zhou and this work

Strain	Genotype	Transgene	Source
ZX2786	*cng-1(jh111); lite-1(ce314)*	-	S. Zhou and this work
ZX2787	*cng-2(tm4267); lite-1(ce314)*	*zxEx1132*	S. Zhou
ZX2788	*cng-2(tm4267); lite-1(ce314)*	-	S. Zhou
ZX2789	*cng-1(jh111)*	*zxEx1132*	S. Zhou and this work
ZX2790	*cng-2(tm426*	*zxEx1132*	S. Zhou
ZX2791	*cng-3(jh113)*	*zxEx1132*	S. Zhou and this work
ZX2792	*unc-103(n1213)*	*zxEx1132*	A. Pieragnolo and this work
ZX2793	*egl-2(rg4)*	*zxEx1132*	A. Pieragnolo and this work
ZX2794	*che-6(e1126)IV*	*zxEx1132*	This work
ZX2795	Wild type	*zxEx1132*	This work
ZX2796	*lite-1(ce314)*	*zxEx1297[punc-17::SthK::Sl2::GFP; punc-17::YFP::BeCyclOp(E497K,C566D)::Sl2::mCherry; pmyo-2::mCherry]*	This work
ZX2797	*lite-1(ce314)*	*zxEx1298[punc-17::SthK::Sl2::GFP; punc-17::YFP::BeCyclOp(E497K,C566D)::Sl2::mCherry; pmyo-2::mCherry]*	This work
ZX2798	*lite-1(ce314)*	*zxEx1317[punc-17::SthK::Sl2::GFP; punc-17::YFP::BeCyclOp(E497K,C566D)::Sl2::mCherry; pmyo-2::mCherry]*	This work
ZX2799	*lite-1(ce314)*	*zxEx1324[pmyo-3::BeCyclOp(aa171-399)::mCherry]*	This work

Strain	Genotype	Transgene	Source
ZX2970	*lite-1(ce314)*	*zxEx1326[pmyo-3::BeCyclOp(aa139-399)::mCherry]*	This work
ZX2971	*lite-1(ce314)*	*zxEx1327[pmyo-3::BeCyclOp(aa139-442)::mCherry]*	This work
ZX2972	*lite-1(ce314)*	*zxEx1328[pmyo-3::BeCyclOp(aa139-626)::mCherry]*	This work
ZX2973	*lite-1(ce314)*	*zxEx1329[pmyo-3::BeCyclOp(aa1-442)::mCherry]*	This work
ZX2974	*lite-1(ce314)*	*zxEx1330[pmyo-3::BeCyclOp(aa1-399)::mCherry]*	This work
ZX2975	*lite-1(ce314)*	*zxEx1331[pmyo-3::BeCyclOp(aa397-626)::mCherry]*	This work
ZX2976	*lite-1(ce314)*	*zxEx1332[pmyo-3::BeCyclOp(aa442-626)::mCherry]*	This work
ZX2977	*lite-1(ce314)*	*zxEx1333[pmyo-3::BeCyclOp(aa1-178)::mCherry]*	This work
ZX2978	*lite-1(ce314)*	*zxEx1334[pmyo-3::BeCyclOp(aa230-626)::mCherry]*	This work
ZX2979	*lite-1(ce314)*	*zxEx889[pmyo-3::tax-2::GFP, pmyo-3::tax-4::GFP, pmyo-2::mCherry]; zxEX1335[pmyo-3::BeCyclOp(aa139-626)::Sl2::GFP]*	This work
ZX2984	*lite-1(ce314)*	*zxEx889[pmyo-3::tax-2::GFP, pmyo-3::tax-4::GFP, pmyo-2::mCherry]; zxEx1336[pmyo-3::BeCyclOp(aa397-626)::Sl2::GFP]*	This work
ZX2985	*lite-1(ce314)*	*zxEx851[pmyo-3::BeCyclOp::SL2::mCherry, pmyo-3::tax-2::GFP, pmyo-3::tax-4::GFP]; zxEx1338[pmyo-3::BeCyclOp(aa139-442)::Sl2::GFP, pmyo-2::mCherry]*	This work
ZX2986	*lite-1(ce314)*	*zxEx1338[pmyo-3::BeCyclOp(aa139-442)::Sl2::GFP, pmyo-2::mCherry]*	This work
ZX2987	*lite-1(ce314)*	*zxEx1335[pmyo-3::BeCyclOp(aa139-626)::Sl2::GFP]*	This work

Strain	Genotype	Transgene	Source
ZX2988	*lite-1(ce314)*	*zxEx1336[pmyo-3::BeCyclOp(aa397-626)::Sl2::GFP]*	This work
ZX2989	*lite-1(ce314)*	*zxEx1339[pmyo-3::BeCyclOp(aa442-626)::Sl2::GFP]*	This work
ZX2990	*lite-1(ce314)*	*zxEx1340[pmyo-3::BeCyclOp(aa230-626)::Sl2::GFP]*	This work
ZX2991	*lite-1(ce314)*	*zxEx889[pmyo-3::tax-2::GFP, pmyo-3::tax-4::GFP, pmyo-2::mCherry]; zxEx1341[pmyo-3::BeCyclOp(aa1-146)::Sl2::mCherry; pmyo-3::BeCyclOp(aa397-626)::Sl2::GFP]*	This work
ZX2992	*lite-1(ce314)*	*zxEx889[pmyo-3::tax-2::GFP, pmyo-3::tax-4::GFP, pmyo-2::mCherry]; zxEx1342[pmyo-3::BeCyclOp(aa1-146)::Sl2::mCherry; pmyo-3::BeCyclOp(aa442-626)::Sl2::GFP]*	This work
ZX2993	*lite-1(ce314)*	*zxEx889[pmyo-3::tax-2::GFP, pmyo-3::tax-4::GFP, pmyo-2::mCherry]; zxEX1343[pmyo-3::BeCyclOp(aa1-178)::Sl2::mCherry; pmyo-3::BeCyclOp(aa230-626)::Sl2::GFP]*	This work
ZX2994	*lite-1(ce314)*	*zxEx1342[pmyo-3::BeCyclOp(aa1-146)::Sl2::mCherry; pmyo-3::BeCyclOp(aa442-626)::Sl2::GFP]*	This work
ZX2995	*lite-1(ce314)*	*zxEx1343[pmyo-3::BeCyclOp(aa1-178)::Sl2::mCherry; pmyo-3::BeCyclOp(aa230-626)::Sl2::GFP]*	This work
ZX2996	*lite-1(ce314)*	*zxEx1344[pmyo-3::BeCyclOp(aa1-178)::Sl2::mCherry]*	This work
ZX3022	*lite-1(ce314)*	*zxEx851 [pmyo-3::BeCyclOp::SL2::mCherry, pmyo-3::tax-2::GFP, pmyo-3::tax-4::GFP]; zxEx1337[pmyo-3::BeCyclOp(aa1-146)::Sl2::GFP, pmyo-2::mCherry]*	This work
ZX3023	*lite-1(ce314)*	*zxEx1337[pmyo-3::BeCyclOp(aa1-146)::Sl2::GFP, pmyo-2::mCherry]*	This work

Strain	Genotype	Transgene	Source
ZX3024	*lite-1(ce314)*	*zxEx851[pmyo-3::BeCyclOp::SL2::mCherry, pmyo-3::tax-2::GFP, pmyo-3::tax-4::GFP]; zxEx1350[pmyo-3::BeCyclOp(aa230-626)::Sl2::GFP, pmyo-2::mCherry]*	This work
ZX3025	*lite-1(ce314)*	*zxEx1350[pmyo-3::BeCyclOp(aa230-626)::Sl2::GFP, pmyo-2::mCherry]*	This work
ZX3026	*lite-1(ce314)*	*zxEx889[pmyo-3::tax-2::GFP, pmyo-3::tax-4::GFP,pmyo-2::mCherry]; zxEx1351[pmyo-3::BeCyclOp(aa171-399)::Sl2::GFP, pmyo-3::BeCyclOp(aa230-626)::Sl2::GFP, pmyo-3::mCherry]*	This work
ZX3027	*lite-1(ce314)*	*zxEx889[pmyo-3::tax-2::GFP, pmyo-3::tax-4::GFP, pmyo-2::mCherry]; zxEX1352[pmyo-3::BeCyclOp(aa139-442)::Sl2::GFP, pmyo-3::BeCyclOp(aa139-626)::Sl2::GFP, pmyo-3::mCherry]*	This work
ZX3028	*lite-1(ce314)*	*zxEx1352[pmyo-3::BeCyclOp(aa139-442)::Sl2::GFP, pmyo-3::BeCyclOp(aa139-626)::Sl2::GFP, pmyo-3::mCherry]*	This work
ZX3029	*lite-1(ce314)*	*zxEx889[pmyo-3::tax-2::GFP, pmyo-3::tax-4::GFP, pmyo-2::mCherry]; zxEx1353[pmyo-3::BeCyclOp(aa1-442)::Sl2::GFP, pmyo-3::BeCyclOp(aa139-626)::Sl2::GFP, pmyo-3::mCherry]*	This work
ZX3030	*lite-1(ce314)*	*zxEx889[pmyo-3::tax-2::GFP, pmyo-3::tax-4::GFP, pmyo-2::mCherry]; zxEx1354[pmyo-3::BeCyclOp(aa1-442)::Sl2::GFP, pmyo-3::BeCyclOp(aa397-626)::Sl2::GFP, pmyo-3::mCherry]*	This work

2.1.11. Consumables

Table 11: Used consumables.

Description	Type	Manufacturer
Centrifuge tube	15 and 50 mL	Greiner Bio-One
Columns	Mobicols	Mobitec
Cover slip	Squared cover slip 22x22 mm	Carl Roth
Disposable tips	0.5-10 µL, 10-200 µL, 100-1000 µL	Greiner
Glass capillary	1B 100 F-4	World Precision Instruments
Glass pipettes	5, 10, and 25 mL	Brand
Microcentrifuge tube	200 µL Row of 8x 200 µL 1.5 and 2 mL	Sarstedt neoLab Carl Roth
Microcentrifuge plate	96x 200 µL	Carl Roth
Microplate	96-well	Greiner
Microscope slide	-	Carl Roth
Objective immersion oil	Immersol 518F	Carl Zeiss
OptiPlate-384	White Opaque 384-well Microplate	Perkin Elmer
Parafilm	Parafilm M	VWR
Petri dish	60/15 mm, 100/20 mm and 150/20 mm	Greiner Bio One
Protective gloves	Rotiprotect latex and nitrile	Carl Roth

2.1.12. Software

Table 12: Used software.

Name	Version	Manufacturer
Arduino	1.8	Arduino Team
Argus X1	3	Biostep
Axio Vision	4.5	Carl Zeiss
Clone Manager	9	Sci Ed Central
EndNote X5	15.0.1.5774	Thomson Reuters
FIJI	1.52i	Fiji contributors
GraphPad Prism	8.2.263	GraphPad
ImageJ	1.52i	Wayne Rasband
KNIME Desktop	2.12	KNIME.com
Micro-Manager	1.4	Open Imaging
Microsoft Office	16.0.14026.20270	Microsoft
Origin	9.75	OriginLab
SnapGene	1.3.3.	GSL Biotech LLC
VirtualDub	1.10.4	Avery Lee
Windows Media Player	12	Microsoft
ZEN lite 2012	1.1.1.0 blue edition	Carl Zeiss

2.2. Methods

2.2.1. Molecular biological methods

Molecular biological methods described in this study were used for molecular cloning, preparation, and purification of recombinant plasmid DNA. Molecular cloning strategies were planned *in silicio* using the programs SnapGene and Clone Manager 9. In general, restriction enzyme-based cloning was applied. In case of failure, or no

availability of suitable restriction sites, Gibson assembly was executed to generate the recombinant plasmid.

2.2.1.1. Polymerase Chain Reaction

The polymerase chain reaction (PCR) is a technique for the amplification of a specific DNA-Sequence *in vitro*. In this study, PCR was performed for molecular cloning of recombinant plasmids and *C. elegans* genotyping. In PCR, the desired fragment in the DNA template (plasmid or genomic *C. elegans* DNA) is flanked by two complementary oligonucleotide primers, termed forward primer (5`-end on antisense strand) and reverse primer (3`-end on sense strand). The PCR consists of the DNA template, both oligonucleotide primers, a thermostable polymerase, a buffer for the polymerase and deoxyribonucleoside triphosphates (dNTPs) in a water solution. The reaction is classified into three main steps – denaturation in which the double-stranded DNA template is separated into two singe-stranded DNA templates – annealing whereas the complementary oligonucleotides hybridize to the singe-stranded DNA templates – elongation in which the DNA polymerase catalyses the synthesis of double-stranded DNA with complementary DNA nucleotides starting at the oligonucleotide's primers. The steps are repeated for a distinct number of cycles, leading to the exponentially amplification of the target DNA fragment, whereas each newly synthesized fragment serves as a new template. As polymerase, the Phusion DNA polymerase was used for molecular cloning, since the polymerase has a higher fidelity and a proof reading 3´- 5´exonuclease activity, achieving a reduced error rate during polymerization. For PCR-based *C. elegans* genotyping, the Taq DNA polymerase was used or, in case of failure, the Phusion DNA polymerase. The general PCR set ups are listened in table 13. For analytical PCRs (e.g. Gradient PCR or Colony PCR), the volume was scaled to 20 µl, whereas for preparative PCRs, the volume was upscaled to 250 µl. The reaction conditions for the Phusion and Taq DNA polymerases are specified in table 14 and 15, respectively. In this context, the primer annealing temperature is dependent on the binding ability of the oligonucleotides (GC content, length), and the elongation time varies based on the length of the amplified PCR product. Primer design was performed *in silico* using the programs Clone Manager 9 and SnapGene. After PCR, the products were separated,

extracted, purified, and concentrated using agarose gel electrophoresis, followed by gel extraction, or via purification and concentration of DNA fragments. Finally, the DNA concentration of the sample was determined using Genova photometer.

Table 13: Basic PCR setup for molecular cloning (Phusion DNA polymerase) and C. elegans genotyping (Taq DNA polymerase).

Substance	Volume [µl]	Final concentration
DNA template	Variable (Phusion) 2.5 µl Proteinkinase K digest (Taq)	1 – 100 ng/µl
Forward primer (10 µM)	2.5 (Phusion) 0.6 (Taq)	0.5 µM (Phusion) 0.24 µM (Taq)
Reverse primer (10 µM)	2.5 (Phusion) 0.6 (Taq)	0.5 µM (Phusion) 0.24 µM (Taq)
dNTPs (10 mM)	1 1	200 µM (Phusion) 400 µM (Taq)
Polymerase buffer (10x)	10 (Phusion) 2.5 (Taq)	1x 1x
DNA polymerase	0.7 (Phusion) 0.25 (Taq)	1.4 U (Phusion) 1.25 U (Taq)
ddH_2O	add to 50 (Phusion) add to 25 (Taq)	-

Table 14: Thermocycling conditions for Phusion DNA polymerase-based PCR.

Step	Temperature [°C]	Time [s]	Cycles
Initial denaturation	98	30	1
Denaturation	98	10	
Primer annealing	Primer specific	30	30-35
Primer elongation	72	30 (per kb)	
Final Extension	72	600	1

Table 15: Thermocycling conditions for Taq DNA polymerase-based PCR.

Step	Temperature [°C]	Time [s]	Cycles
Initial denaturation	95	30	1
Denaturation	95	15	
Primer annealing	Primer specific	30	30-35
Primer elongation	68	60 (per kb)	
Final Extension	68	600	1

2.2.1.2. Site-directed mutagenesis

Site-directed mutagenesis is a method to introduce specific and intentional changes in the DNA sequence of the gene of interest and gene products. In this study, site directed mutagenesis was applied to convert the guanylyl cyclase domains of the CyclOps BeCyclOp and CaCyclOp into adenylyl cyclase domains. Primers for site-directed mutagenesis were designed *in silico* using the programs SnapGene and Clone Manager 9, and PCR was exerted using the Phusion DNA polymerase. Subsequently, the reaction mixture was incubated at 37 °C overnight with the enzyme DpnI to digest the parental methylated DNA, followed by the purification and concentration of the PCR product and heat shock transformation into *E. coli* cells. Screening for the desired recombinant plasmid was executed via plasmid DNA purification, analytical restriction digest and DNA sequencing and alignment.

2.2.1.3. Preparative and analytical restriction digest

In molecular biology, restriction endonucleases are used to cleave DNA into linear fragments at or near specific recognition sites, termed restriction sites, which are palindromic sequences consisting of 4 – 8 bp. In general, type II endonucleases are utilized due to their feature to cut the DNA within or at short distances from the recognition site, generating fragments with blunt or sticky ends (3`or 5` overhang), allowing their ligation with DNA fragments, cleaved by the same enzyme, and thus containing complementary ends. In this study, restriction digest was applied for molecular cloning, i.e. a preparative restriction digest (plasmid DNA or purified PCR product) was conducted, followed by agarose gel electrophoresis, gel extraction and

DNA fragment ligation or Gibson assembly to generate a new recombinant plasmid. Further, analytical restriction digest was performed to screen for and verify the correct recombinant plasmid, and its analysis of the respective DNA fragment pattern via agarose gel electrophoresis.

Restriction digests were performed according to the manufacturer`s instructions, using 10 µg plasmid DNA or 1 - 10 µg purified PCR product for preparative purposes and 100 – 1000 ng plasmid DNA for analytical purposes, in a 50 or 10 µl rection volume, respectively. Concentration of the applied restriction enzyme depends on its activity in U (one U digests 1 µg in 1 h at 37 °C).

2.2.1.4. Agarose gel electrophoresis

Agarose gel electrophoresis is a technique to separate and identify DNA fragments after PCR or preparative and analytical restriction digest after their size. Here, negatively charged DNA molecules migrate to the positively charged pole in an electric field, and the running speed of the molecules depends on their size, i.e. larger or circular molecules exhibit a decreased running speed in the polymerized gel in comparison to smaller linear molecules.

For agarose gel electrophoresis, 1 - 2% agarose was dissolved in 1x TAE-buffer, heated in a microwave oven, and poured into a chamber. The size of the pockets was adjusted in dependence of the sample volume. Samples and DNA ladder were mixed with DNA loading dye for visualization of the DNA during electrophoresis, to bind divalent metal ions and to inhibit metal dependent nucleases, and to increase the density of the sample so that the sample layers the bottom of the pocket. As reference, GeneRuler DNA ladder was applied. Electrophoresis was conducted for 45 - 60 min using a voltage of 130 - 145 V. For DNA visualization, the gel was incubated in a 1% ethidium bromide (EtBr) staining solution (0.1% (w/v) EtBr in ddH_2O) for 15 min, which intercalates between the base pairs of the DNA double helix. Gel analysis was performed using the program Argus X1 V.3 and the gel documentation system.

2.2.1.5. DNA gel extraction

In molecular biology, DNA gel extraction is applied to extract and purify PCR products or cleaved linear DNA fragments after their separation via agarose gel electrophoresis, aiming on their separation from components of preceding reactions (e.g. primers, nucleotides, EtBr, enzymes/proteins). Here, DNA gel extraction was conducted after preparative restriction digest of plasmid DNA, or after the amplification of specific DNA sequences using PCR. For DNA gel extraction, the desired DNA fragment was excised from the agarose gel using a scalpel and the gel documentation system, using a minimum of UV illumination to prevent possible DNA damages of the DNA molecules. DNA extraction was performed using the QIAquick Gel Extraction Kit according to the manufacturer`s instructions. The Kit is based on the silica membrane technology, separating DNA molecules (70 bp – 10 kb) by a reversible binding of the molecules to the silica membrane. To increase the yield of the extracted DNA, following deviation to the manual was performed: In the elution step, the incubation with 20 µl ddH_2O was increased to 10 min.

2.2.1.6. Purification and concentration of DNA fragments

Purification and concentration of DNA fragments is a method to concentrate and purify DNA fragments from impurities of preceding reactions (e.g. enzymes, salts). In this study, it was performed after preparative restriction digest of PCR products or site-directed mutagenesis. The QIAquick PCR Purification Kit was utilized according to the manufacturer`s instructions. The Kit is based on the silica membrane technology to purify DNA fragments (100 bp – 10 kb). For an increased yield of DNA sample, a deviation is present in the elution step: Incubation of the DNA sample with 20 µl ddH_2O was increased to 10 min.

2.2.1.7. Determination of DNA concentration

To determine the DNA concentration of a sample, the optical density at a wavelength of 260 nm is measured, at which the purines and pyrimidines of the DNA depict the maximum absorption. Here, determination of DNA concentration was performed

using Genova photometer after DNA gel extraction, purification and concentration of DNA fragments and plasmid DNA preparation.

2.2.1.8. DNA dephosphorylation

DNA dephosphorylation was applied to prevent re-ligations of linearized plasmid DNA fragments by the T4 DNA ligase and thus to reduce the occurrence of false positive clones after transformation of a newly created recombinant plasmid. After preparative restriction digest of DNA molecules, a phosphate residue remains at the 5`-end. Dephosphorylation was performed using the Antarctic phosphatase, that non-specifically catalyses the dephosphorylation of 3`- and 5`-ends of DNA and RNA phosphomonoesters, as well as NTP or dNTPs. The reaction mixture was incubated for 1 h at 37 °C, followed by a heat inactivation of the enzyme for 5 min at 70 °C.

2.2.1.9. DNA fragment ligation

In molecular biology, DNA fragment ligation is utilized to covalently link linear DNA fragments obtained by preparative restriction digest and PCR. In this study, the T4 DNA ligase was applied, catalysing the formation of a phosphodiester bound of adjacent 3`-hydroxyl and 5`-phosphate termini's, thus enabling the linkage of cohesive and blunt ends. To increase the yield of successful DNA ligation, the molar ratio between vector and insert was 1:6, and different amounts of vector DNA (20 and 50 fmol) were used. Ligation reaction was carried out for 1 h at room temperature (RT) or 16 °C overnight. Subsequently, 5 µl of the reaction mixture were used for heat shock transformation into *E. coli* cells.

2.2.1.10. Gibson Assembly of multiple DNA fragments

Gibson Assembly is a molecular biological method for the assembly of multiple DNA fragments in a single, isothermal reaction. The technique combines three enzymatic activities: 5` exonuclease activity to generate long overhangs – polymerase activity to fill the gaps of the annealed singe-stranded regions – ligase activity to seal the nick

and covalently link the DNA fragments. Gibson Assembly was performed according to the manufacturer`s instructions. To increase the yield of successful assembled DNA fragments, 100 ng vector DNA and a 3-fold molar excess of insert DNA was utilized. Finally, 5 µl of the reaction mixture were used for heat shock transformation into *E. coli* cells.

2.2.1.11. Heat shock transformation

Heat shock transformation technique is used to insert a foreign plasmid or ligation product into bacterial cells (e.g. *E. coli*), aiming on the amplification and screening of recombinant plasmids in molecular cloning. In this study, artificial competence of the bacteria cells was induced using calcium chloride, and the competent cells were stored in 100 µl aliquots at -80 °C.

For ligation reaction, 50 µl cell aliquots were thawed on ice and the appropriate amount of plasmid DNA (Ligation and Gibson mixture 5 µl, re-transformation 1-10 ng) were mixed with the bacteria cells and incubated for 30 min on ice. Subsequently, a heat shock for 45 s at 42 °C was performed, leading to the absorption of the plasmid DNA by the bacteria cells. The mixture was incubated for 3 min on ice, followed by the addition of 500 µl SOC or LB medium to the mixture. The aliquot was incubated for 1 h at 37 °C in a shaker. Bacteria cells were centrifuged for 5 min at 2500 g, and 400 µl of the supernatant were removed and the cells were resuspended in the remaining supernatant. Finally, the mixture was plated on LB agar plates (containing 100 ng/µl ampicillin) and the plates were incubated at 37 °C for 16 h and stored at 4 °C. For screening of the desired recombinant plasmid in molecular cloning and plasmid amplification, single *E. coli* colonies were used to inoculate small (3 ml) or large (150 ml) cultures. For this purpose, bacteria colonies were picked using a sterile pipette tip and added to the LB medium (containing 100 ng/µl ampicillin) and grown at 37 °C overnight.

2.2.1.12. Plasmid DNA preparation (Miniprep/Midiprep)

Plasmid DNA preparation was performed to extract and purify plasmid DNA *from E. coli* cells for analytical restriction digest (Miniprep) or preparative (Midiprep) purposes

such as molecular cloning or transformation of *C. elegans* using microinjection. Miniprep was performed using a 3 ml bacteria culture and the Roti-Prep Plasmid Mini kit, whereas Midiprep was performed using a 150 ml bacteria culture and the NucleoBond PC 100 kit. Both Kits based on alkaline lysis of the bacteria cells followed by the separation of plasmid and genomic DNA using centrifugation or filtration, respectively. The kits were conducted according to the manufacturer`s instructions.

2.2.1.13. Plasmid DNA sequencing and alignment

The DNA sequencing technique is used to determine the order of nucleotides in DNA molecules. In this work, DNA sequencing was performed to verify the sequence of specific sections of newly synthesized plasmid DNAs. DNA sequencing was conducted by the companies Eurofins Genomic and Microsynth AG utilizing the Sanger sequencing method, and preparation of sequencing samples were performed according to the company's protocols. 50-100 or 40-100 ng/µl plasmid DNA were premixed with 2 or 3 µl sequencing primer (10 µM) to end volumes of 17 or 15 µl, respectively. Sequencing results were aligned to the *in silico* plasmid DNA sequence to verify the recombinant plasmid using the program Clone Manager 9.

2.2.1.14. Cloning strategies

pTH09 [*pmyo-3::BeCyclOp::BeCyclOp::TAP::SL2::mCherry*]: PCR of pTH05 using the primers oTH27 and oTH28. PCR of pJN63 using the primers oTH25 and oTH26. Restriction digest of pJN63 with KpnI und XbaI and Gibson Assembly to pTH09.

pTH10 [*pmyo-3::BeCyclOp(aa1-146)::SL2::GFP*]: Restriction digest of pTH06 and pCS175 using AgeI and EcoRI. Ligation to pTH10.

pTH11 [*punc-17::BeCyclOp[E497K,C566D]::SL2::mCherry*]: PCR of pJN63 using the primers oTH38 and oTH39. Restriction digest of the PCR product and pJN72 using KpnI and BclI. Ligation to pTH11.

pTH12 [*pmyo-3::BeCyclOp[E497K,C566D]::SL2::mCherry*]: PCR of pTH11 using the primers oTH01 and oTH04. Restriction digest of the PCR product and pTH01 with KpnI and XbaI. Ligation to pTH12.

pTH15 [*pmyo-3::2xLyn::YFP::biPAC*]: PCR of pGEM::2xLyn::YFP::biPAC using the primers oTH46 and oTH47. Restriction digest of the PCR product and pTH02 using XbaI und BbvCI. Ligation to pTH15.

pTH16 [*pmyo-3::2xLyn::YFP::bPAC*]: PCR of pGEM::2xLyn::YFP::bPAC using the primers oTH46 and oTH49. Restriction digest of the PCR product and pTH02 with XbaI and BbvCI. Ligation to pTH16.

pTH17 [*pmyo-3::2xLyn::YFP::bPAC(F198Y)]*: PCR of pGEM::2xLyn::YFP::bPAC(F198Y) using the primers oTH46 and oTH49. Restriction digest of the PCR product and pTH02 using XbaI und BbvCI. Ligation to pTH17.

pTH18 [*pmyo-3::SthK::mCherry*]: PCR of L1_CMV_SthK_mCherry using the primers oTH50 and oTH51. Restriction digest of the PCR product and pTH02 using XbaI and SfbI. Ligation to pTH18.

pTH19 [*pmyo-3::SthK::SL2::mCherry*]: PCR of L1_CMV_SthK_mCherry using the primers oTH50 and oTH52. Restriction digest of the PCR product and pTH02 using XbaI und KpnI. Ligation to pTH19.

pTH20 [*pmyo-3::SthK::SL2::GFP*]: Restriction digest of pTH19 and pTH10 using XbaI and KpnI. Ligation to pTH20.

pTH21 [*punc-17::SthK::mCherry*]: Restriction digest of L1_CMV_SthK_mCherry and pTH03 using NheI and SbfI. Ligation to pTH21.

pTH23 [*punc-17::SthK::SL2::GFP*]: Restriction digest of pTH22 and pTH10 using ApaI and KpnI. Ligation to pTH23.

pTH32 [*pmyo-3::YFP::CaCyclOp(E497K,C566D)::SL2::mCherry*]: PCR of pTH16 using the primers oTH69 and oTH71. PCR of pTH01 using the primers oTH72 and oTH12. Restriction digest of pTH02 using XbaI and KpnI. Gibson Assembly to pTH32.

pTH33 [*pmyo-3::YFP::BeCyclOp(E497K,C566D)::SL2::mCherry*]: PCR of pTH16 using the primers oTH69 and oTH70. PCR of pTH12 using the primers oTH56 and

oTH01. Restriction digest of pTH02 using XbaI and KpnI. Gibson Assembly to pTH33.

pTH41 [*punc-17::YFP::BeCyclOp(E497K,C566D)::SL2::mCherry*]: PCR of pTH33 using the primers oTH81 and oTH12. Restriction digest of the PCR product and pTH04 using NheI and KpnI. Ligation to pTH41.

pTH42 [*punc-17::YFP::CaCyclOp(E497K,C566D)::-SL2::mCherry*]: PCR of pTH32 using the primers oTH81 and oTH12. Restriction digest of the PCR product and pTH04 using NheI and KpnI. Ligation to pTH42.

pTH44 [*pET-29::BeCyclOp::Strep*]: cDNA encoding BeCyclOp, codon optimized for *E. coli* expression fused to a C-terminal Strep tag, was synthesized by Twist Bioscience (South San Francisco, USA) in a pET-29 vector.

pTH45 [*pmyo-3::BeCyclOp(aa1-178)::SL2::mCherry*]: PCR of pJN63 using the primers oTH1 and oTH126. Restriction digest of the PCR product and pJN63 using KpnI and XbaI. Ligation to pTH45.

pTH46 [*pmyo-3::BeCyclOp(aa171-399)::mCherry]:* PCR of pJN63 using the primers oTH116 and oTH117. PCR of pTH19 using the primers oTH114 and oTH115. Gibson Assembly to pTH46.

pTH47 [*pmyo-3::BeCyclOp(aa139-399)::mCherry]:* PCR of pJN63 using the primers oTH118 and oTH119. Restriction digest of the PCR product and pTH46 using NotI and XbaI. Ligation to pTH47.

pTH48 [*pmyo-3::BeCyclOp(aa139-626)::mCherry]:* PCR of pJN63 using the primers oTH118 and oTH120. Restriction digest of the PCR product and pTH46 using NotI and XbaI. Ligation to pTH48.

pTH49 [*pmyo-3::BeCyclOp(aa1-399)::mCherry]:* PCR of pJN63 using the primers oTH01 and oTH117. Restriction digest of the PCR product and pTH46 using NotI and XbaI. Ligation to pTH49.

pTH50 [*pmyo-3::BeCyclOp(aa171-399)::SL2::GFP*]: PCR of pJN63 using the primers oTH116 and oTH121. Restriction digest of the PCR product and pTH10 using KpnI and XbaI. Ligation to pTH50.

pTH52 [*pmyo-3::BeCyclOp(aa139-626)::SL2::GFP*]: PCR of pJN63 using the primers oTH118 and oTH4. Restriction digest of the PCR product and pTH10 using KpnI and XbaI. Ligation to pTH52.

pTH55 [*pmyo-3::BeCyclOp(aa397-626)::mCherry]:* PCR of pJN63 using the primers oTH03 and oTH120. Restriction digest of the PCR product and pTH46 using NotI and XbaI. Ligation to pTH55.

pTH57 [*pmyo-3::BeCyclOp(aa139-442)::mCherry]:* PCR of pJN63 using the primers oTH118 and oTH123. Restriction digest of the PCR product and pTH46 using NotI and XbaI. Ligation to pTH57.

pTH58 [*pmyo-3::BeCyclOp(aa1-442)::mCherry]:* PCR of pJN63 using the primers oTH03 and oTH123. Restriction digest of the PCR product and pTH46 using NotI and XbaI. Ligation to pTH58.

pTH59 [*pmyo-3::BeCyclOp(aa442-626)::mCherry]:* PCR of pJN63 using the primers oTH124 and oTH120. Restriction digest of the PCR product and pTH46 using NotI and XbaI. Ligation to pTH59.

pTH60 [*pmyo-3::BeCyclOp(aa139-442)::SL2::GFP*]: PCR of pJN63 using the primers oTH118 and oTH128. Restriction digest of the PCR product and pTH10 using KpnI and XbaI. Ligation to pTH60.

pTH61 [*pmyo-3::BeCyclOp(aa1-442)::Sl2::GFP*]: PCR of pJN63 using the primers oTH1 and oTH128. Restriction digest of the PCR product and pTH10 using KpnI and XbaI. Ligation to pTH61.

pTH62 [*pmyo-3::BeCyclOp(aa442-626)::SL2::GFP*]: PCR of pJN63 using the primers oTH124 and oTH4. Restriction digest of the PCR product and pTH10 using KpnI and XbaI. Ligation to pTH62.

pTH63 [*pmyo-3::BeCyclOp(aa1-178)::mCherry]:* PCR of pJN63 using the primers oTH01 and oTH125. Restriction digest of the PCR product and pTH46 using NotI and XbaI. Ligation to pTH63.

pTH65 [*pmyo-3::BeCyclOp(aa230-626)::mCherry]:* PCR of pJN63 using the primers oTH127 and oTH120. Restriction digest of the PCR product and pTH46 using NotI and XbaI. Ligation to pTH65.

pTH66 [*pmyo-3::BeCyclOp(aa230-626)::SL2::GFP*]: PCR of pJN63 using the primers oTH127 and oTH4. Restriction digest of the PCR product and pTH10 using KpnI and XbaI. Ligation to pTH66.

2.2.2. Caenorhabditis elegans methods

2.2.2.1. Maintenance of *C. elegans*

C. elegans strains were cultivated on NGM plates (containing 0.2 % streptomycin (w/v)) seeded with the bacterial strain OP50-1 as food source. For this purpose, 60- and 100-mm petri dishes were filled with 8 or 20 ml NGM, respectively. The dishes dried overnight at RT and were stored at 4 °C. NGM plates were supplemented with 200 or 1000 µl OP50-1 liquid culture, dried overnight at RT or for 2 h at 30 °C. The OP50-1 strain is resistant to streptomycin, and is uracil auxotroph to prevent overgrowth of the bacterial lawn (Brenner, 1974). Depending on the desired growth period, the *C. elegans* strains were cultivated at 16, 20, 25 °C or at RT. Transfer of single animals was conducted using a heat-sterilized platin wire covered with a small layer of bacteria, or in case of behavioural experiments via a hair pick made of human eye lashes to prevent the transmission of bacteria. Transfer of a higher number of animals was performed via the upside-down transfer of a small NGM piece of a populated plate, excised using a sterilized spatula. A stereo microscope provided with a transmitter light source was utilized for the visualization of the animals.

2.2.2.1.1. Cultivation on egg-plates

Large scale cultivation of *C. elegans* was performed on egg-plates according to Hochbaum et al. 2010. To this end, a 145 mm petri dish was filled with 40 ml NGM and dried overnight at RT. The yolk of 10 eggs were transferred into a 500 ml sterile bottle and LB medium was added up to 400 ml. The suspension was incubated at 60 °C for 1 h in a water bath to inactivate the lysozyme of the yolks. 150 ml of the bacteria culture HB101 were centrifuged at 2500 rpm for 15 min at 4 °C, and the bacteria pellet was resuspended in 40 ml fresh LB medium and added to the RT

tempered yolk-LB mixture. The bacteria strain is not uracil auxotroph, enabling a better growth on NGM plates compared to the OP50-1 strain, and thus provides more food options to obtain a high yield of animals. 10 ml of the yolk-LB-HB101 mixture were transferred on a NGM plate and incubated overnight at RT. Next, the remaining liquid was discarded, and the plates dried overnight at RT. The plates were stored at 4 °C or directly used for worm cultivation. *C. elegans* strains were cultivated on egg-plates till a high population density was reached.

Worm harvesting was performed by washing the animals off the egg-plates using 50 ml 4 °C cold ddH_2O. The animal suspension was centrifuged at 2500 rpm for 5 min at 4 °C, and the supernatant was removed. The animal pellet was washed three times with 50 ml 4 °C cold ddH_2O to remove components of the yolk-LB-HB101 plates. After the last centrifugation step, the animals were resuspended 1 : 1 in buffer D + goodies and the suspension was dropped into liquid nitrogen. For cell disruption, the drops were grounded in a mortar to a fine powder, and the powder was stored at – 80 °C.

In this study, the worm powder was used for detergent screening and TAP purification of BeCyclOp::TAP and BeCyclOp::BeCyclOp::TAP, and for TEV cleavage analysis.

2.2.2.1.2. Decontamination

Decontamination of *C. elegans* strains was performed to remove the animals from foreign bacteria, yeast, or mold. For this purpose, 10 adult animals were placed in a drop (~ 50 µl) of bleach solution beyond the bacterial lawn of a fresh NGM plate and incubated for 10 - 30 min until the animals have dissolved. The solution causes the decomposition of the contaminants and of the animals, leaving the *C. elegans* eggs which are robust and not affected by this treatment. The eggs were transferred to the bacterial lawn to ensure the survival of the freshly hatched larvae. At the next day, the larvae were transferred on a fresh NGM plate.

2.2.2.1.3. Male generation

In *C. elegans* populations, males occur only at low frequency (~ 0.2 - 0.5 %) by spontaneous non-disjunction in the hermaphrodite germ line (Hodgkin *et al.*, 1979). The frequency could be increased by crossing with hermaphrodites (~ 50%) or by heat shock (2 - 5%) (Walsh *et al.*, 2020; Wood, 1988).

In this study, males were used for the generation of new transgenic *C. elegans* strains. Male frequency was increased by heat-shock treatment, whereas five L4 stage hermaphrodites were incubated for 4 – 6 h at 30 °C. After 3 – 5 days, plates were screened after males, which were used for a cross with their own genotype to obtain a higher yield of males for subsequent crosses.

2.2.2.2. Generation of transgenic *C. elegans* strains

2.2.2.2.1. Transformation of *C. elegans* using microinjection

Microinjection is a technique to insert foreign DNA into *C. elegans*, generating new transgenic *C. elegans* strains (Mello *et al.*, 1991). In this study, the method was applied to implement new optogenetic tools in *C. elegans*, to analyse the expression pattern and level of a protein of interest, and to overexpress TAP-tagged BeCyclOp monomer and concatamer in *C. elegans* muscle cells.

For this purpose, a microinjection mix containing the exogenous plasmid DNA is injected into the distal arms of the gonads of young adult hermaphrodites. This region is an ideal target because the oocytes create a syncytium during maturation, and thus the exogenous DNA could be engulfed by the nuclear envelope forming immature oocytes which subsequently got fertilized and finally were sequestered through the vulva of the animals. Extrachromosomal arrays contain multiple copies of the injected plasmid DNA, are generated by homologous recombination, and could be transmitted to the first-generation progeny (F1). In general, only a fraction of the F1 progeny contain the arrays and transmit the transgene through many subsequent generations, often accompanied without changes in the expression or heritability. Though, these arrays have a varying degree of mitotic instability and incomplete inheritance (Mello *et al.*, 1991). To identify transgenic lines carrying the

extrachromosomal arrays, markers are co-injected, especially reporter gene constructs coding for a fluorescence protein.

For transformation of *C. elegans* using microinjection, the subsequent injection mix in table 16 was applied. To facilitate extrachromosomal array formation, the final DNA concentration was set to 100 ng/µl. As marker plasmids, *pmyo-2::mCherry*; *pmyo-2::CFP* or *pmyo-3::mCherry* were used. To prevent clogging of the injection needle, the injection mix was centrifuged for 10 min at 13300 rpm, and 15 µl of the supernatant was used for microinjection.

Table 16: Injection mix composition.

Substance	Volume of final concentration
Injection buffer	3 µl
Plasmid(s) of interest	0.01 to 100 ng/µl
Marker plasmid	1.5 to 3 ng/µl
Fill DNA	add to 100 ng/µl
ddH_2O	add to 30 µl

Custom made injection needles were produced using glass capillaries pulled with a P-97 microelectrode puller. For needle filling, 0.5 µl of the injection mix was pipetted onto the opening end of the needle which gets filled due to capillary forces. Subsequently, the filled needle was mounted to the stereo microscope Axiovert 40 CFL (Zeiss) using an air pressure outlet connected to a micromanipulator. A coverslip with dried agarose (2% (w/v) in ddH_2O) was fixed on a microscope slide, carved on one edge, covered at this place with halocarbon oil and placed on the microscope stage. The needle tip was broken by gently touching it to one of the carvings in the injection pad, in combination with induced air pressure. Young adult hermaphrodites (5 - 20) were immobilized in halocarbon oil on the agar pad using a hair pick to prevent drying and moving of the animals. The needle tip was inserted into the gonad of the animal and the DNA mix was injected using air pressure. 5 injected animals were transferred in M9 buffer on OP50-1 seeded NGM plates to recover them from the oil and cultivated at RT for 3 - 5 days. Selection was performed on a Leica MZ 16 F fluorescence microscope based on the used selection marker. Single F1 transgenic animals were separated on OP50-1 NGM plates and screened for transgenic F2 progenies with a high transmission rate.

For optogenetic experiments, the generated strains contain the loss-of-function mutation *lite-1(ce314)*. Reason for this was that the nematode expresses LITE-1, which is an ultraviolet/blue-light sensor, whose activation provokes an escape response in the animal (Edwards *et al.*, 2008). Thus, during the experiments the triggering of the escape behaviour should be prevented.

2.2.2.2.2. Crossing of *C. elegans*

Crossing of *C. elegans* strains was applied to transfer extrachromosomal arrays between strains, to exchange mutations between genotypes, or to outcross background mutations after UV irradiation, by cross-fertilization of hermaphrodites and the sperm contributed by a male after mating. Crossing of *C. elegans* strains was performed by placing L4 hermaphrodites with adult males in a ratio of 1:3 on a NGM plate. After 12 - 16 h, the hermaphrodites were separated on OP50-1 NGM plates and incubated at RT. After 1 - 2 days, crossing was evaluated by the occurrence of males. Depending on the genotype, F1 heterozygous males were used in a second cross (outcrossing after UV irradiation; outcrossing of *lite-1(ce314)*) or F1 heterozygous hermaphrodites were singled on OP50-1 NGM plates. F2 animals were separated on OP50-1 NGM plates and F3 animals were screened for fluorescent markers and homozygosity using PCR-based genotyping.

2.2.2.2.3. Genomic integration of extrachromosomal DNA in *C. elegans*

Extrachromosomal arrays are not transmitted to all progenies of a transgenic strain and exhibits mosaicism in their expression. To solve this problem, transgenes could be integrated into the genome of *C. elegans*. In this work, transgenes containing TAP-tagged BeCyclOp monomer and concatamer used for tandem affinity purification were integrated into the genome. Genomic integration was performed via UV irradiation, which causes chromosomal breaks followed by ligation of extrachromosomal arrays during DNA repair. 100 transgenic L4 hermaphrodites were transferred on a NGM plate and irradiated with two pulses of 33.3 mJ interspaced by a 30 s break using a Stratagene UV crosslinker (Stratalinker). Animals rested for 1 h at RT, and batches of 10 worms were transferred on OP50-1 NGM plates and

cultivated at RT until starvation (F3 generation). Plates were chunked to OP50-1 NGM plates and incubated for 1 day at RT. 800 transgenic animals were singled to OP50-1 NGM plates and allowed to grow until starvation at RT. Plates were screened for the 100 % presence of the transgene via fluorescence marker. Successfully integrated strains were outcrossed 3 - 5 times with the same genotype to eliminate background mutations in the genome. Further, PCR-based genotyped was executed to verify the presence of the transgene in the genome, and expression of the protein of interest was analysed by fast protein extraction from *C. elegans*.

2.2.2.3. Isolation of genomic DNA from *C. elegans*

Genomic DNA from *C. elegans* was isolated via worm lysis and served as template for subsequent PCR-based genotyping. 1 - 10 animals were transferred into a reaction tube containing 2.5 µl SEWLB with proteinase K (0.4 µg/ml), and incubated for 30 min at -80 °C for cell break, followed by an incubation at 60 °C for 60 min for worm lysis and 15 min at 95 °C to inactivate the proteinase K.

2.2.2.3.1. PCR-based genotyping of *C. elegans*

PCR-based genotyping was performed after crossing of *C. elegans* to identify and verify a homozygous genotype of the F3 progeny, and to verify genomic integrated transgenes. For this purpose, wild type and mutant genotypes were compared after differences in their genome, i.e. a deletion or a point mutation in the DNA sequence, causing a knockout of a gene of interest. Therefore, PCR-based amplification was applied using two oligonucleotide primers flanking the region of interest, resulting in a PCR product of different length compared to the wild type allele, or alternatively a different length after restriction digest. To identify homozygous strains, wild type or mutant strains served as positive control, whereas a mixture of both genomic DNAs was utilized to identify heterozygous strains. Mutant strains and PCR specifications for genotyping used in this work are summarized in table 17.

Table 17: Mutant C. elegans strains and their PCR specifications for genotyping.

Genotype	Mutation	Oligonucleotides
che-6(e1126)	Substitution (G/A)	oTH96, oTH97
cng-1(jh111)	Deletion (1222 bp)	oTH98, oTH99
cng-2(tm4267)	Insertion (G) Deletion (337 bp)	oTH94, oTH95
cng-3(jh113)	Deletion (882 bp)	oTH100, oTH101
egl-2(rg4)	Deletion (4023 bp)	oTH102, oTH103
lite-1(ce314)	Substitution (C/T)	oCS131, oCS132
unc-103(n1213)	Deletion (*unc-103*)	oTH108, oTH109

2.2.2.4. Microscopy techniques

2.2.2.4.1. Stereo microscopy

A stereo microscope (dissecting microscope) is an optical device which allows a three-dimensional view of a specimen at low magnification. In this study, the SMZ 645 stereo microscope (Nikon) was utilized for *C. elegans* handling.

2.2.2.4.2. Fluorescence microscopy

A fluorescence microscope is an optical device that uses fluorescence for image generation. In this work, fluorescence microscopy was applied for maintenance and analysis of transgenic *C. elegans* strains expressing fluorescent proteins, and for determination of the expression and distribution of fluorescent tagged proteins.

For handling of transgenic *C. elegans* strains, a Leica MZ 16 F microscope (Zeiss) equipped with filter sets for cyan fluorescent protein (CFP), green fluorescent protein (GFP) and red fluorescent protein (RFP) was used.

For analysis of the expression pattern of fluorescent tagged proteins, transgenic animals were immobilized with 50 mM sodium azide (NaN_3) in ddH_2O on agarose pads (2% (w/v) in M9 buffer) and fixed under a cover slip. Images were acquired using an Axio Scope.A1 microscope (Zeiss) equipped with a 10x objective and 100x

immersion objective, a 50 W HBO mercury lamp, the filter sets F37-525 (for GFP) and F37-580 (for NpHR) (AHF Analysentechnik), and an ORCA Flash 2.8 (Hamamatsu) digital camera. The program micro manager was utilized for adjustment of exposure time, EM Gain, and image acquisition. Images were analysed and processed using the program FiJi.

The expression pattern of BeCyclOp fragments in body wall muscle cells was analysed using an inverted Axiovert Observer Z1 microscope, equipped with a 40x immersion objective (Zeiss 40x/1.3 oil), a 100 W HBO mercury lamp as light source, and the filter F41-007 (for mCherry) (AHF Analysentechnik). Images were acquired using an ORCA Flash 4.0 (Hamamatsu) digital camera and the software micro manager. Images were edited using the program FiJi.

For determination of protein expression level, Zeiss Cell Observer SD Spinning Disc Confocal microscope (Zeiss) was used, equipped with a 10x objective, 514 nm excitation laser and an EM-C2 (Rolera) camera. The software ZEN was used to acquire z-stacks (0.3 µm intervals), using a 40% laser power, an EM Gain of 150, full resolution and 100 ms exposure time. Images were saved as 16-bit czi files and analysis was performed using the program ImageJ by drawing regions of interest along the whole body of the animal to measure the mean fluorescence intensity.

2.2.2.5. *C. elegans* behaviour analysis

One day prior to the behaviour experiments, transgenic L4 hermaphrodites were transferred to OP50-1 NGM plates and cultivated at RT in dark. For optogenetic experiments comprising microbial rhodopsins, animals were transferred on OP50-1 NGM plates containing 200 µM ATR (diluted in 100 % ethanol) or without ATR as negative control.

For investigation of spectral tuning of BeCyclOp using artificial retinal analogue, animals were transferred on OP50-1 NGM plates containing 200 µM analogue (II, IV, V, VI, VII, VIII, IX (AzimiHashemi *et al.*, 2014)). In case of optogenetic experiments involving the synthetic phytochrome-linked cyclase PaaC+7, animals were

transferred on OP50-1 NGM plates supplemented with 1 mM biliverdin (diluted in 100% DMSO).

For all optogenetic experiments, light intensity was measured using a S120UV Sensor with PM 100 D power meter.

2.2.2.5.1. Swimming behaviour analysis

Swimming behaviour analysis was performed either in a 96-well microtiter plate (small scale) and manually scoring of the swimming cycles, or in 30 mm NGM petri dishes (containing 2.5 ml NGM; large scale) and automatically scoring of the swimming frequency.

Small scale swimming analysis was performed using an Axio Scope.A1 microscope (Zeiss) equipped with a 4x objective, a Powershot G9 camera (Canon), a 50 W HBO mercury lamp and red filtered transmission light (675 ± 50 nm bandpass filter; dark condition). 100 µl NGM and 50 µl of M9 buffer were filled in a well of a 96-well microtiter plate, respectively. 6 – 12 young adult hermaphrodites were transferred to the well under red light (650 ± 50 nm) and incubated for at least 10 min in the dark. Animals were recorded for 30 in dark, followed by 30 s blue (1, 0.2, 0.4 mW/mm^2; 470 ± 40 nm) or green light (1 or 1.35 mW/mm^2; 530 ± 50 nm), and if necessary 30 s, 60 s or 270 s in dark. Swimming cycles were manually counted for defined time periods of 15 s or 30 s (defined as a complete sinusoid movement in a swimming cycle) using the program Windows Media Player.

Large scale swimming analysis was conducted using a tracker based on the `Multi Worm Tracker`, equipped with a petri dish holder, a Falcon 4M30 camera (DALSA), a f/4.0 Rodagon camera lens (Rodenstock), a custom-made aluminium ring containing six Blue HighPower-LEDs (Ledxon) focusing the light onto the center of the petri dish holder and infrared Power LEDs (850 nm) (Winger Electronics) as background light source. 40 – 70 young adult hermaphrodites were washed off from a 60 mm OP50-1 NGM plate under red light (650 ± 50 nm) using 800 µl M9 buffer and a glass Pasteur pipette and were transferred into a reaction tube. Animals settled for 5 min, followed by replacement of about 700 µl M9 buffer by fresh buffer to remove bacteria, and their transfer on 30 mm NGM plates. Animals were incubated for at least 10 min in

M9 buffer and in darkness before measurement. Video acquisition was performed using the video acquisition software MS-Acqu. Animals were recorded for 60 s in dark, 60 s during light application (0.9 mW/mm^2; 470 nm), and 60 s in dark. The `wrMTrck` plugin in ImageJ was utilized for automated tracking and quantification of the swimming cycles of each video. Tracks were validated and combined for each animal using a custom written Java Script (swimming_tracks_processing_v1.2) by Dennis Vettkötter.

2.2.2.5.2. Crawling behaviour analysis

Crawling behaviour analysis on solid media was conducted using a worm tracker as previously described (Stirman *et al.*, 2011). A mechanical shutter (Sutter Instruments) between the projector and the Axiovert 35 microscope (Zeiss) was used to synchronize the light application. Further, the transmission light was filtered through a red 675 ± 50 nm bandpass filter. Single young adult hermaphrodites were placed on NGM plates under red light (>600 nm) in a dark room and kept for 15 min in darkness before measurement. Animals were tracked for 15 s in dark, 25 s during light (0.9 mW/mm^2; 470 nm), and 15 s after light. Bending angles, body length and crawling speed values were determined using a custom-made workflow in KNIME as previously described (Steuer Costa *et al.*, 2017).

Body length values > 25% and crawling speed values which depicted deviations > 1.25 mm/s with respect to the mean first five seconds of the video were excluded, and videos containing > 15% of discarded data points were excluded. Calculated bending angle, body length and crawling speed values of each animal were normalized to the averaged values before light application (0 – 15 s).

2.2.2.5.3. Body length measurement

Body length measurements were executed as previously described (Liewald *et al.*, 2008). Young adult hermaphrodites were individually placed under red light (>600 nm) on plain NGM plates and assayed on an Axio Scope.A1 microscope (Zeiss) equipped with a 10x objective, a Powershot G9 camera (Canon), a 50 W HBO

mercury lamp and transmission light filtered through a red 675 ± 50nm bandpass filter (dark condition). Animals were stimulated with blue (0.1, 0.2, 0.4, 0.9, or 2.1 mW/mm^2; 470 ± 40 nm) or green (0.9 mW/mm^2; 530 ± 50) light. The duration of the light pulse was defined by a computer-controlled shutter (Sutter Instruments). Animals were recorded for 5 s in dark, 2 - 15 s during light, and 5 – 600 s in dark. Body length values were calculated using a custom-made workflow in KNIME, in which the length of each animal was normalized to the averaged values measured before light (0 – 5 s). Values below 80% or above 120% were excluded, and the length profiles were averaged for each strain.

2.2.2.6. *In vitro* determination of cNMP content using *C. elegans* extract

For *C. elegans* extract preparation, 60 young adult hermaphrodites were transferred under red light (>600 nm) into a reaction tube containing 50 µl M9 buffer and 1 mM 3-IBMX. Control animals (dark condition) were placed for 30 s or 15 min on an Axio Scope.A1 microscope (Zeiss) equipped with a 4x objective, a 50 W HBO mercury lamp and transmission light filtered through a red 675 ± 50 nm bandpass filter. For light condition, animals were illuminated with blue light (0.5 mW/mm^2; 470 ± 40) for 30 s or 15 min. For cell disruption, animals were subjected to three freeze–thaw cycles using liquid nitrogen, and vortexed with 0.25- to 0.5- mm glass beads for 5 min. The sample was centrifuged at 2000 rpm for 1 min, and the supernatant was utilized for measurement of the cNMP content. For determination of the cAMP content, the AlphaScreen cAMP Detection Kit (PerkinElmer) was applied, whereas for cGMP measurement the cGMP Direct Chemiluminescent ELISA Kit (Arbor Assays) was used. Both assays were performed using the CLARIOstar PLUS (BMG Labtech) Microplate Reader.

2.2.3. Biochemical methods

2.2.3.1. Fast protein extraction from *C. elegans*

Fast protein extraction from *C. elegans* was performed for rapid validation of the gene expression of a gene of interest of transgenic strains. In this study, fast protein extraction was utilized after microinjection and genomic integration to evaluate the accurate expression of TAP-tagged BeCyclOp monomer and concatamer. For this purpose, transgenic strains were grown on 60 mm NGM plates till a high population density was reached. Animals were washed off using 2 ml ddH_2O and centrifuged at 2500 rpm for 2 min. The supernatant was removed and replaced by 1 ml ddH_2O, and the aliquot was centrifuged at 2500 rpm for 2 min again. The supernatant was removed and 30 µl ESB were added to the worm pellet, followed by boiling at 100 °C for 3 min. About 30 µl 0.25- to 0.5- mm glass beads were added, and the aliquot was vortexed for 2 min, followed by the addition of 70 µl ESB and a second boiling at 100 °C for 1 min. The sample was centrifuged at 13300 rpm for 1 min, and 20 µl of the supernatant were used for analysis using sodium dodecyl sulfate polyacrylamide gel electrophoresis (SDS-PAGE).

2.2.3.2. Detergent screen for BeCyclOp solubilization and tandem affinity precipitation of TAP-tagged BeCyclOp

To purify overexpressed BeCyclOp monomer and concatamer out of *C. elegans* muscle cells, both proteins were C-terminally fused to a TAP-tag. This affinity tag is composed out of two IgG binding domains of *Staphylococcus aureus* protein A (ProtA) and a calmodulin binding peptide (CBP) separated by a TEV cleavage site. The tandem affinity purification strategy consists of two sequential affinity purification steps. In the first affinity purification, the ProtA portion binds to the IgG constant (F_c) region, followed by the release of the TAP-tagged protein by TEV cleavage. In the second affinity purification, the CBP portion binds to Calmodulin and the protein is eluted using EGTA, a Ca^{2+} chelator (Puig *et al.*, 2001).

For purification and subsequent characterization of membrane proteins, they must be extracted from biological membranes. For this purpose, detergents are utilized, which are amphipathic molecules with a polar head and a long hydrophobic carbon chain. Above the critical micelle concentration (CMC), they form micelles in which membrane proteins are embedded and thus remain in aqueous solution, allowing their isolation and purification.

In this study, the Detergent Screening Set Classic (Biozym) was used to screen detergents after their ability to solubilize BeCyclOp::TAP out of *C. elegans* membranes. For this purpose, 1 g worm powder of a non-integrated BeCyclOp::TAP expressing strain was resuspended and homogenized using a tissue homogenizer in 3 ml buffer D (0.5 mM DTT, 0.5 mM PMSF, 1 mM EDTA, 1 µg/ml TAME, one cOmplete Protease Inhibitor Cocktail tablet, 1 % detergent). As detergents, Triton X-100, Tween-20, Decylmaltoside (DM), Dodecylmaltoside (DDM), N,N-Dimethyldodecylamine N-oxide (LDAO), Octylglucoside (OG), and Octylthioglucoside (OTG)) were applied. The aliquots were incubated for 6 h at 4 °C in a head over tail rotor and subsequently centrifuged at 13300 rpm for 30 min at 4 °C. The resulting supernatants were analysed via SDS-PAGE and western blotting.

After evaluation of BeCyclOp::TAP solubilization, the solubilizates of DDM, LDAO, OG and Triton X-100 were used for subsequent precipitation of BeCyclOp. Three aliquots were applied, comprising only the first or second affinity purification step, or the sequential execution of both tandem affinity precipitation steps. Tandem affinity purification buffers (IPP150, IPP150 Calmodulin binding buffer, IPP150 Calmodulin elution buffer, TEV cleavage buffer) were prepared containing the following detergent percentage: DDM (cmc: 0.008 %), LDAO (cmc: 0.023 %), Triton X-100 (cmc: 0.02 %) = 0.05 %; OG (cmc: 0.53 %) = 0,7 %.

For ProtA affinity precipitation, 850 µl solubilized BeCyclOp::TAP were incubated with 50 µl IgG-Agarose beads overnight at 4 °C in a head over tail rotor. The aliquot was centrifuged at 5000 rpm for 5 min at 4 °C. The beads were washed three times with 1 ml IPP150 buffer and 1 ml TEV cleavage buffer and incubated with 10 U TEV protease in 1 ml TEV cleavage buffer for 3 h at for 4 °C in a head over tail rotor. The sample was centrifuged at 5000 rpm for 5 min at 4 °C, and the beads and the eluates were analysed via SDS-PAGE and western blotting.

For CBP affinity precipitation, 850 µl solubilized BeCyclOp::TAP were incubated with 50 µl Calmodulin-Agarose beads over night at 4 °C in a head over tail rotor. The aliquot was centrifuged at 5000 rpm for 5 min at 4 °C. The beads were washed three times with 1 ml IPP150 Calmodulin binding buffer (4 mM CaCl2), and elution was performed by addition of 250 µl IPP150 Calmodulin elution buffer. The sample was centrifuged at 5000 rpm for 5 min at 4 °C, and the beads and the eluates were analysed via SDS-PAGE and western blotting.

For the sequential execution of both tandem affinity precipitation steps, after conducting the ProtA affinity precipitation, 1 ml IPP150 Calmodulin binding buffer (4 mM CaCl2) and 50 µl Calmodulin-Agarose were added to the supernatant and incubated over night at 4 °C in a head over tail rotor. The sample was centrifuged at 5000 rpm for 5 min at 4 °C, and the beads were washed three times with 1 ml IPP150 Calmodulin binding buffer (4 mM CaCl2), and elution was executed by addition of 250 µl IPP150 Calmodulin elution buffer. The sample was centrifuged at 5000 rpm for 5 min at 4 °C, and the beads and the eluates were analysed via SDS-PAGE and western blotting.

For analysis, the beads were resuspended in 150 µl SDS sample buffer (4x), and the supernatants were diluted in SDS sample buffer (4x), and 20 µl were applied for analysis via SDS-PAGE and western blotting analysis.

2.2.3.3. TEV protease cleavage analysis

TEV protease cleavage analysis was performed to validate successful cleavage of the TEV cleavage site within the TAP-tag of BeCyclOp::TAP and thus its elution from the IgG-Agarose beads.

For TEV cleavage analysis, three aliquots were applied, one without TEV protease, one with TEV protease, and one with TEV protease and subsequent loading onto a chromatography column and the collection of the TEV eluate.

1 g worm powder of a non-integrated BeCyclOp::TAP expressing strain was resuspended in 3 ml buffer D (0.5 mM DTT, 0.5 mM PMSF, 1 mM EDTA, 1 µg/ml TAME, one cOmplete Protease Inhibitor Cocktail tablet, 1 % Triton X-100) and homogenized using a tissue homogenizer, respectively. The aliquots were incubated

for 2 h at 4 °C in a head over tail rotor and centrifuged at 13300 rpm for 30 min at 4 °C. 10 µl IgG-Agarose beads were added to the supernatants and incubated for 1 h at 4 °C in a head over tail rotor. The samples were centrifuged at 2500 rpm for 5 min at 4 °C, and the beads were washed with 1 ml buffer D (0.5 mM DTT, 0.5 mM PMSF, 1 mM EDTA, 1 µg/ml TAME, one cOmplete Protease Inhibitor Cocktail tablet, 1 % Triton X-100). The beads were incubated without TEV protease, or with 25 U TEV protease in 250 µl TEV cleavage buffer for 2 h at 4 °C in a head over tail rotor. One TEV protease containing aliquot was loaded onto a chromatography column, the eluate was collected and diluted in SDS sample buffer (4x), and the beads were resuspended in 150 µl SDS sample buffer (4x).

For analysis, the supernatants of the remaining two aliquots were diluted in SDS sample buffer (4x), and 20 µl were applied for analysis via SDS-PAGE and western blotting analysis.

2.2.3.4. Tandem affinity purification of Tap-tagged BeCyclOp monomer and concatamer

Purification of TAP-tagged BeCyclOp monomer and concatamer were performed two times with slight deviations in the protocol (respective steps for the individual purification trials are indicated as follow: first purification trial = 1.P.; second purification trial = 2.P.)

For BeCyclOp monomer and concatamer purification, 50 g worm powder were slowly thawed on ice and diluted 1 : 1 with buffer D (0.5 mM DTT, 0.5 mM PMSF, 1 mM EDTA, 1 µg/ml TAME, one cOmplete Protease Inhibitor Cocktail tablet), followed by homogenization using a tissue homogenizer. For membrane preparation, the homogenate was centrifuged (1.P.: 37000 rpm for 1 h at 4 °C (70 Ti rotor), 2.P.: 4000 rpm for 15 min at 4 °C, followed by a centrifugation of the supernatant at 37000 rpm for 1 h at 4 °C (70 Ti rotor)). The supernatant was removed, and the membrane pellet was resuspended 1 : 1 in buffer D (+ 0.5 mM DTT, 0.5 mM PMSF, 1 mM EDTA, 1 µg/ml TAME, one cOmplete Protease Inhibitor Cocktail tablet, 1 % Triton X-100). For 2.P., both membrane pellets were combined. The membranes were homogenized using a tissue homogenizer and stirred for 4.5 h at 4 °C to solubilize TAP-tagged BeCyclOp monomer or concatamer. The mixture was centrifuged (1.P.: 37000 rpm

for 1 h at 4 °C (70 Ti rotor), 2.P.: 4000 rpm for 15 min at 4 °C, followed by a centrifugation of the supernatant at 37000 rpm for 1 h at 4 °C (70 Ti rotor)), and the clear interphase (10 ml extract) was either directly utilized for tandem affinity purification (1.P.), or dialyzed twice against buffer D + 0.05 % Triton X-100 overnight and for 4 h at 4 °C under stirring (2.P.). For dialysis, the Zellutrans Roth dialysis tube (Carl Roth) with a molecular weight cut off of 12 – 14 kDa was used. The extract was incubated in a head over tail rotor with 300 µl IgG-Agarose beads overnight at 4 °C. The aliquot was added to a chromatography column, and the beads were washed with 30 ml IPP150 buffer and with 10 ml TEV cleavage buffer. Next, the beads were incubated with TEV protease (Sigma; 1.P.: 100 U; 2.P.: 50 U) in TEV cleavage buffer (1.P.: 10 ml; 2.P.: 1 ml) for 5 h at 4 °C. The eluate was collected in a 15 ml falcon tube, and 3 ml calmodulin binding buffer were added. For Calmodulin and CBP binding, $CaCl_2$ (1 M stock solution in ddH_2O) was added to a final concentration of 2 mM. Calmodulin-beads (1.P.: 300 µl; 2.P.: 100 µl) were added to the solution, and the aliquot was incubated in a head over tail rotor overnight at 4 °C. The mixture was added to a chromatography column, and the beads were washed with 30 ml IPP150 calmodulin binding buffer. Elution was performed using 10 bed volumes of IPP150 calmodulin elution buffer, and the eluate was collected in about 10 single fractions. Protein concentration of the samples were determined via Bradford assay, and the samples were analysed via SDS-PAGE, followed by western blotting or silver staining.

2.2.3.5. Determination of protein expression level using *C. elegans* extract

Determination of protein expression level of proteins of interest using *C. elegans* extract was performed to compare the relative expression level of photoactivatable nucleotidyl cyclase in muscle cells of *C. elegans* indirectly via mCherry expression, as each photoactivatable nucleotidyl cyclase transgene expressed mCherry from a bicistronic mRNA. For this purpose, 20 transgenic adult hermaphrodites were transferred into a reaction tube containing 20 µl M9 buffer. For cell disruption, three freeze-thaw cycles using liquid nitrogen were executed. Next, 4 µl SDS sample buffer (4x) were added, followed by boiling at 95 °C for 10 min and an incubation on ice for

5 min. The sample was loaded on a 12 % SDS polyacrylamide gel, followed by western blot analysis.

2.2.3.6. Bradford assay for quantitative protein determination

The Bradford assay is a spectroscopic analytical technique to measure the concentration of proteins in a solution based on the absorbance shift of the dye Coomassie Brilliant Blue G-250. The dye exists in three forms, an anionic (blue), neutral (green), and cationic (red) form. Under acidic conditions, the cationic form is converted into the anionic form which binds to the protein by noncovalent (van der Waals force) and electrostatic interaction (binds primarily to basic, especially arginine, and aromatic residues). The cationic, unbound form (green/red) has an absorption maximum at 465 nm, which is shifted to 595 nm in the anionic bound form, and the increase of absorbance is proportional to the amount of bound dye, allowing the determination of the amount of protein in the sample (Compton *et al.*, 1985).

Bradford measurement was performed using the Pierce Coomassie Plus Bradford Assay Reagent (Thermo Fisher Scientific) and the Genova photometer. 5 µl sample were diluted in 995 µl Bradford solution in a disposable cuvette and incubated at RT for 5 min. Protein concentration of the sample was measured at 595 nm. For standard curve generation, BSA samples (0.125; 0.25; 0.5; 1; 2; 5; 10 [mg/ml]) were measured in triplicates, and calculated mean values were plotted against the BSA concentration, followed by linear regression analysis. Single measurements of the samples were conducted, and the protein concentration of the sample was determined using the BSA standard curve.

2.2.3.7. SDS-PAGE Sodium dodecyl sulfate polyacrylamide gel electrophoresis

SDS-PAGE is a technique to separate proteins in an electric field based on their size under denaturizing conditions. The discontinuously SDS-PAGE was described by Laemmli and allows the separation of proteins between 5 – 250 kDa (Laemmli, 1970). The SDS gel is divided into a stacking gel with a pH of 6.8 and a separating

gel with a pH 8.8. The SDS present in the sample buffer binds to and causes the denaturation of the proteins, leading to constant negatively charged SDS-protein-complexes of different sizes, which migrates to the anode in an electric field. Due to the low pH of the stacking gel, the glycine (leading ion) in the sample buffer is negatively charged and depicts the highest migration speed through the gel. Against this, the negatively charged chloride ions (follow ions) depict a slow migration speed, resulting to a focusing of the proteins in between both ions. The higher pH in the separating gel causes the deprotonation of the glycine molecules, thus converting them to following ions and the proteins can separate according to their size. The compositions of the separating gel (12 or 7.5 %) and stacking gel (5 %) are depicted in table 18.

For SDS-PAGE, samples were diluted with SDS-Sample-buffer (4x) and 20 µl were applied onto a gel. Samples obtained from detergent screen and subsequent tandem affinity precipitation of BeCyclOp and TEV protease cleavage analysis were boiled for 5 min at 95 °C.

For TAP-tagged BeCyclOp monomer and concatamer purification samples, protein concentration was measured via Bradford assay and if possible, 60 µg protein per sample were loaded onto the SDS gel. In cases of low protein concentration of the sample, 15 µl sample were loaded onto the gel. As size marker, PageRuler Prestained Protein Ladder or PageRuler Prestained Plus Protein Ladder (Thermo Fisher Scientific) were utilized (6 µl). Electrophoresis was conducted at 90 V until the sample entered the separating gel, and at 120 V for about 120 min. Two gels were performed, one for western blot analysis and one for silver staining.

Table 18: SDS gel preparation, consisting of a 5 % stacking gel, and a 12 or 7.5 % separating gel.

Solution/reagent	**Separating gel (12 %) [µl]**	**Separating gel (7.5 %) [µl]**	**Stacking gel (5 %) [µl]**
ddH_20	5250	7500	5800
Rotiphorese Gel 30	6000	3750	1660
Laemmli B	3750	3750	-
Laemmli C	-	-	2500
APS (10 %)	150	150	80

Solution/reagent	Separating gel (12 %) [µl]	Separating gel (7.5 %) [µl]	Stacking gel (5 %) [µl]
TEMED	8	8	6

2.2.3.8. Western blotting and immunological detection

Western blotting is an immunological technique for the detection of proteins of interest after their electrophoretic separation. Here, proteins are transferred after their electrophoretic separation via SDS-PAGE from the gel onto a positively charged membrane (e.g. nitrocellulose or PVDF), a process which is termed `Blotting`. This protein transfer is performed by a vertical connected electric field, whereby the proteins migrate towards the anode. Due to ionic and polar interactions, proteins adhere to the membrane, and the proteins of interest could be immunologically detected via antibody binding (Towbin *et al.*, 1979).

In this study, the Semi-Dry Blotter `Pegasus` (Phase) was utilized. For western blotting, two pieces of filter paper were soaked in transfer buffer (1x). As membrane, a PVDF (Carl Roth; drenched in MeOH)) or Roti-NC transfer membrane (Carl Roth; moistened in transfer buffer (1x)) were used. The Western blotting composition is depicted in table 19.

Table 19: Western blotting composition.

Anode
Filter paper
PVDF/Roti-NC membrane
SDS gel
Filter paper
Cathode

Western blotting was performed at 25 V for 10 min.

For immunological detection, different primary and secondary antibodies were used, depending on the protein of interest. The target proteins, the used primary and secondary antibodies and their working concentrations are summarized in table 20.

Table 20: Target proteins and applied primary and secondary antibodies for their immunological detection.

Target protein	Primary antibody	Working concentration	Secondary antibody	Working concentration
α-tubulin	anti-α-tubulin (Piperno and Fuller Cat# 4A1, RRID:AB_2732839)	1:50	anti-mouse-HRP (Thermo Fisher Scientific)	1:100
BeCyclOp::Strep	Anti-Strep Tag II (Antibodies-online)	1:40	anti-rabbit-HRP (Carl Roth)	1:1000
BeCyclOp::TAP/Concatamer::TAP	anti-TAP (Thermo Fisher Scientific)	1:1000	anti-rabbit-HRP (Carl Roth)	1:1000
BeCyclOp::TAP/Concatamer::TAP	anti-TAP (Thermo Fisher Scientific)	1:1000	anti-rabbit-HRP (Bethyl Laboratories)	1:50000
BeCyclOp::TAP	PAP (Sigma Aldrich)	1:1000	-	-
mCherry	anti-mCherry (OriGene)	1:10000	anti-rabbit-HRP (Carl Roth)	1:3000

After blotting, the membrane was blocked for 1 h at RT in blocking buffer. Next, the blot was incubated with the respective primary antibody in blocking buffer for 1 h at RT or overnight at 4 °C. After three washing steps with TBS-T, the blot was incubated with the respective secondary antibody in blocking buffer for 1 h at RT or overnight at 4 °C. The blot was washed three times with TBS-T, and detection was performed using the GE Healthcare Amersham™ ECL Prime Western-Blot-Detection Reagent (Cytivia) according to the manual and via ChemoCam (Intas). Imaging was

done with a sequential integration of 20 pictures and an exposure time of 10 s for each picture.

Western blot analysis was performed using the Gel Analyzer plugin in ImageJ. For determination of the relative expression level of photoactivatable nucleotidyl cyclase in muscle cells, the percent values of each line were normalized to the percent value of BeCyclOp(A-2x) strain (ZX2613), exhibiting the lowest α-tubulin content, and the mCherry/α-tubulin ratio was calculated.

2.2.3.9. Silver staining

Silver staining is a technique to detect proteins after their electrophoretic separation on SDS polyacrylamide gels, enabling the detection of proteins in the low nanogram range. The method is composed out of the fixation of proteins, followed by sensitization, silver impregnation and the image development (Merril *et al.*, 1981). Silver ions interact and bind with certain functional groups within the proteins (e.g. Asp, Glu, His, Cys, Lys), and under appropriate conditions it is reduced to metallic silver to visualize the proteins within the gel. The used solutions and their composition for silver staining of one polyacrylamide gel is visible in table 21.

Table 21: Solutions and their composition for silver staining of one polyacrylamide gel.

Solution	Compound	Volume or mass for 1 polyacrylamide gel
Acetone stock	Acetone	60 ml
	ddH_2O	60 ml
TCA stock	TCA [6.1 N]	750 µl
	ddH_2O	750 µl
$AgNO_3$ stock	$AgNO_3$	200 mg
	ddH_2O	1 ml
Sodium thiosulfate stock	$Na_2S_2O_3$ $5H_2O$	200 mg
	ddH_2O	1 ml
Fixation	Acetone stock	60 ml
	TCA stock	1.5 ml
	37 % formaldehyde	25 µl

Solution	Compound	Volume or mass for 1 polyacrylamide gel
Pretreat 1	Acetone stock	60 ml
Pretreat 2	$Na_2S_2O_3$ $5H_2O$ stock	100 µl
	ddH_2O	60 ml
Impregnate	$AgNO_3$ stock	800 µl
	37% formaldehyde	600 µl
	ddH_2O	60 ml
Develop	Na_2CO_3	1.2 g
	37% formaldehyde	25 µl
	$Na_2S_2O_3$ $5H_2O$ stock	25 µl
	ddH_2O	60 ml
Stop	Acetic acid (99%)	600 µl
	ddH_2O	59.4 ml

The silver staining protocol used in this study is depicted in table 22.

Table 22: Silver staining protocol.

Step	Solution	Time
Fixation	Fixation	5 min
Rinse	ddH_2O	3x5s
Wash	ddH_2O	5 min
Rinse	ddH_2O	3x5s
Pretreat	Pretreat 1	5 min
Pretreat	Pretreat 2	1 min
Rinse	ddH_2O	3x5s
Impregnate	Impregnate	8 min
Rinse	ddH_2O	3x5s
Develop	Develop	(10-20s)
Stop	Stop	30s
Rinse	ddH_2O	10s

2.2.4. Data and statistical analysis

In *C. elegans* behavioural analysis, data were obtained and summarized from at least three independent measurements, involving animals from different stages (L4 – adult) of the same genotype, which were grown and measured on different days. The number of measured animals is indicated as n. Data are shown as mean ± SEM or mean, median, interquartile range (IQR), whiskers (1.5 * IQR) and outliers. Statistical analyses were executed using the programs GraphPad Prism 8 or Microsoft Excel 2019. Student`s t test, one-way or two-way ANOVA and subsequent Bonferroni correction as post hoc test were executed. Significant differences are depicted in * $p<0.05$, ** $p<0.01$ and ***$p<0.001$.

3. RESULTS

3.1. Generation and implementation of optogenetic tools for cNMP generation, functionally coupled to CNGCs for activation and silencing of excitable cells in *C. elegans*

The optogenetic toolbox in *C. elegans* for cNMP generation and hyperpolarization is restricted to soluble adenylyl cyclases, the membrane-bound BeCyclOp, the engineered soluble bPGC, and hyperpolarizing rhodopsins. Missing are membrane-bound photoactivatable adenylyl cyclases and hyperpolarizers based on the manipulation of K^+-currents. In this study, novel membrane-bound photoactivatable adenylyl cyclases were engineered and characterized by behavioural experiments, *in vitro* cNMP measurements and *in vivo* expression levels. Furthermore, the *Catenaria anguillulae* CyclOp was assessed with respect to its applicability in *C. elegans*. Besides to this, photoactivatable nucleotidyl cyclase were functionally coupled to CNGCs for cell de- or hyperpolarization, and evaluated by swimming and body length analysis.

3.1.1. Optogenetic tools for cGMP generation coupled to the TAX-2/-4 CNGC for cell activation

Characterization of new optogenetic tools for cGMP generation required their co-expression with the TAX-2/-4 CNGC (EC_{50}^{cGMP} = 8.4 µM; EC_{50}^{cAMP} = 300 µM, in HEK293 cells (Komatsu *et al.*, 1999)) in body wall muscle cells of *C. elegans*. Expression of CaCyclOp in muscle cells was achieved by subcloning the coding sequence into a vector containing the *myo-3* promoter. Since a C-terminal fusion of BeCyclOp with YFP increased its guanylyl cyclase activity in the dark (measured in membrane preparations from *Xenopus* oocytes (Gao *et al.*, 2015)), CaCyclOp and the mCherry fluorescence reporter were expressed from bicistronic mRNAs, including the trans-splicing sequence SL2. To compare light triggered cGMP production between CaCyclOp and the implemented BeCyclOp and bPGC, equal amounts of plasmid DNA were injected into the strain ZX1741 (*pmyo-3::tax-2::GFP, pmyo-3::tax-4::GFP, pmyo-2::mCherry*) to ensure similar expression levels of TAX-2/-4 between

the strains. To analyse light evoked cGMP generation by the photoactivatable guanylyl cyclases, body length measurements with blue light stimulation were performed. Since the nematode expresses the ultraviolet/blue-light sensor LITE-1, whose activation via short-wavelength light triggers a phototactic escape response in the animal, the strains used for optogenetic experiments contain the loss-of-function mutation *lite-1(ce314)* as background. Thus, triggering of the LITE-1 induced behaviour response during the experiments should be prevented (Edwards *et al.*, 2008). Illumination of animals, co-expressing TAX-2/-4 and CaCyclOp, caused light dependent muscle contractions of about 3.5 % within ~ 3.1 s (τ ~ 0.88 ± 0.02 s), whereas for animals expressing TAX-2/-4 and BeCyclOp, the strongest effects, i.e. a decrease in body length of about 9 % within ~ 1.3 s (τ ~ 0.23 ± 0.01 s), was observed. For the soluble bPGC, light application reduced the body length of about 2.5 % within ~ 5 s (τ ~ 1.78 ± 0.05 s). To verify that the light evoked effects were not caused by unspecific light responses independent by photoactivatable guanylyl cyclases, animals only expressing TAX-2 and TAX-4 (raised with ATR) or co-expressing TAX-2/-4 and BeCyclOp or CaCyclOp raised without ATR (rendering the CyclOps nonfunctional) were performed. Using the same light conditions, no changes in the body lengths were detected (Figure 20 A, B). Thus, the body length measurements indicate that BeCyclOp might has the highest light-inducible cGMP production and the fastest cGMP generation rate, whereas CaCyclOp and bPGC might produce comparable amounts of cGMP at slightly different turnover rates. However, the differences in the behavioural changes could be due to differences in the expression levels of the enzymes.

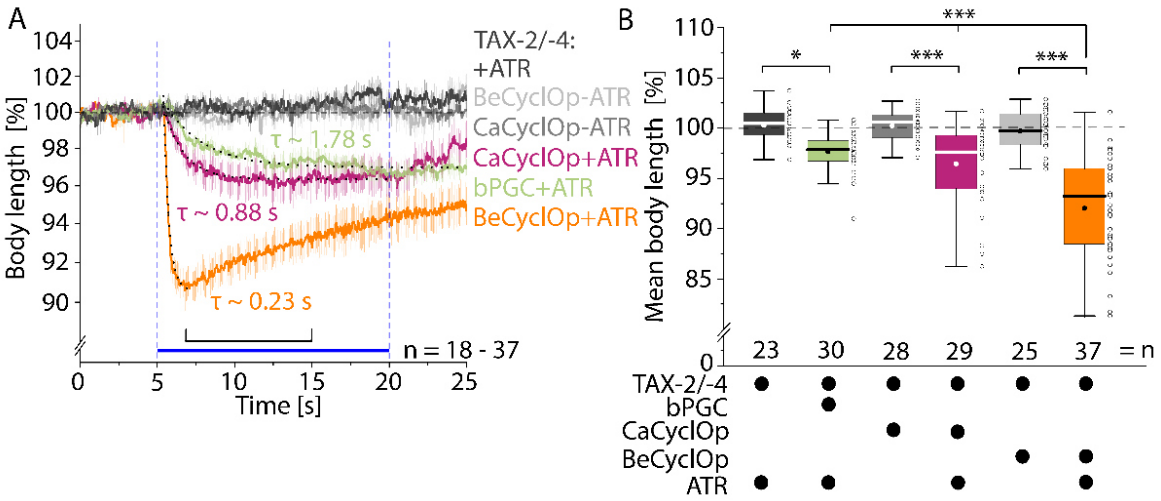

Figure 20: Photoactivatable guanylyl cyclases vary in cGMP production rate and magnitude, enabling different amplitudes and ON-kinetics for cell depolarization by coupling to TAX-2/-4 in body wall muscle cells. *A) Body length analysis ±SEM of animals, co-expressing either BeCyclOp, CaCyclOp, or bPGC and the TAX-2/-4 channel, or only expressing TAX-2/-4 in body wall muscle cells. Blue bar indicates the period of illumination (0.9 mW/mm²; 470 nm). Animals were raised with (+) or without (-) ATR. Mono-exponential decay fit (dotted lines) was used to determine onset-time constants (τ). B) Mean normalized body lengths for the indicated time period (6.5 – 15 s). The interquartile range (IQR), median (–), mean values (●), individual measurements (o), and whiskers (1.5 * IQR) are depicted. n = number of animals. Statistically significant differences were calculated using one-way ANOVA with Bonferroni correction (*p ≤ 0.05 and ***p ≤ 0.001). Image adapted from (Henss et al., 2021).*

To more rigorously analyse light triggered cGMP generation by the photoactivatable guanylyl cyclases, body length measurements at different light levels were performed, depicting light saturating conditions for each enzyme at 0.2 mW/mm^{2,}, which is comparable to applied intensities for ChR2 activation (Figure 21) (AzimiHashemi *et al.*, 2014; Nagel *et al.*, 2005). Nevertheless, 0.2 mW/mm^2 was used as the minimum light intensity for the light saturation experiments, so light saturation for the enzymes is likely to be achieved at lower light conditions.

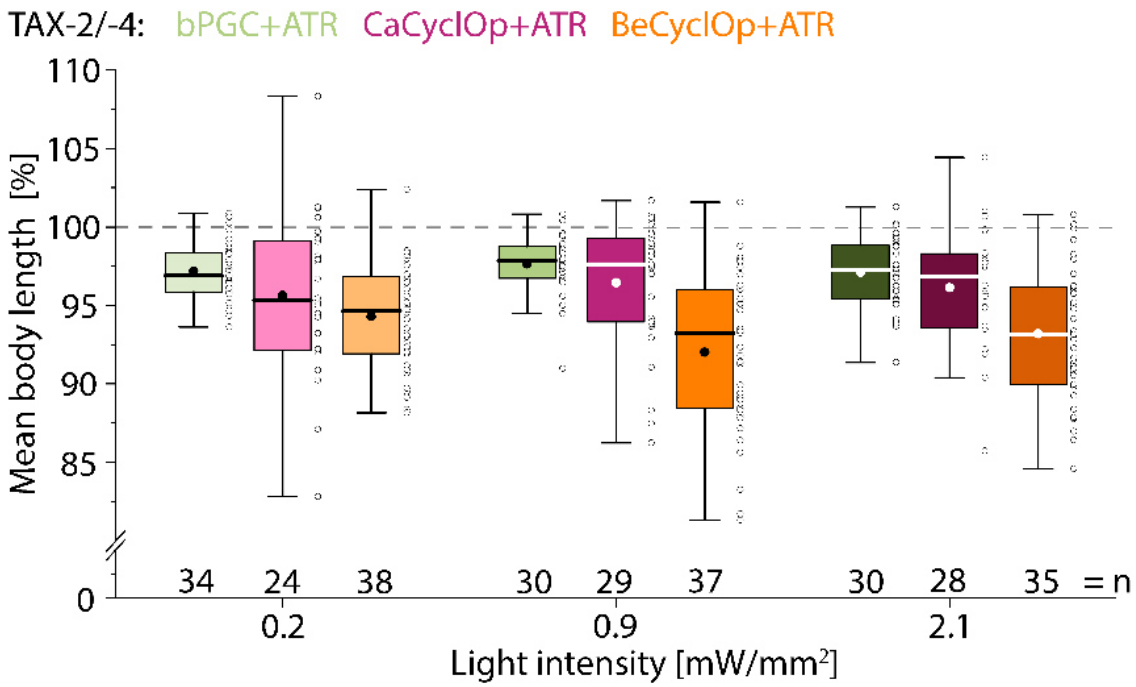

Figure 21: Photoactivatable guanylyl cyclases are saturated at light conditions of ≥ 0.2 mW/mm² in body wall muscle cells. *Quantification of the mean normalized body lengths ±SEM of animals, co-expressing TAX-2/-4 and either BeCyclOp, CaCyclOp, or bPGC in body wall muscle cells, during light stimulation at different light intensities (0.2, 0.9, 2.1 mW/mm²; 470 nm). The interquartile range (IQR), median (–), mean values (●), individual measurements (o), and whiskers (1.5 * IQR) are shown. N = number of animals. Image adapted from (Henss et al., 2021).*

To compare the *in vivo* photoactivatable guanylyl cyclase expression levels, western blot analysis was conducted, in which the protein amount was indirectly determined via mCherry, as each transgene expressed mCherry from a bicistronic mRNA. The highest expression level was detected for BeCyclOp, and the lowest for bPGC (Figure 22). However, the reason for this could be the usage of a codon-optimized BeCyclOp cDNA for expression in *C. elegans*. In summary, BeCyclOp could have the highest light-inducible cGMP production and the fastest cGMP generation rate and thus could be the most potent guanylyl cyclase. Its orthologue CaCyclOp may be characterized by a lower light-inducible cGMP generation and a lower cGMP production rate, and thus could provide a useful membrane-bound alternative to the soluble bPGC to allow fine-control of cGMP levels.

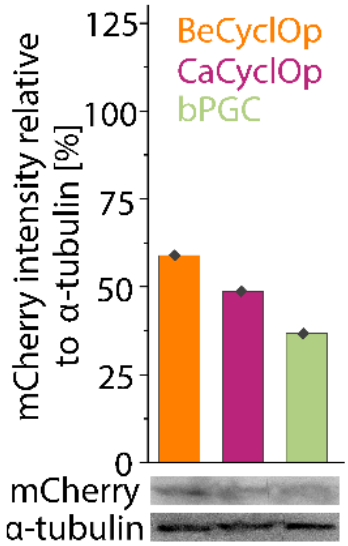

Figure 22: BeCyclOp shows the highest, and bPGC the lowest mRNA levels in body wall muscle cells. *Western blot quantification of C. elegans extracts from animals expressing BeCyclOp, CaCyclOp, or bPGC and mCherry from bicistronic mRNAs (comprising the SL2 trans-splicing sequence). Depicted is the mCherry intensity relative to the α-tubulin signal, normalized to the intensity of the strain ZX2613 (BeCyclOp(A-2x); figure 38 D). N = 1 replicate of n = 20 animals each. Image adapted from (Henss et al., 2021).*

3.1.2. Generation and implementation of membrane-bound photoactivatable adenylyl cyclases in cholinergic motor neurons of *C. elegans*

To generate membrane-bound photoactivatable adenylyl cyclases, the guanylyl cyclase domains of BeCyclOp and CaCyclOp were mutated by site-directed mutagenesis of two to three key amino acids in the active site (Ryu *et al.*, 2010; Scheib *et al.*, 2018). In guanylyl cyclases, these key residues are occupied by glutamate E497 and cysteine C566, which interact with the nitrogen N1 and the carbonyl group C6 of guanine (Linder, 2005). In contrast, in adenylyl cyclases these positions are occupied by lysine K497 and aspartate or threonine D/T566, which interact with the nitrogen N1 and the amino group N6 of adenine (Steegborn, 2014). Moreover, Ryu et al., 2010 found that an aspartate or glutamate residue at position D/E265 can also be required for cAMP selectivity, whereas in eukaryotic guanylyl cyclases this residue is occupied by an arginine. Thus, the guanylyl cyclases were mutated to adenylyl cyclases either by introducing the mutations E497K and C566D (abbreviated as (A-2x)) or by the mutations E497K, H564D, and C566T (abbreviated as (A-3x)). To characterize the novel engineered membrane-bound photoactivatable adenylyl cyclases with respect to their optogenetic cAMP generation, they were

expressed in cholinergic neurons of *C. elegans*, which was achieved by subcloning of the coding sequences into a vector containing the *unc-17* promoter.

3.1.2.1. Swimming behaviour modulation by membrane-bound photoactivatable adenylyl cyclase stimulation

To analyse the functionality of the engineered membrane-bound photoactivatable adenylyl cyclases in *C. elegans* and to evaluate the extent of optogenetic cAMP production, swimming behaviour analyses were performed. Swimming behaviour of *C. elegans* is increased by optogenetic cAMP generation in cholinergic neurons via bPAC (Steuer Costa *et al.*, 2017). Thus, this bPAC evoked change in behaviour was used as positive control and to investigate the effectiveness of the novel membrane-bound photoactivatable adenylyl cyclases. Illumination of animals expressing bPAC or BeCyclOp(A-2x) increased the swimming frequency by about 31 % within 15 s, however, the effect induced by bPAC returned to base line faster (15 s) than the BeCyclOp(A-2x) triggered effect (30 s). For CaCyclOp(A-2x) and BeCyclOp(A-3x) expressing animals, no light dependent change in their behaviour was observed. The reason for this could be a low expression level of the enzymes or the generation of little or no cAMP, which cannot be detected by this behavioural experiment. To verify that the light evoked behavioural changes were caused by membrane-bound photoactivatable adenylyl cyclase activation, the influence of the light pulse on the swimming behaviours of the genetic background *lite-1(ce314)* and of animals expressing the engineered membrane-bound photoactivatable adenylyl cyclases raised without ATR was investigated. Here, no light triggered change in their swimming frequency was detected, confirming that the chromophore retinal is required for membrane-bound photoactivatable adenylyl cyclase functionality. However, the control strain expressing BeCyclOp(A-2x) supplemented without ATR depicted a reduced swimming frequency after 15 s light exposure (12 %), which increased back to baseline during subsequent 15 s light application. Because the enzyme is non-functional without ATR supplementation the significant reduction (*p = 0.046) after 15 s could be due to outliers. As control for cGMP production in cholinergic neurons, animals expressing wild type BeCyclOp were analysed, depicting no light evoked influence on their swimming frequency, indicating no apparent influence of cGMP on cAMP dependent neurotransmission in *C. elegans*

cholinergic neurons (Figure 23 A, B). Thus, the swimming behaviour analysis indicates that BeCyclOp(A-2x) is a functional photoactivatable adenylyl cyclase and that it may generate high levels of light-inducible cAMP.

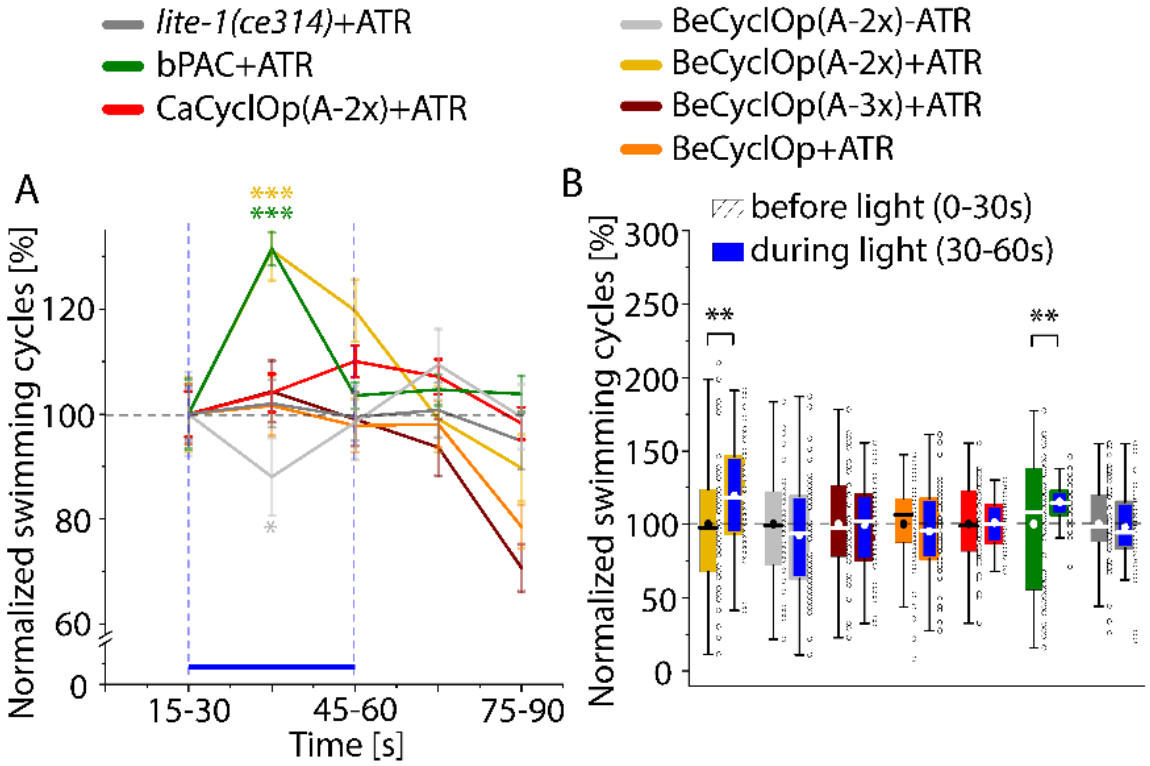

Figure 23: BeCyclOp(A-2x) and bPAC evoke comparably increased swimming cycles, however the effect induced by bPAC decayed faster in cholinergic neurons. *A) Swimming frequencies ±SEM of animals, expressing bPAC, BeCyclOp(A-2x), BeCyclOp(A-3x), wild type BeCyclOp, or CaCyclOp(A-2x) in cholinergic motor neurons of C. elegans, and the genetic background lite-1(ce314). Blue bar indicates the period of illumination (0.2 mW/mm²; 470 nm). Swimming frequencies are normalized to the mean swimming cycles 15 s before illumination (n = 40 – 50). B) Quantification of the mean swimming cycles 30 s before and 30 s during light of the animals in A. Swimming cycles are normalized to the mean swimming frequency 30 s before light application. The interquartile range (IQR), median (–), mean values (●), individual measurements (o), and whiskers (1.5 * IQR) are depicted. n = 40 – 50 animals. Statistically significant differences: one-way ANOVA and Student's t test (*p ≤ 0.05, **p ≤ 0.01 and ***p ≤ 0.001). Image adapted from (Henss et al., 2021).*

In order to possibly improve the expression and/or membrane targeting of the membrane-bound photoactivatable adenylyl cyclases, BeCyclOp(A-2x) and CaCyclOp(A-2x) were N-terminally fused with YFP (Scheib *et al.*, 2018). Stimulation of YFP-BeCyclOp(A-2x) expressing animals increased swimming frequency by about 22 % within 30 s, whereas for YFP-CaCyclOp(A-2x) an increase of about 33 % within 30 s was detected (Figure 24). Accordingly, N-terminal fusion of YFP to CaCyclOp(A-2x) could increase the expression and/or membrane targeting and/or stabilize the

conformation of the enzyme, as observed in *Xenopus* oocytes and hippocampal neurons (Scheib *et al.*, 2018).

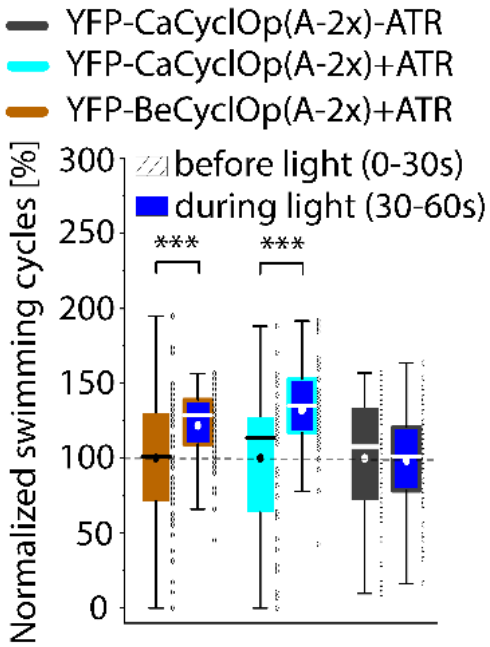

Figure 24: YFP-CaCyclOp(A-2x) triggers the highest increase in swimming frequency during 30 s light application in cholinergic neurons. *Mean swimming rate of animals, expressing YFP-BeCyclOp(A-2x) or YFP-CaCyclOp in cholinergic neurons, 30 s before and 30 s during illumination (0.2 mW/mm^2; 470 nm). Animals were supplemented with (+) or without (-) ATR. Swimming frequencies are normalized to the mean swimming frequency 30 s before light application. The interquartile range (IQR), median (–), mean values (●), individual measurements (o), and whiskers (1.5 * IQR) are depicted. n = 39 – 52 animals. Statistically significant differences were determined using one-way ANOVA and Student's t test (**p ≤ 0.001). Image adapted from (Henss et al., 2021).*

To investigate light dependent cAMP generation by the photoactivatable adenylyl cyclases in more detail, swimming behaviour analyses at different light levels were executed. For bPAC, light evoked effects exhibited a maximum at 0.2 mW/mm^2 (31 %), which dropped at 0.4 mW/mm^2 (9 %) (Figure 25 A, B), while for YFP-BeCyclOp(A-2x), they saturated already at 0.1 mW/mm^2 (Figure 26 A, B). The reason for the decreased frequency at 0.4 mW/mm^2 observed for bPAC expressing animals may be an increased amount of cAMP produced, which amplifies the increase in bending angles and thus causes a decrease in swimming frequency.

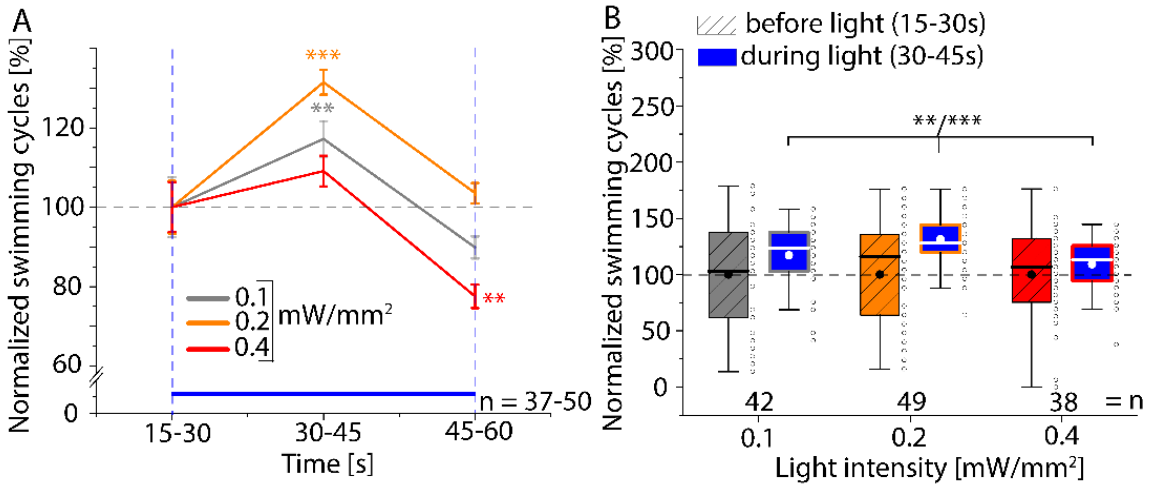

Figure 25: bPAC enhanced swimming rate maximizes at 0.2 mW/mm², and drops at 0.4 mW/mm² in cholinergic neurons. *A) Swimming cycles ±SEM of animals, expressing bPAC in cholinergic neurons during 30 s light exposure (470 nm) at light intensities of 0.1, 0.2 and 0.4 mW/mm². Swimming rates are normalized to the mean swimming frequency 15 s before light stimulation. B) Quantification of the mean swimming cycles 15 s before and 15 s during illumination of the animals in A. The interquartile range (IQR), median (–), mean values (●), individual measurements (o), and whiskers (1.5 * IQR) are illustrated. Blue bar indicates the period of light exposure. n = number of animals. Statistically significant differences: one-way ANOVA and Student's t test (**p ≤ 0.01 and ***p ≤ 0.001). Image adapted from (Henss et al., 2021).*

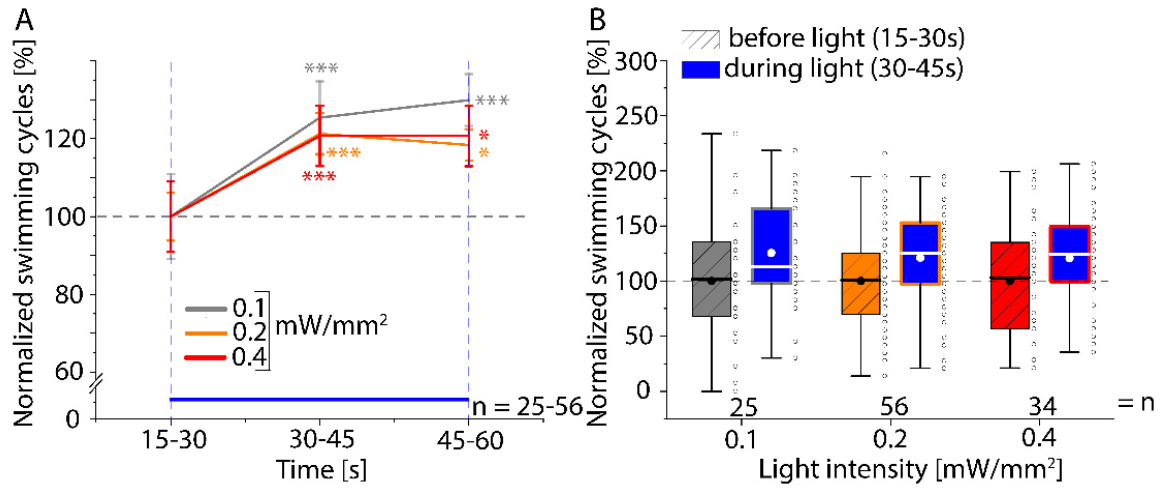

Figure 26: YFP-BeCyclOp(A-2x) increased swimming behaviour saturates at light conditions of 0.1 mW/mm² in cholinergic neurons. *A) Swimming rates ±SEM of animals, expressing YFP-BeCyclOp(A-2x) in cholinergic neurons during 30 s light exposure (470 nm) at light intensities of 0.1, 0.2 and 0.4 mW/mm². Swimming cycles are normalized to the mean swimming frequency 15 s before light stimulation. B) Quantification of the mean swimming rates 15 s before and 15 s during illumination of the animals in A. The interquartile range (IQR), median (–), mean values (●), individual measurements (o), and whiskers (1.5 * IQR) are shown. Blue bar indicates the period of light exposure. n = number of animals. Statistically significant differences were calculated using one-way ANOVA and Student's t test (*p ≤ 0.05 and ***p ≤ 0.001). Image adapted from (Henss et al., 2021).*

To gain insights into possible impacts on neuronal physiology due to protein expression and/or dark nucleotidyl cyclase activity, basal swimming rates of

membrane-bound photoactivatable adenylyl cyclases, wild type BeCyclOp and bPAC expressing animals were calculated and compared to the genetic background *lite-1(ce314)*. Apart from CaCyclOp(A-2x), all analysed photoactivatable nucleotidyl cyclases caused a reduction of the swimming frequency which could be due to a common “toxicity” of the enzymes or basal cNMP formation (Figure 27 A, B). The result may also indicate weak expression of CaCyclOp(A-2x) in *C. elegans* cholinergic neurons. In sum, YFP-BeCyclOp(A-2x), YFP-CaCyclOp(A-2x), and BeCyclOp(A-2x) enhanced swimming behaviour as efficiently as bPAC which could indicate that the engineered enzymes generate high levels of cAMP with high efficiency.

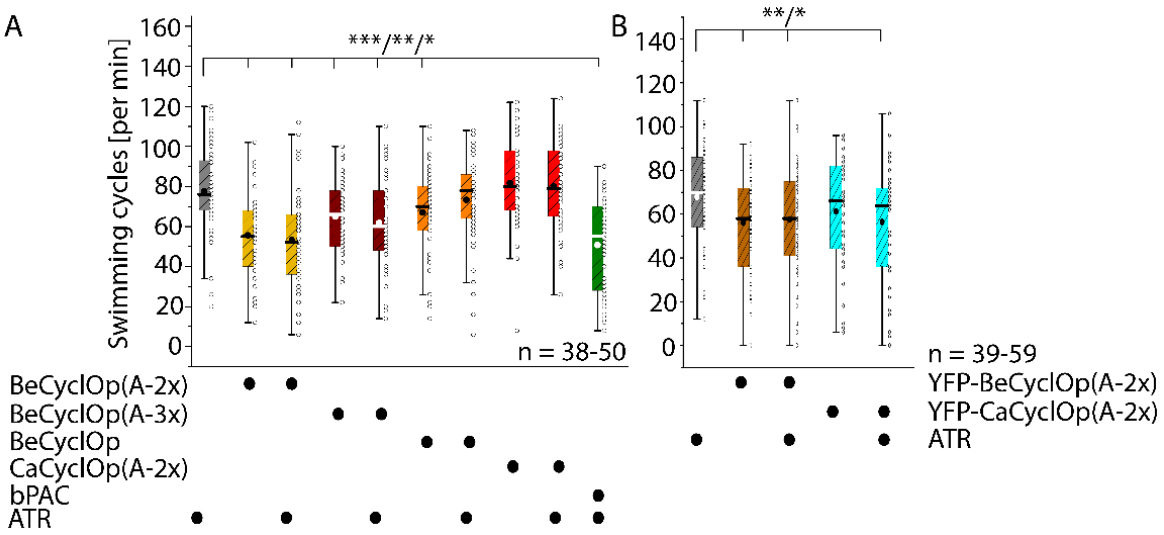

Figure 27: Photoactivatable nucleotidyl cyclases expression in cholinergic neurons reduces basal swimming rate (except CaCyclOp(A-2x)). *Basal swimming rates of animals, expressing A) BeCyclOp(A-2x), BeCyclOp(A-3x), wild type BeCyclOp, CaCyclOp(A-2x), bPAC and B) YFP-BeCyclOp(A-2x) or YFP-CaCyclOp(A-2x) in cholinergic neurons, and the genetic background lite-1(ce314). Animals were raised with (+) or without (-) ATR. The interquartile range (IQR), median (–), mean values (●), individual measurements (o), and whiskers (1.5 * IQR) are depicted. n = number of animals. Statistically significant differences: one-way ANOVA and Student's t test (*p ≤ 0.05, **p ≤ 0.01 and ***p ≤ 0.001). Image adapted from (Henss et al., 2021).*

3.1.2.2. Crawling behaviour modulation by membrane-bound photoactivatable adenylyl cyclase activation on solid substrate

3.1.2.2.1. Membrane-bound photoactivatable adenylyl cyclase illumination increases crawling speed

Since membrane-bound photoactivatable adenylyl cyclase photoactivation increased *C. elegans* swimming behaviour, they were characterized in more detail by analysis of their behaviour modulation on solid substrate, .i.e. crawling speed, body posture and body length. In this context, optogenetic cAMP production by bPAC increased the crawling speed and body posture, and decreased the body length (Steuer Costa *et al.*, 2017). Thus, the experiment should provide further insight into the enzymatic properties and kinetics of the engineered enzymes, as well as the influence of cAMP produced in the cytosol or in close proximity to the plasma membrane on cAMP-dependent neurotransmission. Stimulation of bPAC and BeCyclOp(A-2x) expressing animals showed comparable enhanced crawling speeds of about 40 % within ~12 s (BeCyclOp(A-2x) appeared even more efficient), whereas the bPAC induced behavioural change decayed faster compared to BeCyclOp(A-2x). The faster decaying responses observed in bPAC-evoked effects (swimming and crawling) may indicate that PDEs do not reach and degrade cAMP produced near the membrane as rapidly as in the cytosol. As controls, the effect of light application on the crawling speeds of animals, expressing BeCyclOp(A-2x) raised without ATR, and the genetic background *lite-1(ce314)* were examined, depicting no change in their behaviour (Figure 28 A, B). In regard of YFP-CyclOp(A-2x)s, illumination increased the crawling speeds of about 35 % within ~12 s (Figure 29 A, B). Thus, photoactivation of BeCyclOp(A-2x), YFP-CaCyclOp(A-2x), and BeCyclOp(A-2x) caused similar enhanced or even more potent crawling speed changes as bPAC, which could indicate that the engineered membrane-bound photoactivatable adenylyl cyclases produce cAMP at high levels with high efficiency.

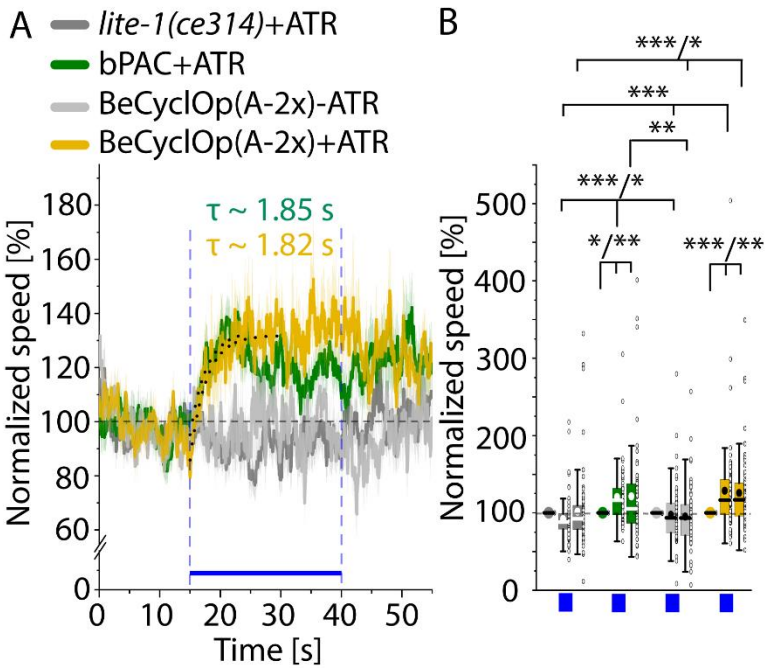

Figure 28: BeCyclOp(A-2x) and bPAC evoke comparably enhanced crawling speeds, however the effect induced by bPAC decayed faster in cholinergic neurons. *A) Crawling speeds ±SEM of animals, expressing bPAC or BeCyclOp(A-2x) in cholinergic neurons, and the genetic background lite-1(ce314). Blue bar indicates the period of light exposure (0.2 mW/mm²; 470 nm). Onset-time constants (τ) were calculated using a mono-exponential growth fit (dotted lines). n = 47 – 72 animals. B) Quantification of the mean normalized speed of the time periods before (0 – 15 s), during (15 – 40 s, blue bar), and after (40 – 55 s) light application. n = 66 – 72 animals. The interquartile range (IQR), median (–), mean values (●), individual measurements (o), and whiskers (1.5 * IQR) are depicted. Statistically significant differences were determined using one-way ANOVA with Bonferroni correction (*p ≤ 0.05, **p ≤ 0.01 and ***p ≤ 0.001). Image adapted from (Henss et al., 2021).*

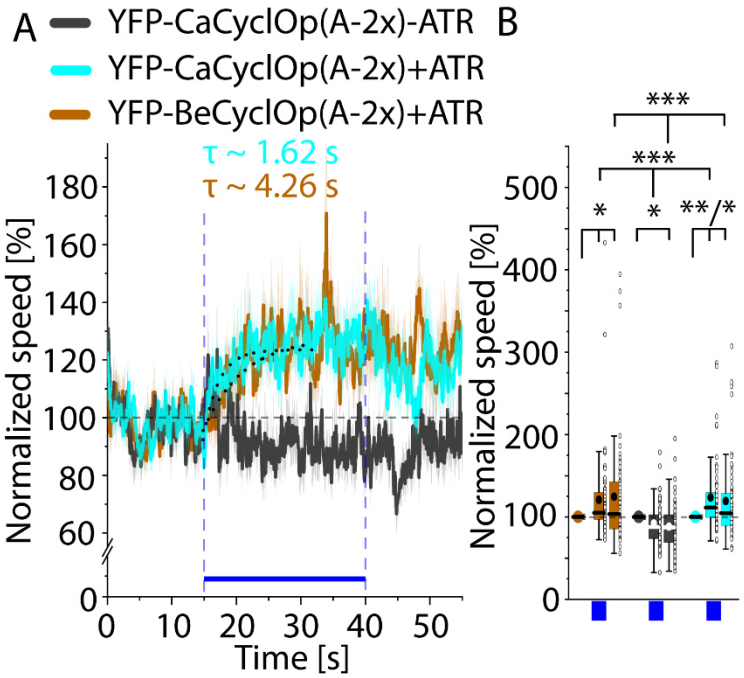

Figure 29: YFP-CyclOp(A-2x)s raise crawling speeds nearly comparably strong as bPAC and BeCyclOp(A-2x) in cholinergic neurons. *A) Crawling speeds ±SEM of animals, expressing YFP-BeCyclOp(A-2x) or YFP-CaCyclOp(A-2x) in cholinergic neurons. Blue bar indicates the period of light exposure (0.2 mW/mm²; 470 nm). Mono-exponential growth fit (dotted lines) was used to calculate onset-time constants (τ). n = 47 – 64 animals. B) Quantification of the mean normalized speed of the time periods before (0 – 15 s), during (15 – 40 s, blue bar), and after (40 – 55 s) light exposure. n = 58 – 61 animals. The interquartile range (IQR), median (–), mean values (●), individual measurements (o), and whiskers (1.5 * IQR) are shown. Statistically significant differences: one-way ANOVA with Bonferroni correction (*p ≤ 0.05, **p ≤ 0.01 and ***p ≤ 0.001). Image adapted from (Henss et al., 2021).*

To get more insights into possible negative impacts on neuronal physiology due to protein expression and/or dark nucleotidyl cyclase activity, the basal crawling speeds of membrane-bound photoactivatable adenylyl cyclases, wild type BeCyclOp and bPAC animals were examined and compared to the genetic background *lite-1(ce314)*. Here, only BeCyclOp(A-2x) expressing animals decreased the basal crawling speed, independent of ATR addition (Figure 30 A, B). The reason for this may be constitutive cAMP production by the adenylyl cyclase domain, which is independent of light regulation by the rhodopsin moiety.

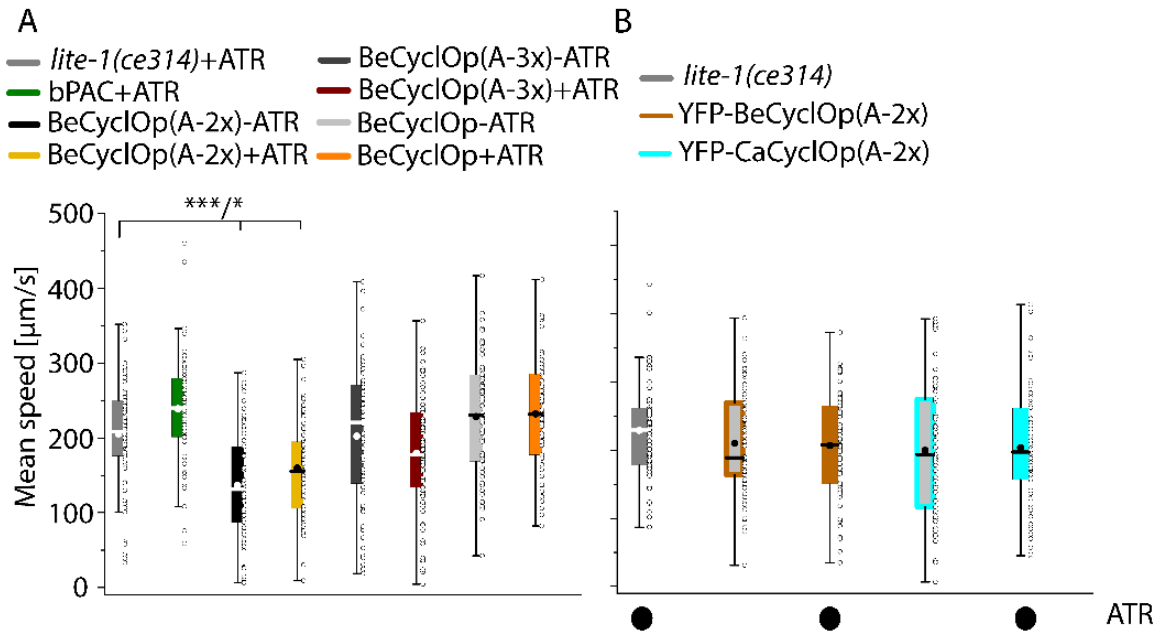

Figure 30: Only BeCyclOp(A-2x) expression in cholinergic neurons reduces basal crawling speed, independent of ATR addition. *Basal crawling speeds of animals, expressing A) BeCyclOp(A-2x), BeCyclOp(A-3x), wild type BeCyclOp, bPAC and B) YFP-BeCyclOp(A-2x) or YFP-CaCyclOp(A-2x) in cholinergic neurons, and the genetic background lite-1(ce314). Animals were raised with (+) or without (-) ATR. The interquartile range (IQR), median (–), mean values (●), individual measurements (o), and whiskers (1.5 * IQR) are depicted. n = 55 - 73 animals. Statistically significant differences: one-way ANOVA with Bonferroni correction (*p ≤ 0.05 and ***p ≤ 0.001). Image adapted from (Henss et al., 2021).*

3.1.2.2.2. Membrane-bound photoactivatable adenylyl cyclase stimulation elicits no obvious changes on body posture

To further analyse the influence of cAMP, produced by membrane-bound photoactivatable adenylyl cyclases, on locomotion behaviour on solid substrate, the impact of these tools on body posture was examined. The body bending on solid substrate is enhanced by bPAC activation in cholinergic neurons, providing an additional behavioural readout to compare cAMP-dependent neurotransmission in cholinergic neurons induced by soluble bPAC and the engineered membrane-bound enzymes. Here, stimulation of bPAC expressing animals increased the mean body bending of about 15 % within 17 s. In contrast to this, illumination of BeCyclOp(A-2x) expressing animals depicted no change in their body bending, and behaved as control animals raised without ATR, or the genetic background *lite-1(ce314)* (Figure 31 A, B).

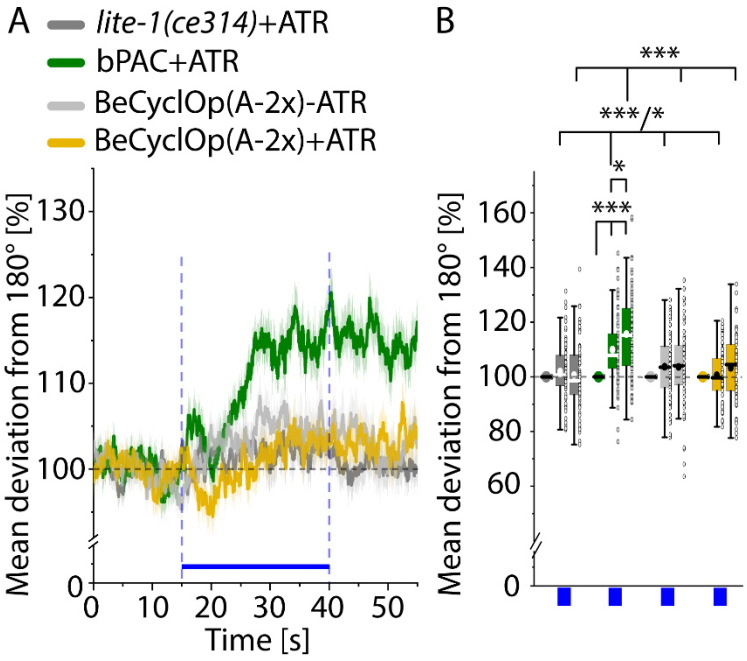

Figure 31: In contrast to bPAC, BeCyclOp(A-2x) photoactivation in cholinergic neurons evokes no change in the mean bending angles. *A) Bending angles ±SEM of animals, expressing bPAC or BeCyclOp(A-2x) in cholinergic neurons, and the genetic background lite-1(ce314). Blue bar indicates the period of light exposure (0.2 mW/mm^2; 470 nm). n = 47 – 72 animals. B) Quantification of the mean normalized bending angles of the time periods before (0 – 15 s), during (15 – 40 s, blue bar), and after (40 – 55 s) light application. n = 66 – 72 animals. The interquartile range (IQR), median (–), mean values (●), individual measurements (o), and whiskers (1.5 * IQR) are illustrated. Statistically significant differences: one-way ANOVA with Bonferroni correction (*p ≤ 0.05 and ***p ≤ 0.001). Image adapted from (Henss et al., 2021)*

Also, photoactivation of YFP-CyclOp(A-2x)s expressing animals showed no obvious change in body bending. However, YFP-CaCyclOp(A-2x) expressing animals depicted a light triggered increase of the mean body bending of about 6 % after light application, an effect which was also detected for control animals supplemented without ATR (Figure 32 A, B). Reason for this might be a behavioural change triggered by turning of the light. In sum, membrane-bound photoactivatable adenylyl cyclases activation had no impact on *C. elegans* body bending, as observed for bPAC. The reason may be that cytosolic cAMP production by bPAC in cholinergic neurons triggers activation of undesired cAMP signalling pathways in addition to cAMP dependent neurotransmission, causing the increase in body bending on solid substrate.

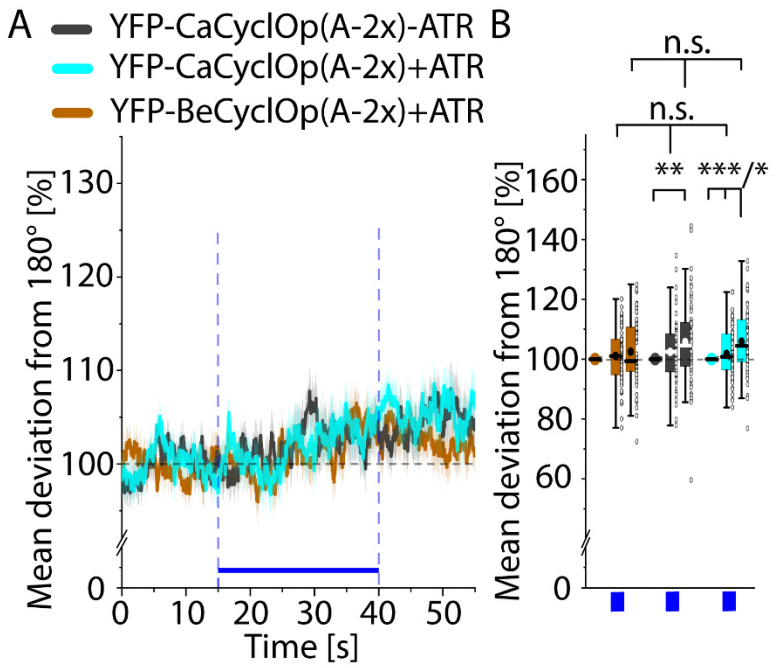

Figure 32: YFP-CyclOp(a-2x)s light stimulation in cholinergic neurons produce no obvious change in the mean bending angles. *A) Bending angles ±SEM of animals, expressing YFP-BeCyclOp(A-2x) or YFP-CaCyclOp(A-2x) in cholinergic neurons, and the genetic background lite-1(ce314). Blue bar indicates the period of light exposure (0.2 mW/mm^2; 470 nm). n = 47 – 72 animals. B) Quantification of the mean normalized bending angles of the time periods before (0 – 15 s), during (15 – 40 s, blue bar), and after (40 – 55 s) stimulation. n = 58 – 61 animals. The interquartile range (IQR), median (–), mean values (●), individual measurements (o), and whiskers (1.5 * IQR) are illustrated. Statistically significant differences: one-way ANOVA with Bonferroni correction (non-significant (n.s.), *p ≤ 0.05, **p ≤ 0.01 and ***p ≤ 0.001). Image adapted from (Henss et al., 2021)*

3.1.2.2.3. Membrane-bound photoactivatable adenylyl cyclase activation triggers minor changes in body length

In addition to analyses of the crawling speed and body bending, the influence of membrane-bound photoactivatable adenylyl cyclases activation on *C. elegans* body length on solid substrate was studied. The body length on solid substrate is reduced by bPAC activation in cholinergic neurons, providing an additional behavioural readout to compare cAMP-dependent neurotransmission in cholinergic neurons induced by soluble bPAC and the engineered membrane-bound enzymes. In this context, illumination of bPAC expressing animals reduced the body length of about 4 % within 20 s, whereas BeCyclOp(A-2x) expressing animals depicted a reduction of the body length of about 2 % during light application, which is nearly comparable to the effect observed for control animals raised without ATR, but slightly stronger than the observed effect for the genetic background *lite-1(ce314)* (~1 %) (Figure 33 A, B). The reason for the slight reduction in body length observed for the genetic

background *lite-1(ce314)* might be explained by an additional photoreceptor in *C. elegans* that senses blue light (470 nm) and slightly affects the behaviour of the animals.

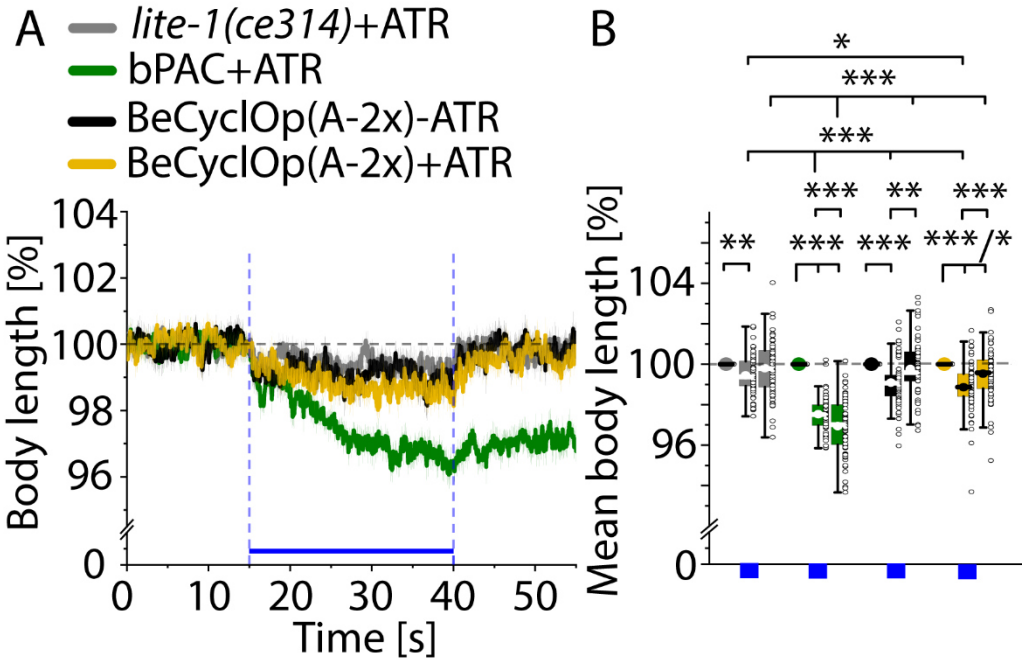

Figure 33: Photo stimulation of BeCycIOp(A-2x) in cholinergic neurons slightly decreases the body length, though not reaching the extend triggered by bPAC. *A) Body lengths ±SEM of animals, expressing bPAC or BeCycIOp(A-2x) in cholinergic neurons, and the genetic background lite-1(ce314). Blue bar indicates the period of light exposure (0.2 mW/mm²; 470 nm). n = 47 – 72 animals. B) Quantification of the mean normalized body lengths of the time periods before (0 – 15 s), during (15 – 40 s, blue bar), and after (40 – 55 s) light exposure. n = 55 – 73 animals. The interquartile range (IQR), median (–), mean values (●), individual measurements (o), and whiskers (1.5 * IQR) are illustrated. Statistically significant differences: one-way ANOVA with Bonferroni correction (*p ≤ 0.05, **p ≤ 0.01 and ***p ≤ 0.001). Image adapted from (Henss et al., 2021).*

In case of YFP-CyclOp(A-2x)s expressing animals, light stimulation triggered a decrease of the body length of about 2 % during light application, similar to control animals without addition of ATR, and the genetic background *lite-1(ce314)* (Figure 34 A-C). In conclusion, body length reductions by YFP-BeCycIOp(A-2x) and YFP-CaCycIOp(A-2x) are comparable to that observed in control animals, whereas stimulation of BeCycIOp(A-2x) reduced animal body length more to that observed in the genetic background *lite-1(ce314)*, which may be due to higher expression of the enzyme in cholinergic neurons and higher levels of light-generated cAMP. Nevertheless, the reduction evoked by BeCycIOp(A-2x) activation did not reach the same extent as induced by bPAC activation. The reason may be that cytosolic cAMP production by bPAC in cholinergic neurons triggers activation of undesired cAMP

signalling pathways in addition to cAMP dependent neurotransmission, causing the reduction in body length on solid substrate.

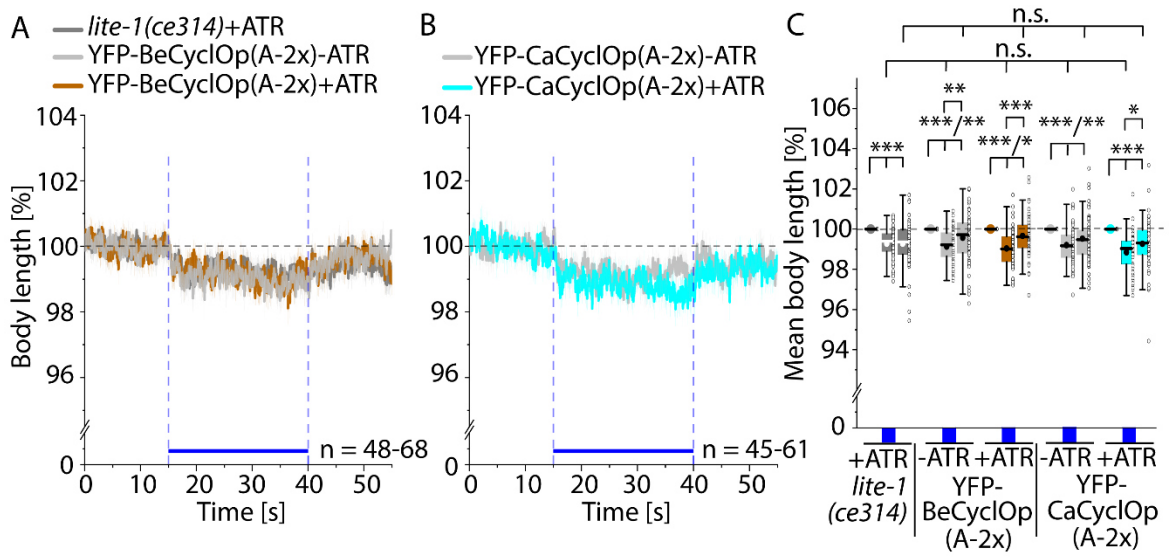

Figure 34: YFP-CyclOp(A-2x)s photoactivation in cholinergic neurons produce no obvious reduction in body length. *Body lengths ±SEM of A) the genetic background lite-1(ce314), and of animals expressing YFP-BeCyclOp(A-2x), or B) YFP-CaCyclOp(A-2x) in cholinergic neurons. Blue bar indicates the period of light exposure (0.2 mW/mm^2; 470 nm). n = number of animals. C) Quantification of the mean normalized body lengths of the time periods before (0 – 15 s), during (15 – 40 s, blue bar), and after (40 – 55 s) light exposure. n = 58 – 68 animals. The interquartile range (IQR), median (–), mean values (●), individual measurements (o), and whiskers (1.5 * IQR) are shown. Statistically significant differences: one-way ANOVA with Bonferroni correction (non-significant (n.s.), *p ≤ 0.05, **p ≤ 0.01 and ***p ≤ 0.001). Image adapted from (Henss et al., 2021).*

3.1.2.3. Determination of photoactivatable adenylyl cyclase expression levels in cholinergic neurons

To more rigorously classify the evoked behavioural changes, the expression levels of bPAC-YFP and YFP-CyclOp(A-2x)s were compared via confocal fluorescence microscopy, and the mean fluorescence intensities were determined. Both YFP-BeCyclOp(A-2x) and YFP-CaCyclOp(A-2x) depicted similar expression levels, which were ~1.4-fold lower than the level of the soluble bPAC (Figure 35 A-D). Thus, the increased diversity of the behavioural output detected for cytosolic cAMP production by bPAC, i.e. increased bending angles and a decreased body length, could be due to the higher expression level of bPAC. Interestingly, despite lower expression, the membrane-bound photoactivatable adenylyl cyclases evoked similar enhanced locomotion behaviours, i.e. crawling and swimming, which may indicate a more specific activation of cAMP-dependent neurotransmission.

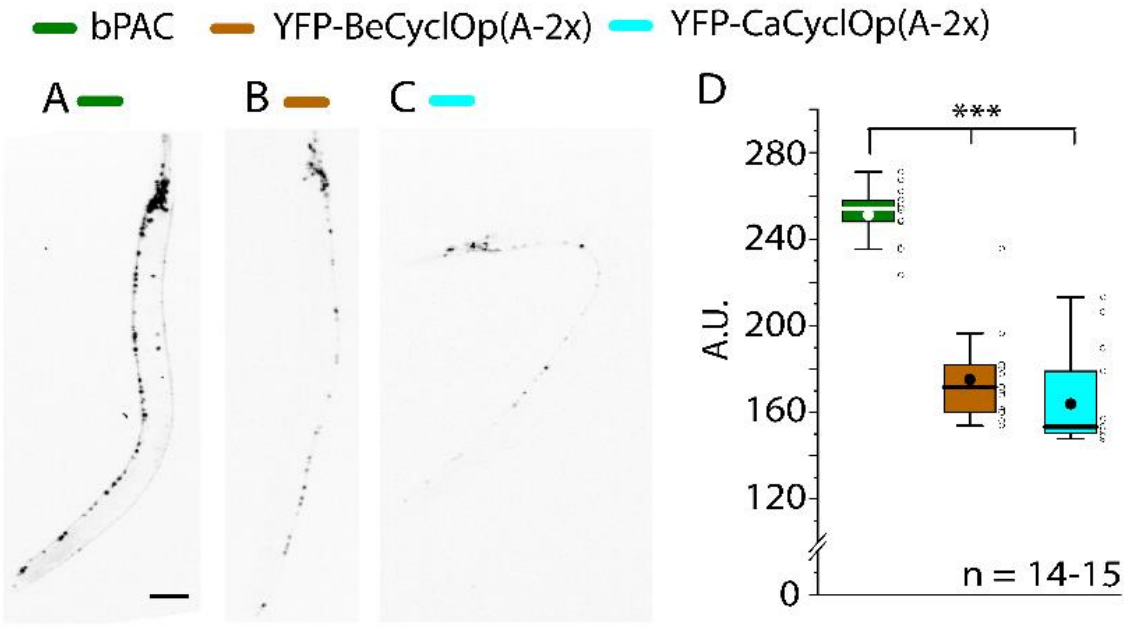

Figure 35: Membrane-bound photoactivatable adenylyl cyclases are expressed at much lower levels than bPAC in cholinergic neurons. *Confocal fluorescence images of animals, expressing A) bPAC, B) YFP-BeCyclOp(A-2x) or C) YFP-CaCyclOp(A-2x) in cholinergic neurons using the unc-17 promoter. Scale bar = 50 µm. D) Mean fluorescence intensities. The interquartile range (IQR), median (–), mean values (●), individual measurements (o), and whiskers (1.5 * IQR) are depicted. n = number of animals. Statistically significant differences were calculated using one-way ANOVA with Bonferroni correction (***p ≤ 0.001). Image adapted from (Henss et al., 2021).*

3.1.3. Photoactivatable adenylyl cyclases coupled to the TAX-2/-4 CNGC for cell activation

Locomotion behaviour analysis in liquid and on solid media provided a strong indication for optogenetic cAMP production by the engineered membrane-bound photoactivatable adenylyl cyclases. However, the actual extent of the specificity switch and potentially remaining cGMP generation could not be answered this way. To this end, the coding sequences of membrane-bound photoactivatable adenylyl cyclases were subcloned into a vector containing the *myo-3* promoter, and equal amounts of plasmid DNA were injected into the strain ZX1741, generating strains which co-express TAX-2/-4 and the respective membrane-bound photoactivatable adenylyl cyclases in body wall muscle cells. This channel is mainly specific for cGMP, but at high concentrations it is also activated by cAMP (200-fold lower sensitivity). To gain more insights into the specificity switch of the membrane-bound photoactivatable adenylyl cyclases, body length measurements were performed. In this context, cGMP production would efficiently activate the channel and cause body

contraction, whereas cAMP would evoke contraction if considerable amounts would be generated, or a mixture of cAMP and cGMP. Except for CaCyclOp(A-2x), illumination of all membrane-bound photoactivatable adenylyl cyclases in TAX-2/-4 expressing animals triggered similar body contractions of about 2 – 3.5 % within ~ 2.5 s, which slightly differ in their time course. Here, the effect evoked by TAX-2/-4; BeCyclOp(A-2x) decayed much more slowly. Importantly, none of the engineered enzymes evoked a similar reduction in body length as BeCyclOp, which could indicate a high specificity for cAMP generation and no or less remaining cGMP production. Moreover, the non-detectable effect in TAX-2/-4; CaCyclOp(A-2x) animals could indicate that the enzyme is weakly expressed in *C. elegans* and/or generates no or only marginal amounts of cAMP. Interestingly, the decay rate of YFP-BeCyclOp(A-2x) mediated muscle contraction was faster when compared to BeCyclOp(A-2x). Reason for this could be a higher expression level of BeCyclOp(A-2x) than of YFP-BeCyclOp(A-2x). While CaCyclOp(A-2x) activation induced no obvious effect, YFP-CaCyclOp(A-2x) was able to induce light dependent body length reductions (Figure 36 A, B). This could be due to an increased expression level and/or membrane targeting of the enzyme by addition of the N-terminal YFP.

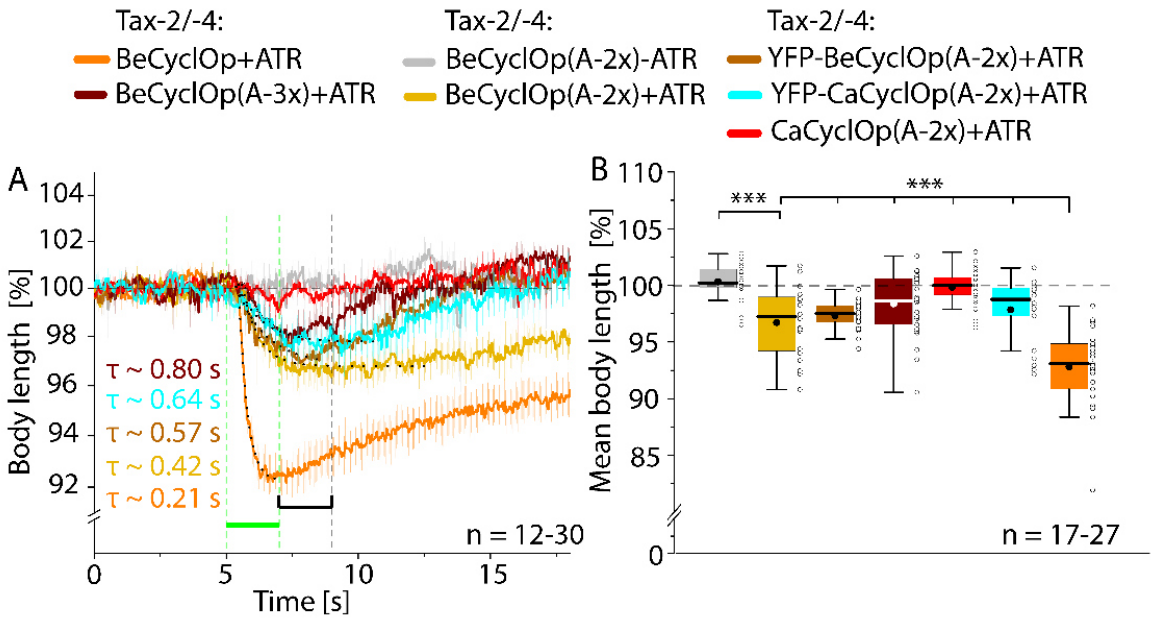

Figure 36: Membrane-bound photoactivatable adenylyl cyclases and TAX-2/-4 CNGC depict different efficiencies and kinetics for cell depolarization in body wall muscle cells. *A) Body length analysis ±SEM of animals co-expressing BeCyclOp(A-2x), YFP-BeCyclOp(A-2x), BeCyclOp(A-3x), wild type BeCyclOp, CaCyclOp(A-2x), or YFP-CaCyclOp(A-2x) and the TAX-2/-4 channel in body wall muscle cells. Green bar indicates the period of illumination (0.9 mW/mm²; 535 nm). Animals were raised with (+) or without (-) ATR. Mono-exponential decay fit (dotted lines) was used to determine onset-time constants (τ). B) Quantification of the mean normalized body lengths for the indicated time period (7 – 9 s). The interquartile range (IQR), median (–), mean values (●), individual measurements (o), and whiskers (1.5 * IQR) are shown. n = number of animals. Statistically significant differences were calculated using one-way ANOVA with Bonferroni correction (***p ≤ 0.001). Image adapted from (Henss et al., 2021).*

To classify cNMP production by BeCyclOp(A-2x) in more detail, light triggered body length changes (2s light pulse; 0.9 mW/mm^2; 470 nm) were compared between TAX-2/-4; bPAC and TAX-2/-4; BeCyclOp(A-2x) expressing animals. In this context, bPAC evoked stronger body contractions than BeCyclOp(A-2x) (9 and 4.5 %, respectively), which may be due to a higher light-inducible cAMP production or higher expression level of bPAC (Figure 37 A, B). Noteworthy, BeCyclOp(A-2x) expressing animals showed an altered morphology, independent of ATR supplementation, i.e. shortened and wider body, while none of the other strains appeared to be affected by transgene expression. This morphology change could indicate that the adenylyl cyclase domain constitutively generates cAMP independently of light regulation by the rhodopsin domain.

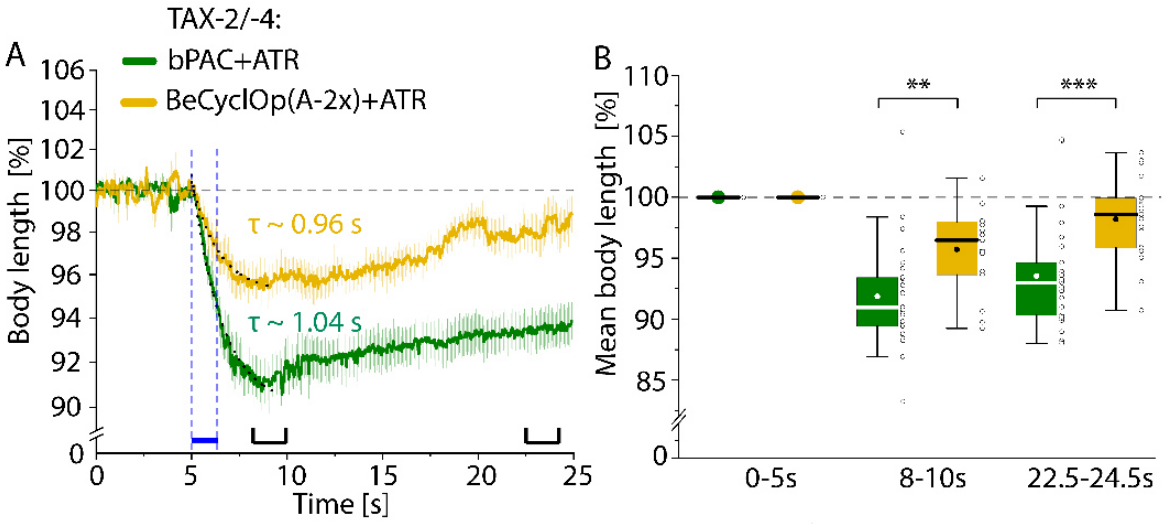

Figure 37: bPAC stimulation evokes stronger body contraction than BeCyclOp(A-2x), indicating higher overall cAMP generation in body wall muscle cells. *A) Body lengths ±SEM of animals co-expressing TAX-2/-4 and bPAC or BeCyclOp(A-2x) in body wall muscle cells. Blue bar indicates the period of illumination (0.9 mW/mm^2; 470 nm). Onset-time constants (τ) were calculated using a mono-exponential decay fit (dotted lines). n = 16 – 27 animals. B) Mean normalized body lengths for the time periods before (0 – 5 s), during (8 – 10 s), and after (22.5 – 24.5 s) light exposure. The interquartile range (IQR), median (–), mean values (●), individual measurements (o), and whiskers (1.5 * IQR) are depicted. n = 19 – 28 animals. Statistically significant differences: one-way ANOVA with Bonferroni correction (**p ≤ 0.01 and ***p ≤ 0.001). Image adapted from (Henss et al., 2021).*

To determine the expression level of the respective photoactivatable adenylyl cyclases, confocal fluorescence microscopy and western blot analysis were performed. Here, the highest expression levels were examined for BeCyclOp(A-2x), BeCyclOp(A-3x) and bPAC, whereas YFP-CyclOp(A-2x)s and CaCyclOp(A-2x) exhibited half or intermediate expression levels (Figure 38 A-D). Thus, the similar expression levels of BeCyclOp(A-2x), BeCyclOp(A-3x), and bPAC could indicate that bPAC has a higher light-inducible cAMP production than BeCyclOp(A-2x), and that BeCyclOp(A-3x) produce small amounts of cAMP that were not detectable in the swimming behaviour analysis. Moreover, the addition of the N-terminal YFP to CaCyclOp(A-2x) might increase the expression and/or stabilize the conformation of the enzyme in *C. elegans*.

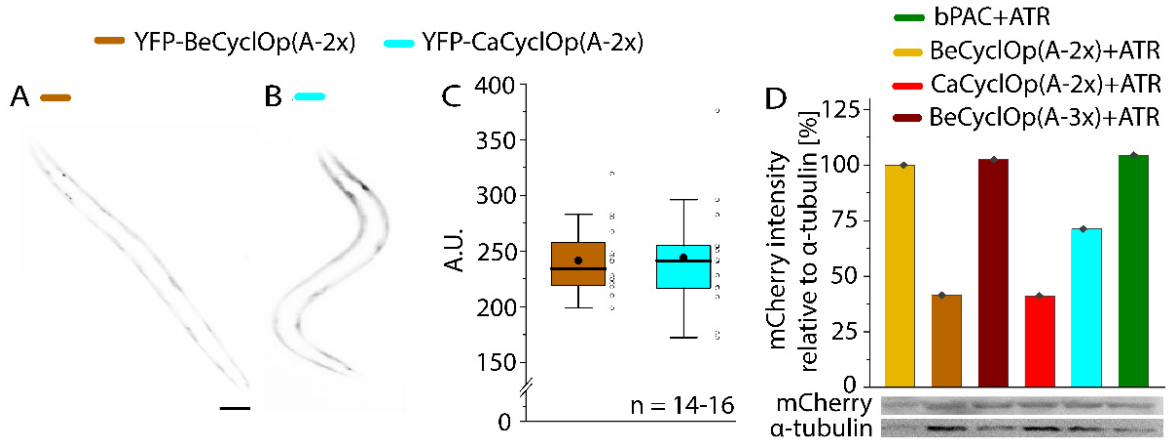

Figure 38: BeCyclOp(A-2x), BeCyclOp(A-3x) and bPAC depict the highest mRNA levels, whereas YFP-CyclOp(A-2x)s shows about half or intermediate expression levels in body wall muscle cells. *Confocal fluorescence micrographs of animals, expressing A) YFP-BeCyclOp(A-2x) or B) YFP-CaCyclOp(A-2x) in body wall muscle cells using the myo-3 promoter. Scale bar = 50 µm. C) Mean fluorescence intensities. The interquartile range (IQR), median (–), mean values (●), individual measurements (o), and whiskers (1.5 * IQR) are illustrated. n = number of animals. D) Western blot quantification of C. elegans extracts from animals, expressing bPAC, BeCyclOp(A-2x), BeCyclOp(A-3x) or CaCyclOp(A-2x), and mCherry from bicistronic pre-mRNAs (comprising the SL2 trans-splicing sequence). Shown is the mCherry intensity relative to the α-tubulin signal, normalized to the intensity of the strain ZX2613 (BeCyclOp(A-2x). N = 1 replicate of n = 20 animals each. Image adapted from (Henss et al., 2021).*

3.1.4. Determination of nucleotidyl specificity and cNMP levels of photoactivatable nucleotidyl cyclases using *C. elegans* extracts

To determine the nucleotidyl specificity and the amount of generated cNMP of the engineered membrane-bound photoactivatable adenylyl cyclases, *in vitro* assays for cAMP and cGMP quantification were performed. Furthermore, this should allow a better classification of the results from the behavioural experiments. For this purpose, the photoactivatable nucleotidyl cyclases were expressed in *C. elegans* muscle cells, and the cNMP content of a fixed number of animals (i.e., their entire body) after 15 min blue light application was investigated. For BeCyclOp(A-2x), YFP-BeCyclOp(A-2x) and YFP-CaCyclOp(A-2x), a high cAMP level produced in transgenic *C. elegans* tissue was determined (39, 57, 40 nM, respectively), though they did not reach the same extent as produced by bPAC (142 nM). Importantly, no basal cyclase activity was measured, as the cAMP levels in dark were as in non-transgenic control animals (~3 nM), and no residual cGMP production was observed for all engineered membrane-bound photoactivatable adenylyl cyclases. In conjunction with the expression analysis, the results may indicate higher light-inducible cAMP production by bPAC compared with BeCyclOp(A-2x), that YFP-CyclOp(A-2x)s may be the most

potent enzymes for cAMP production, and that BeCyclOp(A-3x) may be a useful tool for generating lower amounts of cAMP. Furthermore, the result could emphasize an increased expression and/or an increased stabilization of the protein conformation of CaCyclOp(A-2x) by adding the N-terminal YFP. In case of photoactivatable guanylyl cyclases, bPGC and CaCyclOp produced comparable cGMP levels (18, 13 nM, respectively), whereas the highest cGMP level was determined for BeCyclOp (74 nM) (Figure 39 A, B). Thus, the engineered membrane-bound photoactivatable adenylyl cyclases generate cAMP in high magnitudes and with high specificity.

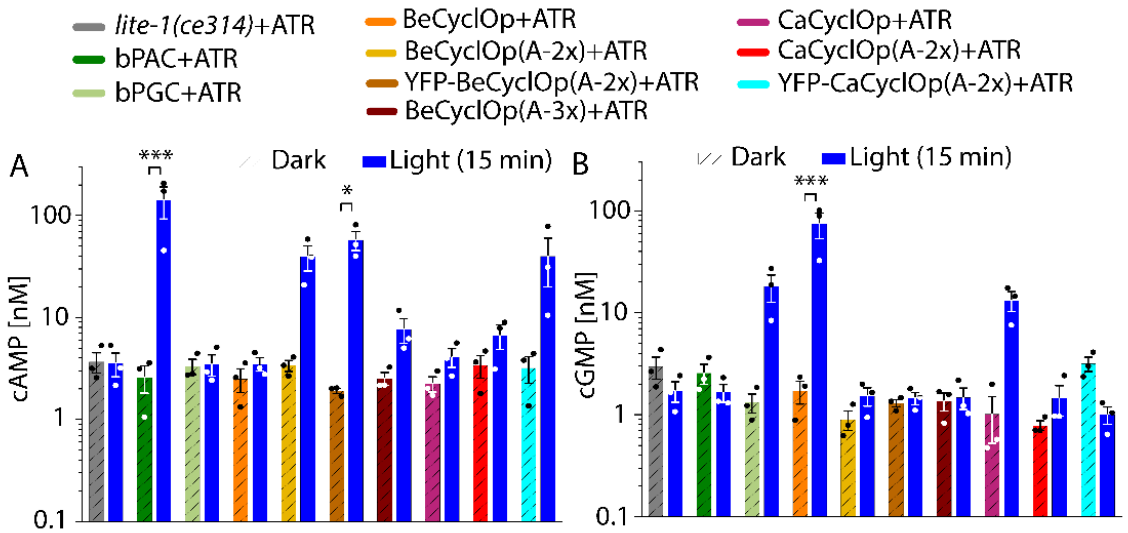

Figure 39: Membrane-bound photoactivatable adenylyl cyclases generate (and accumulate) cAMP at high levels in vivo, with high specificity. *A-B) Quantification of A) cAMP and B) cGMP levels using C. elegans extracts. Animals expressing bPAC, bPGC, BeCyclOp, BeCyclOp(A-2x), YFP-BeCyclOp, BeCyclOp(A-3x), CaCyclOp, CaCyclOp(A-2x), or YFP-CaCyclOp(A-2x) in body wall muscle cells were stimulated with blue light (0.5 mW/mm²; 470 nm, 15 min) or as dark condition, incubated with red filtered transmission light (675 nm; 15 min). Depicted are the mean values ±SEM comprising the individual measured values (●). n = 3 samples of 60 animals each. Statistically significant differences were calculated using two-way ANOVA with Bonferroni correction (*p ≤ 0.05 and ***p ≤ 0.001). Image adapted from (Henss et al., 2021).*

To examine optogenetic cAMP generation at conditions that match the behavioural experiments, cAMP levels were quantified for bPAC and YFP-BeCyclOp(A-2x) expressing animals, stimulated for 30 s with blue light. In this context, a significantly higher cAMP level was measured for bPAC (86 nM) compared to YFP-BeCyclOp(A-2x) (22 nM) containing lysates (Figure 40). In summary, bPAC generated a higher amount of optogenetic cAMP levels under the applied experimental conditions, possibly due to a higher expression level or light-inducible cAMP generation rate compared with the engineered membrane-bound photoactivatable adenylyl cyclases, which could lead to a greater diversity of the behavioural output observed in the

behavioural experiments (i.e., increased bending angles and a decreased body length). In addition, the membrane-bound photoactivatable adenylyl cyclases elicited similarly enhanced locomotion behaviours (i.e., crawling and swimming), which may indicate more specific activation of cAMP-dependent neurotransmission.

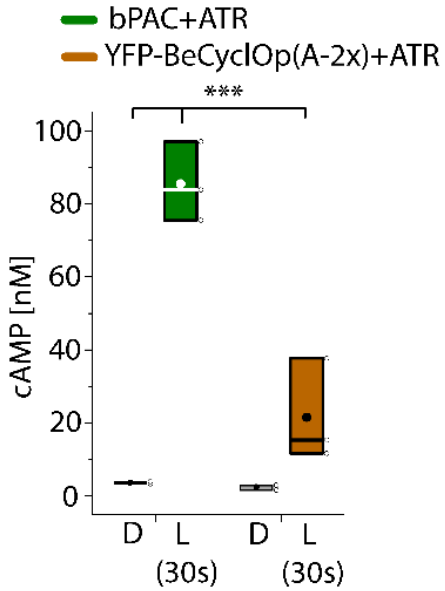

Figure 40: Under conditions matching the light conditions of behavioural experiments, bPAC produced ca. 4x more cAMP than YFP-BeCyclOp(A-2x). *Quantification of cAMP levels using C. elegans extracts. Animals expressing bPAC or YFP-BeCyclOp(A-2x) in body wall muscle cells were illuminated for 30 s with blue light (light = L) (0.5 mW/mm^2; 470 nm) or with red filtered transmission light (675 nm) (dark = D). The interquartile range (IQR), median (–), mean values (●), individual measurements (o), and whiskers (1.5 * IQR) are shown. N = 3 replicates of n = 60 animals each. Statistically significant differences: two-way ANOVA with Bonferroni correction (***p ≤ 0.001). Image adapted from (Henss et al., 2021).*

3.1.5. BeCyclOp and the cGMP-gated BeCNG1 channel for K^+-based hyperpolarization

So far, the proton pump Arch, the chloride pump NpHR, and the anion channel GtACR have been established as hyperpolarizing optogenetic tools in *C. elegans* (Bergs *et al.*, 2018; Chow *et al.*, 2010; Husson *et al.*, 2012; Zhang *et al.*, 2007a). However, their application is accompanied by undesired changes in ion distribution across the membrane and requires continuous light stimulation (Mahn *et al.*, 2016; Wiegert *et al.*, 2016). To overcome these limitations, photoactivatable nucleotidyl cyclases were combined with cyclic nucleotide-gated potassium channels for cell hyperpolarization based on K^+-currents. For this purpose, a mechanism found in the aquatic fungus *Blastocladiella emersonii* was adapted to *C. elegans*. In this context,

the cGMP-gated K^+-channel BeCNG1 acts as an effector protein downstream of BeCyclOp and participates in the phototactic response of the zoospore (Avelar *et al.*, 2015). To assess this system for its potential to function in *C. elegans*, the proteins were co-expressed in *C. elegans* muscle cells. For this purpose, A. Hirschhäuser subcloned the coding sequence of BeCNG1 into a vector containing the *myo-3* promoter. To investigate the expression of BeCNG1 in *C. elegans* muscle cells, he C-terminally fused the protein to YFP and analysed its expression via fluorescence microscopy, where intracellular protein aggregates were visible, but no correct membrane localization could be detected (ZX2279; 5 ng/µl BeCNG1-YFP). Further, he evaluated the functionality of the BeCNG1; BeCyclOp system (ZX2231; 15 ng/µl BeCyclOp plasmid DNA and 10 ng/µl BeCNG1 plasmid DNA) via body length measurements and observed a slight light provoked muscle hyperpolarization, that was not significant (Master Thesis A. Hirschhäuser). Therefore, I have generated a new BeCNG1-YFP; BeCyclOp expressing strain by microinjection (ZX2326; 15 ng/µl BeCyclOp plasmid DNA and 40 ng/µl BeCNG1 plasmid DNA) with an increased expression level of BeCNG1-YFP. To examine protein expression of both proteins, I performed fluorescence microscopy. BeCNG1-YFP depicted a clustered appearance along the muscle membrane, whereas expression of BeCyclOp was indirectly observed via mCherry expression (from a bicistronic transcript) in the cytosol of the muscle cells (Figure 41 A, B).

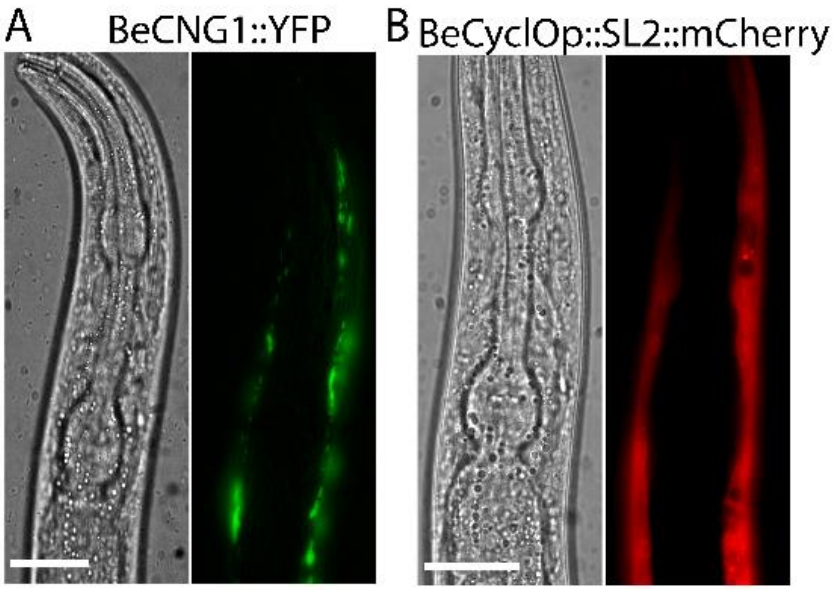

Figure 41: Expression pattern of BeCNG1::YFP BeCyclOp::SL2::mCherry using the myo-3 promoter. *Fluorescence images (right) and DIC brightfield images (left) of animals, co-expressing A) BeCNG1::YFP and B) BeCyclOp::SL2::mCherry in body wall muscle cells using the myo-3 promoter. Scale bar = 50 µm. Image adapted from (Henss et al., 2021).*

To analyse the functionality of the two component optogenetic system, body length measurements were conducted. Illumination of animals, co-expressing BeCNG1-YFP and BeCyclOp and raised with ATR, triggered a slightly increased body length of about 1 % within ~ 3 s, which remained at this level even after turning the light off. The reason for the moderately evoked effect could be a pre-activation of the BeCNG1 channel or a general toxicity of the channel due to its tendency to form protein aggregates that trigger endoplasmic reticulum stress. The sustained effect could be explained by the large amount of cGMP produced by BeCyclOp and the low PDE activity in body wall muscle cells. No body elongation was detected for control animals, supplemented without ATR (Figure 42 A, B). In sum, BeCNG1 and BeCyclOp caused moderate but long-lasting optogenetic hyperpolarization of *C. elegans* muscle.

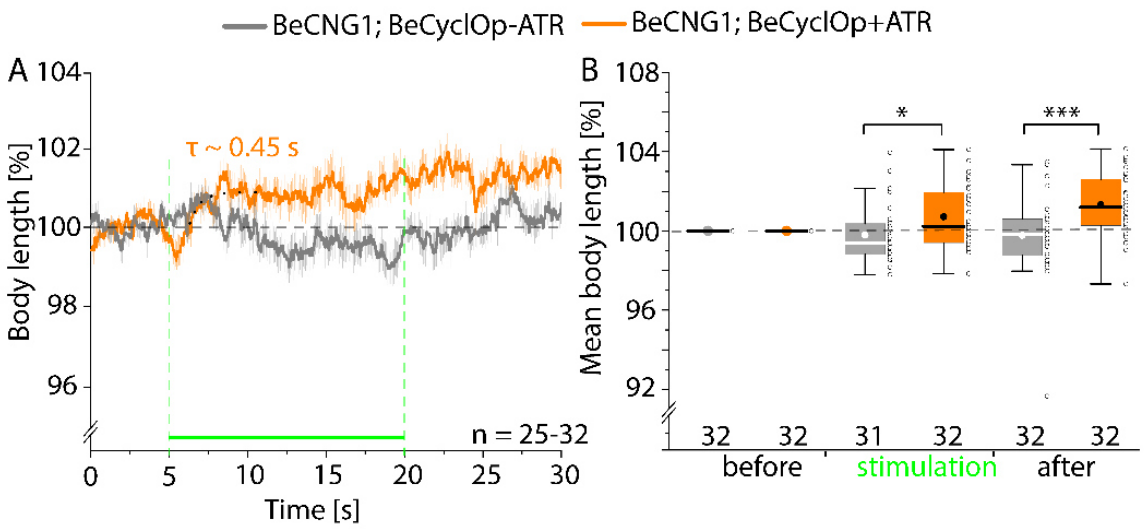

Figure 42: BeCyclOp and BeCNG1 trigger moderate, but long-lasting hyperpolarization of body wall muscle cells. *A) Body length analysis ±SEM of animals co-expressing BeCNG1 and BeCyclOp in body wall muscle cells. Green bar indicates the period of illumination (0.9 mW/mm²; 535 nm). Mono-exponential growth fit (dotted lines) was used to determine onset-time constants (τ). Animals were raised with (+) or without (-) ATR. B) Mean normalized body lengths for the time periods before (0 – 5 s), during (5 – 20 s), and after (20 – 30 s) light application. The interquartile range (IQR), median (–), mean values (●), individual measurements (o), and whiskers (1.5 * IQR) are shown. n = number of animals. Statistically significant differences were determined using one-way ANOVA with Bonferroni correction (*p ≤ 0.05 and ***p ≤ 0.001). Image adapted from (Henss et al., 2021).*

3.1.6. bPAC and the cAMP-gated potassium channel SthK for cell inhibition

Previously, a two component optogenetic system for cell inhibition, comprising bPAC and the cAMP-gated SthK channel from *Spirochaeta thermophila* was utilized to manipulate K^+-currents in various model organisms (Beck *et al.*, 2018; Bernal Sierra *et al.*, 2018). I adapted this system to use in *C. elegans* and evaluated its properties in muscle cells and cholinergic motor neurons by performing body length measurements and swimming behaviour analysis.

3.1.6.1. Characterization of the bPAC / SthK two-component optogenetic system in body wall muscle cells

To analyse the functionality of the system in *C. elegans* muscle cells, the coding sequence of SthK was subcloned into a vector containing the *myo-3* promoter. For investigation of SthK expression in *C. elegans* muscle, the protein was C-terminally fused to mCherry, whereas for functionality analysis, SthK and mCherry were expressed from a bicistronic mRNA. Fluorescence microscopy was performed to

examine SthK expression in body wall muscle cells, depicting a clustered appearance along the muscle membrane (Figure 43).

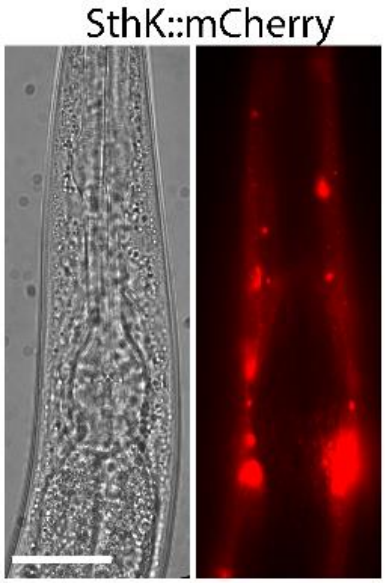

Figure 43: Expression pattern of SthK::mCherry using the myo-3 promoter. *Fluorescence (right) and DIC brightfield image (left) of an animal expressing SthK::mCherry in body wall muscle cells using the myo-3 promoter. Scale bar = 50 µm. Image adapted from (Henss et al., 2021).*

To assess the functionality of the SthK and bPAC system in *C. elegans*, a strain co-expressing SthK and bPAC was generated, and analysed *via* body length measurements. Light stimulation of animals co-expressing bPAC and SthK evoked body elongation of about 4 % within 1.1 s, which is comparable to other strong hyperpolarizers like GtACR2 or Arch (Bergs *et al.*, 2018; Husson *et al.*, 2012). No light evoked body length increase was observed for control animals, only expressing SthK (Figure 44 A, B).

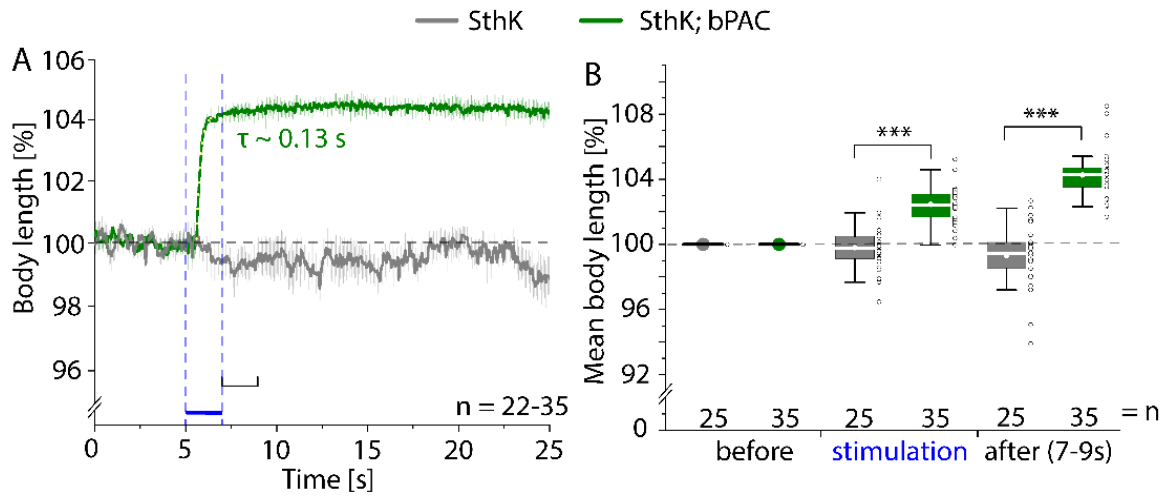

Figure 44: bPAC and SthK light stimulation in body wall muscle cells provoke fast and robust muscle hyperpolarization. *A) Body lengths ±SEM of animals co-expressing SthK and bPAC in body wall muscle cells. Blue bar indicates the period of illumination (0.9 mW/mm²; 470 nm). Onset-time constants (τ) were calculated using a mono-exponential growth fit (dotted lines). B) Quantification of the mean normalized body lengths for the time periods before (0 – 5 s), during (5 – 7 s), and after (7 – 9 s) light exposure. The interquartile range (IQR), median (–), mean values (●), individual measurements (o), and whiskers (1.5 * IQR) are illustrated. n = number of animals. Statistically significant differences: one-way ANOVA with Bonferroni correction (***p ≤ 0.001). Image adapted from (Henss et al., 2021).*

To investigate the duration of the light induced muscle hyperpolarization, body length measurements were extended up to 10 min after light application (1 s). Here, bPAC; SthK triggered hyperpolarization constantly increased the body length by up to ~ 6.5 % within ca. 5.5 minutes and decayed to 3.7 % in the remaining 4.5 minutes (Figure 45). This demonstrated a long-lasting persistence of cAMP generated by bPAC, probably due to low PDE activity in body wall muscle cells, as well as extensive non-desensitizing activity and conductance of the SthK channel.

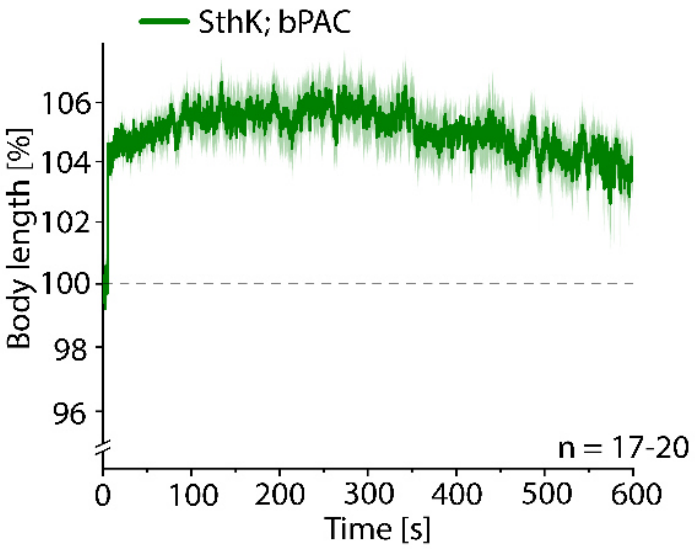

Figure 45: bPAC and SthK evoked muscle elongation lasted up to 10 min. *Body length measurement ±SEM of animals co-expressing SthK and bPAC in body wall muscle cells. Animals were stimulated for 1 s with blue light (0.9 mW/mm²; 470 nm) after 5 s. n = number of animals. Image adapted from (Henss et al., 2021).*

To characterize the system in more detail, i.e. a possible pre-activation of the SthK channel due to intrinsic cAMP or bPACs dark activity, swimming behaviour analyses were performed. Here, expression of SthK reduced the basal swimming rate compared to the genetic background *lite-1(ce314)* (50 vs 90 cycles per min, respectively), which was further decreased by co-expression of bPAC to 20 cycles per min. Simulation of animals co-expressing bPAC and SthK evoked a complete arrest of their swimming behaviour (0.5 cycles per min). This effect was not observed in animals only expressing SthK, or in the genetic background *lite-1(ce314)* (Figure 46). In sum, SthK and bPAC triggered light dependent, robust and long-term muscle hyperpolarization, but intrinsic cAMP is already sufficient to activate SthK, whereas the additional cAMP produced by bPAC in the dark was too high to allow meaningful use of SthK. For this reason, a less potent and completely dark-inactive photoactivatable adenylyl cyclase would be required. In addition, a tissue with increased PDE activity of endogenous PDEs would be helpful, e.g., cholinergic motor neurons that use intrinsic cAMP signalling and therefore presumably express PDEs.

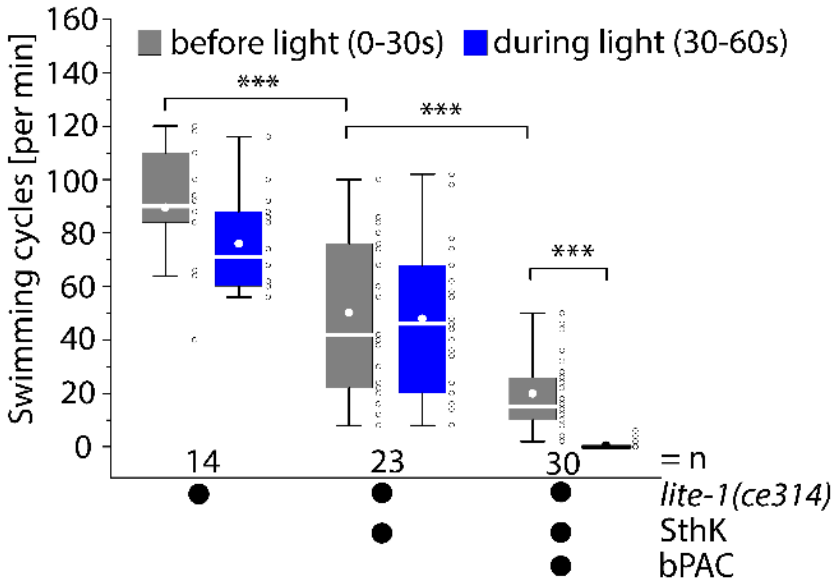

Figure 46: SthK pre-activation by intrinsic cAMP and increased cAMP level due to bPACs dark activity reduce basal swimming rate, and illumination of SthK; bPAC evoked a complete arrest of the swimming behaviour. *Swimming frequencies ±SEM of animals expressing only SthK, or co-expressing SthK and bPAC in body wall muscle cells, and the genetic background lite-1(ce314). Swimming rates were calculated 30 s before, and 30 s during light exposure (0.2 mW/mm²; 470 nm). The interquartile range (IQR), median (–), mean values (●), individual measurements (o), and whiskers (1.5 * IQR) are depicted. n = number of animals. Statistically significant differences were calculated using one-way ANOVA and Student's t test (***p ≤ 0.001). Image adapted from (Henss et al., 2021).*

3.1.6.2. Application of the bPAC / SthK system in cholinergic motor neurons

After implementation of the SthK / bPAC system in *C. elegans* muscle cells, the system was assessed for its ability to hyperpolarize *C. elegans* cholinergic neurons. For this purpose, the coding sequence was subcloned into a vector containing the *unc-17* promoter. For detection of SthK expression, the protein was C-terminally fused to mCherry, and for functionality analysis, SthK and mCherry were expressed from bicistronic mRNAs. Fluorescence microscopy was performed to investigate the expression of SthK in cholinergic neurons, confirming the expression of SthK-mCherry (Figure 47). However, correct membrane localization could not be confirmed at the magnification used.

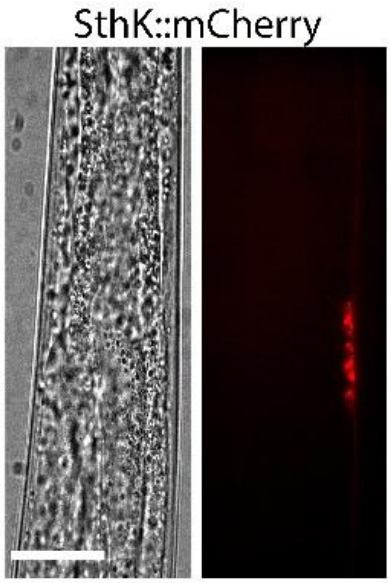

Figure 47: Expression pattern of SthK::mCherry using the unc-17 promoter. *Fluorescence (right) and DIC brightfield image (left) of an animal expressing SthK::mCherry in cholinergic neurons using the unc-17 promoter. Scale bar = 50 µm. Image adapted from (Henss et al., 2021).*

To evaluate the ability of the system to silence cholinergic neurons of *C. elegans*, swimming behaviour analyses were executed. Expression of SthK alone reduced the basal swimming rate in wild type animals and in the genetic background *lite-1(ce314)* (93 vs 81 and 68 vs 59 cycles per min, respectively), and was further decreased by co-expression of bPAC (11 cycles per min, in *lite-1(ce314)* background). Light stimulation of animals, co-expressing bPAC and SthK caused nearly a complete arrest of the swimming frequency (2 cycles per min), which was not detected in control animals, only expressing SthK or bPAC, the genetic background *lite-1(ce314)* or wild type animals (Figure 48). This again indicates pre-activation of SthK due to intrinsic cAMP and additional cAMP produced by bPAC in the dark, presumably due to a high affinity of SthK for cAMP. Because the expected PDE activity in cholinergic neurons was unable to antagonize the pre-activation of the channel triggered by bPACs dark activity, this combination appears to be of limited utility in *C. elegans* unless investigators aim for a sustained K^+-based inhibition of the desired cell type.

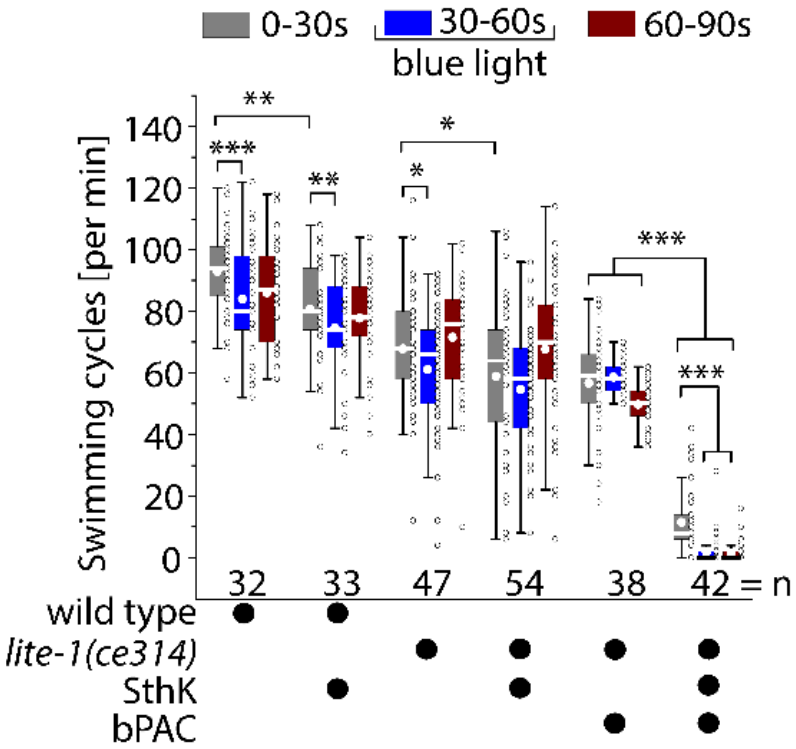

Figure 48: Pre-activation of SthK reduces basal swimming frequencies, and photo activation of SthK and bPAC provoke a nearly complete arrest of the swimming behaviour. *Swimming rates ±SEM of animals expressing only SthK or bPAC, or co-expressing SthK and bPAC in cholinergic neurons, the genetic background lite-1(ce314) and wild type animals. Swimming cycles were calculated 30 s before and 30 s after a 30 s light pulse (0.4 mW/mm²; 470 nm). The interquartile range (IQR), median (–), mean values (●), individual measurements (o), and whiskers (1.5 * IQR) are depicted. n = number of animals. Statistically significant differences were calculated using one-way ANOVA and Student's t test (*p ≤ 0.05, **p ≤ 0.01 and ***p ≤ 0.001). Image adapted from (Henss et al., 2021).*

To examine the duration of SthK and bPAC induced neuronal hyperpolarization, swimming behaviour analysis was extended up to 240 s after light application. This demonstrated a long-lasting effect, and the swimming frequency began to increase again only after 90 – 150 s following the end of the light pulse (Figure 49). In sum, SthK and bPAC are able to hyperpolarize *C. elegans* cholinergic neurons, however, the reduction of the swimming cycles of the SthK and bPAC system was substantial in the dark, and thus this two-component optogenetic system appears to be of limited use in *C. elegans*.

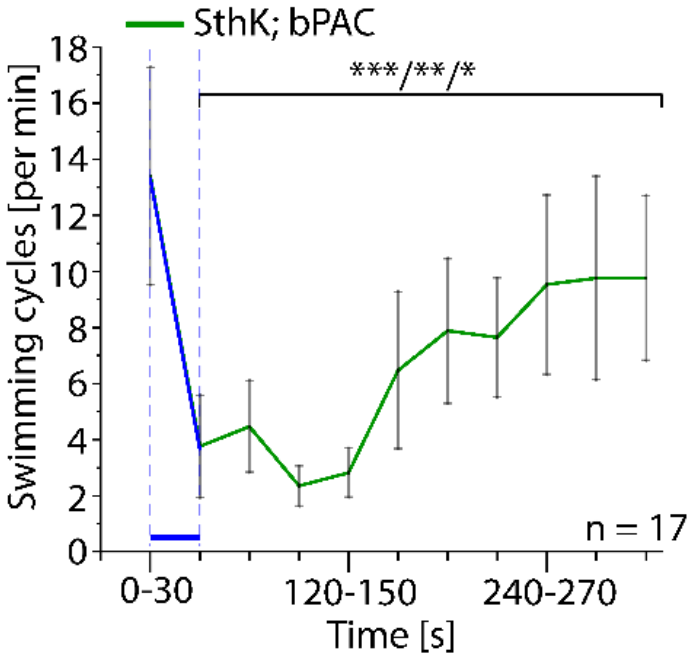

Figure 49: bPAC and SthK evoked arrest of swimming behaviour last up to 90 – 150 s. *Swimming frequencies ±SEM of animals, co-expressing SthK and bPAC in cholinergic neurons 30 s before and 270 s after 30 s light exposure (0.4 mW/mm^2; 470 nm). n = number of animals. Statistically significant differences: paired Student's t test (*p ≤ 0.05, **p ≤ 0.01 and ***p ≤ 0.001). Image adapted from (Henss et al., 2021).*

3.1.7. Membrane-bound photoactivatable adenylyl cyclases and the SthK CNGC for cell silencing

Due to the high sensitivity of the SthK channel and its activation at low cAMP levels, and bPACs dark activity and high magnitude of generated cAMP, SthK was combined with the engineered membrane-bound photoactivatable adenylyl cyclases. The hyperpolarizing potential and light control of these tool combinations were analysed in *C. elegans* muscle cells and cholinergic neurons.

3.1.7.1. Characterization of the membrane-bound photoactivatable adenylyl cyclase and SthK systems in body wall muscle cells

Because additional cAMP produced by bPAC in dark was too high to enable meaningful application of the SthK / bPAC system in *C. elegans*, the channel was combined with the engineered membrane-bound photoactivatable adenylyl cyclases to combine it with a less potent and completely dark-inactive photoactivatable

adenylyl cyclase. To assess and compare the SthK and membrane-bound photoactivatable adenylyl cyclase systems for their ability to hyperpolarize *C. elegans* muscle cells, equal amounts of plasmid DNA of the respective membrane-bound photoactivatable adenylyl cyclases were injected into the strain ZX2393 (*pmyo-3::SthK::SL2::GFP; pmyo-2::mCherry*) to ensure similar expression levels of SthK, and the strains were analysed via body length measurements. Light stimulation of SthK; BeCyclOp(A-2x) and SthK; BeCyclOp(A-3x) expressing animals increased the body length of about 3 and 5 % within ~1.5 s, respectively. The effects remained constant for SthK; BeCyclOp(A-2x) and decayed a few seconds after turning off light for SthK; BeCyclOp(A-3x). As control, the influence of light application on SthK; BeCyclOp(A-3x) expressing animals raised without ATR was examined, depicting no light dependent increase of the body length. No light triggered increase of the body length was detected for SthK; CaCyclOp(A-2x) expressing animals which could be explained by a weak expression, instable conformation and/or poor membrane targeting of CaCyclOp(A-2x) in *C. elegans*. SthK was also co-expressed with wild type BeCyclOp. Interestingly, illumination of these animals reduced the body length of about 2.5 % within 2.8 s, which was not observed in control animals, not supplemented with ATR (Figure 50 A, B). In sum, the systems SthK; BeCyclOp(A-2x) and SthK; BeCyclOp(A-3x) were able to hyperpolarize *C. elegans* muscle cells whereas the systems differ in the magnitude and the duration of the evoked effect. The reason could be a higher optogenetic cAMP production by BeCyclOp(A-2x) and a pre-activation of SthK due to additional cAMP produced by BeCyclOp(A-2x) in dark.

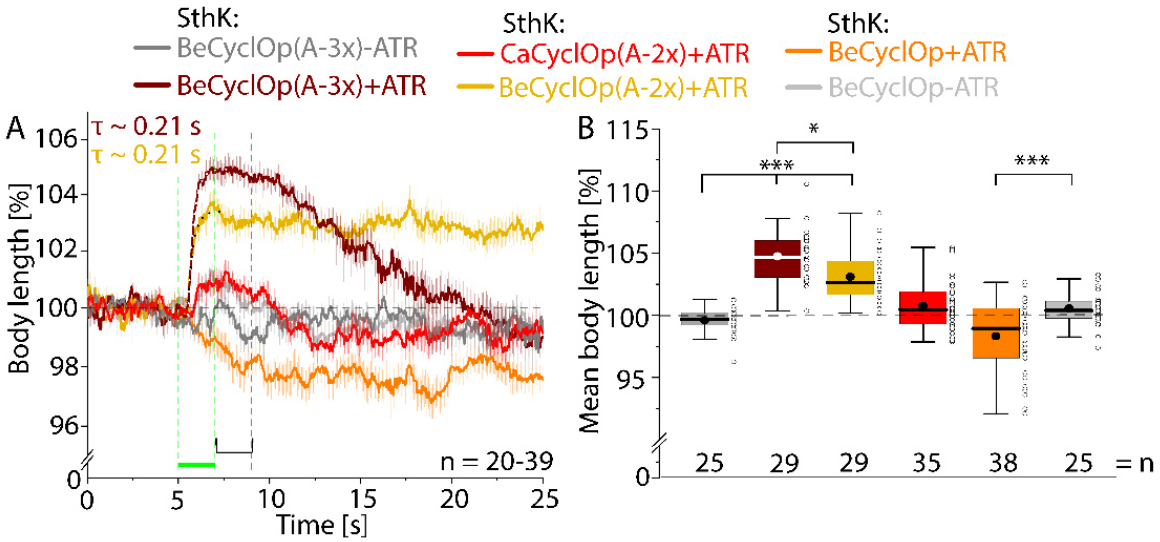

Figure 50: BeCyclOp(A-3x) and SthK induce a strong muscle hyperpolarization. *A) Body length analysis ±SEM of animals, co-expressing SthK and wild type BeCyclOp, BeCyclOp(A-2x), BeCyclOp(A-3x), or CaCyclOp(A-2x) in body wall muscle cells. Green bar indicates the period of illumination (0.9 mW/mm²; 535 nm). Mono-exponential decay fit (dotted lines) was used to determine onset-time constants (τ). B) Quantification of the mean normalized body lengths for the indicated time period (7 – 9 s). The interquartile range (IQR), median (–), mean values (●), individual measurements (o), and whiskers (1.5 * IQR) are depicted. n = number of animals. Statistically significant differences were determined using one-way ANOVA with Bonferroni correction (*p ≤ 0.05 and ***p ≤ 0.001). Image adapted from (Henss et al., 2021).*

To further characterize the systems in more detail and to investigate if co-expression of the tools impaired muscle physiology already in dark, an effect that is not measurable with body length measurements, analyses of swimming behaviour were performed. Here, animals co-expressing SthK and BeCyclOp(A-2x) depicted a high variability in their swimming rate, independent of the supplementation of ATR, which could be explained by a constitutive cAMP generation by the adenylyl cyclase domain, that is independent of light-regulation by the rhodopsin moiety. This effect was not detected for SthK; BeCyclOp(A-3x) expressing animals. In contrast to this, expression of SthK; CaCyclOp(A-2x) reduced the basal swimming rate in comparison to only SthK expressing animals (52 and 26 cycles per min, respectively). Light stimulation of SthK; BeCyclOp(A-2x) and SthK; BeCyclOp(A-3x) expressing animals decreased the swimming rates from 58 and 47 to 22 and 13 cycles per min, respectively. In case of the combination of SthK with wild type BeCyclOp, illumination caused an increase of the swimming frequency from 43 to 54 cycles per min (Figure 51). The reason could be that the SthK channel is preactivated by intracellular cAMP and that the cGMP generated upon activation of BeCyclOp could act either as an antagonist or as an agonist with low efficacy. In conclusion, the combination SthK

and BeCyclOp(A-3x) appears to be the most favourable tool for K^+-based silencing. However, expression of SthK alone reduced the basal swimming rates compared to the genetic background *lite-1(ce314)* (from 82 to 52 swimming cycles), suggesting that even in muscle cells intrinsic cAMP levels are sufficient to pre-activate the channel or that the channel is generally toxic, e.g., because of its tendency to form protein aggregates that induce endoplasmic reticulum stress.

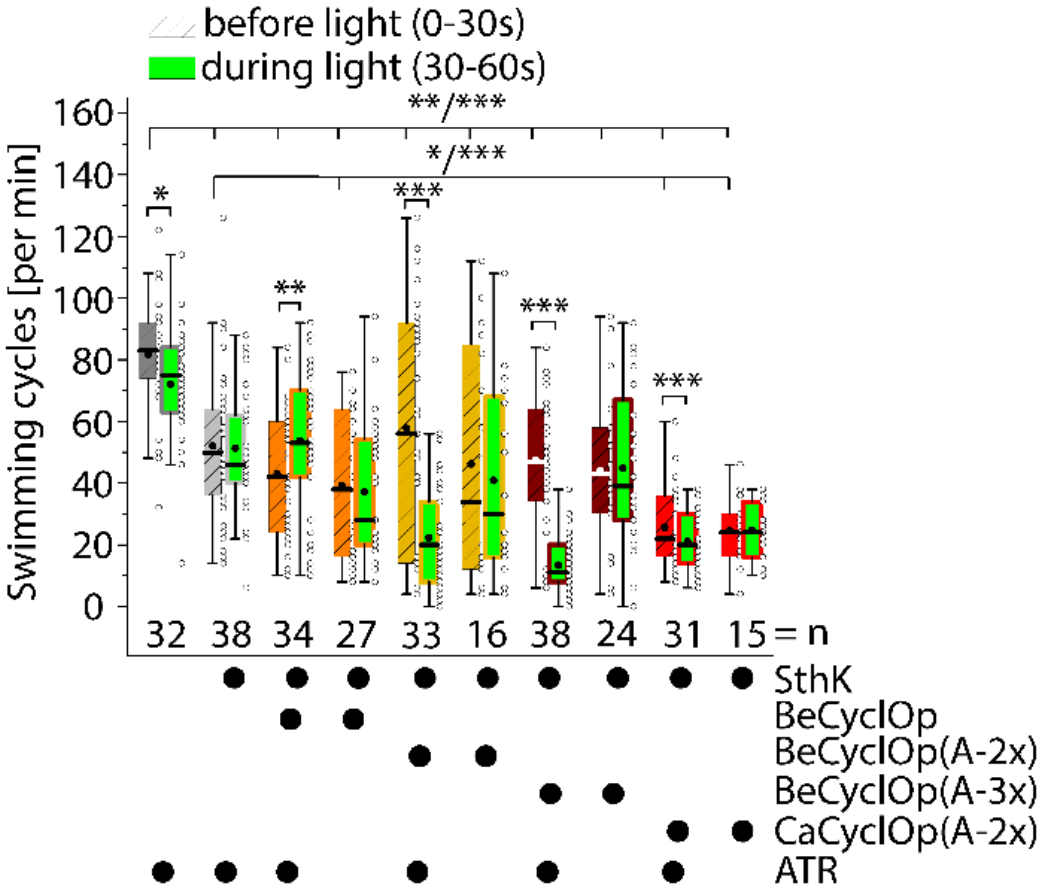

Figure 51: Co-expression of BeCyclOp(A-3x) causes no further pre-activation of SthK, and light stimulation strongly reduce the swimming rate. *Swimming frequencies ±SEM of animals, expressing the SthK channel alone or with wild type BeCyclOp, BeCyclOp(A-2x), BeCyclOp(A-3x), or CaCyclOp(A-2x) in body wall muscle cells, respectively, in the genetic background lite-1(ce314). As non-transgenic control the genetic background lite-1(ce314) was measured. Swimming rates were calculated 30 s before and 30 s during light application (1 mW/mm²; 535 nm). The interquartile range (IQR), median (–), mean values (●), individual measurements (o), and whiskers (1.5 * IQR) are illustrated. n = number of animals. Statistically significant differences: one-way ANOVA and Student's t test (*p ≤ 0.05, **p ≤ 0.01 and ***p ≤ 0.001). Image adapted from (Henss et al., 2021).*

3.1.7.2. Application of the membrane-bound photoactivatable adenylyl cyclase and SthK systems in cholinergic motor neurons

Since the systems SthK; BeCyclOp(A-2x) and SthK; BeCyclOp(A-3x) successfully hyperpolarized *C. elegans* muscle cells, and the reduction of the swimming frequency was negligible in the dark, both systems were further investigated for their effects on cell physiology and their potential to hyperpolarize cholinergic motor neurons of *C. elegans* via swimming behavioural analysis. In this context, it was not possible to obtain membrane-bound photoactivatable adenylyl cyclase and SthK co-expressing transgenes using the same SthK expression level as for SthK; bPAC. Consequently, the expression level of SthK was decreased and varied for both membrane-bound photoactivatable adenylyl cyclases. However, all transgenes caused a reduction of the basal swimming frequency in comparison to the genetic background *lite-1(ce314)* (25 – 38 vs 70 cycles per min) (Figure 52 A). Illumination of these animals decreased the swimming cycles to about 8 – 23 cycles per min. After the end of the light application, swimming frequency raised again to initial levels (Figure 52 B).

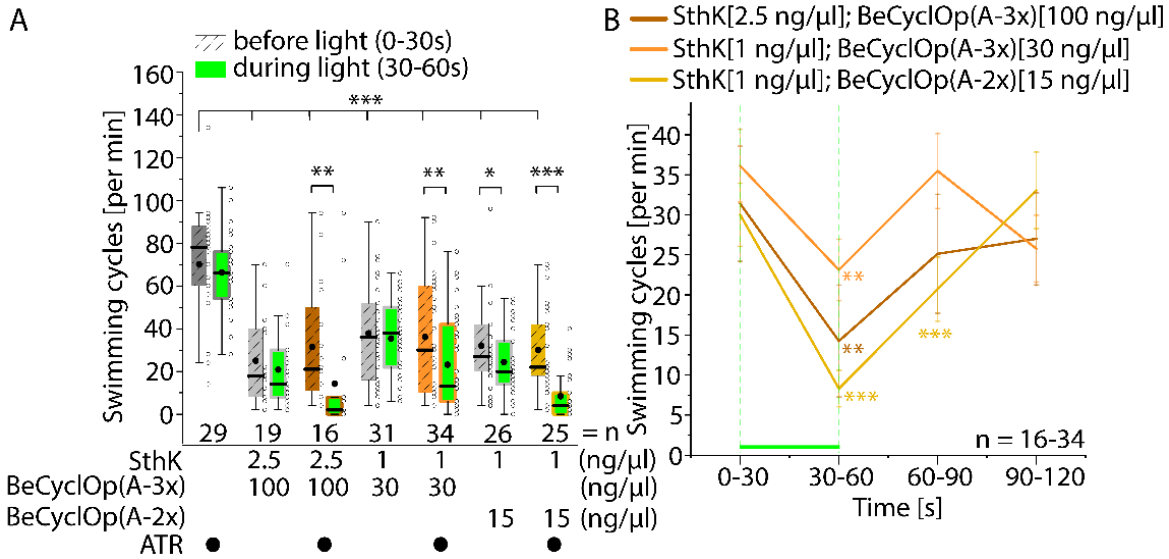

Figure 52: Membrane-bound photoactivatable adenylyl cyclase and SthK co-expression in cholinergic neurons reduce basal swimming rate, and illumination triggered a robust decrease of the swimming cycles, increasing again after turning off light. *A) Swimming cycles ±SEM of animals, co-expressing the SthK channel and BeCyclOp(A-3x) or BeCyclOp(A-2x) in cholinergic neurons, and the genetic background lite-1(ce314). Swimming rates were calculated 30 s before and 30 s during light exposure (1.35 mW/mm²; 535 nm). Transgenic strains were created using different amounts of plasmid DNA (indicated by ng/µl). The interquartile range (IQR), median (–), mean values (●), individual measurements (o), and whiskers (1.5 * IQR) are shown. B) Swimming frequencies ±SEM of animals in A, 30 s before and 60 s after a 30 s light application (1.35 mW/mm²; 535 nm). n = number of animals. Statistically significant differences: one-way ANOVA and Student's t test (*p ≤ 0.05, **p ≤ 0.01 and ***p ≤ 0.001). Image adapted from (Henss et al., 2021).*

In an attempt to further optimize the SthK and membrane-bound photoactivatable adenylyl cyclase system, YFP-BeCyclOp(A-2x) was co-expressed with low levels of SthK. Here, it was possible to restore the basal swimming cycles of the transgenic animals to that of the genetic background (*lite-1(ce314)*), however, no light evoked reduction of the swimming rate was observed (Figure 53 A, B). In conclusion, SthK and membrane-bound photoactivatable adenylyl cyclases are able to hyperpolarize cholinergic neurons, however, they also effect the neuronal physiology, most likely due to basal generated cAMP already activating a highly conductive SthK channel even at very low expression levels.

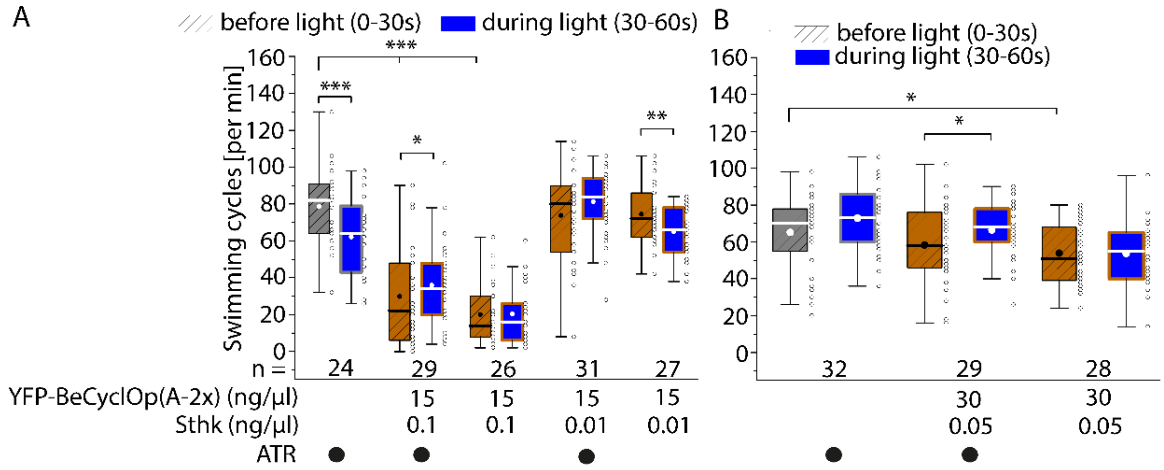

Figure 53: Titration of YFP-BeCyclOp(A-2x) and SthK expression levels did not optimize the system. *A-B) Swimming rates ±SEM of animals, co-expressing the SthK channel and YFP-BeCyclOp(A-2x) in cholinergic neurons, and the genetic background lite-1(ce314). Swimming cycles were calculated 30 s before and 30 s during light exposure (0.4 mW/mm^2; 470 nm). Transgenic strains were created using different amounts of plasmid DNA (indicated by ng/µl). The interquartile range (IQR), median (–), mean values (●), individual measurements (o), and whiskers (1.5 * IQR) are depicted. n = number of animals. Statistically significant differences were determined using one-way ANOVA and Student's t test (*p ≤ 0.05, **p ≤ 0.01 and ***p ≤ 0.001). Image adapted from (Henss et al., 2021).*

3.2. BeCyclOp purification

At the beginning of this study, full length BeCyclOp was poorly characterized by *in vitro* experiments and spectroscopy analyses. Until now, no full-length protein structure of BeCyclOp has been determined, although very recent work based on *AlphaFold2* provides a potentially useful model of CaCyclOp (Fischer *et al.*, 2021). To this end, BeCyclOp and a stabilized BeCyclOp dimer (concatamer; two covalently linked monomers) should be purified to enable molecular characterization and structural

analysis of BeCyclOp. The strategy of choice was to express C-terminally TAP-tagged BeCyclOp monomer as well as a concatamer of BeCyclOp-BeCyclOp-TAP in *C. elegans* muscle cells and to purify the proteins using tandem affinity purification.

3.2.1. Purification of BeCyclOp monomer

In my MSc thesis, I confirmed the expression of BeCyclOp::TAP and could isolate the protein out of solubilizate (Triton X-100 was used as detergent). Further, functionality analysis showed no major impact of the C-terminal TAP-tag on light-activated guanylyl cyclase activity.

3.2.1.1. Detergent screening for BeCyclOp solubilization

To evaluate and improve BeCyclOp solubilization, a detergent screen was executed. For this purpose, worm homogenate of a non-integrated BeCyclOp::TAP expressing strain was utilized, using the following detergents: Dodecylmaltoside (DDM), Decylmaltoside (DM), Octylglucoside (OG), Dimethyldodecylamine N-oxide (LDAO), Octylthioglucoside (OTG), Triton X-100 and Tween-20. To assess BeCyclOp::TAP solubility, the protein was precipitated out of the solubilizates using IgG-agarose and analysed via SDS-PAGE and western blot analysis. Here, the highest amount of solubilized BeCyclOp was obtained with Triton X-100 (22 a.u.), whereas comparable amounts were achieved with the detergents DDM, DM, OG, LDAO and Tween-20 (2.2 – 6.4 a.u.). In contrast to this, no solubilized BeCyclOp::TAP was detected for OTG (Figure 54 A, B). Thus, Triton X-100 achieved the highest solubility of BeCyclOp::TAP.

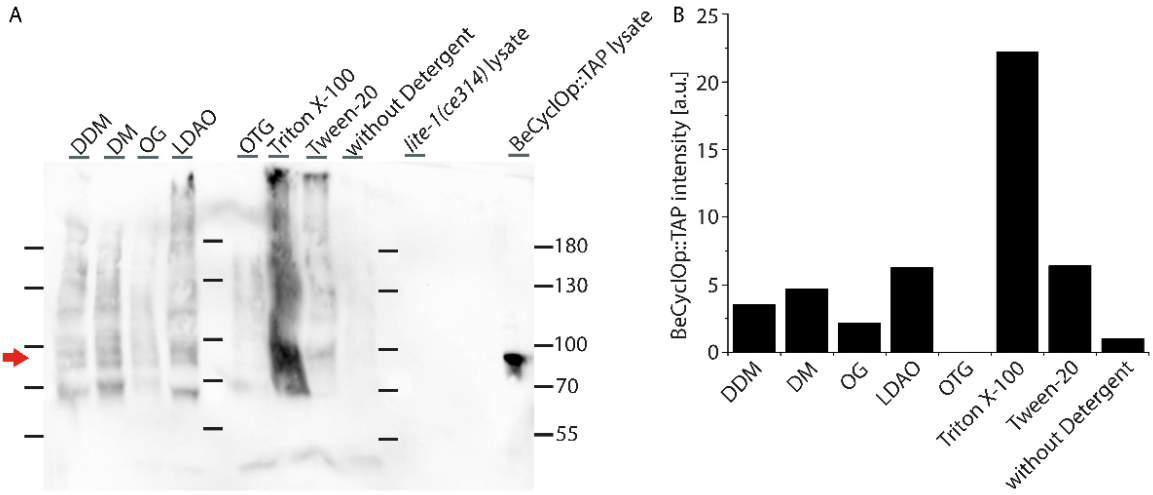

Figure 54: Triton X-100 achieves highest amount of solubilized BeCyclOp::TAP. *A) Western blot analysis after detergent screening for BeCyclOp solubilization (PAP 1:1000). As detergents, DDM, DM, OG, LDAO, OTG, Triton X-100 and Tween-20 were utilized. Lysate of the genetic background lite-1(ce314) was used as negative control, and lysate of BeCyclOp::TAP expressing animals as positive control. The red arrow at around 88 kDa reflects BeCyclOp::TAP. B) Quantification of the BeCyclOp::TAP intensities in A. For determination of the BeCyclOp::TAP intensities, the protein bands at around 88 kDa were analysed.*

3.2.1.2. Tandem affinity precipitation analysis using BeCyclOp solubilizates

After successful solubilization of BeCyclOp::TAP with various detergents, new BeCyclOp::TAP solubilizates using worm powder of a non-integrated strain (DDM, LDAO, OG, Triton X-100 as detergents) were prepared and used for tandem affinity precipitation analysis. In this context, the individual steps or both precipitation schemes were executed and assessed regarding successful binding of BeCyclOp::TAP to, and elution from, the affinity columns. Regarding the first precipitation step, the binding of IgG-Agarose to the ProtA portion of the TAP-tag, BeCyclOp::TAP was detected in the IgG-Agarose containing fraction (P) of LDAO and OG solubilizates, but not in the elution fractions (E). Elution was performed for 3 h at 4°C using 10 U TEV protease. No isolated BeCyclOp::TAP was detected in solubilizates using the detergents DDM and Triton X-100 (Figure 55).

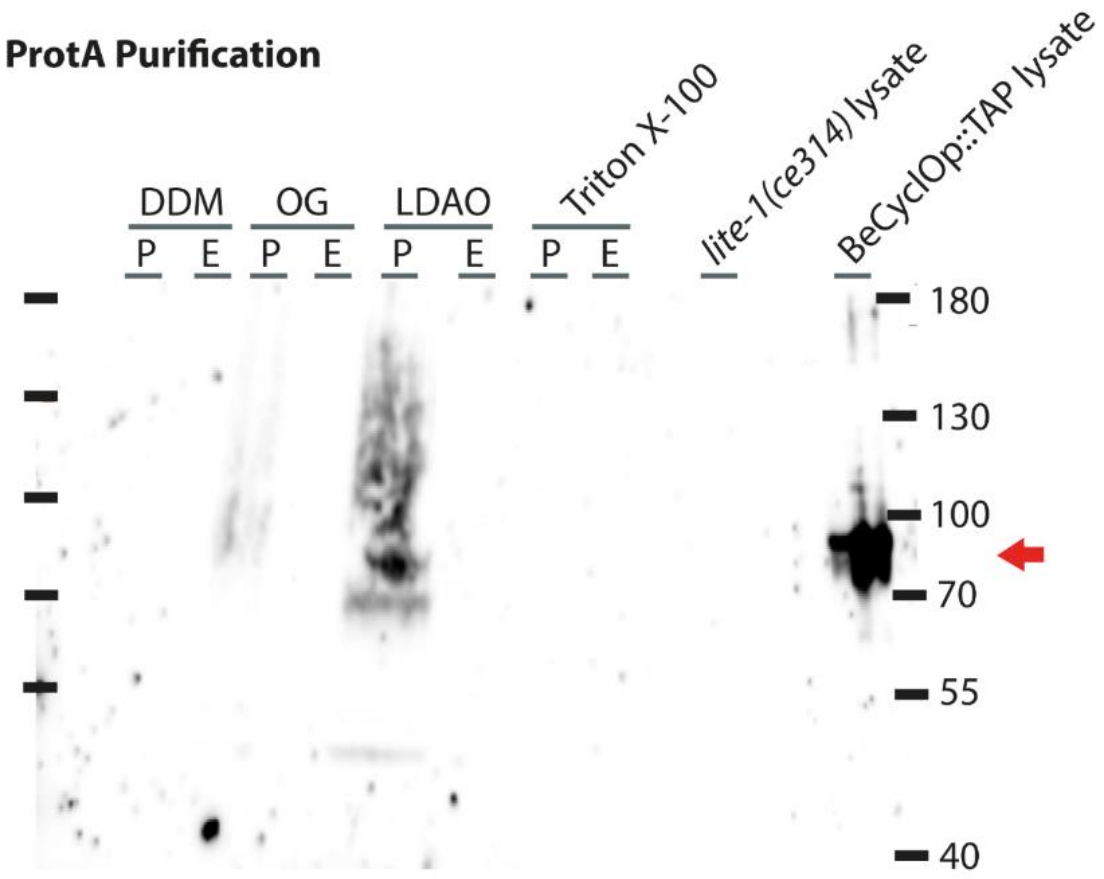

Figure 55: IgG-Agarose precipitates BeCyclOp::TAP out of LDAO and OG solubilizates. *ProtA affinity precipitation of BeCyclOp::TAP out of BeCyclOp solubilizates (anti-TAP 1:1000). BeCyclOp::TAP was solubilized with either DDM, OG, LDAO or Triton X-100. E = Eluate after TEV-cleavage and centrifugation, P = IgG-Agarose beads. As controls, proteins of the genetic background lite-1(ce314) and of BeCyclOp::TAP expressing animals were applied. The red arrow at around 88 kDa reflects BeCyclOp::TAP.*

To test the prospective second precipitation step, Calmodulin-Agarose should bind to the CBP of the TAP-tag. Here, BeCyclOp::TAP was detected in the Calmodulin-Agarose precipitate (P) of Triton X-100, LDAO, OG and DDM solubilizates, whereas the strongest signal was determined for Triton X-100. Further, eluted BeCyclOp::TAP was verified in the elution fractions (E) of Triton X-100 and LDAO samples, but not in the DDM and OG samples (Figure 56). Elution was performed using 2 mM of the Ca^{2+} chelator EGTA.

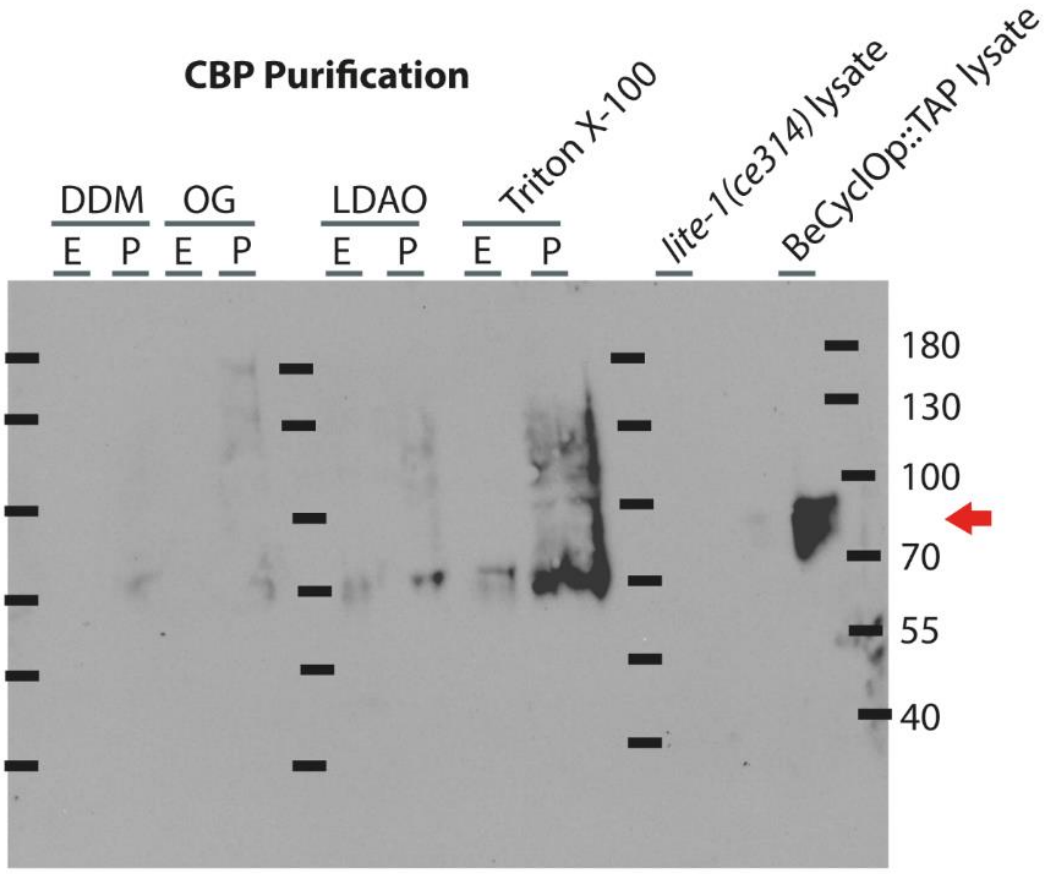

Figure 56: Calmodulin-agarose precipitates BeCyclOp::TAP out of Triton X-100, LDAO, OG and DDM solubilizates. *Calmodulin binding peptide (CBP) affinity precipitation of BeCyclOp::TAP out of BeCyclOp solubilizates (PAP 1:1000). BeCyclOp::TAP was solubilized with either DDM, OG, LDAO or Triton X-100. E = Eluate after CBP elution and centrifugation, P = Calmodulin-Agarose beads. Lysates of the genetic background lite-1(ce314) and of BeCyclOp::TAP expressing animals were used as controls. The red arrow at around 88 kDa reflects BeCyclOp::TAP.*

In order to precipitate BeCyclOp::TAP by sequential execution of both tandem affinity precipitation steps, no signal for BeCyclOp::TAP was detected in any sample (Figure 57). In conclusion, IgG-Agarose precipitates BeCyclOp out of LDAO and OG solubilizates, but elution via TEV protease cleavage failed. Further, Calmodulin-Agarose precipitates BeCyclOp::TAP out of all analysed samples, and successful elution of BeCyclOp::TAP was verified for Triton X-100 and LDAO samples.

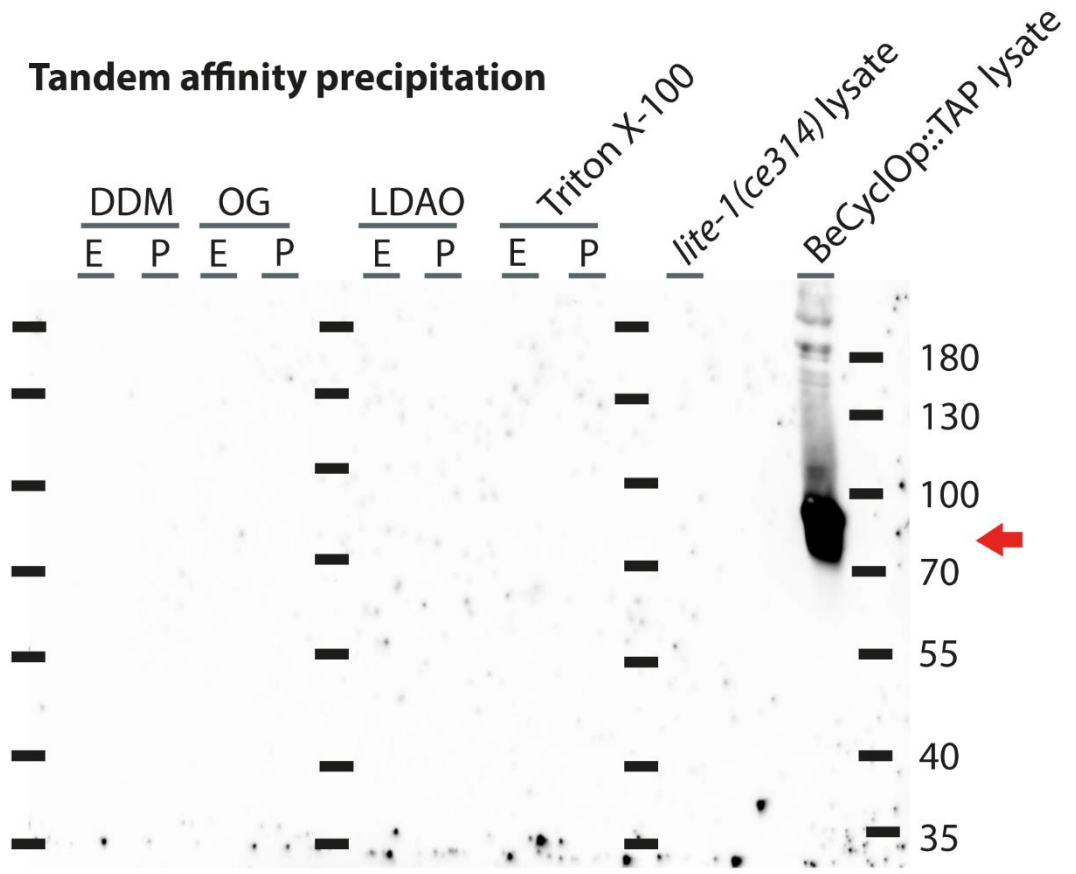

Figure 57: Tandem affinity precipitation test depicts no signal for BeCyclOp::TAP. *Tandem affinity precipitation of BeCyclOp::TAP out of BeCyclOp solubilizates (anti-TAP 1:1000). BeCyclOp::TAP was solubilized with either DDM, OG, LDAO or Triton X-100. E = Eluate after CBP elution and centrifugation, P = Calmodulin-Agarose beads. As controls, proteins of the genetic background lite-1(ce314) and of BeCyclOp::TAP expressing animals were applied. The red arrow at around 88 kDa indicates BeCyclOp::TAP.*

3.2.1.3. TEV protease cleavage analysis

To assess cleavage of the TAP-tag at the TEV-cleavage site via TEV protease, a TEV protease cleavage test was performed. For this purpose, BeCyclOp::TAP solubilizates (Triton X-100 as detergent) using worm powder of a non-integrated strain were prepared, and the protein was precipitated via IgG-Agarose beads. Next, 3 aliquots were prepared and incubated with (2 aliquots) and without (1 aliquot) TEV protease (25 U TEV protease for 2 h at 4 °C). One TEV protease containing sample was applied on a chromatography column and the eluate was collected. From this aliquot, the IgG-Agarose-beads and the eluate were used for subsequent analysis. Samples were analysed via SDS-PAGE and western blotting, then the PAP soluble antibody complex was utilized for detection of uncleaved BeCyclOp::TAP, and the

anti-TAP antibody for cleaved BeCyclOp::TAP. Successfully cleaved BeCyclOp::TAP was verified in both TEV protease containing samples (Figure 58 A, B). Thus, TEV protease cleaves the TAP-tag at the TEV cleavage site.

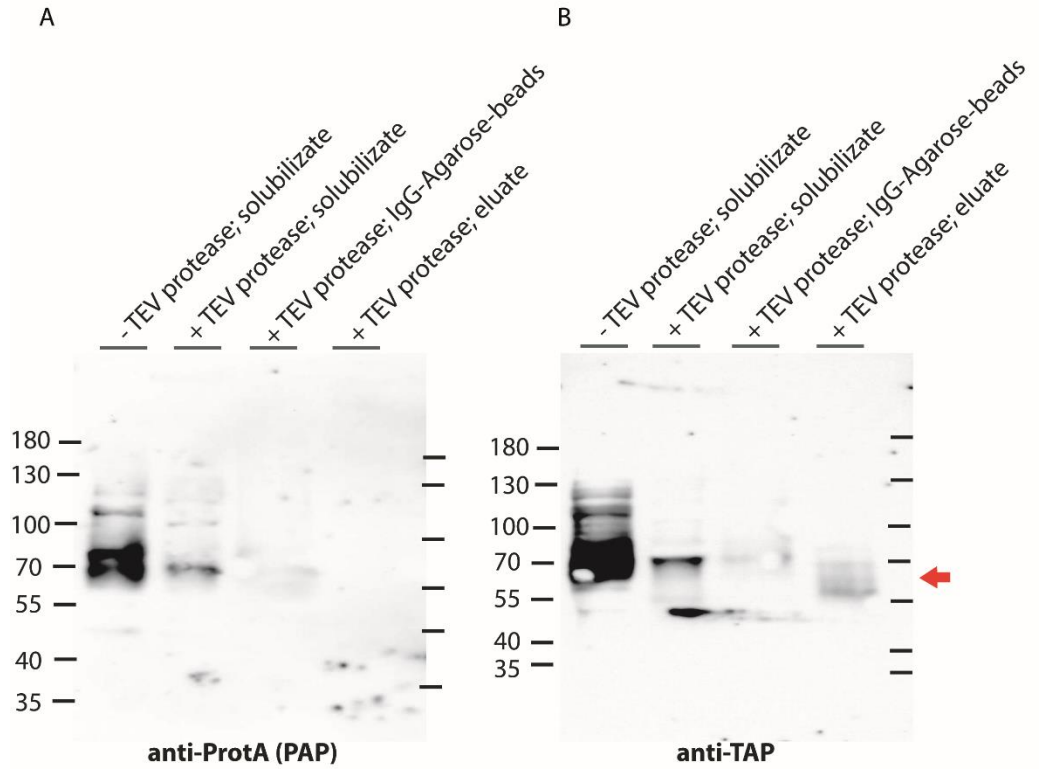

Figure 58: TEV cleavage test shows successful cleavage of the TAP-tag through the TEV protease. *Western Blot analysis to verify TEV cleavage. A) Uncleaved BeCyclOp::TAP was detected using peroxidase-anti-peroxidase (PAP), and B) cleaved BeCyclOp::TAP using anti-TAP antibody. The red arrow at around 60 kDa indicates cleaved BeCyclOp::TAP.*

3.2.1.4. Tandem affinity purification of BeCyclOp

To enable purification of BeCyclOp::TAP out of *C. elegans* muscle cells, the transgene was integrated into the *C. elegans* genome via UV irradiation and backcrossed 5 times. Gene expression of BeCyclOp::TAP was verified via SDS-PAGE and western blot analysis after fast protein extraction from *C. elegans* (Figure 59).

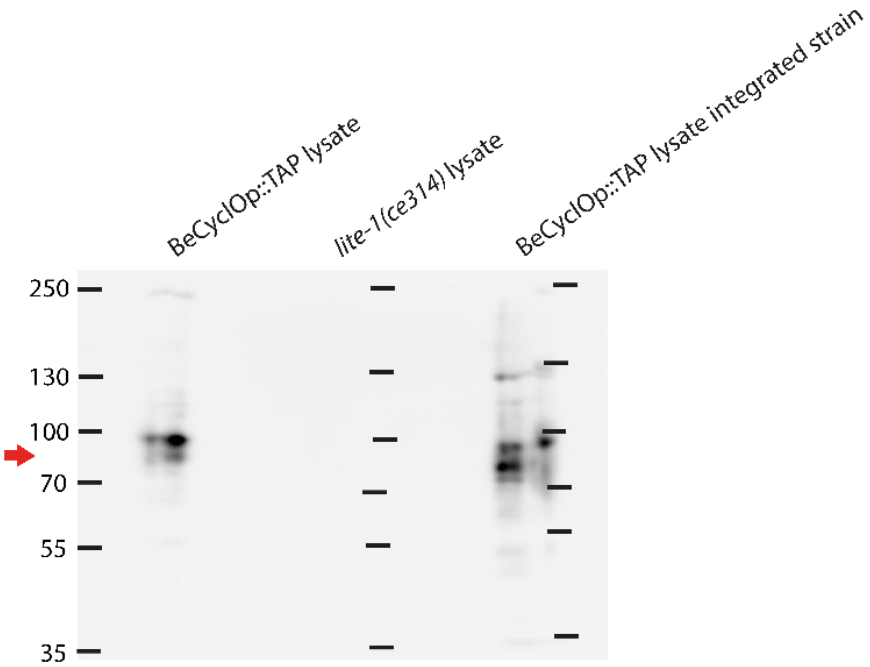

Figure 59: Confirmation of BeCyclOp::TAP expression after integration in C. elegans genome. *Western blot analysis after fast protein extraction from C. elegans (PAP 1:1000). BeCyclOp::TAP transgene was integrated into the C. elegans genome via UV irradiation. Lysates of the genetic background lite-1(ce314) and of BeCyclOp::TAP expressing animals were used as controls. The red arrow at around 88 kDa indicates BeCyclOp::TAP.*

Next, the integrated strain was cultivated on egg plates to obtain sufficient amounts of worms for subsequent tandem affinity purification of BeCyclOp::TAP. For protein solubilization, Triton X-100 was chosen as detergent since it depicted the highest solubility for BeCyclOp::TAP. Purification samples were analysed via SDS-PAGE and western blot analysis. Here, a high amount of BeCyclOp::TAP was detected in the worm lysate, however, it was not possible to isolate BeCyclOp::TAP in high amounts out of the solubilizate via IgG-Agarose, indicated by a high signal of BeCyclOp::TAP in the IgG-Agarose flow-through (Figure 60).

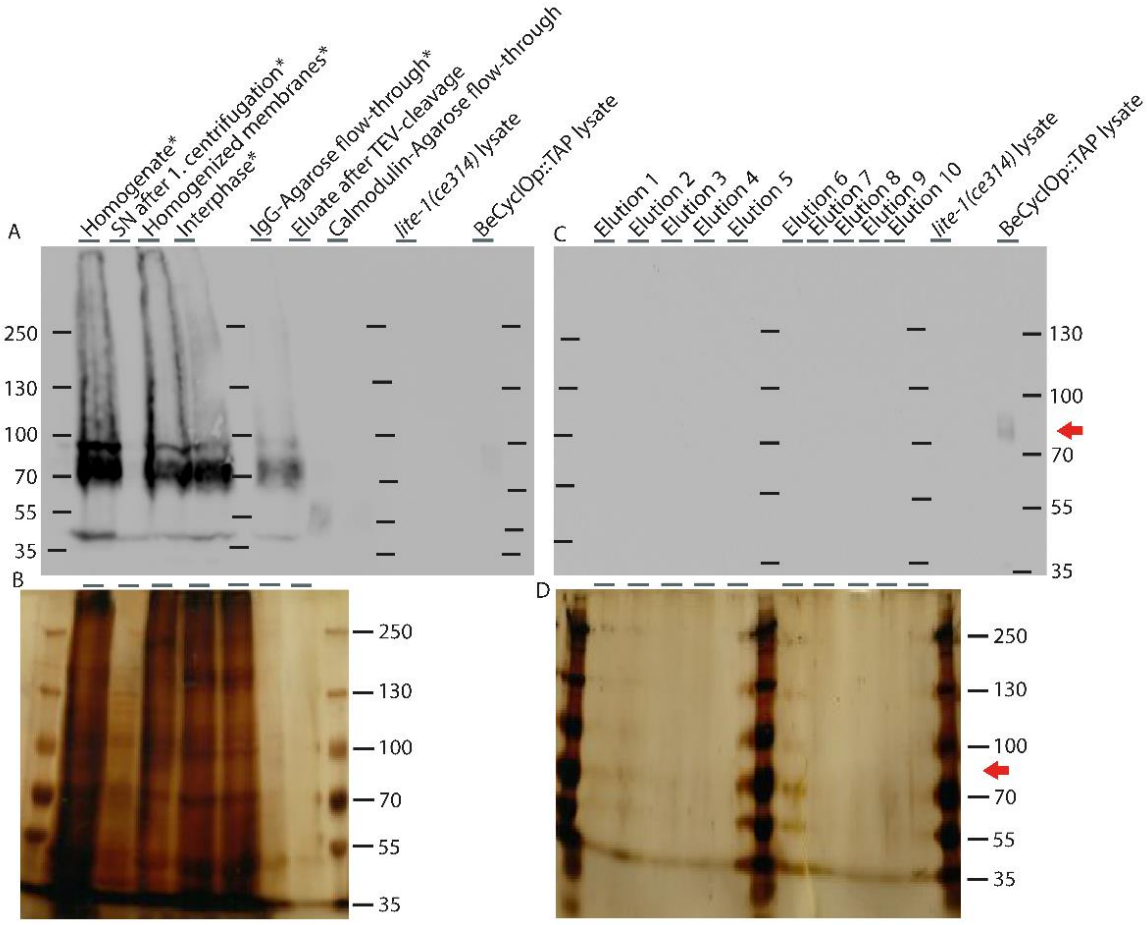

Figure 60: Tandem affinity purification exhibits strong signal of BeCyclOp::TAP in IgG-agarose flow through. *Western blot analysis and silver staining of A, B) tandem affinity purification samples and C, D) elution fractions of BeCyclOp::TAP purification (anti-TAP 1:1000). * indicates application of 60 µg protein per sample. As controls, proteins of the genetic background lite-1(ce314) and of BeCyclOp::TAP expressing animals were applied. The red arrow at around 88 kDa indicates BeCyclOp::TAP.*

Since binding of solubilized BeCyclOp::TAP to IgG-Agarose was inefficient, tandem affinity purification of BeCyclOp was repeated with following change: a dialysis step of the solubilizate was executed to reduce the Triton X-100 concentration in the sample, which may interfere on IgG-Agarose ProtA binding. Western blot analysis of the purification samples revealed no obvious presence of BeCyclOp::TAP in the IgG-Agarose flow through, however, no BeCyclOp::TAP could be detected in the TEV eluate and subsequent elution fractions (Figure 61).

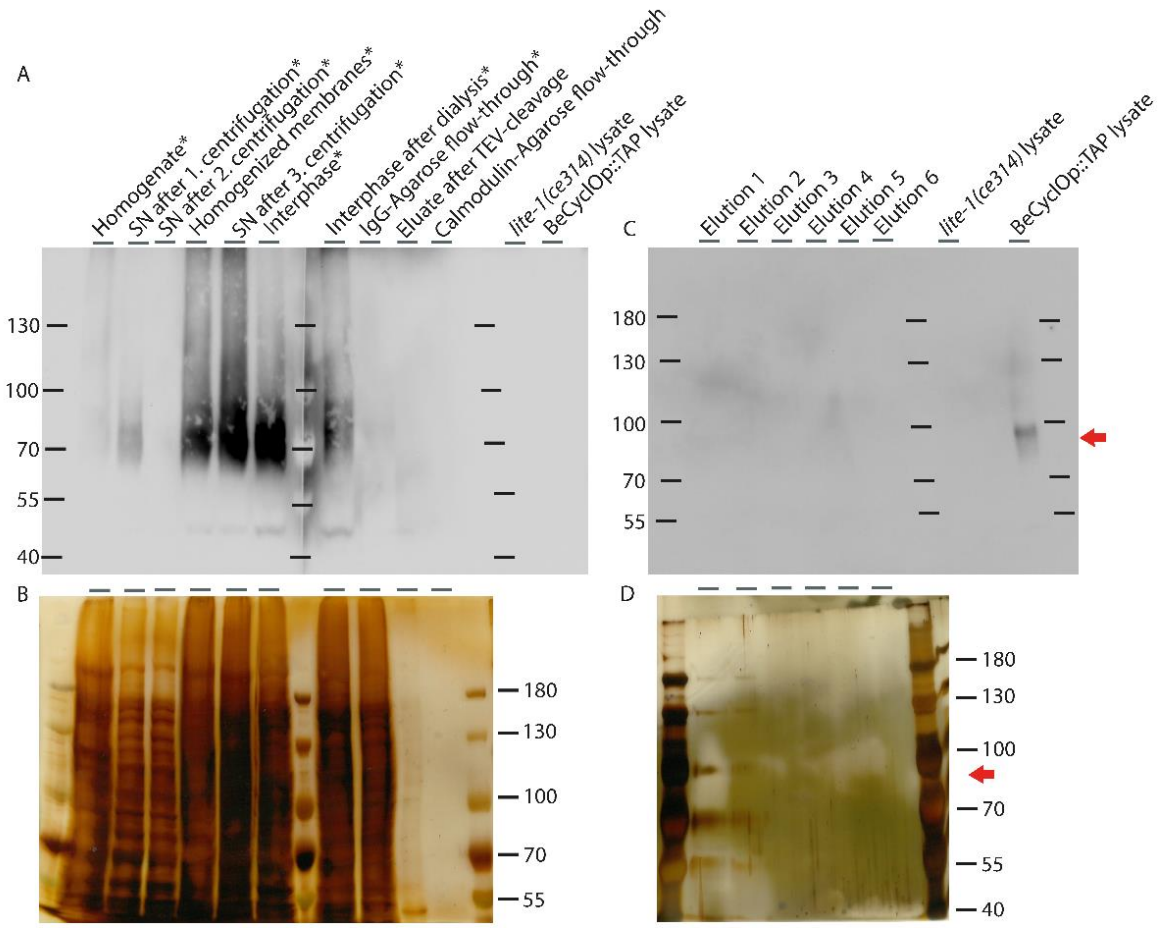

Figure 61: Addition of dialysis step strongly reduced BeCyclOp::TAP content in IgG-Agarose flow through. *Western blot analysis and silver staining of A, B) tandem affinity purification samples and C, D) elution fractions of BeCyclOp::TAP purification (anti-TAP 1:1000). * indicates application of 60 µg protein per sample. Lysates of the genetic background lite-1(ce314) and of BeCyclOp::TAP expressing animals were used as controls. The red arrow at around 88 kDa indicates BeCyclOp::TAP.*

In order to investigate a possible BeCyclOp::TAP precipitation due to dialysis accompanied by a reduction of the Triton X-100 concentration from 1 to 0.05 %, the dialyzed solubilized BeCyclOp::TAP interphase was centrifuged, and the resulting pellet and the supernatant were analysed via SDS-PAGE and western blot analysis. Here, BeCyclOp::TAP was detected in both fractions, indicating a partially precipitation of BeCyclOp::TAP due to reduction of the Triton X-100 concentration (Figure 62). Thus, binding of IgG-Agarose to ProtA is impaired by Triton X-100, and a reduction of the Triton X-100 concentration in BeCyclOp::TAP solubilizates caused partially the precipitation of the protein.

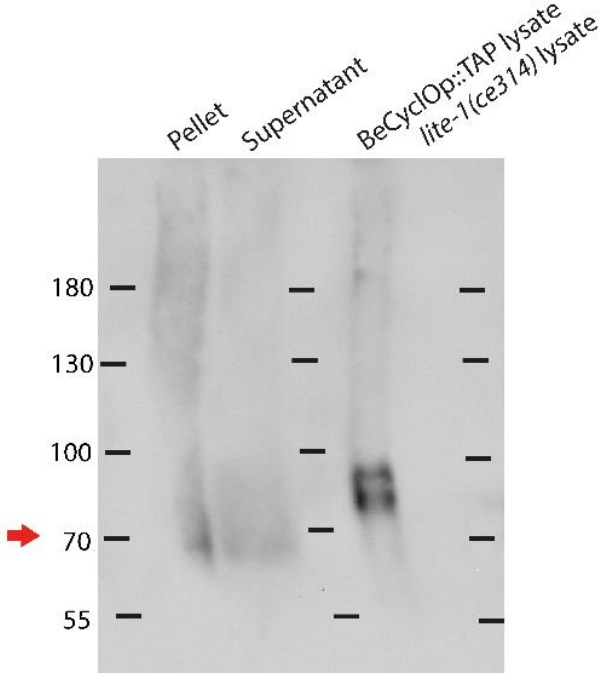

Figure 62: BeCyclOp::TAP partially precipitates after dialysis. *Western blot analysis of solubilized BeCyclOp::TAP after dialysis, centrifuged for 17000 g for 10 min, thus separated into pellet (P) and supernatant (SN) fraction (anti-TAP 1:1000). Lysates of the genetic background lite-1(ce314) and of BeCyclOp::TAP expressing animals were used as controls. The red arrow at around 70 kDa indicates BeCyclOp::TAP.*

3.2.2. BeCyclOp concatamer purification

To enable structural analysis of BeCyclOp, a stabilized dimer (concatamer) should be expressed in *C. elegans* muscle cells and purified using tandem affinity purification.

3.2.2.1. Gene expression analysis

For generation of a BeCyclOp concatamer and expression in muscle cells via the *myo-3* promoter, Gibson assembly was performed to covalently link two BeCyclOp monomers, separated by an $(GGGGS)_4$-linker, and C-terminally fused to a TAP-tag. Strains were generated by injection of various plasmid concentrations (15, 50, 100 ng/µl) into *lite-1(ce314)*, or for functional analysis into ZX1741 (expresses TAX-2/-4 in body wall muscle cells). To analyse expression of the BeCyclOp concatamer in the generated strains, gene expression was analysed via SDS-PAGE and western blot analysis after fast protein extraction from *C. elegans*. Here, strains expressing either BeCyclOp concatamer, BeCyclOp monomer or a mixture of both were identified, and three strains were selected for subsequent functionality analysis (Figure 63). These

strains were selected for subsequent functionality analysis as they exhibited no or minor expression of by-products that may influence the behavioural output of the body length measurement, albeit the strains contained a low expression level of the concatamer.

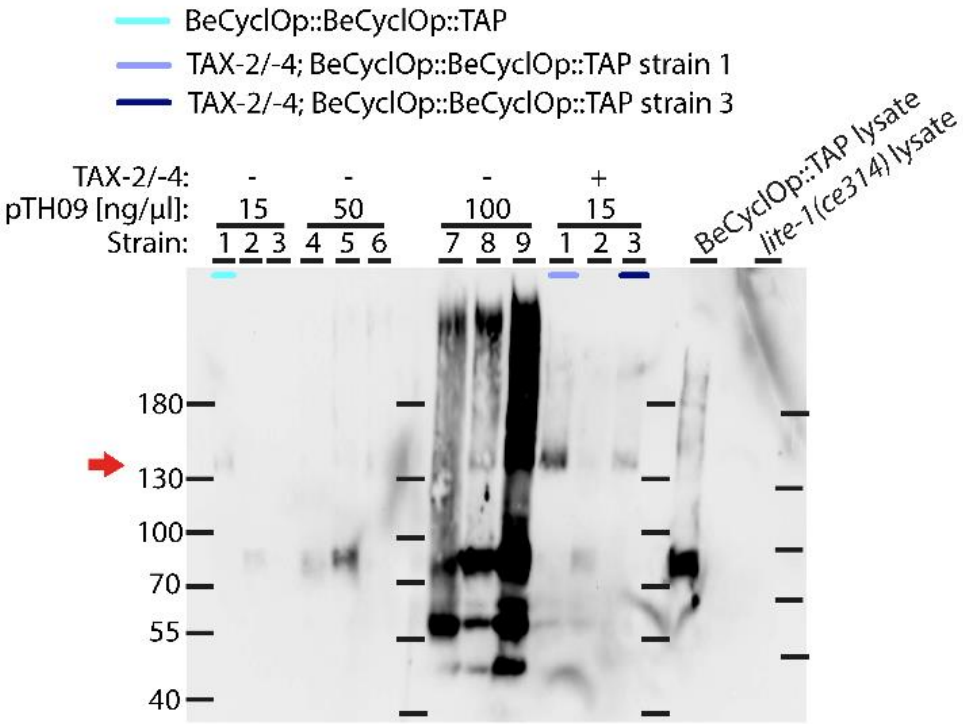

Figure 63: BeCyclOp Concatamer is expressed in C. elegans muscle cells. *Western blot analysis after fast protein extraction from C. elegans (PAP 1:1000). Strains were generated using different amounts (15, 50 and 100 ng/µl) of pTH09, injected into the genetic background lite-1(ce314) (- TAX-2/-4) or into ZX7141 (+ TAX-2/-4).* Coloured *strains were selected for subsequent functionality analysis and integration of the transgene into the genome. As controls, proteins of the genetic background lite-1(ce314) and of BeCyclOp::TAP expressing animals were applied. The red arrow at around 156 kDa indicates BeCyclOp Concatamer.*

3.2.2.2. Concatamer functionality analysis

To evaluate the functionality of the engineered BeCyclOp concatamer, body length measurements were performed and compared to TAX-2/-4; BeCyclOp expressing animals. Two TAX-2/-4; Concatamer expressing strains were selected for functional analysis to investigate light evoked cGMP production by BeCyclOp concatamer in more detail. Here, both strains depicted light evoked body contractions of about 4 – 6 % within 1 s, which relaxed to about 2 % within 7.5 s after turning off light. However, they did not reach the extent evoked by wild type BeCyclOp and TAX-2/-4, which could be due to a lower expression level of the concatamer or a negative influence of the linker on light-induced conformational changes of the N- and C-terminal domains.

No body reductions were observed in control animals, expressing only BeCyclOp concatamer or TAX-2/-4, the genetic background *lite-1(ce314)*, or TAX-2/-4; concatamer expressing animals raised without ATR (Figure 64 A-D). Although statistical analysis was not performed because of the small number of animals measured, the BeCyclOp concatamer appears to be functional, and covalent linkage of both monomers had no major negative impact on light dependent guanylyl cyclase activity.

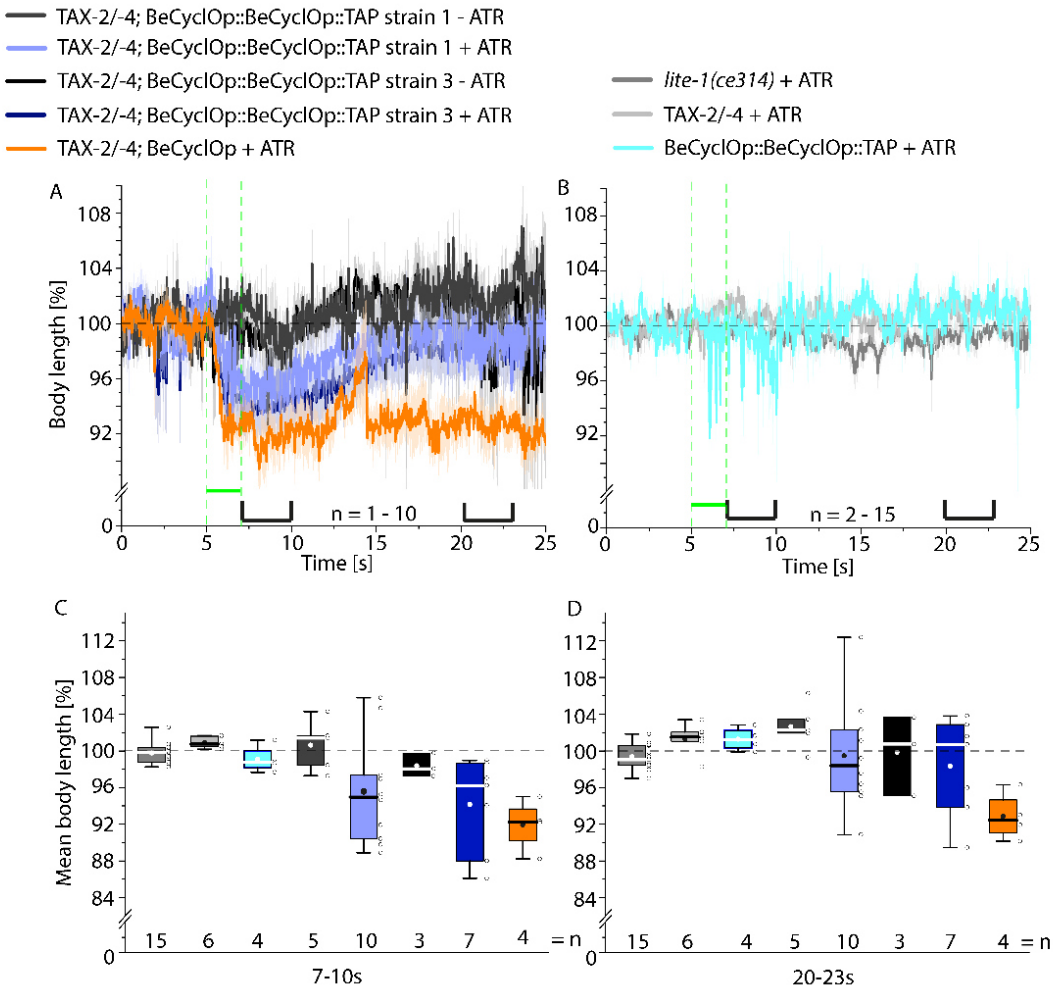

Figure 64: BeCyclOp concatamer is functional, though not reaching the same level of activity as the BeCyclOp monomer. *Body length measurements ±SEM of animals, A) co-expressing TAX-2/-4 and BeCyclOp concatamer or BeCyclOp::TAP, or B) only expressing TAX-2/-4 or BeCyclOp concatamer in body wall muscle cells, and the genetic background lite-1(ce314). Animals were raised with (+) or without (-) ATR. Green bar indicates the period of illumination (0.9 mW/mm²; 535 nm). Quantification of the mean normalized body lengths for the indicated time periods C) (7 – 9 s) and D) (20 – 23 s). The interquartile range (IQR), median (–), mean values (●), individual measurements (o), and whiskers (1.5 * IQR) are shown. n = number of animals.*

To enable tandem affinity purification of the BeCyclOp concatamer, the transgene was integrated into the *C. elegans* genome via UV irradiation and backcrossed 5x

times. Gene expression of BeCyclOp concatamer was verified via SDS-PAGE and western blot analysis after fast protein extraction from *C. elegans* (Figure 65).

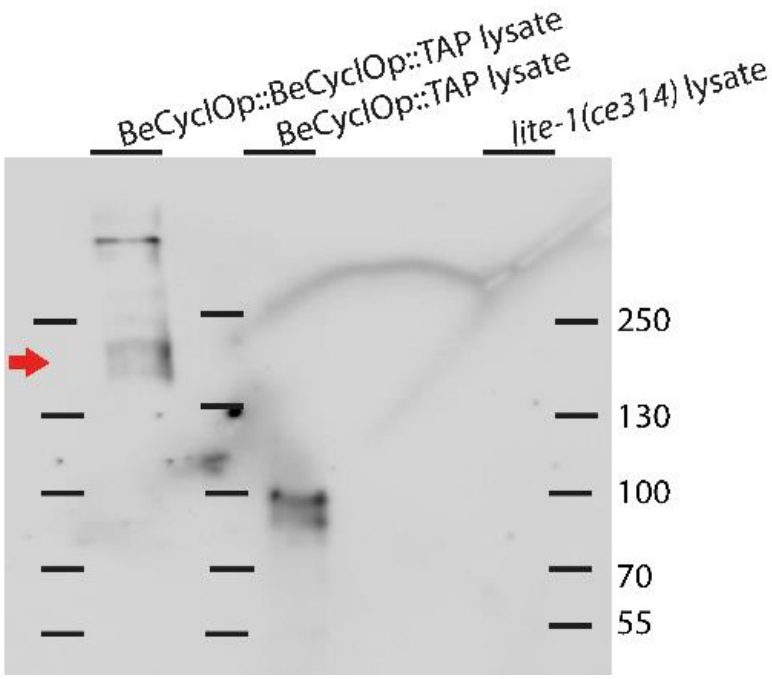

Figure 65: Confirmation of BeCyclOp concatamer expression after integration in C. elegans genome. *Western blot analysis after fast protein extraction from C. elegans (PAP 1:1000). BeCyclOp concatamer transgene was integrated into the C. elegans genome via UV irradiation. Lysates of the genetic background lite-1(ce314) and of BeCyclOp::TAP expressing animals were used as controls. The red arrow at around 156 kDa indicates BeCyclOp Concatamer.*

3.2.2.3. Tandem affinity purification of BeCyclOp Concatamer

Next, the large-scale breeding of the integrated strain on egg plates was performed, followed by tandem affinity purification of BeCyclOp concatamer. For protein solubilization, Triton X-100 was chosen as detergent since it depicts the highest solubility for BeCyclOp monomer. Purification samples were analysed via SDS-PAGE and western blot analysis. Unfortunately, BeCyclOp concatamer was cleaved into monomers during homogenization of the worm lysate, indicated by the BeCyclOp::TAP signal in the homogenate sample (Figure 66). Thus, BeCyclOp concatamer is cleaved by proteases during homogenization of *C. elegans* membranes.

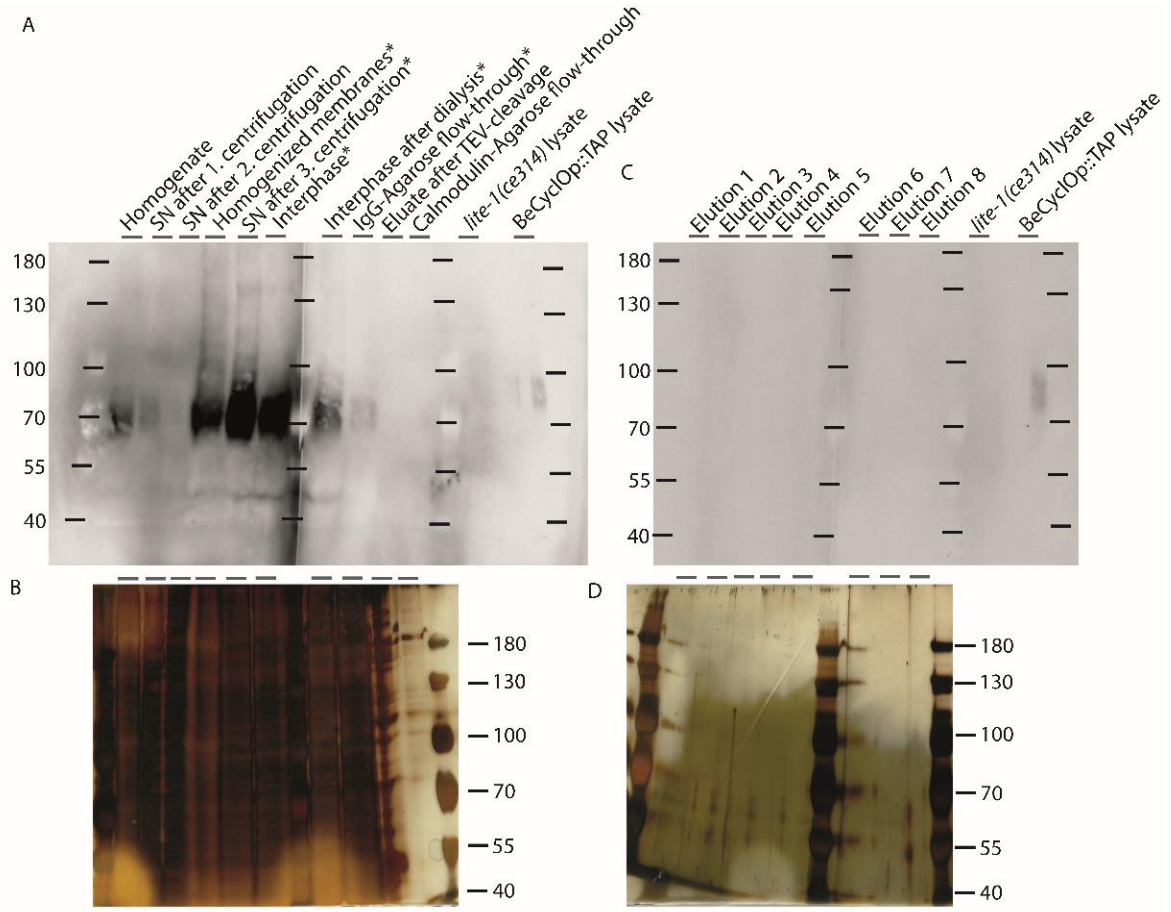

Figure 66: Tandem affinity purification depicts cleavage of BeCyclOp concatamer into BeCyclOp monomers. *Western blot analysis and silver staining of A, B) tandem affinity purification samples and C, D) elution fractions of BeCyclOp::TAP purification (anti-TAP 1:1000). * indicates application of 60 µg protein per sample. Lysates of the genetic background lite-1(ce314) and of BeCyclOp::TAP expressing animals were used as controls. The red arrow at around 156 kDa indicates BeCyclOp Concatamer.*

3.2.2.4. Increase of protease inhibitor concentration

Since BeCyclOp concatamer is cleaved by *C. elegans* proteases during homogenization of worm membranes, an experiment with an increased protease inhibitor concentration was executed. For this purpose, worm powder of the integrated strain was incubated for 1 h at RT (to force protease activity) with various protein inhibitor concentrations (0.5, 2, 4 and 8-fold; calculated regarding the volume of worm powder) and samples were analysed via SDS-PAGE and western blot analysis. Here, an increasing signal for BeCyclOp concatamer was detected with raised protease inhibitor concentration, whereas the signal for BeCyclOp monomer decays with elevated inhibitor concentrations (Figure 67).

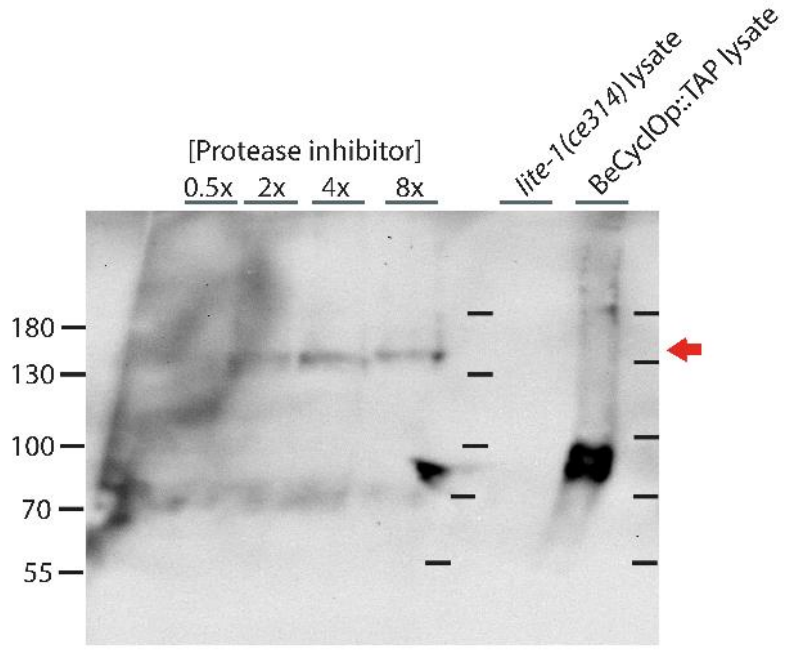

Figure 67: Increase of protease inhibitor concentration successfully inhibit BeCyclOp concatamer cleavage into monomers. *Western blot analysis of BeCyclOp concatamer containing worm lysates, incubated with different protease inhibitor concentrations (0.5, 2, 4 or 8-fold; calculated regarding the volume of worm powder) (anti-TAP 1:1000). Lysates of the genetic background lite-1(ce314) and of BeCyclOp::TAP expressing animals were used as controls. The red arrow at around 156 kDa indicates BeCyclOp Concatamer.*

3.3. Investigation of cAMP effectors in *C. elegans* muscle cells

Recently, a former PhD student in the Gottschalk lab, J. Nagpal, found that optogenetic cAMP generation by bPAC in *C. elegans* muscle cells caused muscle relaxation, i.e. evoked an increase in the body length of about 2 %. Thus, elevated cAMP levels in *C. elegans* muscle cells induced muscle hyperpolarization. In order to investigate a possible mechanism for cAMP induced muscle relaxation, a cAMP modulated ion channel in the plasma membrane was assumed. To identify ion channels with a cAMP binding domain, a sequence alignment of PKA´s regulatory subunit Riα (PDB entry 1NE6) against the *C. elegans* genome was executed (Appendix figure 88), identifying four cyclic nucleotide-gated (CNG) ion channels (CNG-1, CNG-2, CNG-3 and CHE-6) and two voltage-gated potassium channels (EGL-2, UNC-103), which were selected for further investigation. An overview of the six channels is summarized in table 23.

Table 23: Overview of the six channels which could act as possible cAMP effectors in C. elegans muscle cells for muscle relaxation. The table is adopted from S. Zhou's BSc Thesis. This information was extracted from the respective WormBase and CeNGEN (Hammarlund et al., 2018) entries, and from the REFs (Cho et al., 2005; Cho et al., 2004; Garcia et al., 2003; Park et al., 2020; Reiner et al., 2006; Smith et al., 2013) .

Channel	Channel type	Expressed in body wall muscle cells (according to CeNGEN)	Experimentally confirmed expression in	Known to be involved in
CNG-1	CNGC	yes	Amphid and head neurons	Sensory perception of chemical stimuli
CNG-2	CNGC	no	Amphid neurons	Sensory perception of chemical stimuli
CNG-3	CNGC	no	Amphid neurons	Transduction, growth regulation, thermosensation
CHE-6	CNGC	no	ASEL, ASER, AWCL, AWCR	Gustatory sensory transduction
EGL-2	VGKC	no	Intestinal cells, lumbar and sensory neurons, vulval muscle	Chemosensory behaviour, muscle contraction, oviposition
UNC-103	VGKC	yes	Body wall muscle, neurons, non-striated muscle	Mating, Muscle contraction

3.3.1. Cytosolic and local optogenetic cAMP generation caused muscle relaxation in *lite-1(ce314)* background

Since cytosolic and local (membrane proximal) optogenetic cAMP generation in *C. elegans* cholinergic neurons caused differences in the evoked behavioural outputs (crawling speed, swimming rate, body contraction evoked by stimulation of body wall muscles), the effect of local optogenetic cAMP generation in body wall muscle cells on the body length of *C. elegans* was assessed. For this purpose, body length measurements of animals, expressing BeCyclOp(A-2x) were performed and compared to animals expressing bPAC. In both cases, illumination triggered an elongation of the body length of about 2 % within 1.5 s, which nearly remained at this level even after turning off light (Figure 68 A, B). Thus, optogenetic cAMP generation caused muscle relaxation, independent of the cellular localization of its generation.

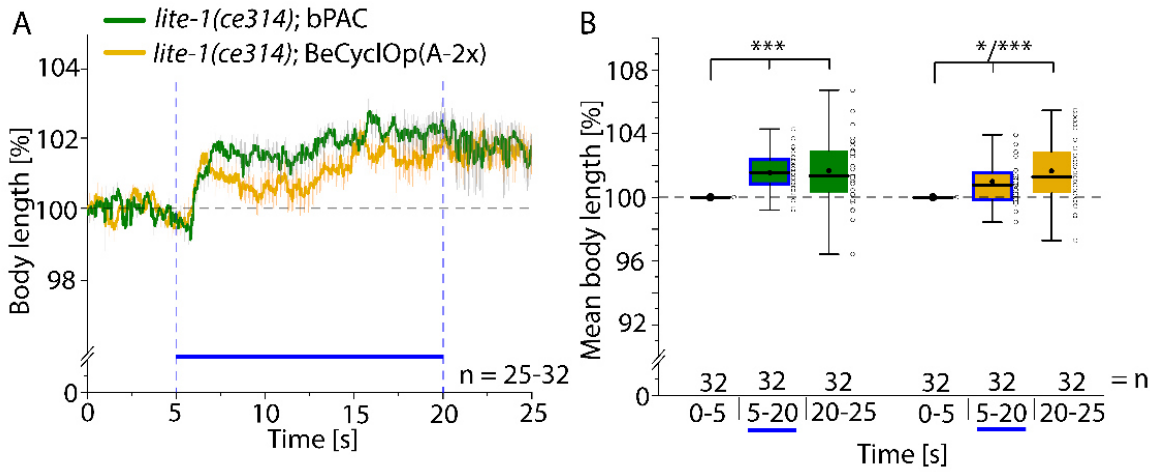

Figure 68: bPAC and BeCyclOp(A-2x) activation increase the body length by 1 – 2 %. *A) Body length analysis ±SEM of animals, expressing bPAC or BeCyclOp(A-2x) in body wall muscle cells. Blue bar indicates the period of illumination (0.9 mW/mm^2; 470 nm). B) Mean normalized body lengths for the time periods before (0 - 5s), during (5 – 20 s), and after (20 – 25 s) light application. The interquartile range (IQR), median (–), mean values (●), individual measurements (o), and whiskers (1.5 * IQR) are depicted. n = number of animals. Statistically significant differences were calculated using one-way ANOVA with Bonferroni correction (*p ≤ 0.05 and ***p ≤ 0.001).*

3.3.2. Swimming behaviour modulation by bPAC

Because only slight changes of the body length were evoked by bPAC activation, which would make it more difficult to distinguish differences between wild type and mutant, another assay was chosen. Swimming behaviour analysis was performed as a more sensitive assay to facilitate screening for a possible cAMP effector. To this end, A. Pieragnolo studied the impact of optogenetic cAMP generation by bPAC in *C.*

elegans muscle cells on the swimming behaviour of these animals. Here, illumination strongly reduced the swimming rate from 70 to 23 thrashes per min. As control, she investigated the influence of light application on the swimming frequency of the genetic background *lite-1(ce314)* and found no light dependent change in their swimming rate (Figure 69). In conclusion, optogenetic cAMP generation reduced the swimming frequency of the animals, so swimming behaviour analysis was used as complementary assay for screening after cAMP effectors.

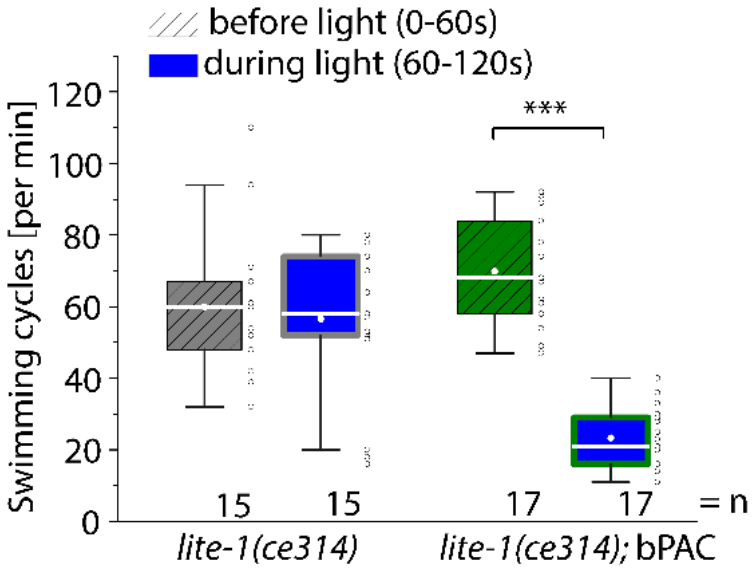

Figure 69: bPAC stimulation strongly reduces the swimming frequency. *Swimming frequencies of animals, expressing bPAC in body wall muscle cells, and the genetic background lite-1(ce314). Swimming rates were calculated 60 s before, and 60 s during light exposure (0.2 mW/mm^2; 470 nm). The interquartile range (IQR), median (–), mean values (●), individual measurements (o), and whiskers (1.5 * IQR) are shown. n = number of animals. Statistically significant differences: two-way ANOVA with Bonferroni correction (***p ≤ 0.001).*

3.3.3. Investigation of cAMP effectors in *lite-1(ce314)* channel loss of function genetic background

To evaluate the six identified channels for a possible participation in cAMP induced muscle relaxation, the strain ZX2617 (expressing bPAC in muscle cells, *lite-1(ce314)* background) was crossed with the respective channel loss of function mutant, generating bPAC expressing strains in double mutant background (channel loss of function and *lite-1(ce314)*), in channel loss of function background, and in wild type background. Generation of the strains was performed with the help of A. Pieragnolo and S. Zhou. Investigation of optogenetically triggered muscle relaxation in double mutant background was performed by S. Zhou in her BSc thesis. The summarized

results of the body length measurements and swimming behaviour analysis are summarized in figures 70 and 71. In regard of body length analysis, she found that optogenetic cAMP generation in all channel loss of function *lite-1(ce314)* mutants evoked no or very weak body elongations (+1 %). For swimming behaviour analysis, she found that cAMP generation by bPAC in most mutant strains strongly decreased the swimming rates of the animals (~52 - 72 % after 60 s light application; 470 nm; 0.2 mW/mm^2), though they did not reach the extent as detected for the *lite-1(ce314)* control and the mutant *egl-2(rg4); lite-1(ce314)*. In addition, she found that bPAC activation in *unc-103(n1213); lite-1(ce314)* background caused a delayed and smaller decrease of the swimming frequency (21 %). In summary, these results could be a hint for a possible modulatory role of the channels in cAMP induced muscle hyperpolarization, especially of UNC-103.

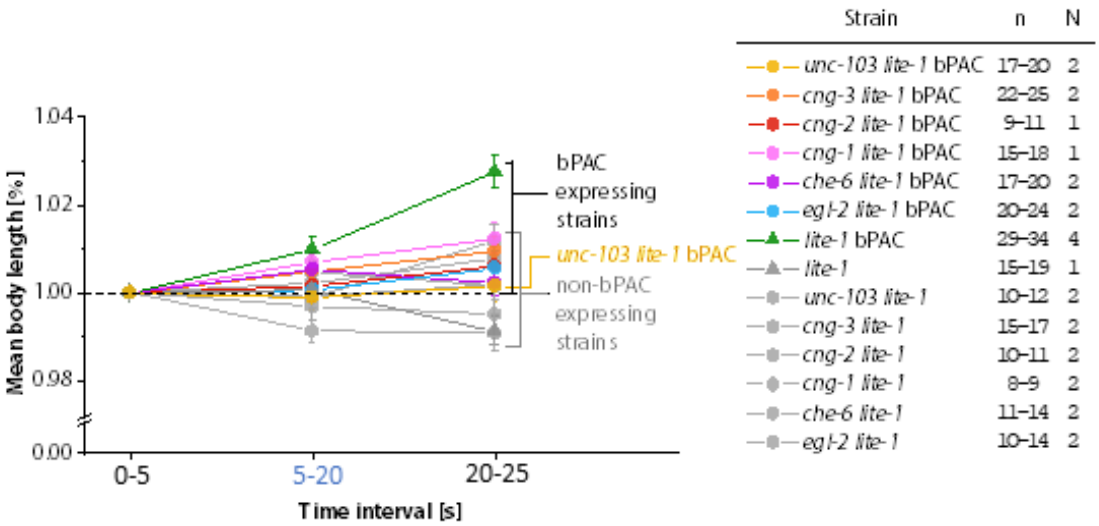

Figure 70: Influence of optogenetic cAMP generation through bPAC on the body length in channel loss of function lite-1(ce314) background. *Normalized body lengths ±SEM of animals, expressing bPAC in body wall muscle cells of channel loss of function lite-1(ce314) or only in lite-1(ce314) background, and the genetic backgrounds as controls. Animals were illuminated with blue light (470 nm; 0.2 mW/mm²), which is highlighted in blue. n = number of animals, N = independent measurements. Image adapted from S. Zhou's BSc Thesis.*

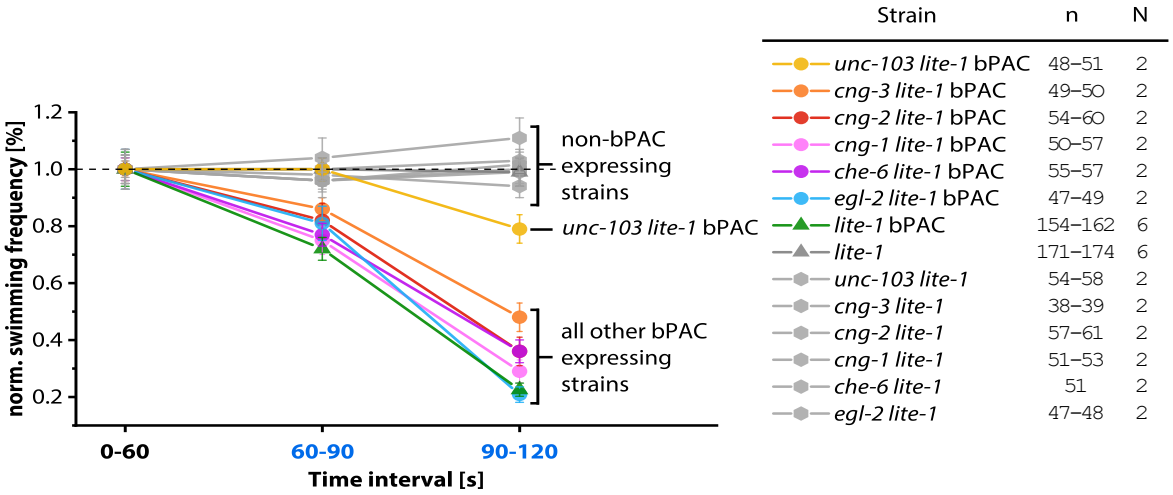

Figure 71: Influence of optogenetic cAMP generation through bPAC on the swimming rate in channel loss of function lite-1(ce314) background. *Normalized swimming rates ±SEM of animals, expressing bPAC in body wall muscle cells of channel loss of function lite-1(ce314) or only in lite-1(ce314) background, and the genetic backgrounds as controls. Animals were illuminated with blue light (470 nm; 0.2 mW/mm²), which is highlighted in blue. n = number of animals, N = independent measurements. Image adapted from S. Zhou's BSc Thesis.*

Since body length measurements and swimming behaviour analysis performed by S. Zhou in her BSc thesis highlight UNC-103 as potential cAMP effector in cAMP induced muscle hyperpolarization, I have repeated the body length analysis to obtain a more detailed picture of cAMP induced muscle hyperpolarization and its influence on the body length of the *unc-103 lite-1(ce314)* background. For this purpose, the

following changes were made: increase of the light intensity (0.9 mW/mm^2), reduction of the light pulse duration (5 s), and prolongation of the body length measurement after light application (113 s). Also, experiments with extended light pulse duration were executed (113 s) to increase the optogenetically generated cAMP level. In case of the body length measurement using a 5 s light pulse, bPAC activation induced constantly increasing body elongations in *lite-1(ce314)* and *lite-1(ce314); unc-103(n1213)* animals, reaching a plateau of about 4 %, 70 s after turning off light (Figure 72 A, B). Interestingly, extension of the light pulse elongated the body length in *lite-1(ce314)* background more quickly, i.e. about 4 % within 15 s after turning on light, which further increased to about 6 % to the end of light application. In *lite-1(ce314) unc-103(n1213)* background, bPAC evoked body elongation raised more slowly, reaching a plateau of about 3 % after 55 s light exposure (Figure 72 C, D). In both experiments, no body length increase was observed for the *lite-1(ce314)* control animals. Although statistical analysis could not be performed because of the small number of animals measured, the result gives an indication of the possible involvement of UNC-103 in the muscle hyperpolarization provoked by cAMP.

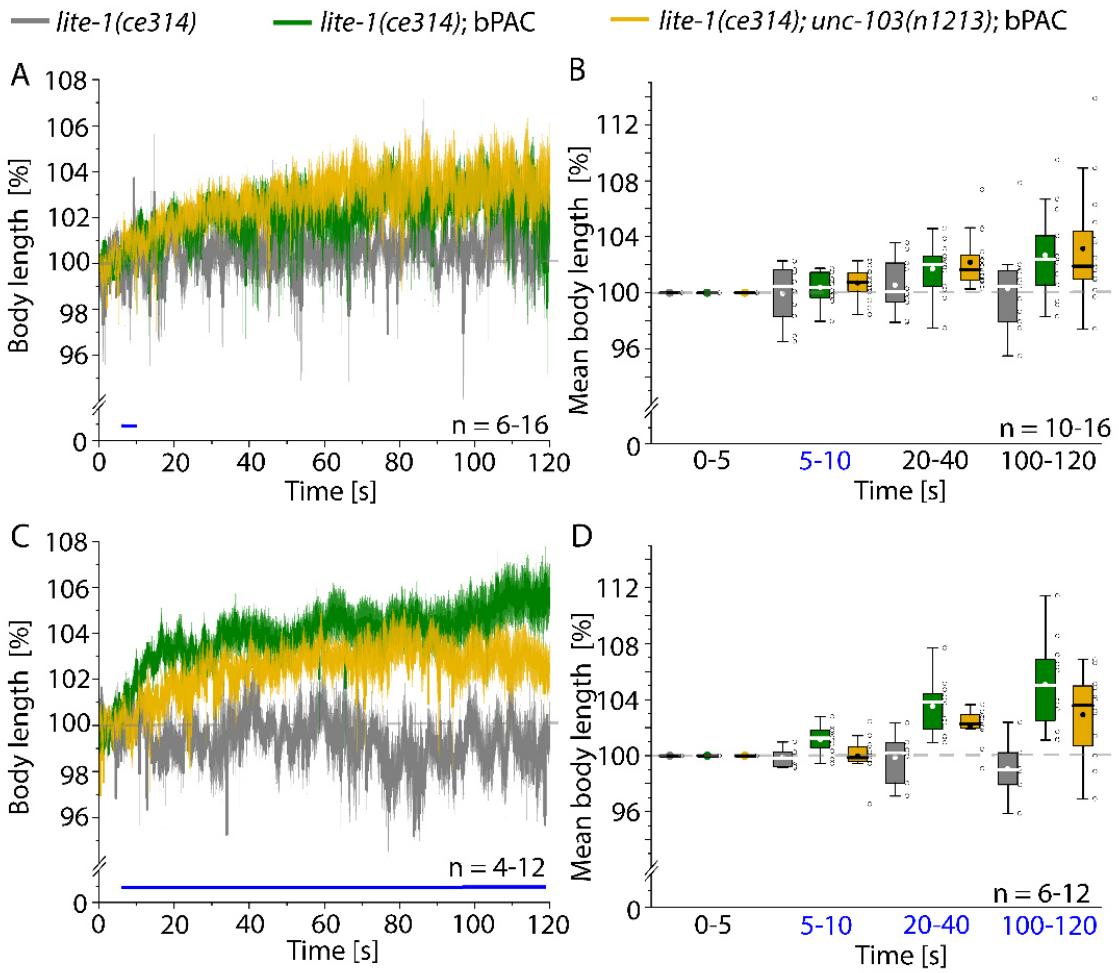

Figure 72: Optogenetic cAMP generation by bPAC evokes muscle elongation in lite-1(ce314) unc-103(n1213) background. *A, C) Body length analysis ±SEM of animals, expressing bPAC in body wall muscle cells of lite-1(ce314) or lite-1(ce314) unc-103(n1213) background, and of the genetic background lite-1(ce314), using a A) 5 s or C) 115 s light pulse. Blue bar indicates the period of illumination (0.9 mW/mm²; 470 nm). B, D) Quantification of the mean normalized body lengths for the indicated time periods before (0 – 5 s), B) during light (5 – 10 s) and after light (20 – 40 and 100 – 120 s), and C) during light (5 – 10, 20 – 40 and 100 – 120 s). The interquartile range (IQR), median (–), mean values (●), individual measurements (o), and whiskers (1.5 * IQR) are shown. n = number of animals.*

3.3.4. bPAC induced muscle relaxation in wild type animals

In addition, bPAC evoked muscle relaxation was investigated in wild type background to exclude impacts of the *lite-1* mutation on the behavioural output. Interestingly, bPAC stimulation caused no body length increase under the same experimental conditions as observed for the *lite-1(ce314)* background. Reason for this could be the intrinsic photophobic response of the animals, triggered by blue light sensation by the ultraviolet/blue-light sensor LITE-1, that caused an escape behaviour of the animals that counteracts the cAMP induced muscle elongation (Edwards *et al.*, 2008). In

contrast to this, optogenetic cAMP production by bPAC strongly decreased the swimming frequency to about 22 % during 60 s light exposure, which slightly increased to 28 % 60 s after turning off light. This strong light-induced reduction is comparable to the results in *lite-1(ce314)* background obtained by S. Zhou in her BSc Thesis (Figure 71). No light dependent reduction of the swimming rate was observed in non-transgenic animals (Figure 73 A-C).

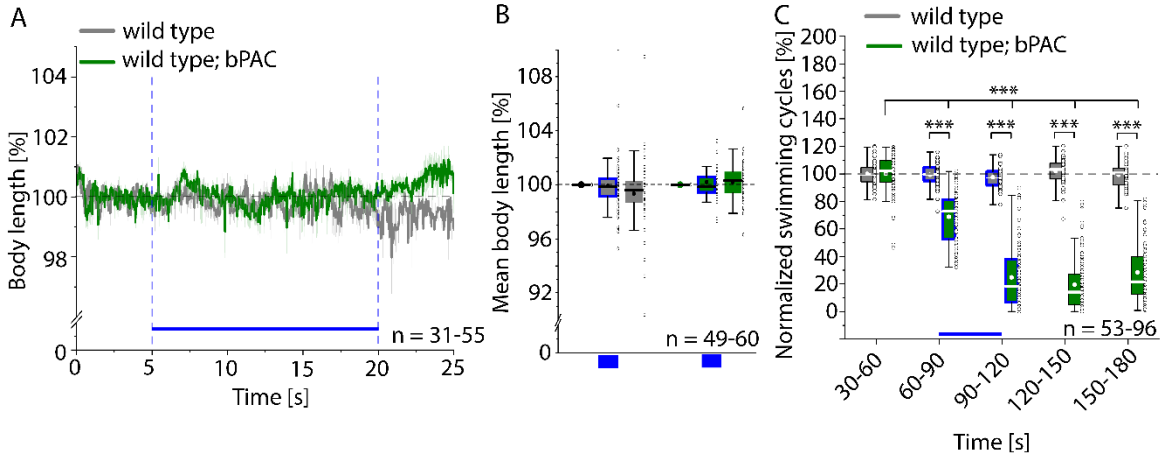

Figure 73: bPAC activation in body wall muscle cells causes no obvious increase of the body length under these experimental conditions, but strongly decreased the swimming cycles in wild type animals. *A) Body length measurements ±SEM of animals, expressing bPAC in body wall muscle cells of wild type background. Blue bar depicts the period of illumination (0.9 mW/mm²; 470 nm). B) Mean normalized body lengths of animals in A, before (0 – 5 s), during (5 – 20 s), and after (20 – 25 s) light exposure. C) Swimming frequencies of animals, expressing bPAC in body wall muscle cells, and of wild type animals. Swimming rates were determined 60 s before, 60 s during, and 60 s after light application (0.9 mW/mm²; 470 nm), and normalized to the mean swimming frequencies 30 s before the light stimulus. The interquartile range (IQR), median (–), mean values (●), individual measurements (o), and whiskers (1.5 * IQR) are depicted. Blue bar indicates the period of illumination. n = number of animals. Statistically significant differences were determined using two-way ANOVA with Bonferroni correction (***p ≤ 0.001).*

Since bPAC stimulation did not evoke an obvious body length increase, further body length measurements were performed with following changes: reduced light pulse duration (5 s) and an extended measurement after light application (113 s), and experiments with extended light pulse duration (113 s) to elevate the optogenetic generated cAMP level. Activation of bPAC using a 5 s light pulse triggered body elongation, reaching a plateau of about 3 % 23 s after light exposure (Figure 74 A, B). In contrast to this, continuous light application caused a constantly increasing body length, achieving an elongation of about 6 % at the end of light application (Figure 74 C, D). In summary, optogenetic cAMP production in muscle cells of wild type animals caused muscle relaxation, as evidenced by an increase in body length and a decrease in swimming speed.

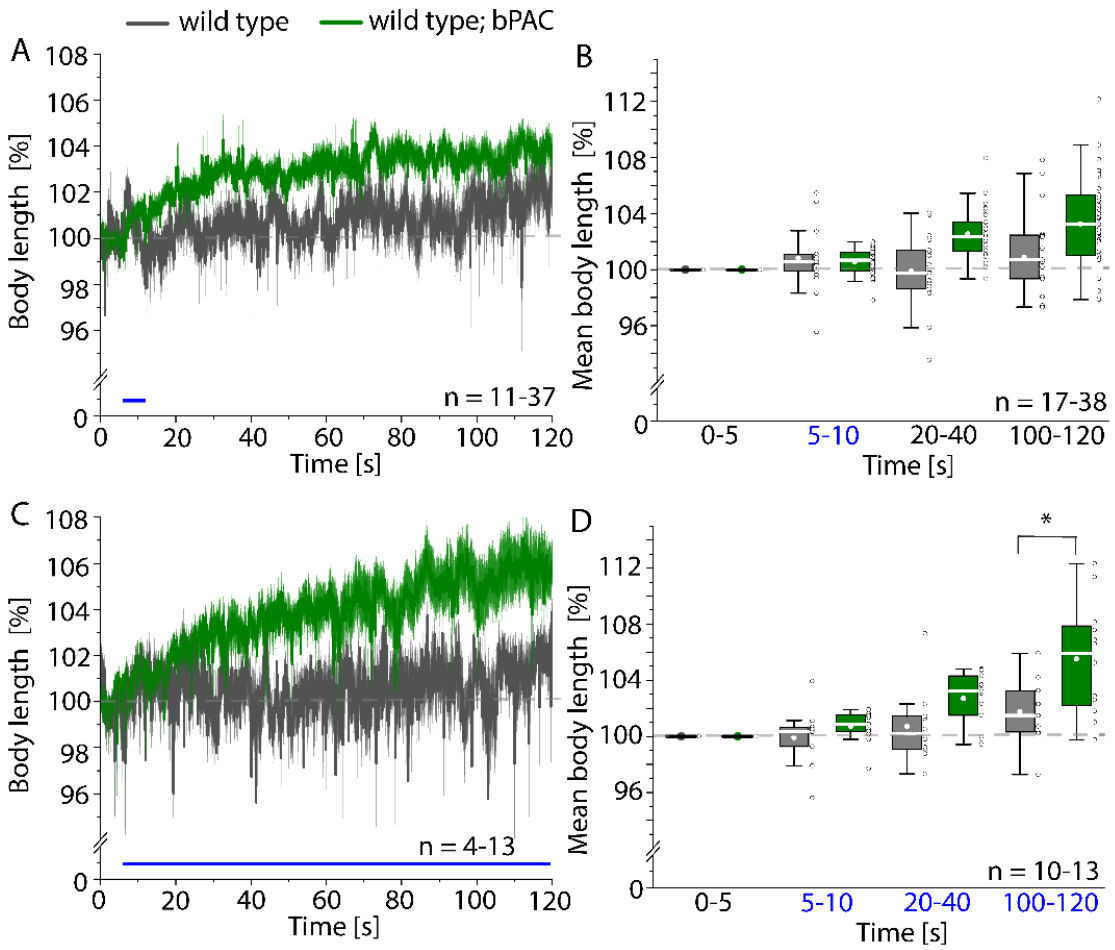

Figure 74: Optogenetic cAMP generation through bPAC evokes muscle relaxation in wild type animals. *A, C) Body length analysis ±SEM of animals, expressing bPAC in body wall muscle cells of wild type background, and of wild type animals, using a A) 5 s or C) 115 s light pulse. Blue bar indicates the period of illumination (0.9 mW/mm²; 470 nm). B, D) Quantification of the mean normalized body lengths for the indicated time periods before (0 – 5 s), B) during light (5 – 10 s) and after light (20 – 40 and 100 – 120 s), and C) during light (5 – 10, 20 – 40 and 100 – 120 s). The interquartile range (IQR), median (–), mean values (●), individual measurements (o), and whiskers (1.5 * IQR) are depicted. n = number of animals. Statistically significant differences were calculated using one-way ANOVA with Bonferroni correction (*p ≤ 0.05).*

3.3.5. Investigation of cAMP evoked muscle relaxation in channel loss of function background

To further assess the six channels after their possible participation as cAMP effector in optogenetically induced muscle relaxation, cAMP evoked muscle hyperpolarization was studied in loss of function mutants of the channels to be tested, in a background expressing wild type LITE-1. For this purpose, swimming behavioural analysis was performed.

Stimulation of bPAC in *cng-1(jh111)* background strongly reduced the swimming rate to 11 % during 60 s light exposure, which slowly recovered, but only to 16 % at 60 s

after the end of the light exposure (Figure 75). The decrease in swimming speed (89 %) is greater than in wild-type animals (75 %), contrasting with the results made for the *cng-1(jh111); lite-1(ce314)* background compared with the control *lite-1(ce314)* (~72 vs. 77 %). Therefore, it seems unlikely that CNG-1 plays a crucial role in the muscle hyperpolarization induced by cAMP, although it cannot be excluded that it contributes to muscle relaxation.

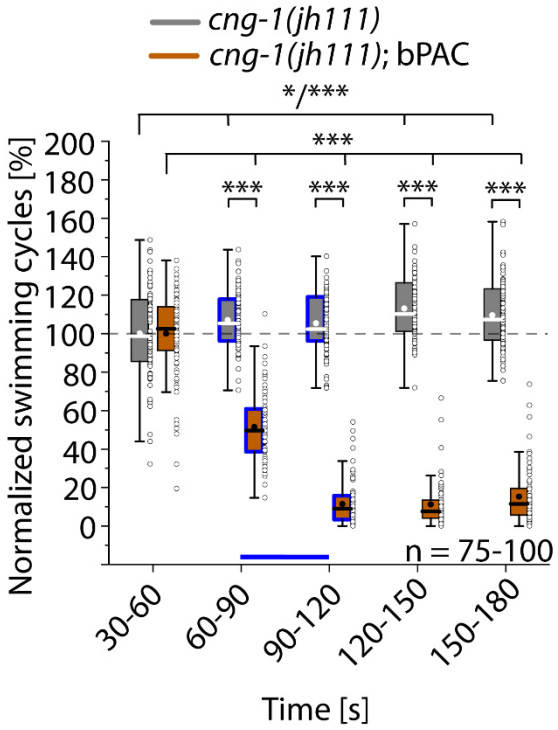

Figure 75: Optogenetic cAMP generation triggers muscle relaxation in cng-1(jh111) mutant background. *Swimming frequencies of animals, expressing bPAC in body wall muscle cells, and the genetic background cng-1(jh111). Swimming cycles were calculated 60 s before, 60 s during, and 60 s after light exposure (0.9 mW/mm^2; 470 nm), and normalized to the mean swimming frequencies 30 s before the light stimulus. The interquartile range (IQR), median (–), mean values (●), individual measurements (o), and whiskers (1.5 * IQR) are shown. Blue bar indicates the period of illumination. n = number of animals. Statistically significant differences were calculated using two-way ANOVA with Bonferroni correction (*p ≤ 0.05 and ***p ≤ 0.001).*

In regard of *cng-2(tm4267)* background, illumination of bPAC strongly decreased the swimming frequency to 18 % (Figure 76). The induced behavioural change remained at the respective level during the further measurement. The reduction in swimming frequency (82 %) is greater than in wild-type animals (75 %) and contrasts with the results obtained for *cng-2(tm4267); lite-1(ce314)* background compared with the control *lite-1(ce314)* (~65 vs. 77 %). Therefore, it seems unlikely that CNG-2 plays a vital role in cAMP induced muscle hyperpolarization, although it cannot be excluded that it contributes to muscle relaxation.

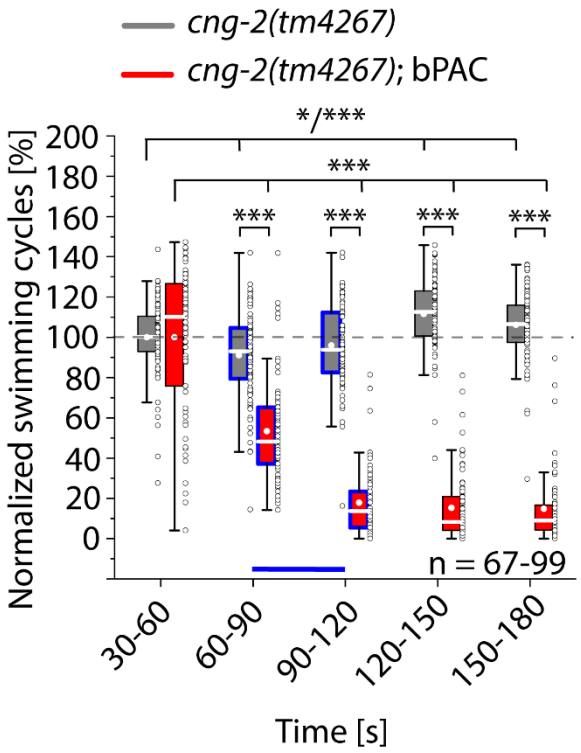

Figure 76: bPAC stimulation in cng-2(tm4267) background reduces the swimming rate. *Swimming rates of animals, expressing bPAC in body wall muscle cells, and the genetic background cng-2(tm4267). Swimming frequencies were determined 60 s before, 60 s during, and 60 s after light exposure (0.9 mW/mm^2; 470 nm), and normalized to the mean swimming frequencies 30 s before the light stimulus. The interquartile range (IQR), median (–), mean values (●), individual measurements (o), and whiskers (1.5 * IQR) are depicted. Blue bar indicates the period of illumination. n = number of animals. Statistically significant differences: two-way ANOVA with Bonferroni correction (*p ≤ 0.05 and ***p ≤ 0.001).*

In case of *cng-3(jh113)* animals, optogenetic cAMP production triggered a reduction of the swimming cycles to 33 %, which increased to 43 % 60 s after turning off light (Figure 77). The reduction in swimming speed (67 %) is less than in wild-type animals (75 %), an observation also made for the *cng-3(jh113); lite-1(ce314)* background compared with the control *lite-1(ce314)* (~52 vs. 77 %), which could be explained by a possible participation of CNG-3 in cAMP induced muscle hyperpolarization.

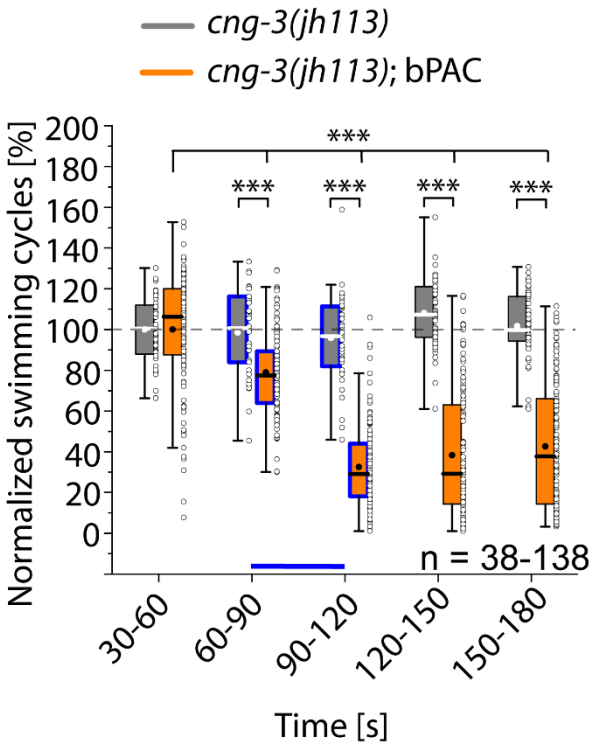

Figure 77: Optogenetic cAMP production evokes muscle hyperpolarization in cng-3(jh113) background. *Swimming frequencies of animals, expressing bPAC in body wall muscle cells, and the genetic background cng-3(jh113). Swimming rates were calculated 60 s before, 60 s during, and 60 s after light application (0.9 mW/mm²; 470 nm), and normalized to the mean swimming frequencies 30 s before the light stimulus. The interquartile range (IQR), median (–), mean values (●), individual measurements (o), and whiskers (1.5 * IQR) are shown. Blue bar indicates the period of illumination. n = number of animals. Statistically significant differences were calculated using two-way ANOVA with Bonferroni correction (***p ≤ 0.001).*

Behavioural analysis of optogenetically evoked muscle relaxation in *che-6(e1123)* background depicted a light triggered decrease of the swimming rate of 60 % 60 s after light exposure, a decrease that is smaller than in wild-type animals (75 %) (Figure 78). Interestingly, this observation was also made for the *che-6(e1123); lite-1(ce314)* background compared with the control *lite-1(ce314)* (~65 vs. 77 %). Reason for this could be that CHE-6 act as cAMP effector and participates in cAMP evoked muscle relaxation.

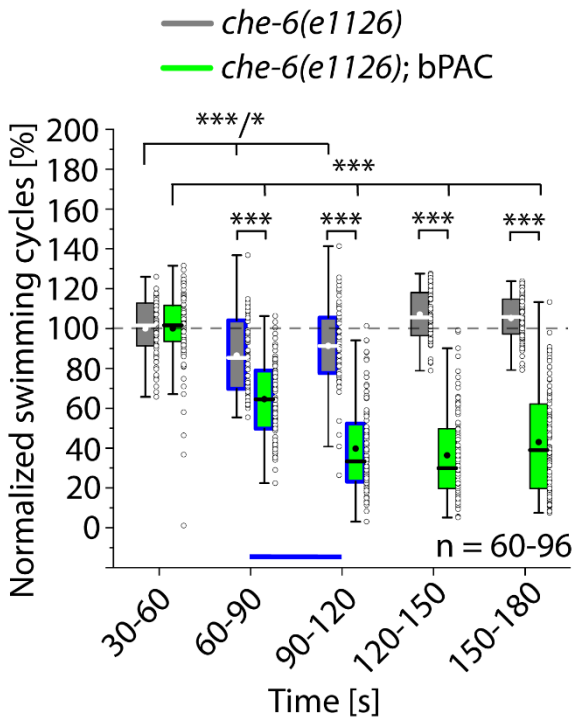

Figure 78: bPAC activation in che-6(e1126) background reduces the swimming frequency. *Swimming cycles of animals, expressing bPAC in body wall muscle cells, and the genetic background che-6(e1126). Swimming frequencies were determined 60 s before, 60 s during, and 60 s after light exposure (0.9 mW/mm²; 470 nm), and normalized to the mean swimming frequencies 30 s before the light stimulus. The interquartile range (IQR), median (–), mean values (●), individual measurements (o), and whiskers (1.5 * IQR) are depicted. Blue bar indicates the period of illumination. n = number of animals. Statistically significant differences: two-way ANOVA with Bonferroni correction (*p ≤ 0.05 and ***p ≤ 0.001).*

For *egl-2(rg4)* animals, bPAC activation induced a reduction of the swimming frequency to 36 %. After light application, the swimming cycles raised to 48 % (Figure 79). Thus, optogenetic cAMP generation resulted in a smaller reduction of the swimming rate in the channel loss of function mutant (64 %) than in the wild type control (75 %), whereas similar swimming speed reductions were observed for the *lite-1(ce314)* control and the mutant *egl-2(rg4); lite-1(ce314)* (~77 %) (Figure 71). Therefore, it seems unlikely that EGL-2 plays a crucial role in cAMP-induced muscle hyperpolarization, although it cannot be excluded that it contributes to muscle hyperpolarization.

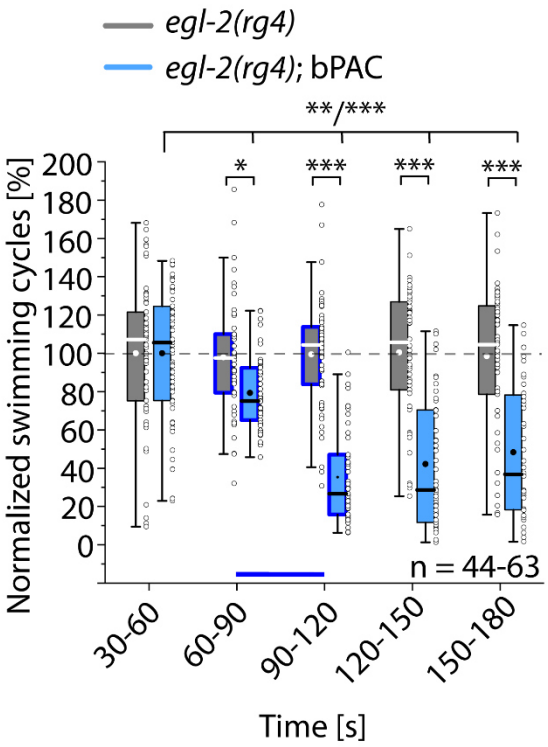

Figure 79: cAMP production by bPAC evokes muscle relaxation in egl-2(rg4) background. *Swimming rates of animals, expressing bPAC in body wall muscle cells, and the genetic background egl-2(rg4). Swimming rates were calculated 60 s before, 60 s during, and 60 s after light application (0.9 mW/mm²; 470 nm), and normalized to the mean swimming frequencies 30 s before the light stimulus. The interquartile range (IQR), median (–), mean values (●), individual measurements (o), and whiskers (1.5 * IQR) are shown. Blue bar indicates the period of illumination. n = number of animals. Statistically significant differences: two-way ANOVA with Bonferroni correction (*p ≤ 0.05, **p ≤ 0.01 and ***p ≤ 0.001).*

Behavioural analysis of optogenetic cAMP triggered muscle relaxation in *unc-103(n1213)* background showed a reduction of the swimming rate to 36 % (Figure 80). The decrease in swimming speed (64 %) is lower than in wild-type animals (75 %), consistent with the result made for the *unc-103(n1213); lite-1(ce314)* background compared with the control *lite-1(ce314)* (~21 vs. 77 %). The reason for this could be that UNC-103 act as cAMP effector in *C. elegans* muscle cells.

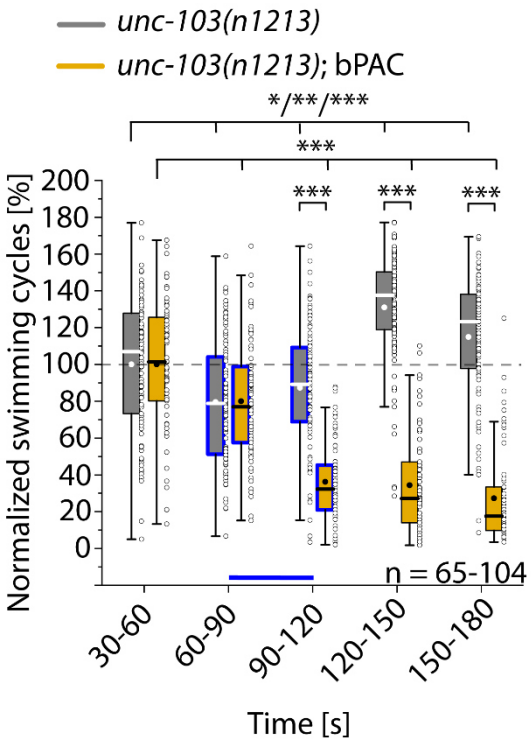

Figure 80: bPAC stimulation in unc-103(n1213) decreases the swimming rate. *Swimming frequencies of animals, expressing bPAC in body wall muscle cells, and the genetic background unc-103(n1213). Swimming cycles were calculated 60 s before, 60 s during, and 60 s after light exposure (0.9 mW/mm²; 470 nm), and normalized to the mean swimming frequencies 30 s before the light stimulus. The interquartile range (IQR), median (–), mean values (●), individual measurements (o), and whiskers (1.5 * IQR) are depicted. Blue bar indicates the period of illumination. n = number of animals. Statistically significant differences were determined using two-way ANOVA with Bonferroni correction (*p ≤ 0.05, **p ≤ 0.01 and ***p ≤ 0.001).*

Furthermore, basal swimming rates of the channel loss of function mutants with or without expression of bPAC in muscle cells were compared to wild type animals to assess possible impacts on *C. elegans* swimming behaviour. Here, *unc-103(n1213)* showed the strongest reduction of the basal swimming cycles (60 thrashes per min) compared to wild type animals (113 cycles per min). For *egl-2(rg4)*, *cng-1(jh111)* and *cng-2(tm4267)*, comparably decreased basal swimming frequencies were observed (71 – 82 cycles per min), whereas *cng-3(jh113)* and *che-6(e1126)* animals depicted no reduced basal swimming rates. The reason for the reduced basal swimming frequencies could be an involvement of the channels in the regulation of the swimming behaviour of the animals. Also, the strains were not backcrossed during strain generation by crossing, so mutations could arise that could affect the swimming behaviour of the animals. Expression of bPAC in muscle cells reduced basal swimming frequencies only in *cng-2(tm4267)*, *cng-3(jh113)* and *che-6(e1126)* background (Figure 81). The reason could be the compensatory overexpression of a

channel involved in cAMP-induced muscle hyperpolarization and activated by the dark activity of bPAC.

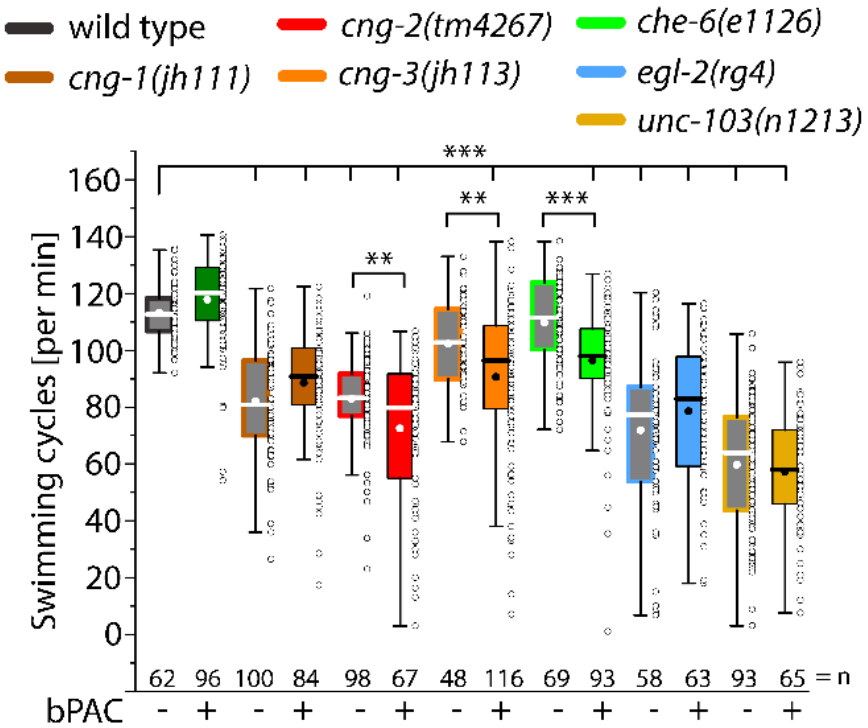

Figure 81: Most channel loss of function strains exhibit reduced basal swimming rates. *Basal swimming frequencies of wild type animals and the mutant strains cng-1(jh111), cng-2(tm4267), cng-3(jh113), che-6(e1126), egl-2(rg4), unc-103(n1213). Strains express (+) or do not express (-) bPAC in body wall muscle cells. The interquartile range (IQR), median (–), mean values (●), individual measurements (o), and whiskers (1.5 * IQR) are depicted. n = number of animals. Statistically significant differences: one-way ANOVA with Bonferroni correction (**p ≤ 0.01 and ***p ≤ 0.001).*

The results of swimming behavioural analysis of optogenetic cAMP evoked muscle relaxation in channel loss of function mutants is summarized in figure 82 and appendix figure 91. bPAC stimulation reduced swimming rates for all mutants, which is delayed for *unc-103(n1213)*, *egl-2(rg4)*, *cng-3(jh113)* and *che-6(e1126)*, and accelerated for *cng-1(jh111)* and *cng-2(tm4267)* compared to wild type animals. In sum, ontogenetically caused muscle relaxation was observed in all channel loss of function backgrounds.

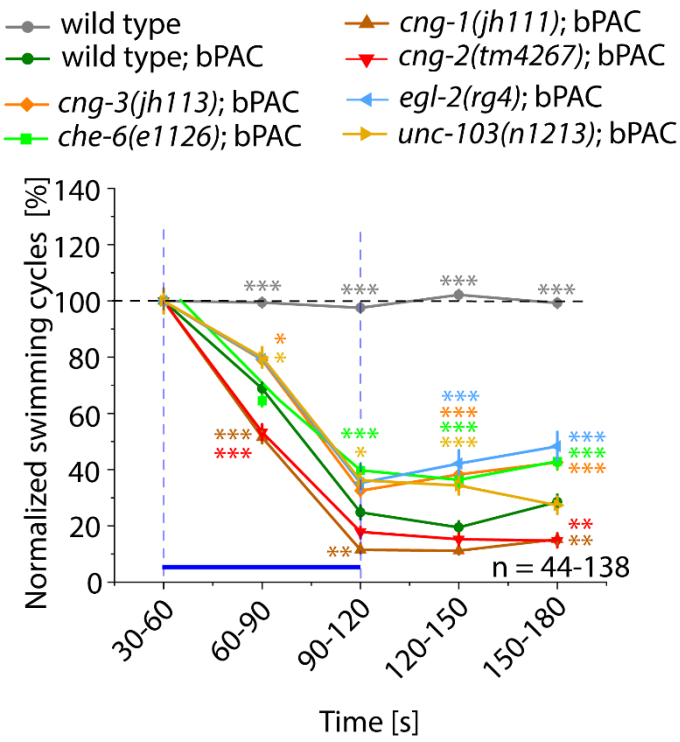

Figure 82: Optogenetic cAMP production reduced swimming frequency in all mutant strains. *Swimming frequencies ±SEM of animals, expressing bPAC in body wall muscle cells of cng-1(jh111), cng-2(tm4267), cng-3(jh113), che-6(e1126), egl-2(rg4), unc-103(n1213) or wild type background, and of wild type animals. Swimming cycles were calculated 60 s before, 60 s during, and 60 s after light exposure (0.9 mW/mm^2; 470 nm), and normalized to the mean swimming frequencies 30 s before the light stimulus. n = number of animals. Statistically significant differences to bPAC in wild type background were calculated using two-way ANOVA with Bonferroni correction (*p ≤ 0.05, **p ≤ 0.01 and ***p ≤ 0.001).*

4. DISCUSSION

4.1. Optogenetic manipulation of cNMP levels, coupled to CNGCs for cell de- and hyperpolarization

In the past decade, the optogenetic toolbox for the manipulation of ion currents and cAMP levels in *C. elegans* expanded. The latter includes the microbial photoactivatable adenylyl cyclases euPAC and bPAC and the synthetic phytochrome-linked photoactivatable adenylyl cyclases IlaC22 k27 and PaaC (Etzl *et al.*, 2018; Ryu *et al.*, 2014; Steuer Costa *et al.*, 2017; Weissenberger *et al.*, 2011). However, they are only soluble proteins and thus they do not precisely mimic physiological cAMP signalling occurring in microdomains in close proximity to the plasma membrane. Here, cAMP is predominantly generated by membrane-bound adenylyl cyclases, that are located in microdomains together with GPCRs, PK(A) and their targets, enabling spatially and temporal regulation of cAMP signalling (Bock *et al.*, 2020; Cooper *et al.*, 2014). In regard to optogenetic tools for cell hyperpolarization, the proton pump Arch, the chloride pump NpHR, and the anion channel GtACR2 were implemented (Bergs *et al.*, 2018; Chow *et al.*, 2010; Husson *et al.*, 2012; Zhang *et al.*, 2007a). However, application of these tools is limited due to the requirement of continuous light stimuli or undesired changes in the ion distributions (Mahn *et al.*, 2016; Wiegert *et al.*, 2016).

For this reason, the attempt of this work was to address these problems by developing and implementing novel optogenetic tools in *C. elegans* – membrane bound photoactivatable adenylyl cyclases for the manipulation of cAMP mediated signalling in close proximity to the plasma membrane as well as two-component optogenetic silencing systems based on the coupling of photoactivatable nucleotidyl cyclases and either the cAMP-gated SthK or the cGMP-gated BeCNG1 channel for the manipulation of K^+-currents. Because second messenger production is accompanied by signal amplification of the primary signal, coupling of photoactivatable nucleotidyl cyclases and CNGCs provides useful optogenetic tools due to their reduced need for light. Thus, another attempt of this work was to establish multicomponent optogenetic systems for cell depolarization based on the coupling of photoactivatable nucleotidyl cyclases and the TAX-2/-4 excitatory CNGC.

4.1.1. Implementation of CaCyclOp in *C. elegans* muscle cells

The optogenetic toolbox for the manipulation of cGMP mediated signalling in *C. elegans* consisted of the natural membrane-bound BeCyclOp and the artificial soluble bPGC (also termed BlgC or EROS) (Gao *et al.*, 2015; Kim *et al.*, 2015; Woldemariam *et al.*, 2019). The latter was engineered by mutating three amino acids (K197E/D265K/T267G) in the ATP binding region of the adenylyl cyclase domain of bPAC and generates cGMP with low efficiency and slow kinetics (Gao *et al.*, 2015; Ryu *et al.*, 2010; Woldemariam *et al.*, 2019). In contrast to this, BeCyclOp enables the production of much larger amounts of cGMP (L/D = 5000) at a high turnover rate (turnover (20°C) ~17 cGMP s^{-1}) (Gao *et al.*, 2015). Thus, one attempt of this thesis was to implement a tool with features in between those of BeCyclOp and bPGC.

Several orthologous CyclOps were assessed for light-regulated cGMP production by *in vitro* assays based on the measurement of the cNMP content from CyclOp containing oocyte membranes. Here, CaCyclOp showed the highest ratio of light versus dark activity (L/D = 230) after BeCyclOp (L/D = 5000), and thus was selected for characterization in *C. elegans* (Gao *et al.*, 2015). To assess the performance of the novel CyclOp in *C. elegans*, an *in vivo* test system established by Gao et al., 2015 was applied. This system consists of the TAX-2/-4 excitatory CNGC which is co-expressed with a photoactivatable guanylyl cyclase in *C. elegans* muscle cells. Photoactivation of the PGC triggers cGMP production and subsequent activation of the TAX-2/-4 CNGC, that caused muscle depolarization and further body contraction, a quantifiable behavioural readout (Gao *et al.*, 2015). To enable a more accurate comparison between the enzymatic features of the novel CaCyclOp and the established BeCyclOp and bPGC, the proteins were co-expressed using equal expression levels of TAX-2/-4.

Photoactivation of CaCyclOp co-expressed with TAX-2/-4 in body wall muscle cells caused slower and less pronounced body contractions compared to its orthologue BeCyclOp (~3.5 % peak contraction with a contraction on rate of ~0.88 s for CaCyclOp vs ~9 % peak contraction and a contraction on rate of ~0.23 s for BeCyclOp) (Figure 20). The difference in the evoked magnitudes can be explained by the lower light-inducible cGMP production by CaCyclOp, confirming the *in vitro* cGMP measurements of different fungal CyclOps in *Xenopus* oocytes membranes published

by Gao et al., 2015. The higher cGMP generation rate by BeCyclOp can be explained by its higher substrate affinity for GTP (K_M = 0.92 mM for solubilized BeCyclOp vs K_M = 6.1 mM for solubilized CaCyclOp) and by the faster evolution of the M signalling state (8 ms for BeCyclOp rhodopsin domain vs 31.4 ms for CaCyclOp rhodopsin moiety) (Scheib *et al.*, 2018; Scheib *et al.*, 2015). A reason for this could also be a lower expression level of CaCyclOp in body wall muscles. In contrast to CaCyclOp; TAX-2/-4 mediated muscle depolarization that reached a constant plateau during sustained illumination, BeCyclOp; TAX-2/-4 evoked body contraction decayed after its maximal turning point, which can be explained by the desensitization of the activated TAX-2/-4 CNGC (Figure 20). Further, it was shown that the rhodopsin moiety of BeCyclOp is only moderately resistant to high light intensities, bleaches during sustained light application, and thus caused a loss of available BeCyclOp molecules in the photocycle over time. In contrast to this, the rhodopsin domain of CaCyclOp depicted a higher photostability and thus no or only marginal numbers of molecules of CaCyclOp are depleted during constant illumination (Penzkofer *et al.*, 2017; Scheib *et al.*, 2018; Scheib *et al.*, 2015). Photoactivation of bPGC co-expressed with TAX-2/-4 caused the slightest body contraction of the analysed photoactivatable guanylyl cyclases, i.e. ~2.5 % peak contraction with a contraction on rate of ~1.78 s (Figure 20). This observation is consistent with previously reported findings in which BeCyclOp generated 50 times higher cGMP levels than bPGC, despite illumination conditions favouring bPGC (blue light). Moreover, the authors' found that bPGC generates cGMP with slower kinetics relative to BeCyclOp and determined for both the turnover number, that were ~0.2 cGMP s^{-1} and ~17 cGMP s^{-1}, respectively (Gao *et al.*, 2015; Woldemariam *et al.*, 2019). Further, it was shown that bPGC has substantial dark activity and ~10 % residual cAMP activity *in vitro*, whereas BeCyclOp and CaCyclOp have no detectable dark activity and are highly specific guanylyl cyclases (Gao *et al.*, 2015; Ryu *et al.*, 2010; Scheib *et al.*, 2018; Scheib *et al.*, 2015). Characterization of the nucleotidyl specificity and cNMP levels of the photoactivatable guanylyl cyclases using *C. elegans* extracts confirmed the high GTP specificity of both CyclOps (Figure 39). However, no residual cAMP activity and no basal cGMP production was determined for bPGC (Figure 39). Reason for this could be that the applied *in vitro* cNMP measurement involves the detection of the cNMP levels of a fixed number of animals (i.e. their entire body), and thus do not reflect the exact nucleotide content within the muscle cells. Also, compensatory

effects in *C. elegans* body wall muscle cells due to an increased expression level of PDEs could counteract the basal activity of the enzyme. For all analysed photoactivatable guanylyl cyclases, light saturation conditions in *C. elegans* were reached at intensities of ≥ 0.2 mW/mm^2, that is comparable to applied intensities for ChR2 activation (Figure 21) (AzimiHashemi *et al.*, 2014; Nagel *et al.*, 2005). Nevertheless, 0.2 mW/mm^2 was applied as minimal light intensity for the light saturation experiments, thus light saturation for the enzymes is presumably reached at lower light conditions. Moreover, half maximal activation intensities were determined for BeCyclOp ($K_{0.5}$ = 0.055 mW/mm^2; in *Xenopus* oocytes membranes), for CaCyclOp ($K_{0.5}$ = 0.027 mW/mm^2; in *Xenopus* oocytes membranes), and for bPAC ($K_{0.5}$ = 0.004 mW/mm^2; of purified protein *in vitro*), implying the fastest photocycle for BeCyclOp and the slowest for bPAC/bPGC (Gao *et al.*, 2015; Scheib *et al.*, 2018; Stierl *et al.*, 2011). In sum, BeCyclOp is the most potent tool for cGMP generation, and CaCyclOp is a useful, membrane-bound alternative to the soluble bPGC (Figure 83). However, photoactivation of BeCyclOp caused the generation of high cGMP levels within a few seconds, and depending on the cell type of interest, its application could be accompanied by overactivation of cGMP mediated signalling pathways, or by cross-talk to cAMP or NTP utilizing pathways (e.g. by macroscopic depletion of GTP), and thus could interfere with the metabolism of the cell or the cellular output. To prevent these undesired side effects, application of CaCyclOp would represent a useful alternative, since it is characterized by a lower light-inducible cGMP generation, lower cGMP production rate, but a similarly high substrate specificity relative to BeCyclOp. Hence, CaCyclOp enables fine-tuning of cGMP levels and is a beneficial optogenetic tool for cGMP mediated signalling, encompassing membrane-bound guanylyl cyclases for signal transduction.

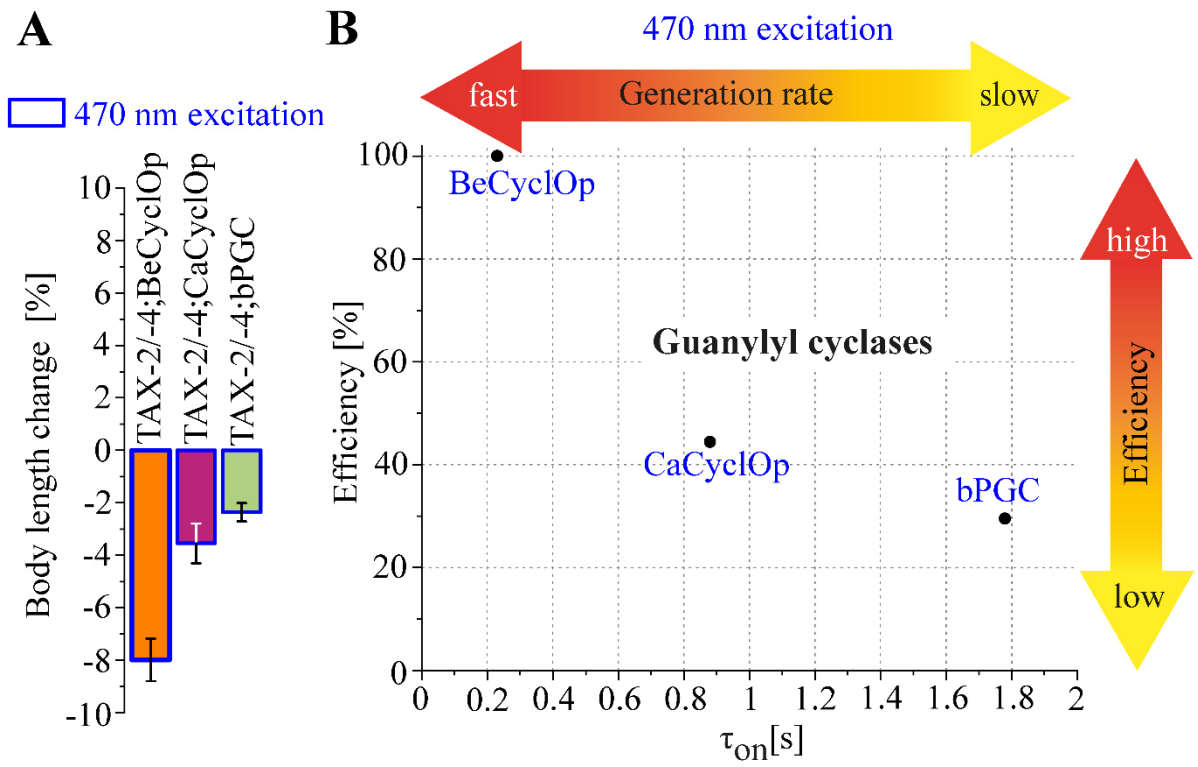

Figure 83: Evaluation of photoactivatable guanylyl cyclases characterized in this thesis. *A) Summary of body length reductions provoked by the depolarizing multicomponent optogenetic systems consisting of a photoactivatable guanylyl cyclase (BeCyclOp, CaCyclOp, or bPGC) and the TAX-2/-4 cyclic nucleotide gated channel. Illustrated is the mean normalized body length decrease (±SEM) relative to the initial body length of the animal before light exposure. B) Schematic overview of the photoactivatable guanylyl cyclases co-expressed with the excitatory TAX-2/-4 channel in body wall muscle cells of C. elegans, categorized by the time course of induced muscle contractions (proxy for cGMP production rate (τ)) and efficiency. For efficiency calculations, the most effective tool (BeCyclOp) was arbitrarily set as 100 % efficient, and the body length reductions for each tool (at 0.9 mW/mm²; 470 nm) were determined relative to the maximum body length reduction induced by the most effective tool. Classification of the tools could be altered by adjusting the expression levels and the applied light intensity. Image adapted and modified from (Henss et al., 2021).*

4.1.2. Optogenetic manipulation of cAMP mediated signalling in vicinity to the plasma membrane

CyclOps are particular in combining a rhodopsin and a guanylyl cyclase domain, yielding efficient membrane-bound photoactivatable guanylyl cyclases for cGMP mediated signalling (Avelar *et al.*, 2014; Gao *et al.*, 2015; Scheib *et al.*, 2018; Scheib *et al.*, 2015). GTP specificity is determined by two to three amino acids in the active site of the cyclase domain, and can be interconverted by mutagenesis into cyclases of high ATP specificity (Linder, 2005; Ryu *et al.*, 2010; Sunahara *et al.*, 1998). Hence, highly efficient light-regulatable membrane-bound photoactivatable guanylyl cyclases

can be converted into membrane-bound photoactivatable adenylyl cyclases. To characterize the engineered membrane-bound photoactivatable adenylyl cyclases regarding their optogenetic cAMP production and cAMP mediated signalling, the proteins were expressed in cholinergic motor neurons and evaluated in comparison to the implemented soluble bPAC. Here, optogenetic cAMP generation by bPAC caused increased neurotransmission and behaviours. The evoked behavioural changes can be evaluated on the one hand by determination of the swimming rate in liquid and on the other hand by calculation of the crawling speed and body bending on solid substrate (Steuer Costa *et al.*, 2017). Beyond that, the artificial membrane-bound photoactivatable adenylyl cyclases were further characterized in *C. elegans* muscle cells using the *in vivo* test system established by Gao et al., 2015, and their nucleotide specificity switch from GTP to ATP as well as the extent of light-dependent cAMP generation were determined using *C. elegans* extracts.

Determination of the nucleotide specificity and the cNMP content using *C. elegans* extracts showed the highest levels of light-induced cAMP generation for the membrane-bound photoactivatable adenylyl cyclases BeCyclOp(A-2x), YFP-BeCyclOp(A-2x), and YFP-CaCyclOp(A-2x) (39, 57, 40 nM, respectively) over a long illumination period (15 min), however they did not reach the extent produced by the soluble bPAC (142 nM) (Figure 39 A). In contrast, low magnitudes of generated cAMP were measured for the versions BeCyclOp(A-3x) and CaCyclOp(A-2x) (8 and 7 nM, respectively). Moreover, no obvious residual cGMP and basal activity was detected for any of the analysed membrane-bound photoactivatable adenylyl cyclases (Figure 39 B). Thus, introducing the point mutations E497K/C566D into both CyclOps successfully converted the membrane-bound photoactivatable guanylyl cyclases into membrane-bound photoactivatable adenylyl cyclases. Additionally, the guanylyl cyclase domain of BeCyclOp was changed by the point mutations E497K/H564D/C566T into an adenylyl cyclase domain. The results are in agreement with earlier studies, in which the double mutations converted both CyclOps into highly specific membrane-bound photoactivatable adenylyl cyclases, and complementary triple mutations transformed bPAC into a guanylyl cyclase (Ryu *et al.*, 2010; Scheib *et al.*, 2018). The difference in the magnitude of light-induced cAMP generation between the soluble bPAC and the membrane-bound photoactivatable adenylyl cyclases can be explained by their enzymatic properties. In this context, for bPAC a higher light versus dark activity (L/D = ~350 in *E. coli*) in comparison to YFP-

BeCyclOp(A-2x) (L/D = 220 in *Xenopus* oocyte membranes) and YFP-CaCyclOp(A-2x) (L/D = 280 in *Xenopus* oocyte membranes) was reported (Ryu *et al.*, 2010; Scheib *et al.*, 2018). Also, the magnitude of optogenetic cAMP production is influenced by the expression level of the proteins, that is expected to be higher for the soluble bPAC relative to the membrane-bound photoactivatable adenylyl cyclases. However, determination of the expression levels of the photoactivatable adenylyl cyclases in body wall muscle cells by determination of the mCherry content (photoactivatable adenylyl cyclases and mCherry are expressed from bicistronic pre-mRNAs) in *C. elegans* extracts depicted similar expression levels for bPAC, BeCyclOp(A-2) and BeCyclOp(A-3x), that is 1.4-fold higher than for YFP-CaCyclOp(A-2x) and 2.4-fold higher than for CaCyclOp(A-2x) and YFP-BeCyclOp(A-2x) (Figure 38). Though, the expression levels were estimated indirectly by measuring the mCherry content, and thus not necessarily resemble the exact protein level within the muscle cells since the proteins can differ in their half-lives and their stability. Also, accumulation of the soluble mCherry can distort the experimental outcome. Using a more accurate approach, i.e. calculation of the mean fluorescence intensities of YFP-tagged proteins, exhibited similar expression levels of both YFP-CyclOps in body wall muscle cells and cholinergic motor neurons, that is ~1.4-fold lower relative to the soluble bPAC in cholinergic motor neurons (Figure 35 and 38). As mentioned above, no basal cyclase activity was detected for the analysed membrane-bound photoactivatable adenylyl cyclases using *C. elegans* extracts. However, for the variants BeCyclOp(A-2x) (38-fold higher relative to an inactive variant in HEK293 cell membranes), YFP-BeCyclOp(A-2x) (5-fold higher relative to the non-injected oocyte), and YFP-CaCyclOp(A-2x) (2.6-fold higher relative to the non-injected oocyte) constitutively active cyclase activity was reported recently (Scheib *et al.*, 2018; Trieu *et al.*, 2017). In case of BeCyclOp(A-2x), basal cAMP production in body wall muscle cells altered the morphology of some animals, i.e. shortened and wider body, that was observed in animals raised with and without ATR. Also, animals co-expressing BeCyclOp(A-2x) and SthK in body wall muscle cells supplemented with or without ATR depicted a high variability in their swimming frequencies. This could be explained by a constitutive cAMP generation by the adenylyl cyclase domain, that is independent of light-regulation by the rhodopsin moiety.

To further characterize the membrane-bound photoactivatable adenylyl cyclases regarding their optogenetic cAMP generation and to extend their application beyond their primary application as tool for the modulation of cAMP levels, the enzymes were co-expressed with the TAX-2/-4 CNGC in body wall muscle cells and evaluated in comparison to wild type BeCyclOp via body length measurements. The channel is mostly sensitive to cGMP, however it can also be activated by cAMP at high concentrations (EC_{50}^{cGMP} = 8.4 µM; EC_{50}^{cAMP} = 300 µM, in HEK293 cells) (Komatsu *et al.*, 1999). Photoactivation of all analysed membrane-bound photoactivatable adenylyl cyclases caused similarly pronounced body contractions (~ 2 – 3.5 % peak contraction with contraction on rates of ~0.42 s for BeCyclOp(A-2x), ~0.57 s for YFP-BeCyclOp(A-2x), ~0.64 s for YFP-CaCyclOp(A-2x), and ~0.80 s for BeCyclOp(A-3x)), and were thus not as efficient as wild type BeCyclOp (~8 % peak contraction with a contraction on rate of ~0.21 s; Figure 36). The difference in the magnitude and contraction on rates of light-induced muscle contraction between wild type BeCyclOp and the engineered CyclOp versions could be explained mainly by the largely reduced activation of the TAX-2/-4 channel due to cAMP. Further, it can be explained by differences in their enzymatic activities, whereby the membrane-bound photoactivatable adenylyl cyclases are characterized by a lower cNMP turnover and a lower L/D ratio relative to their wild type counterparts. Here, both YFP-CyclOps depicted a cAMP turnover of ~ 40 min^{-1} (determined in oocyte membranes) in contrast to cGMP turnovers of ~ 64 min^{-1} (of purified BeCyclOp) and ~ 411 min^{-1} (of purified CaCyclOp) (Scheib *et al.*, 2018). Whilst the wild type CyclOps exhibited high L/D ratios (5000 for BeCyclOp and >1000 for CaCyclOp), this is strongly reduced for both YFP-CyclOps (230 for YFP-BeCyclOp and 280 for YFP-CaCyclOp) (Gao *et al.*, 2015; Scheib *et al.*, 2018). The application of the membrane-bound photoactivatable adenylyl cyclases and the TAX-2/-4 CNGC as multicomponent optogenetic systems for cell depolarization are discussed in more detail in section 4.1.3.

Complementary to the characterization of the enzymatic activities of the membrane-bound photoactivatable adenylyl cyclases, the proteins were assessed regarding their potential to trigger and modulate cAMP mediated neurotransmission. Beyond that, the influence of cytosolic and membrane proximal optogenetic cAMP generation should be investigated. For this purpose, the membrane-bound photoactivatable adenylyl cyclases were expressed in cholinergic motor neurons and evaluated and compared to the implemented soluble bPAC via locomotion behaviour analysis on

solid and in liquid media. As mentioned above, amongst the analysed membrane-bound photoactivatable adenylyl cyclases BeCyclOp(A-2x) and both YFP-CyclOps exhibited the highest levels of light induced cAMP generation during sustained stimulation (15 min), though they do not reach the extent produced by bPAC (Figure 39). Further, they were expressed at lower levels compared to bPAC in cholinergic motor neurons (Figure 35). Photoactivation of these membrane-bound photoactivatable adenylyl cyclases caused similarly enhanced or even more potent behavioural changes (swimming and crawling) as bPAC, whereas a more rapidly decaying response was observed for the bPAC evoked effects (Figure 23, 24, 28, and 29). The latter one could be a hint that PDEs do not access and degrade cAMP produced in close proximity to the membrane as quickly as in the cytosol. Moreover, an increased diversity of the behavioural output was detected for cytosolic cAMP production by bPAC, i.e. increased bending angles and a decreased body length (Figure 31 and 33). This could be a hint that cytosolic cAMP production in cholinergic motor neurons may trigger the activation of undesired cAMP signalling pathways. To compare the levels of light dependent cAMP generation by BeCyclOp(A-2x) and bPAC at light conditions that match the conditions of the behavioural experiments (30 s), cAMP measurements using *C. elegans* extracts were performed. Here, the membrane-bound photoactivatable adenylyl cyclase depicted a 4-fold lower amount of optogenetic cAMP production than the soluble bPAC (Figure 40). In sum, local (membrane proximal) cAMP generation by the membrane-bound photoactivatable adenylyl cyclases may more specifically activate cAMP dependent neurotransmission of cholinergic motor neurons, i.e. an increased mobilization and priming/docking of synaptic vesicles and an increased filling of the synaptic vesicles with the neurotransmitter acetylcholine and thus an increase in locomotion behaviour (Steuer Costa *et al.*, 2017).

For CaCyclOp(A-2x), no obvious light dependent behavioural changes were observed, neither by its activation in cholinergic motor neurons nor by its stimulation in body wall muscle cells and co-expression with CNGCs. Interestingly, in hippocampal neurons only a third of transfected cells depicted light triggered cAMP production by the enzyme (Scheib *et al.*, 2018). Reason for this could be a weak expression, instable conformation and/or poor membrane targeting of the protein in the applied expression systems. Interestingly, addition of an N-terminal YFP strongly improved the performance of the protein in *C. elegans*, *Xenopus* oocytes and in

hippocampal neurons, indicating an improved expression and/ or membrane targeting of the enzyme (Scheib *et al.*, 2018). Apart from CaCyclOp(A-2x), the expression of the membrane-bound photoactivatable adenylyl cyclases, bPAC and wild type BeCyclOp in cholinergic motor neurons caused the reduction of the basal swimming frequency, which could be due to basal cNMP production or a general `toxicity` of these proteins. Nevertheless, the YFP-CyclOp variants depicted the highest tolerability in cholinergic motor neurons and thus they emerge as the preferred optogenetic tools and would further facilitate studies in e.g. neuropeptidergic signalling, memory function, or cell growth. Concluding, with this study I expand the optogenetic toolbox for cAMP modulation in *C. elegans*, differing in their expression levels, light saturation conditions and their enzymatic properties (Figure 84).

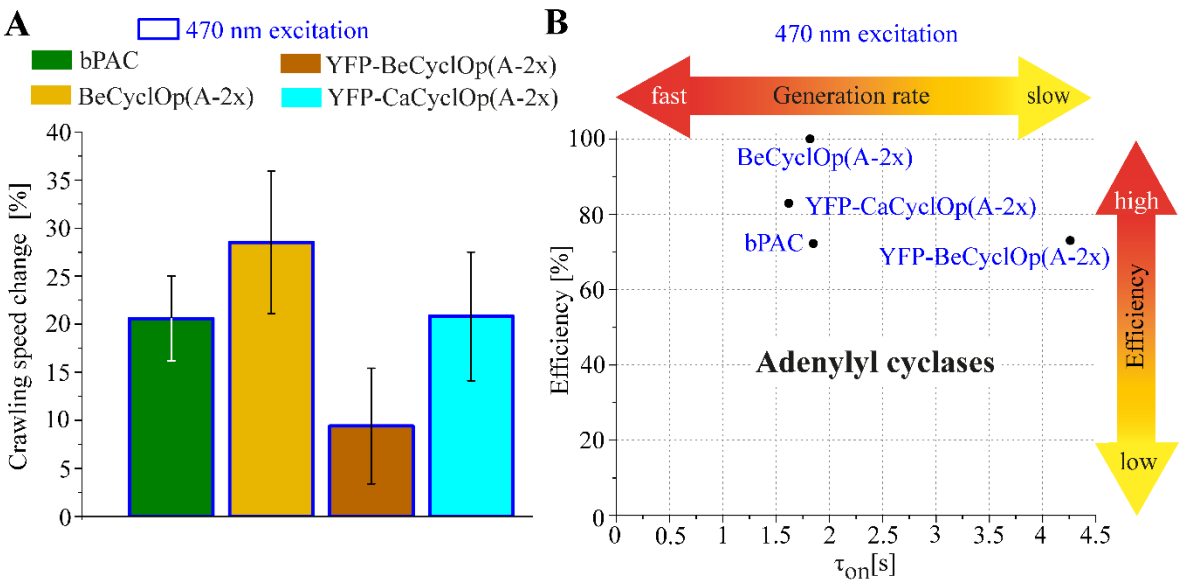

Figure 84: Evaluation of photoactivatable adenylyl cyclases characterized in this thesis. *A) Summary of crawling speed increases evoked by the photoactivatable adenylyl cyclases (bPAC, BeCyclOp(A-2x), YFP-BeCyclOp(A-2x) or YFP-CaCyclOp(A-2x)). Illustrated is the mean normalized crawling speed increase (±SEM) relative to the initial crawling speed of the animal before light exposure. B) Schematic overview of the photoactivatable adenylyl cyclases expressed in cholinergic neurons of C. elegans, categorized by the time course of induced crawling speed increase (proxy for cAMP production rate (τ)) and efficiency. For efficiency calculations, the most effective tool (BeCyclOp(A-2x)) was arbitrarily set as 100 % efficient, and the crawling speed increases for each tool (at 0.2 mW/mm^2; 470 nm) were determined relative to the maximum crawling speed increase induced by the most effective tool. Classification of the tools could be altered by adjusting the expression levels and the applied light intensity. Image adapted and modified from (Henss et al., 2021).*

4.1.3. Multicomponent optogenetic systems for muscle depolarization

Beyond their primary application as optogenetic tools for cNMP generation, the photoactivatable nucleotidyl cyclases can be coupled to CNGCs to manipulate the membrane potential of excitable cells. Depending on the utilized channel, multicomponent optogenetic systems for cell de- or hyperpolarization can be assembled. The benefit of these systems is their reduce need for light, since second messenger generation is accompanied by amplification of the primary signal. Recently, Gao et al., 2015 implemented the first multicomponent optogenetic system for cell depolarization in *C. elegans*, consisting of the excitatory TAX-2/-4 channel and BeCyclOp, that is characterized by a rapid muscle depolarization at very low light intensities. The TAX-2/-4 channel is an intrinsic CNGC that can be found in many *C. elegans* neurons and is composed out of the subunits TAX-2 and TAX-4. Moreover, the channel is mainly gated by cGMP, but also by cAMP at high concentrations (EC_{50}^{cGMP} = 8.4 µM; EC_{50}^{cAMP} = 300 µM), and thus coupling of the channel to the implemented photoactivatable nucleotidyl cyclases should allow cell depolarization of different magnitudes (Komatsu *et al.*, 1999). A further benefit of this system is the relative high conductivity of the TAX-2/-4 channel (56.3 pS), in contrast to ChR2 that has a minor conductance of below 1 pS (Bamann *et al.*, 2008; Feldbauer *et al.*, 2009; Komatsu *et al.*, 1999; Lin *et al.*, 2009; Nagel *et al.*, 2003). However, the multicomponent systems require the expression of three genes (photoactivatable nucleotidyl cyclase and both TAX-2/-4 subunits), which makes them less versatile than ChR2.

Aiming at the expansion of multicomponent optogenetic systems for cell depolarization in *C. elegans*, the TAX-2/-4 CNGC was combined with either wild type CaCyclOp or the engineered membrane-bound photoactivatable adenylyl cyclases and evaluated and compared via body length analysis to the established systems TAX-2/-4; BeCyclOp, TAX-2/-4; bPAC and TAX-2/-4; bPGC (Gao *et al.*, 2015; Nagpal, 2016; Woldemariam *et al.*, 2019). None of the investigated systems were able to evoke comparably strong and fast depolarization effects as the TAX-2/-4; BeCyclOp system (Figure 20 and 36). However, the provoked muscle depolarizations are characterized by different orders of magnitudes and short- and long-lasting effects. Moreover, no desensitization was detected for TAX-2/-4 coupled to CaCyclOp, bPGC or BeCyclOp(A-2x), as it was observed for the system TAX-2/-4;

BeCyclOp. In sum, with this study I established a comprehensive multicomponent optogenetic toolbox for cell depolarization, whereas the systems differ in their efficiency, enzymatic properties, kinetics and short- and long-lasting effects that allows researchers to choose the appropriate tool for their specific application (Figure 85).

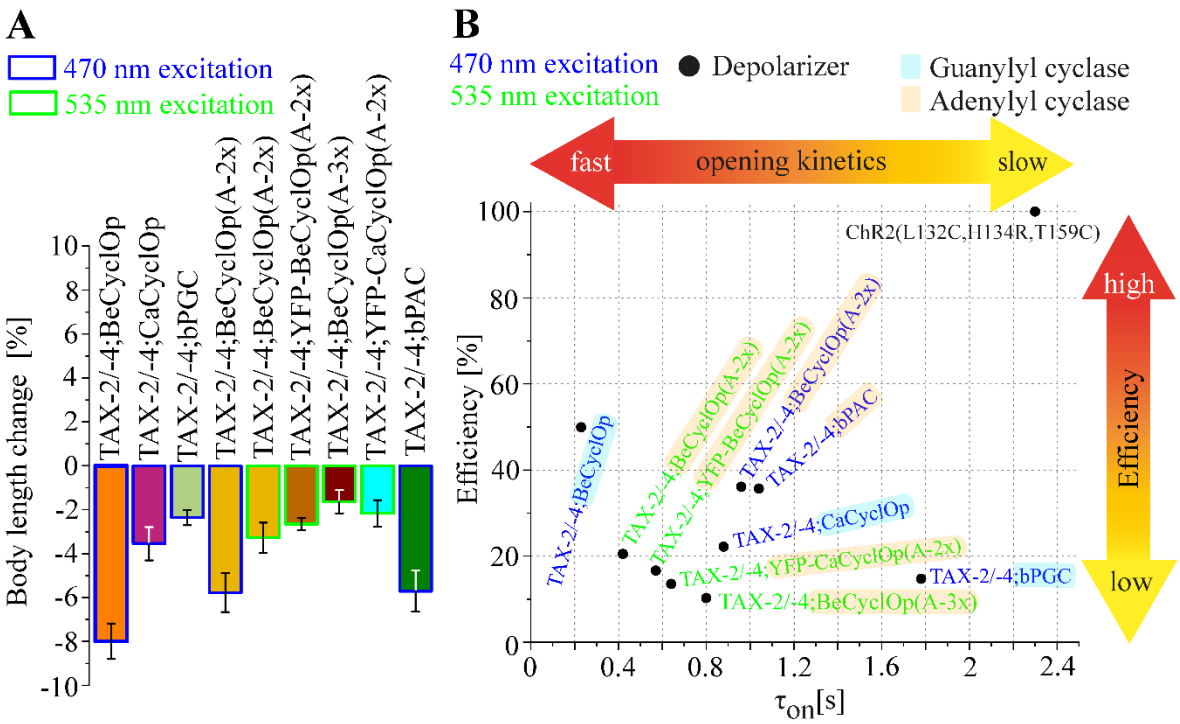

Figure 85: Evaluation of depolarizing multicomponent optogenetic tools characterized in this thesis. *Summary of body length reductions caused by the depolarizing multicomponent optogenetic systems consisting of a photoactivatable nucleotidyl cyclase and the TAX-2/-4 cyclic nucleotide gated channel. Illustrated is the mean normalized body length decrease (±SEM) relative to the initial body length of the animal before light exposure. B) Schematic overview of multicomponent optogenetic depolarizers and ChR2 as `benchmark`, expressed in body wall muscle cells of C. elegans, categorized by the time course of induced muscle contractions (proxy for channel opening kinetics (τ)) and efficiency. For efficiency determinations, the most effective tool (ChR2(L132C, H134R, T159C)) was arbitrarily set as 100 % efficient, and the body length reductions for each tool (at 0.9 mW/mm²; 470 nm; 535 nm) were calculated relative to the maximum body length reduction induced by the most effective tool (Bergs et al., 2018). Classification of the tools could be altered by adjusting the expression levels and the applied light intensity. Image adapted and modified from (Henss et al., 2021).*

4.1.4. Two-component optogenetics for the manipulation of K^+-currents

Complementary to their coupling to the excitatory TAX-2/-4 channel, the photoactivatable nucleotidyl cyclases can be combined with inhibitory CNGCs to hyperpolarize excitable cells based on K^+-currents. For this purpose, the photoactivatable nucleotidyl cyclases were combined with the cGMP-gated K^+-

channel BeCNG1 or the cAMP-gated K^+-channel SthK. The BeCNG1 channel originates from the aquatic fungus *Blastocladiella emersonii*, in which the channel and BeCyclOp are responsible for the phototactic response of the zoospore (Avelar *et al.*, 2015). I adapted this mechanism and assessed its functionality in *C. elegans* body wall muscle cells via body length measurements. Indeed, the system was able to slightly hyperpolarize the cells (~1 % body elongation within ~3 s), an effect that remained even after turning off light (Figure 42). As already mentioned, BeCyclOp is characterized by the generation of a huge amount of cGMP within just a few seconds, and PDE activity in body wall muscle cells is expected to be low, leading to sustained elevated cGMP levels under the applied experimental conditions (15 s light stimulation) (Gao *et al.*, 2015). Hence, to explain the minor induced hyperpolarization of this system, BeCNG1 must be considered in more detail. Analysis of the expression pattern of BeCNG1 depicted an aggregated intracellular appearance in the plasma membrane (Figure 41). However, fluorescence images were acquired using an epifluorescence microscope, and thus an accurate plasma membrane localisation and targeting could not clearly be determined. To examine its distribution and cellular localization more precisely within body wall muscle cells, a confocal microscope would be the method of choice. Since the channel is heterologous expressed, its functionality can be affected on several ways. One the one hand, protein folding can be affected due to the absence of required chaperones, causing misfolding and aggregation of the channel instead of proper folding into its native state. On the other hand, essential post-translational modifications maybe lack in *C. elegans*. Also, the absence of a possibly necessary signal sequence can impair its plasma membrane trafficking and localization. So far, no protein structure of BeCNG1 exists, and thus no conclusion can be drawn on its quaternary protein structure and its occurrence in a homomeric or heteromeric arrangement. Thus, one or more subunits maybe lack that play critical roles for BeCNG1 functionality. Further, the structural mechanism of channel activation upon cGMP binding and subsequent signal propagation causing channel opening remains unclear. Beyond that, the channel was expressed as fusion protein C-terminally tagged with YFP as fluorescence marker, which can promote BeCNG1 aggregation, can impair BeCNG1 properties in its closed state and can influence conformational changes upon cGMP binding. Complementary to its characterization in *C. elegans*, the channel was evaluated by the Nagel group in *Xenopus* oocytes, whereby the channel was

described to be continuously opened and elevated cGMP levels evoked only a slight opening of the channel (Master Thesis A. Hirschhäuser; G. Nagel, personal communication). To investigate the influence of BeCNG1 on body wall muscle cell physiology, A. Hirschhäuser performed swimming behaviour analysis and compared BeCNG1 expressing animals (under the *myo-3* promoter) to the genetic background *lite-1(ce314)*. Here, the animals depicted a 35 % reduced swimming activity compared to the control animals (Master Thesis A. Hirschhäuser). This could either be a hint for a pre-activation of the channel due to intrinsic cGMP and thus a possibly shift in the resting membrane potential of the body wall muscle cells, or a general toxicity of the channel due to its tendency to form protein aggregates that triggers endoplasmic reticulum stress.

A second approach to implement an optogenetic silencing system based on the manipulation of K^+-currents couples the cAMP-gated SthK channel from *Spirochaeta thermophila* with either one of the generated membrane-bound photoactivatable adenylyl cyclases or the soluble bPAC. Recently, the two-component optogenetic silencing system consisting of SthK and bPAC was applied to manipulate K^+-currents in various model organisms (Beck *et al.*, 2018; Bernal Sierra *et al.*, 2018). To assess the functionality of these systems in *C. elegans*, I co-express the SthK channel and either bPAC or one of the membrane-bound photoactivatable adenylyl cyclases in body wall muscle cells and cholinergic neurons and evaluated the systems via swimming behaviour analysis and body length measurements. Amongst the analysed systems, the combinations SthK; bPAC and SthK; BeCyclOp(A-2x) protrude due to their strong and long-lasting hyperpolarization effects. In body wall muscle cells, they evoked body length elongations of ~4 and ~3 %, respectively (Figure 50). Although they did not achieved the maximal body increase as provoked by the `benchmark` hyperpolarizer ACR1 (6.1 %), the initiated effects were long-lasting, i.e. it remained at this level even after turning off light, which was not observed for ACR1 or its `slow` variant ACR1(C102A) (Bergs *et al.*, 2018). Noteworthy, for SthK; bPAC the induced muscle hyperpolarization lasted up to about 10 min after light application (Figure 45). Reason for this could be the lack or low expression level of PDEs in *C. elegans* muscle cells. For ACR1, introduction of the mutation C102A resulted in prolonged current decay (100-fold slower than wild type ACR1) accompanied by a decreased current amplitude (Sineshchekov *et al.*, 2015; Sineshchekov *et al.*, 2016). Application of this variant in body wall muscle cells indeed depicted a reduced maximal body

elongation of 3.4 %, that is 56 % reduced compared to ACR1, and a dramatic decrease in channel closing (τ_{relax} = 26.04 s) (Bergs *et al.*, 2018). Nevertheless, ACR1(C102A) was not able to provoke comparable long-lasting effects as the two-component optogenetic systems SthK; bPAC or SthK; BeCyclOp(A-2x). Summarizing, SthK; bPAC and SthK; BeCyclOp(A-2x) have the benefits to change the distribution of K^+-ions, they require only a short light pulse for activation and can evoke long-lasting effects. In contrary, ACR1 requires a continuous light application, can cause undesired changes in chloride ion distribution, and the `slow` variant ACR(C102A) is not able to provoke comparably long-lasting effects (Bergs *et al.*, 2018; Mahn *et al.*, 2016; Wiegert *et al.*, 2016). In addition to the coupling of SthK to bPAC or BeCyclOp(A-2x), which optogenetically produce a huge amount of cAMP, the channel can be combined with photoactivatable adenylyl cyclases that are characterized by the generation of low levels of cAMP such as BeCyclOp(A-3x) (Figure 39). Interestingly, the SthK; BeCyclOp(A-3x) system provoked the strongest muscle hyperpolarization amongst the analysed systems (~5 %), whereas the effect decays a few seconds after turning off light (Figure 50). Hence, this system represents a useful alternative to ACR1 regarding short-term hyperpolarization. However, termination of the provoked effect is not well controllable as for ACR1 where the animals reached its initial body length nearly after turning off light (Bergs *et al.*, 2018). In general, fast termination of the induced effect is difficult to control for the multicomponent optogenetic systems, in contrast to the established single optogenetic tools where termination is achieved directly either by channel closing or the stop of ion pumping evoked by turning off light, whereas for the two-component optogenetic systems the cNMP must be depleted after light application. No obvious light-dependent behavioural changes were observed for the system SthK; CaCyclOp(A-2x), emphasising CaCyclOp(A-2x)s weak expression, instable conformation and/or poor membrane targeting in *C. elegans* (Figure 50).

Beyond their assessment to hyperpolarize body wall muscle cells, the two-component optogenetic systems were evaluated regarding their ability to silence cholinergic motor neurons of *C. elegans*. Again, the systems SthK; bPAC and SthK; BeCyclOp(A-2x) stick out due do a strong light induced hyperpolarization, i.e. they decreased the swimming frequencies by about 84.4 and 72.3 %, respectively (Figure 48 and 52). However, co-expression of both systems decreased the basal swimming frequencies strongly in comparison to animals, only expressing SthK or the genetic

background *lite-1(ce314)* (Figure 48 and 52). The reduction of the basal swimming rate is discussed in more detail subsequently in this section. Lower light triggered hyperpolarization was observed for the system SthK; BeCyclOp(A-3x), that depicted a reduction of the swimming frequencies of 36 % (SthK [1ng/µl]; BeCyclOp(A-3x) [30 ng/µ]) and 37.5 % (SthK [2.5 ng/µl]; BeCyclOp(A-3x) [100 ng/µl] (Figure 52). However, co-expression of this system reduced the basal swimming rates independently of the injected plasmid concentrations, too.

Examining the expression pattern of the SthK channel in both cell types using an epifluorescence microscope depicted a clustered intracellular appearance in the plasma membrane (Figure 43 and 47). Again, a confocal microscope would be the method of choice to examine the cellular localization of the channel more precisely in body wall muscle cells and cholinergic motor neurons. Expression of the SthK channel alone reduced the basal swimming frequency of the animals, independent of the cell type (body wall muscle cells or cholinergic neurons) (Figure 46 and 48). Reason for this could be a pre-activation of the channel due to intrinsic cAMP, causing a shift of the resting membrane potential of the cells and finally an altered swimming behaviour. Also, a general toxicity of the channel due to the formation of protein aggregates could contribute to the reduced swimming behaviour. The finding, that illumination of animals co-expressing wild type BeCyclOp and SthK caused an increased swimming behaviour and reduced body length argues for a pre-activation of the channel by binding of intracellularly cAMP (Figure 50 and 51). In this context, the generated cGMP upon BeCyclOp activation could act either as an antagonist, or an agonist with low efficacy (Kesters *et al.*, 2015; Schmidpeter *et al.*, 2018). The basal swimming rate is further reduced by co-expression of the channel with the photoactivatable adenylyl cyclases (with exception of BeCyclOp(A-3x) in body wall muscle cells), that highlights the high affinity of SthK for cAMP and a low basal activity of the photoactivatable adenylyl cyclases (Figure 50 and 51). In cholinergic motor neurons and body wall muscle cells, the pre-activation was already substantial in dark for the system SthK; bPAC, wherefor this combination appears of limited use in *C. elegans*, unless researchers aimed on permanent K^+-based inhibition of the desired cell type. Also, the systems SthK; BeCyclOp(A-2x) and SthK; BeCyclOp(A-3x) exhibited substantial pre-activation in dark in cholinergic motor neurons. Expression of YFP-BeCyclOp(A-2x) and low levels of SthK in cholinergic motor neurons restored the basal swimming frequency, however, no light dependent

inhibition was observed (Figure 53). Nevertheless, the system would represent a powerful silencing system for cholinergic motor neurons, as YFP-BeCyclOp(A-2x) is characterized by the generation of high amplitudes of cAMP, and in relation to BeCyclOp(A-2x) depicts less or no dark activity. Thus, the relative expression can be further titrated to achieve an optimum for this system. Concluding, with this thesis I established new two-component optogenetic systems for cell silencing based on the manipulation of K^+-currents, that differ in their efficiency, enzymatic properties, and kinetics (Figure 86).

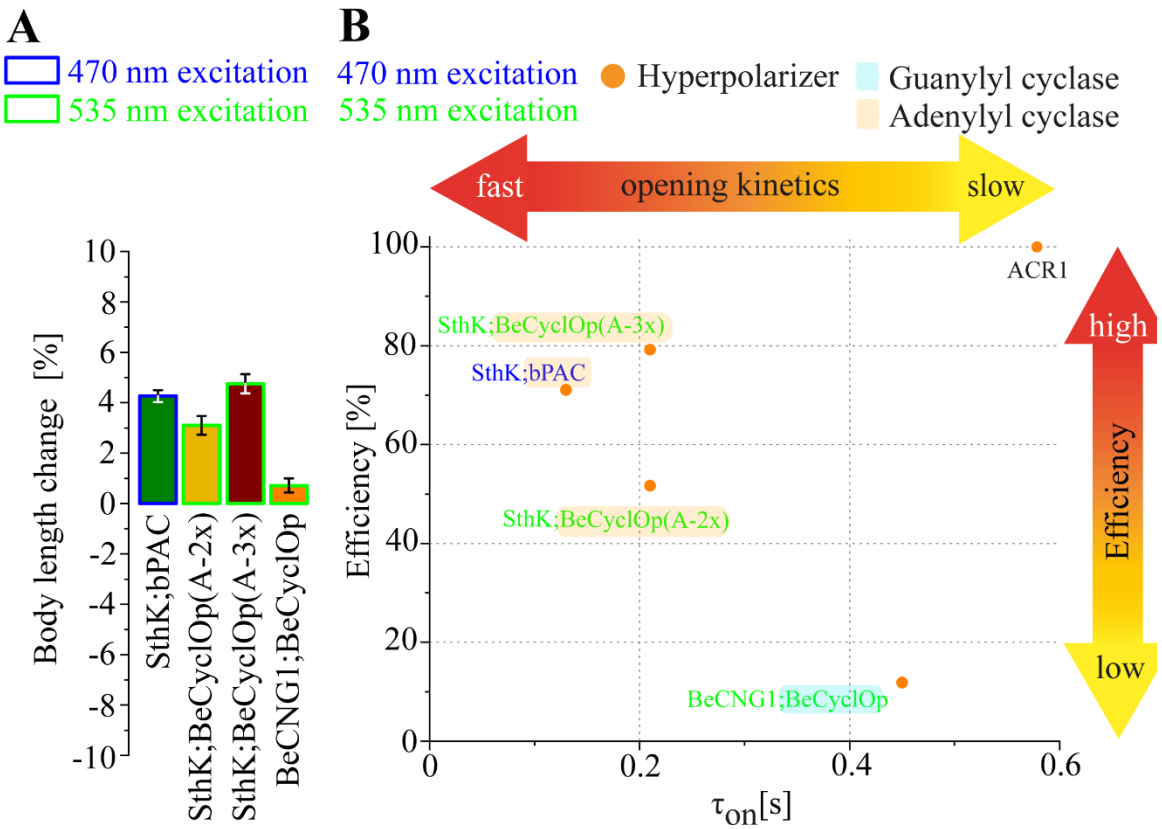

Figure 86: Evaluation of hyperpolarizing two-component optogenetic tools characterized in this thesis. *A) Summary of body length elongations evoked by the hyperpolarizing two-component optogenetic systems consisting of a photoactivatable nucleotidyl cyclase and either the cAMP-gated SthK or the cGMP-gated BeCNG1 cyclic nucleotide gated channel. Illustrated is the mean normalized body length increase (±SEM) relative to the initial body length of the animal before light exposure. B) Schematic overview of two-component optogenetic hyperpolarizers and ACR1 as `benchmark`, expressed in body wall muscle cells of C. elegans, categorized by the time course of induced muscle elongation (proxy for channel opening kinetics (τ)) and efficiency. For efficiency calculations, the most effective tool (ACR1)) was arbitrarily set as 100 % efficient, and the body length reductions for each tool (at 0.9 mW/mm²; 470 nm; 535 nm) were determined relative to the maximum body length increase induced by the most effective tool (Bergs et al., 2018). Classification of the tools could be altered by adjusting the expression levels and the applied light intensity. Image adapted and modified from (Henss et al., 2021).*

4.2. Tandem affinity purification of BeCyclOp monomer and BeCyclOp concatamer

In 2014, BeCyclOp was discovered in the genome of the fungus *Blastocladiella emersonii* where it participates in combination with BeCNG1 in the phototactic response of the zoospore (Avelar *et al.*, 2015; Avelar *et al.*, 2014). BeCyclOp and its orthologue CaCyclOp are members of the Cyclase Opsins, a protein family that belongs together with HKR and RhoPDE to the enzymerhodopsins, a recently discovered class of natural rhodopsins combined to light-regulatable enzyme function (Mukherjee *et al.*, 2019). CyclOps are particular as they combine a rhodopsin domain that is C-terminally fused to a guanylyl cyclase domain, and thus they are of special interest for optogenetic research (Gao *et al.*, 2015; Scheib *et al.*, 2015). Beyond that, CyclOps increasingly come into the focus of many scientists due to their unusual protein architecture, i.e. it's the first known rhodopsin with 8 TM helices and an cytosolic N-terminus (Gao *et al.*, 2015; Scheib *et al.*, 2015). Thus, several questions pertaining this novel protein class needed to be resolved - How are the light-induced changes in the rhodopsin domain transmitted to the guanylyl cyclase domain? What are the functions of the individual domains? How is the guanylyl cyclase domain inhibited in the dark state? What are the spectroscopic properties of the rhodopsin domain? To answer these questions, several research groups tried to purify CyclOps for spectroscopic, biochemical, and structural analysis. However, purification of full-length CyclOps proved to be difficult and posed a problem for the scientists. It was tried to purify full-length BeCyclOp using different expression systems – *E. coli* or *Pichia pastoris*, however it could not be purified in sufficient amount for subsequent analysis (Scheib *et al.*, 2015).

For that reason, the attempt of this thesis was to purify full-length BeCyclOp and a covalently linked BeCyclOp dimer (Concatamer) out of *C. elegans* body wall muscle cells to enable biochemical, spectroscopic, and structural analysis of this novel protein type. For this purpose, the tandem affinity purification method was applied, that is a high affinity strategy which facilitates the purification of low abundant proteins and has successfully applied to purify natively expressed proteins in yeast and in *C. elegans* (Gottschalk *et al.*, 2005; Puig *et al.*, 2001; Rigaut *et al.*, 1999). In my Master Thesis, I successfully confirmed the expression of BeCyclOp::TAP in *C. elegans* muscle cells and could isolate the protein out of a complex mixture of proteins of *C. elegans* solubilizate. To assess the functionality of the fusion protein,

the *in vivo* test system established by Gao et al., 2015 was applied where no major impact on guanylyl cyclase activity was determined (My Master Thesis). To optimize BeCyclOp::TAP solubilization, a detergent screening was performed where highest solubilization was achieved with Triton X-100 (Figure 54). Also, BeCyclOp::TAP was successfully solubilized with the detergents DDM, DM, OG, LDAO and Tween-20, though about 3.4-fold less compared to Triton X-100 (Figure 54 B). No protein solubilization was achieved using OTG as detergent. However, as full-length BeCyclOp was not purified during this thesis and no subsequent functionality assay could be performed, no conclusion can be drawn on a possible negative impact of Triton X-100 on BeCyclOp functionality and an impairment on intermolecular interactions of BeCyclOp dimers. Recently, Trieu et al., 2017 purified full-length BeCyclOp and characterized the protein via spectroscopic and biochemical experiments. For this, they applied HEK293-GnT1^{-} cells as expression system, fused the enzyme to two affinity tags - N-terminally to a C8-tag (PRGPDRPEGIEE) and C-terminally to a 1D4-tag (TETSQVAPA), and solubilized the enzyme with either DM or DDM as detergents (Trieu *et al.*, 2017). Also, BeCyclOps` rhodopsin domain was purified using *Pichia pastoris* as expression system and was solubilized using DDM for spectroscopic analysis (Scheib *et al.*, 2015). Thus, DM and DDM would represent useful alternatives for Triton X-100 to solubilize BeCyclOp out of *C. elegans* membranes. In this work, it was not possible to purify BeCyclOp from crude *C. elegans* extracts via tandem affinity purification. The following issues occurred during purification of full-length BeCyclOp. In the first purification trial, the main amount of BeCyclOp::TAP was present in the IgG-Agarose flow through (Figure 60). This can be explained by an impaired binding of the ProtA portion of the TAP-Tag to the IgG-Agarose beads by the detergent Triton X-100. As a result of this, in a second purification trial a dialysis of the detergent solubilized BeCyclOp::TAP was performed to reduce the concentration of Triton X-100 from 1 to 0.05 %. Indeed, the amount of BeCyclOp::TAP present in the IgG-Agarose flow through strongly decreased which hints at a successful binding of BeCyclOp::TAP to the IgG-Agarose beads (Figure 61). Though, no protein was purified via the second affinity purification step. This can be explained by the following reasons: One the one hand, reduction of the Triton X-100 concentration in BeCyclOp::TAP solubilizates caused partially the precipitation of the protein (Figure 62). On the other hand, elution from the IgG-Agarose via TEV protease was exacerbated due to the applied conditions, i.e. the aliquots were

incubated for 5 h at 4°C. Therefore, it should be possible to purify BeCyclOp::TAP out of *C. elegans* by changing the conditions for TEV cleavage to 16°C for 4 h. Although DM and DDM did not reach the same extend in BeCyclOp::TAP solubilization as Triton X-100, they provide useful alternatives as they were proven to support BeCyclOp functionality (Penzkofer *et al.*, 2017; Scheib *et al.*, 2015; Trieu *et al.*, 2017).

To enable structural analysis of BeCyclOp via cryogenic electron microscopy, a covalently linked BeCyclOp dimer was designed and expressed in *C. elegans* body wall muscle cells and should be purified using the tandem affinity purification method. As fusion protein linker, a $(GGGGS)_4$ was selected to ensure the flexibility of the linked BeCyclOp domains, i.e. of the guanylyl cyclase-terminus of BeCyclOp molecule one and the N-terminus of BeCyclOp molecule two (Chen *et al.*, 2013). Varying plasmid concentrations (15, 50, and 100 ng/µl) were injected for *C. elegans* strain generation and assessed regarding the proper expression of the concatamer via western blot analysis. The full-length protein was identified in 7 of 12 strains that differ in the expression level of the concatamer and the occurrence of by-products (Figure 63). Hence, for subsequent integration of the extrachromosomal array into the genome and following purification of the protein a strain was selected that exhibited no expression of by-products, albeit the strain contained a low expression level of the concatamer. Thereby additional purification steps such as size exclusion chromatography should be prevented that would further cause a loss of protein. To assess the functionality of the concatamer the *in vivo* test system established by Gao et al., 2015 was applied. Here, for the concatamer a lower light-induced muscle contraction was detected compared to the wild type protein (Figure 64). Reason for this could be a possible negative influence of the linker on light-induced conformational changes of the N- and C-terminal domains. In this context, photon absorption and conversion of the rhodopsin moiety into the M signalling state caused conformational changes of the N-terminus i.e. it is proposed to interact with the linker domain or to retract from the β4/5-loop at the guanylyl cyclase moiety, which could be hampered due to the introduction of the $(GGGS)_4$ linker between the N-terminus of one BeCyclOp molecule and the guanylyl cyclase-terminus of the second BeCyclOp molecule (Fischer *et al.*, 2021). However, the reason for this could also be a lower expression level of the concatamer in body wall muscle cells. In this study, it was not possible to purify the BeCyclOp concatamer from crude *C. elegans* extracts

via tandem affinity purification. One main issue emerged for the purification of the concatamer: The protein is cleaved by proteases during homogenization of *C. elegans* membranes into monomers due to a low concentration of applied protease inhibitors. To address this issue the protease inhibitor concentration was increased which successfully prevent cleavage of the concatamer (Figure 65). In sum, by increasing the applied protease inhibitor concentration (8-fold compared to the utilized worm powder) and by adapting the purification protocol changes for TEV protease cleavage, purification of the BeCyclOp concatamer out of *C. elegans* extracts should be possible. Also, detergent screening could be performed to possibly increase concatamer solubilization from *C. elegans* membranes.

4.3. Assessment of CNG-1, CNG-2, CNG-3, CHE-6, EGL-2, and UNC-103 as cAMP effectors in body wall muscle cells

J. Nagpal, a former PhD student in the Gottschalk lab, noticed that optogenetic cAMP production by bPAC in body wall muscle cells caused muscle hyperpolarization, obvious by an increasing body length of the animals. As a possible reason, a cAMP modulated ion channel in the plasma membrane was assumed. For that reason, one attempt of this thesis was to identify a cAMP modulated ion channel that participates in cAMP provoked muscle hyperpolarization. Sequence alignment of the PKA´s regulatory subunit Riα against the *C. elegans* genome identified four CNG ion channels (CNG-1, CNG-2, CNG-3, and CHE-6) and two voltage-gated potassium channels (EGL-2 and UNC-103) as possible cAMP effectors. To investigate the impact of the cellular generation of cAMP on muscle hyperpolarization, the influence of membrane proximal (BeCyclOp(A-2x)) and cytosolic (bPAC) cAMP production on the body length of the animals were examined (Figure 68). Activation of both enzymes caused body elongations of ~2 %, and thus optogenetic cAMP induced muscle hyperpolarization is triggered independent of the cellular generation of cAMP. However, to more accurately determine possible differences between membrane proximal and cytosolic optogenetic cAMP generation and their influence on cAMP provoked muscle hyperpolarization, further behavioural readouts should be evaluated e.g. the crawling speed and mean body bending on solid media using the worm tracker as previously described (Stirman *et al.*, 2011). Because only slight body length elongations are caused by optogenetic cAMP generation which would further

hampers to detect differences between wild type and mutant backgrounds, A. Pieragnolo assessed the impact of cAMP induced muscle hyperpolarization on *C. elegans* swimming behaviour, as this behavioural readout is more sensitive compared to the body length measurement. Indeed, 30 s bPAC activation (0.2 mW/mm^2; 470 nm) strongly decreased the swimming frequency of the animals by 66.7 % wherefore this experiment was utilized as complementary assay for the screening of cAMP effectors (Figure 69). Complementary to the investigation of cAMP provoked muscle hyperpolarization in *lite-1(ce314)* background, the mechanism was assessed in wild type background to evaluate it more close to the natural genetic and physiological conditions. Under the use of the same experimental conditions (5 s before light, 15 s during light, 5 s after light; 0.9 mW/mm^2; 470 nm), no body elongation was detected (Figure 73 A). This could be explained by the intrinsic photophobic response of the animals, triggered by blue light sensation by the ultraviolet/blue-light sensor LITE-1, that caused an escape behaviour of the animals that counteracts the cAMP induced muscle elongation (Edwards *et al.*, 2008). Consequently, the experimental set-up was changed in two ways – For one experiment, the light pulse duration was decreased to 5 s to limit the activation of the phototactic response to a short time frame. Also, to enable the detection of the body elongation, the measurement after light application was extended to 113 s. For a second experiment, the duration of the light pulse was extended to 113 s to constantly increase the cAMP level and to force cAMP induced muscle elongation and thus to overwrite the counteracting escape response of the animals. Indeed, body elongations were observed using both experimental set-ups, whereas for the short light pulse accompanied with the generation of a low level of cAMP, a maximal body elongation of 3 % and for the long light pulse associated with high optogenetic cAMP levels an elongation of 6 % were measured (Figure 74). To complement the characterization of cAMP provoked muscle hyperpolarization in wild type animals, the influence of bPAC activation on the swimming behaviour of the animals was assessed where a 60 s light pulse caused a strong reduction of about 75 %, that sustained for further 60 s (Figure 73 B, C). This strong light-induced reduction is comparable to the results in *lite-1(ce314)* background obtained by S. Zhou in her BSc Thesis and that were also measured using the `Multi Worm Tracker` (Figure 71). To more accurately characterize the cAMP induced muscle hyperpolarization and its impact on the *C. elegans* swimming behaviour, experiments with an extended

recording after light application (>60s) have to be performed to determine the recovering of the basal swimming rate and thus the temporal extent of cAMP provoked muscle hyperpolarization. In sum, optogenetically induced muscle hyperpolarization caused obvious behavioural changes of *C. elegans*, i.e. an elongation of the body length (3-6 %) and a reduction of the swimming rate (75 %). The provoked muscle elongation persists for at least 113 s after light application (5 s light pulse; 0.9 mW/mm^2; 470 nm) and the swimming frequency reduction persists for at least 60 s (60 s light pulse; 0.9 mW/mm^2; 470 nm) after light application.

To evaluate the selected ion channels as potential cAMP effectors in cAMP provoked muscle hyperpolarization, with the help of A. Pieragnolo and S. Zhou, bPAC expressing strains (using the promotor *pmyo-3*) in the following genetic backgrounds were created – channel loss of function, and channel loss of function; *lite-1(ce314)*. Investigation of optogenetically induced muscle hyperpolarization and its impact on the body length in channel loss of function; *lite-1(ce314)* background was performed by S. Zhou in her BSc thesis. Here, no or only minor body elongations (~1 %) were caused in channel loss of function; *lite-1(ce314)* backgrounds as a result of optogenetic cAMP generation in body wall muscle cells, that did not reach the extent provoked in the *lite-1(ce314)* control (~2.5 %) (Figure 70). Thus, these results could be a hint for a possible modulatory role of the channels in cAMP induced muscle hyperpolarization.

The study of optogenetically induced muscle hyperpolarization on swimming behaviour of strains with loss of function channel; *lite-1(ce314)* background was performed by S. Zhou in her BSc thesis. Here, for most mutant strains strong swimming frequency reductions were observed (~52 - 72 %), though they did not reach the extent as detected for the *lite-1(ce314)* control and the mutant *egl-2(rg4); lite-1(ce314)* (~77 %) (Figure 71). In contrast, only a small cAMP induced reduction in swimming frequency was detected for the *unc-103(n1213); lite-1(ce314)* background (21 %) (Figure 71). As this result highlights UNC-103 as cAMP effector in cAMP-induced muscle hyperpolarization, the strain was selected for a more detailed investigation via body length analysis. For this purpose, I have adapted the experimental set-up in two ways. For one measurement, the light pulse was abbreviated to 5 s, whereas the low optogenetic cAMP level should mimic more the physiological conditions, and an extended recording after light to detect the slow increasing body length over the time.

For a second measurement the duration of the light pulse was prolonged to 113 s to force cAMP induced muscle hyperpolarization due to constant cAMP production. Whereas in the first measurement bPAC activation caused similar body elongations in *lite-1(ce314); unc-103(n1213)* and in the *lite-1-(ce314)* control, in the second approach differences in the provoked body elongations were detectable, i.e. the body length increased stronger (~6 vs ~4 %) and faster (reaching of the plateau: 15 vs 55 seconds after turning off light) in the *lite-1(ce314)* control than in *lite-1(ce314); unc-103(n1213)* (Figure 72). Though no statistical analysis due to a low number of measured animals could be performed, the result gives a hint of a possibly participating role of UNC-103 in cAMP provoked muscle hyperpolarization. In channel loss of function mutants, optogenetic cAMP generation strongly reduced the swimming cycles for all strains (~64 - 89 % after 60 s light application; 470 nm; 0.2 mW/mm^2), whereby for the mutants *che-6(e1126)IV* (60 %), unc-103(n1213) (64 %), *egl-2(rg4)* (64 %) and *cng-3(jh113)* (67 %) the reductions reached not the extend as the wild type control (75 %) (Figure 82). In contrast, stronger swimming cycle reductions were detected for the mutants *cng-2(tm4267)* (82 %) and *cng-1(jh111)* (89 %). Summarizing the results of both swimming behaviour analyses, for CNG-3, CHE-6, and UNC-103, bPAC activation caused minor swimming rate reductions in channel loss of function and channel loss of function; *lite-1(ce314)* backgrounds compared to the controls *lite-1(ce314)* and wild type. For EGL-2, optogenetic cAMP generation provoked a similar swimming frequency reduction in double mutant background as in the *lite-1(ce314)* control, but a smaller reduction in the channel loss of function mutant as in the wild type control. For CNG-1 and CNG-2, bPAC activation induced minor swimming rate reductions in double mutant backgrounds as in the *lite-1(ce314)* control, but stronger reductions in channel loss of function backgrounds as for the wild type control.

This enables the following classification of the ion channels as possible cAMP effectors in cAMP induced muscle hyperpolarization: Functional CNGCs consist of one to four α-subunits and a variable number of β-subunits (Pifferi *et al.*, 2006). Their properties depend on the subunit composition, whereas they can differ in their cNMP affinity, channel opening and closing, and ion permeability (Ferkey *et al.*, 2021; Komatsu *et al.*, 1999; O'Halloran *et al.*, 2017). *C. elegans* expresses six CNGCs that are assigned as α-subunits (CNG-1, CNG-3, and TAX-4) or β-subunits (CNG-2, CHE-6, and TAX-2) (Wojtyniak *et al.*, 2013). As mentioned previously, optogenetic cAMP production in body

wall muscle cells of CNG-3 and CHE-6 mutants caused minor swimming frequency reductions compared to the *lite-1(ce314)* and wild type controls. Although CNGCs are primary associated with the depolarization of excitable cells, the results provide evidence for a possible contribution of CNG-3 and CHE-6 to cAMP induced muscle hyperpolarization. Both subunits are predicted to be non-selective cation channels, with both having conserved residues of the selectivity filter motive TIGE in the pore helix domain (Appendix Figure 90). In *C. elegans* AFD neurons, CNG-3 and SLO K^+-channels were shown to contribute together to neuronal hyperpolarization. It is proposed that SLO-1/SLO-2 co-localises with a CNGC (including CNG-3) in microdomains where activation of the CNGC evokes a local influx of Ca^{2+}. This local increase of calcium ions triggers the activation of the SLO-1/SLO-2 K^+-channels and causes hyperpolarization of AFD neurons (Aoki *et al.*, 2018). Thus, it seems possible that CNG-3 and/or CHE-6 forms a functional heteromeric CNGC in *C. elegans* body wall muscle cells that co-localizes with SLO-1 and SLO-2 and that contributes to cAMP induced muscle hyperpolarization. Interestingly, expression of bPAC in body wall muscle cells of the mutant backgrounds *cng-3(jh113)* and *che-6(e1126)* reduced the basal swimming frequencies in both cases (Figure 81). Reason for this could be the overexpression of the respective other channel subunit, or an additional subunit contributing to the CNGC, that is activated by the dark activity of bPAC. It is also possible that the respective homomeric CNGC has a high cAMP affinity that is reduced in the heteromeric channel. For CNG-1 and CNG-2, contradicting results were obtained in both swimming behaviour analyses wherefore it seems unlikely that they play a vital role in cAMP evoked muscle hyperpolarization. Though, it cannot be excluded that they contribute to the proposed CNG-3/CHE-6 CNGC in body wall muscle cells. However, expression of CNG-1, CNG-2, CNG-3, and CHE-6 has not been confirmed in body wall muscle cells, neither experimentally nor by CeNGEN (Table 23).

EGL-2 is highly homologous to *Drosophilia ether-à-go-go* (eag) proteins and therefore presumably functions as voltage-gated potassium channel. They exhibit 54 % sequence similarity in the N-terminus, 75 % in the transmembrane and pore domain, and 81 % in the CNBD (Weinshenker *et al.*, 1999). *Egl-2(rg4)* mutants exhibited a reduced basal swimming rate compared to wild type animals (Figure 81). Reason for this could be that the absence of the channel causes a change in ion concentration gradients across the membrane in the cell type in which it is expressed. Because EGL-2 is expressed in sensory neurons and lumbar neurons (e.g., PVC), it is likely that the shift in ion

concentrations alters neuronal communication and further affects the swimming behaviour of the animal. Another reason could be that EGL-2 contributes to the setting of the resting membrane potential of body wall muscle cells, as has been reported for ERG channels, and that its absence causes a shift in membrane potential that leads to an impaired locomotor behaviour (Akbarali *et al.*, 1999; Shoeb *et al.*, 2003). Optogenetic cAMP generation resulted in a smaller reduction of the swimming rate in the channel loss of function mutant (64 %) than in the wild type control (75 %), whereas similar swimming speed reductions were observed for the *lite-1(ce314)* control and the mutant *egl-2(rg4); lite-1(ce314)* (~77 %). Reason for this may be that EGL-2 could contribute to cAMP induced muscle relaxation, or that the lack of EGL-2 expression is compensated by the overexpression of potassium channels with overlapping functions and that are involved in cAMP induced muscle hyperpolarization. Nevertheless, expression of EGL-2 in body wall muscle cells has not been confirmed experimentally and by CeNGEN, thus its contribution to *C. elegans* body wall muscle physiology appears unlikely (Table 23).

To date, little is known about the channel characteristics, quaternary structure, and the physiological functions of UNC-103. The protein is highly homologous to hERG (*human ether-a-go-go-related gene*), which is the pore-forming subunit of a delayed rectifier voltage-gated K^+ channel, also known as I_{Kr} or Kv11.1 (Garcia *et al.*, 2003; Gutman *et al.*, 2003). The channel consists of 6 transmembrane helices (S1-S6), whereas the helices (S1-S4) build the voltage-sensing domain and the helices S5-S6 together with the intervening pore loop contributes to the pore domain formation. hERG is functional as tetramer whereby the ion conduction pathway is formed by the pore domains of the four subunits. N-terminally it contains a Per-Arnt-Sim (PAS) domain, a unique feature of the *ether-a-go-go*-subfamily, and C-terminally it comprises a CNBD (Vandenberg *et al.*, 2012; Warmke *et al.*, 1994). hERG and UNC-103 exhibit ~70 % sequence similarity in the transmembrane helices S1-S6, the pore forming domain and the CNBD (Collins *et al.*, 2013; Reiner *et al.*, 2006) (Appendix Figure 89). In contrast to other ERG and EAG channels, UNC-103 lacks the N-terminal PAS domain but contains a PDZ motif at its C-terminus (Reiner *et al.*, 2006). The activity of hERG has been shown to be regulated by direct binding of cAMP and by phosphorylation by PKA, but whether it activates or inhibits hERG activity remains unclear, as research has presented conflicting results (Cui *et al.*, 2001; Cui *et al.*, 2000; Shu *et al.*, 2013; Thomas *et al.*, 1999). ERG channels mediate a variety of physiological functions, whereby the contribution of hERG to the repolarization of the

cardiac action potential via the delayed rectifier K^+-current (I_{Kr}) is best studied (Appendix Figure 92) (Grant, 2009). Beyond that, ERG channels are involved in maintaining the resting membrane potential of a variety of excitable cells, e.g. in smooth muscle of the stomach, colon, and oesophageal, but also in neuroendocrine cells or neuroblastoma cells (Akbarali *et al.*, 1999; Arcangeli *et al.*, 1996; Bauer, 1998; Ohya *et al.*, 2002; Shoeb *et al.*, 2003). Based on its homology to hERG, UNC-103 might exert the following physiological functions in body wall muscle cells of *C. elegans*: It might participate in the setting of the resting membrane potential and/or contribute to the repolarization of the body wall muscle cells (Figure 87). Interestingly, the gain-of-function mutation *unc-103(e1597)* causes a reduced excitability of vulval and protractor muscles, presumably due to the efflux of potassium ions and muscle hyperpolarization (Collins *et al.*, 2013; Garcia *et al.*, 2003; Petersen *et al.*, 2004; Reiner *et al.*, 1995). The gain-of-function mutant is based on the mutation A331T in transmembrane helix 6 (S6), which is thought to affect channel gating of UNC-103 (Reiner *et al.*, 2006). A homologous gain-of-function mutation can be found in the hERG channel (A653), whereby the mutation causes an increased efflux of K^+ (Appendix Figure 89) (Stepanovic *et al.*, 2009). Moreover, the loss of function mutation *unc-103(sy673)* and the null mutation *unc-103(n1213)* causes a mild hyper-excitability of vulva muscles and protractor muscles, respectively (Collins *et al.*, 2013; Garcia *et al.*, 2003). Regulation of *C. elegans* egg laying is achieved by alternating between two behavioural states, the inactive phase and the serotonin-triggered active phase. During the inactive phase, the vulval muscles are less excitable to prevent muscle contraction and egg laying. It is proposed that UNC-103 is responsible for the reduced excitability of the vulval muscle in the inactive phase, and that serotonin initiates the active phase via G-protein signalling and possible activation of EGL-19 and/or inhibition of UNC-103 (Collins *et al.*, 2013). Moreover, UNC-103 contributes to the regulation of the contractile behaviour of protractor muscles in males before and during mating, whereby it supresses the protractor muscles to contract until mating signals are sensed (Garcia *et al.*, 2003).

Hence, the physiological function of UNC-103 in body wall muscle might be to adjust the resting membrane potential and to regulate muscle excitability under certain circumstances (Figure 87). Under normal conditions, the channel exists in its closed state and thus does not affect the resting membrane potential. However, it cannot be excluded that the channel is in an open conformation and allows weak conduction of

potassium ions. Sensing of an external signal is the trigger for the change in muscle excitability: The signalling molecule binds to an GPCR and provokes the activation of the heteromeric G-proteins. The activated Gα subunit activates an adenylate cyclase which produces cAMP out of ATP. The second messenger cAMP in turn triggers the activation of UNC-103 and its transition into the open state. Here, different types of activation are possible: cAMP can directly bind to UNC-103 and induce channel-opening and/or indirectly activate the channel via PKA phosphorylation. Also, activation of the channel might be triggered by voltage-sensing by the proposed voltage-sensing domain of UNC-103, and cAMP binding could stimulate channel conductance. If the channel is in an open state that allows weak conductance of K^+, binding of cAMP could increase channel conductance. Since *unc-103(n1213)* bPAC and *unc-103(n1213); lite-1(ce314)* bPAC animals still exhibited a decreasing swimming frequency upon bPAC activation, at least one additional ion channel which is either directly and/or indirectly regulated by cAMP must be involved in cAMP induced muscle hyperpolarization. Possible potassium channel candidates that might contribute to the setting of the resting membrane potential could be the channels IRK-1 and/or IRK-3. These channels are homologous to the G-protein-gated inwardly rectifying potassium channel (Kir3/Girk) and are expressed at low levels in body wall muscle cells according to CeNGEN (Hammarlund *et al.*, 2018). These channels are coupled to GPCRs and are activated by the Gβγ subunits that evokes the efflux of K^+-ions (Jeremic *et al.*, 2021). An additional contribution might be made by the proposed heteromeric channel UNC-93/SUP-9/SUP-10, which depicts gene expression in body wall muscle according to CeNGEN (Hammarlund *et al.*, 2018). The channel is proposed to form a native channel complex, analogous to the heterooctameric K_{ATP} channels that consist of the inwardly rectifying potassium channel subunit Kir 6.x and sulfonylurea receptor subunits (Hibino *et al.*, 2010; Salkoff *et al.*, 2005). These channels are activated via phosphorylation by protein kinase A and C, whereby this modulation plays an important role in smooth muscles (Béguin *et al.*, 1999; Lin *et al.*, 2000; Nelson *et al.*, 1995; Quinn *et al.*, 2004). In addition, K_{ATP} channels couple the cellular metabolism to the movement of potassium ions across the membrane, sensing the depletion of ATP that triggers channel activation (Proks *et al.*, 2004). In conclusion, activation of the potassium channels could lower the resting membrane potential by the efflux of K^+ and thus regulate muscle excitability.

To consider a possible contribution of UNC-103 to body wall muscle repolarization, the gating mechanism of hERG in cardiac action potential must be considered in more detail. In contrast to other voltage-gated potassium channels, the channel is characterized by a slow voltage-dependent transition between the closed and open state (~60 ms at +60 mV) and a fast voltage-dependent transition between the open and inactivated state (1 – 2 ms at + 60 mV) (Shi *et al.*, 2020). This results in a slow transition from the closed to the open conformation and subsequently a rapid inactivation upon membrane depolarization, and conversely a rapid rescue from the inactivated state to the open state followed by a slow conversion into the closed state upon membrane repolarization. As a result, the channel closes slowly during terminal repolarization and remains open for a considerable period until the resting membrane potential has been restored (Shi *et al.*, 2020; Vandenberg *et al.*, 2012). Assumed that UNC-103 contributes to the repolarization of the body wall muscle cells, the channel would be in its closed conformation at the resting potential. Depolarization of the muscle cells and increase of membrane voltage is sensed by the proposed voltage-sensing domain of UNC-103 and causes the slow transition into the open state followed by its rapid inactivation. Subsequent repolarization triggers its fast reactivation from the inactive state and the conduction of potassium ions until the initial resting membrane potential has been restored. Because the transition from the open to the closed state is slow, UNC-103 may be a preferred target for the cell to modulate resting membrane potential and membrane excitability according to the mechanisms described above. However, in *C. elegans* body wall muscle repolarization of the action potential is primary mediated by the potassium channels SHK-1 (also termed Kv1) and SLO-1/SLO-2, wherefore a minor contribution of UNC-103 to the repolarization should be expected (Gao *et al.*, 2022; Gao *et al.*, 2011; Liu *et al.*, 2011). Thus, the primary function of UNC-103 in body wall muscle cells may be to adjust the membrane potential to reduce muscle excitability.

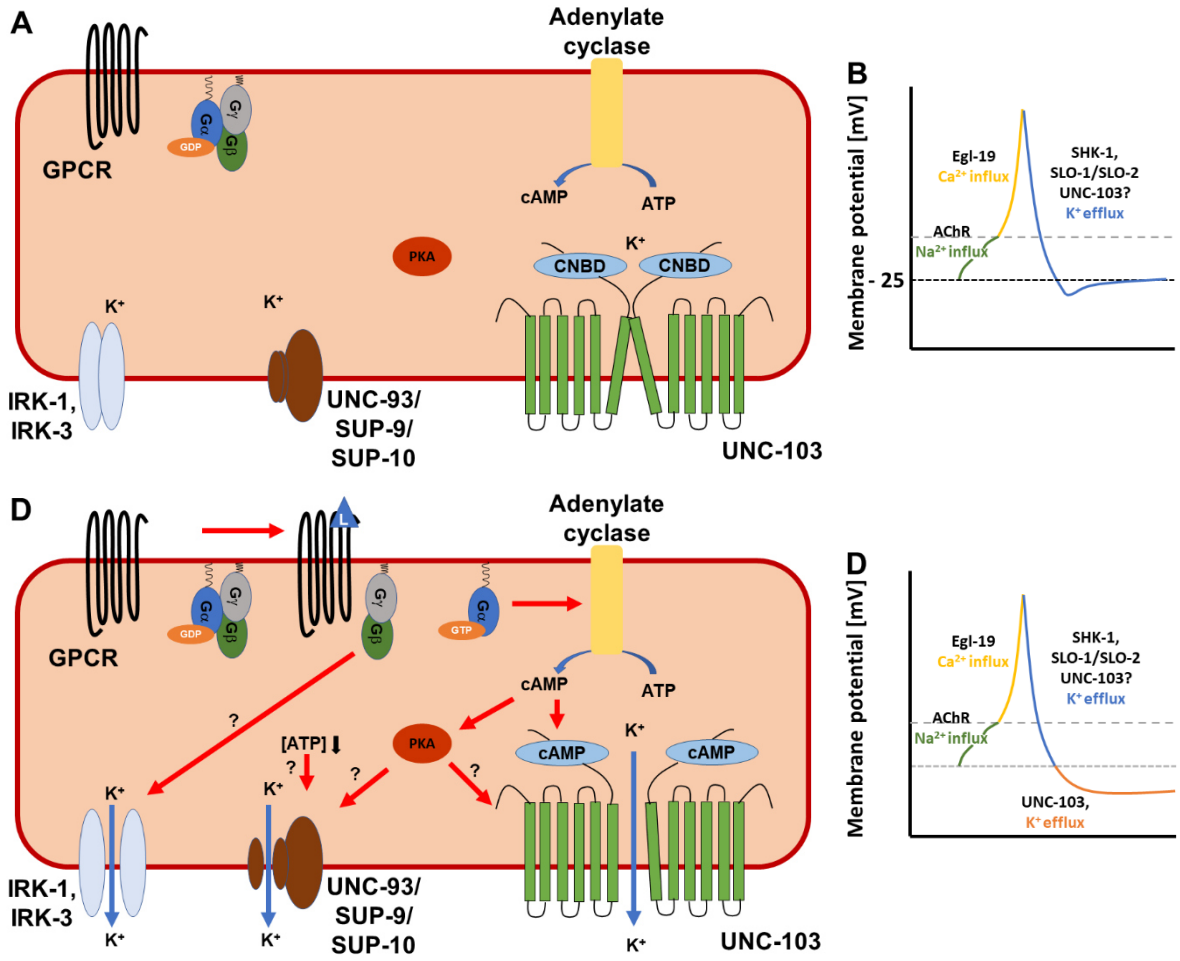

Figure 87: Proposed model for the physiological function of UNC-103 in body wall muscle cells. *A, B) Under normal conditions, UNC-103 exists in its closed state and the resting membrane potential is unaffected. C, D) Binding of an external ligand to a GPCR initiates G-protein coupled signalling that leads to the formation of cAMP by an adenylate cyclase. Elevated cAMP levels activate UNC-103 by direct binding and/ or indirectly via PKA, causing the efflux of K^+. Muscle hyperpolarization could be supported by the activation of IRK1 and/ or IRK-3 via $G\beta\gamma$, as well as by the activation of UNC-93/SUP-9/SUP-10 by PKA or ATP depletion. cAMP induced muscle hyperpolarization could reduce the resting membrane potential to regulate muscle excitability.*

4.4. Outlook

4.4.1. Optogenetic tools for cNMP generation functionally coupled to CNGCs for cell de- and hyperpolarization

Membrane-proximal cAMP generation by the implemented membrane-bound photoactivatable adenylyl cyclases may activate cAMP-dependent signalling more specifically than cytosolic production by bPAC. This will enable to investigate cAMP signalling and the corresponding cellular and behavioural responses in *C. elegans*

closer to natural physiological conditions. Application of the implemented membrane-bound photoactivatable adenylyl cyclases will support to explore neuropeptidergic signalling, learning and memory formation, cell growth and differentiation, or cellular metabolism (Liu *et al.*, 2017; Rahmani *et al.*, 2021; Steuer Costa *et al.*, 2017; Yu *et al.*, 2017). In addition, the application of CaCyclOp will allow fine-tuning of cGMP levels, which will support the study of cGMP-mediated processes such as sensory signalling and plasticity or the regulation of dauer arrest (Bargmann *et al.*, 1991; Birnby *et al.*, 2000; Fielenbach *et al.*, 2008; Schultheis *et al.*, 2011). Specific subcellular targeting of the photoactivatable nucleotidyl cyclases may further promote the studies by enabling cNMP signalling closer to the natural occurring nanodomains.

Beyond that, the functional properties of CyclOps such as the light sensitivity or the absorption spectrum can be altered by using retinal analogues (Appendix Figure 98 and 99) or by introduction of the homologous ChR2 mutations C128S (BeCyclOp(C159)) and D156A (BeCyclOp(D283)) (AzimiHashemi *et al.*, 2014; Bamann *et al.*, 2010; Yizhar *et al.*, 2011). Because the signal provoked by the photoactivatable nucleotidyl cyclases alone or in combination with CNGCs decays slowly in cell types lacking PDEs, they could be combined with the red-light activated phosphodiesterase to accelerate termination of the effect (Gasser *et al.*, 2014). Moreover, the multicomponent systems comprising TAX-2/-4 can further be modified by changing the subunit composition of the CNGC to adjust characteristics such as cNMP affinity or channel closing. Here, *in vitro* experiments showed that the homomeric TAX-4 channels exhibited a 10-fold higher cGMP affinity and stay open seven times as long as the heteromeric TAX-2/-4 channel (Komatsu *et al.*, 1999; O'Halloran *et al.*, 2017). The BeCyclOp; TAX-4 system would have the advantage of requiring lower light intensity for excitation, causing prolonged membrane depolarization, and sparing the expression of another gene (*tax-2*). Moreover, the two component optogenetic silencing systems comprising SthK can be improved by mutating specific residues in the cAMP binding pocket of SthK to generate SthK variants with decreased cAMP affinity. Another modification could be to change its nucleotide specificity to cGMP by mutating the 2 – 3 key amino acids in the active site (Ryu *et al.*, 2010; Scheib *et al.*, 2018). Altering the cNMP properties of SthK will create a more controllable optogenetic silencing tool that can be used in cell types with intrinsic cAMP and thus could have broader application.

4.4.2. Purification of BeCyclOp for biochemical and structural analyses

Until now, no full-length protein structure of a member of the novel Cyclase Opsin protein family exists, although a recent work by the Hegemann group that based on *AlphaFold2* provides a useful model of CaCyclOp (Fischer *et al.*, 2021). Hence, several question pertaining this protein family remains unresolved, i.e. how is the light-absorption by the rhodopsin domain coupled to the generation of cGMP by the guanylyl cyclase domain? How is the guanylyl cyclase activity regulated in the dark state and what are the functions of the individual domains in CyclOp dimers? To this end, purification and subsequent structural analysis of BeCyclOp should further be pursued. Purification of BeCyclOp and the stabilized BeCyclOp concatamer out of *C. elegans* can be attempted by adjusting the TEV protease cleavage conditions (increasing the temperature to 16°C) and by increasing the protease inhibitor concentration (for concatamer purification). Although the detergents DM and DDM did not achieved a comparably high solubility of BeCyclOp as Triton X-100, they can be used as alternatives since they are known to support its functionality (Penzkofer *et al.*, 2017; Scheib *et al.*, 2015; Trieu *et al.*, 2017). Alternatively, the expression and purification methods implemented by Trieu et al., 2017 (for BeCyclOp) or by Fischer et al., 2021 (for CaCyclOp) can be applied.

4.4.3. Investigation of cAMP induced muscle hyperpolarization in *C. elegans*

The finding that *C. elegans* uses cAMP as second messenger in body wall muscle cells to trigger muscle hyperpolarization opens another area of research in this nematode. Although swimming behaviour analysis identified UNC-103, CNG-3, and CHE-6 as possible cAMP effectors contributing to muscle hyperpolarization, many questions remained unresolved, i.e. crucial proteins involved in the pathway, the initiating signal and the neuron(s) responsible, or the fundamental behavioural response to the signal. Neuropeptides, particularly FMRFamide-related peptides, are promising candidates to act as the first messenger, as several of them have been shown to inhibit or increase the frequency of the pharyngeal action potential (*flp-1*, *flp-3*, *flp-9*, *flp-13*, *flp-16*), to affect locomotion and egg-laying behaviour (*flp-1*), or to inhibit locomotion and pharyngeal pumping (*flp-11*) (Li *et al.*, 2008; Nelson *et al.*,

1998; Steuer Costa *et al.*, 2019; Waggoner *et al.*, 2000). As a corresponding GPCR in body wall muscle cells, the receptor NPR-5 might be a candidate (Li *et al.*, 2014). *C. elegans* contains a multitude of heteromeric G-proteins, whereas the proteins GSA-1, EGL-30, GOA-1, GPA-7, GPA-4 come into consideration as the stimulating Gα subunit in cAMP induced muscle hyperpolarization. While the proteins GPC-1 and GPC-2 are candidates for the Gγ subunit, the proteins GPB-1 and GPB-2 may function as interacting Gβ subunit. Possible candidates for the membrane-bound adenylyl cyclase are the cyclases ACY-1 and ACY-3, whose activation results in the formation of the second messenger cAMP, which could activate KIN-1, the corresponding PKA. Complementary to the putative activation of UNC-103, CNG-3, and CHE-6, muscle hyperpolarization could be promoted by the potassium channels IRK-1, IRK-3 and UNC-93/SUP-9/SUP-10. However, contribution of further potassium channels cannot be excluded. For investigation of the stimulatory neuropeptide, the peptides can be externally applied to the animals and their effect on the locomotion behaviour and body length can be assessed. After identification of the signalling neuropeptide, this experiment can serve as starting point for the identification of the corresponding receptor, adenylyl cyclase, and heteromeric G proteins, whereby possible candidates can be knocked out via RNA interference. To identify the responsible protein kinase and other potassium channels, the swimming behaviour analysis experiment used in this work can be applied. In addition, UNC-103 can be analysed electrophysiologically in *Xenopus* oocytes and the influence of cAMP on its functionality be evaluated. Also, the cAMP induced hyperpolarization can be studied electrophysiologically in dissected animals, while the process can be triggered optogenetically via bPAC or by external application of the identified neuropeptide.

5. References

Aamodt E, Aamodt S (2005). Neural Specification and Differentiation. *International Review of Neurobiology* **69:** 73-97.

Ahmad M, Cashmore AR (1993). HY4 gene of A. thaliana encodes a protein with characteristics of a blue-light photoreceptor. *Nature* **366:** 162–166.

Akbarali H, Thatte H, He XD, Giles W, Goyal RK (1999). Role of HERG-like K(+) currents in opossum esophageal circular smooth muscle. *Am J Physiol* **6:** 1284-1290.

Akerboom J, Carreras Calderon N, Tian L, Wabnig S, Prigge M, Tolo J*, et al.* (2013). Genetically encoded calcium indicators for multi-color neural activity imaging and combination with optogenetics. *Frontiers in molecular neuroscience* **6:** 2.

Altenhofen W, Ludwig J, Eismann E, Kraus W, Bönigk W, Kaupp UB (1991). Control of ligand specificity in cyclic nucleotide-gated channels from rod photoreceptors and olfactory epithelium. *Proc. Nadl. Acad. Sci.* **88:** 9868-9872.

Altun ZF, Hall DH (2009a). Introduction. *WormAtlas*.

Altun ZF, Hall DH (2009b). Muscle system, introduction. *WormAtlas*.

Altun ZF, Hall DH (2011). Nervous system, general description. *WormAtlas*.

Anton SE, Kayser C, Maiellaro I, Nemec K, Möller J, Koschinski A*, et al.* (2022). Receptor-associated independent cAMP nanodomains mediate spatiotemporal specificity of GPCR signaling. *Cell* **185**(7)**:** 1130-1142.

Aoki I, Tateyama M, Shimomura T, Ihara K, Kubo Y, Nakano S*, et al.* (2018). SLO potassium channels antagonize premature decision making in C. elegans. *Communications Biology volume* **123**.

Arcangeli A, Faravelli L, Bianchi L, Rosati B, Gritti A, Vescovi A*, et al.* (1996). Soluble or bound laminin elicit in human neuroblastoma cells short- or long-term potentiation of a K+ inwardly rectifying current relevance to neuritogenesis. *Cell Adhes Commun.* **4:** 369-385.

Ardiel EL, Rankin CH (2010). An elegant mind: learning and memory in Caenorhabditis elegans. *Learning & memory* **17**(4)**:** 191-201.

Arenkiel BR, Peca J, Davison IG, Feliciano C, Deisseroth K, Augustine GJ*, et al.* (2007). In vivo light-induced activation of neural circuitry in transgenic mice expressing channelrhodopsin-2. *Neuron* **54**(2)**:** 205-218.

Arrenberg AB, Del Bene F, Baier H (2009). Optical control of zebrafish behavior with halorhodopsin. *Proc Natl Acad Sci U S A* **106**(42)**:** 17968-17973.

Avelar GM, Glaser T, Leonard G, Richards TA, Ulrich H, Gomes SL (2015). A Cyclic GMP-Dependent K+ Channel in the Blastocladiomycete Fungus Blastocladiella emersonii. *Eukaryotic cell* **14**(9)**:** 958–963.

Avelar GM, Schumacher RI, Zaini PA, Leonard G, Richards TA, Gomes SL (2014). A rhodopsin-guanylyl cyclase gene fusion functions in visual perception in a fungus. *Current biology : CB* **24**(11)**:** 1234–1240.

Azimi Hashemi N, Bergs ACF, Schuler C, Scheiwe AR, Steuer Costa W, Bach M*, et al.* (2019). Rhodopsin-based voltage imaging tools for use in muscles and neurons of Caenorhabditis elegans. *Proc Natl Acad Sci U S A* **116**(34)**:** 17051-17060.

AzimiHashemi N, Erbguth K, Vogt A, Riemensperger T, Rauch E, Woodmansee D*, et al.* (2014). Synthetic retinal analogues modify the spectral and kinetic characteristics of microbial rhodopsin optogenetic tools. *Nat Commun* **5:** 5810.

Balashov SP, Ebrey TG (2001). Trapping and spectroscopic identification of the photointermediates of bacteriorhodopsin at low temperatures. *Photochemistry and Photobiology* **73**(5)**:** 453-462.

Bamann C, Gueta R, Kleinlogel S, Nagel G, Bamberg E (2010). Structural guidance of the photocycle of channelrhodopsin-2 by an interhelical hydrogen bond. *Biochemistry* **49**(2)**:** 267-278.

Bamann C, Kirsch T, Nagel G, Bamberg E (2008). Spectral characteristics of the photocycle of channelrhodopsin-2 and its implication for channel function. *Journal of molecular biology* **375**(3)**:** 686-694.

Barbagallo B, Prescott HA, Boyle P, Climer J, Francis MM (2010). A dominant mutation in a neuronal acetylcholine receptor subunit leads to motor neuron degeneration in Caenorhabditis elegans. *The Journal of neuroscience : the official journal of the Society for Neuroscience* **30**(42)**:** 13932-13942.

Barends TR, Hartmann E, Griese JJ, Beitlich T, Kirienko NV, Ryjenkov DA*, et al.* (2009). Structure and mechanism of a bacterial light-regulated cyclic nucleotide phosphodiesterase. *Nature* **459**(7249)**:** 1015-1018.

Bargmann CI (2006). Chemosensation in C. elegans. *WormBook : the online review of C. elegans biology:***:** 1-29.

Bargmann CI (1998). Neurobiology of the Caenorhabditis elegans genome. *Science* **282**(5396)**:** 2028-2033.

Bargmann CI, Horvitz HR (1991). Control of larval development by chemosensory neurons in Caenorhabditis elegans. *Science* **251**(4998)**:** 1243-1246.

Barrière A, Félix M-A (2005). Isolation of C. elegans and related nematodes. *The C. elegans Research Community, WormBook***:** 1-19.

Barros F, de la Pena P, Dominguez P, Sierra LM, Pardo LA (2020). The EAG Voltage-Dependent K(+) Channel Subfamily: Similarities and Differences in Structural Organization and Gating. *Frontiers in pharmacology* **11:** 411.

Bauer C (1998). The erg inwardly rectifying K+ current and its modulation by thyrotrophin-releasing hormone in giant clonal rat anterior pituitary cells. *Journal of Physiology* **510:** 63 - 70.

Beck S, Yu-Strzelczyk J, Pauls D, Constantin OM, Gee CE, Ehmann N*, et al.* (2018). Synthetic Light-Activated Ion Channels for Optogenetic Activation and Inhibition. *Frontiers in neuroscience* **12:** 643.

Béguin P, Nagashima K, Nishimura M, Gonoi T, Seino S (1999). PKA-mediated phosphorylation of the human KATP channel separate roles of Kir6.2 and SUR1 subunit phosphorylation. *The EMBO journal* **18**(17)**:** 4722–4732.

Bellmann D, Richardt A, Freyberger R, Nuwal N, Schwarzel M, Fiala A*, et al.* (2010). Optogenetically Induced Olfactory Stimulation in Drosophila Larvae Reveals the Neuronal Basis of Odor-Aversion behavior. *Frontiers in behavioral neuroscience* **4:** 27.

Benndorf K, Koopmann R, Eismann E, Kaupp UB (1999). Gating by Cyclic Gmp and Voltage in the α Subunit of the Cyclic Gmp–Gated Channel from Rod Photoreceptors. *J Gen Physiol* **114:** 477–489.

Bergs A, Schultheis C, Fischer E, Tsunoda SP, Erbguth K, Husson SJ*, et al.* (2018). Rhodopsin optogenetic toolbox v2.0 for light-sensitive excitation and inhibition in Caenorhabditis elegans. *PloS one* **13**(2)**:** e0191802.

Berman HM, Ten Eyck LF, Goodsell DS, Haste NM, Kornev A, Taylor SS (2005). The cAMP binding domain: an ancient signaling module. *Proc Natl Acad Sci U S A* **102**(1)**:** 45-50.

Bernal Sierra YA, Rost BR, Pofahl M, Fernandes AM, Kopton RA, Moser S*, et al.* (2018). Potassium channel-based optogenetic silencing. *Nature communications* **9**(1)**:** 4611.

Berndt A, Lee SY, Ramakrishnan C, Deisseroth K (2014). Structure-Guided Transformation of Channelrhodopsin into a Light-Activated Chloride Channel. *Science* **344**(6182)**:** 420-424.

Berndt A, Lee SY, Wietek J, Ramakrishnan C, Steinberg EE, Rashid AJ*, et al.* (2016). Structural foundations of optogenetics Determinants of channelrhodopsin ion selectivity. *PNAS* **113**(4)**:** 822–829.

Berndt A, Schoenenberger P, Mattis J, Tye KM, Deisseroth K, Hegemann P*, et al.* (2011). High-efficiency channelrhodopsins for fast neuronal stimulation at low light levels. *Proceedings of the National Academy of Sciences of the United States of America* **108**(18)**:** 7595–7600.

Berndt A, Yizhar O, Gunaydin LA, Hegemann P, Deisseroth K (2009). Bi-stable neural state switches. *Nat Neurosci* **12**(2)**:** 229-234.

Biel M, Michalakis S (2009). Cyclic Nucleotide-Gated Channels. *cGMP: Generators, Effectors and Therapeutic Implications. Handbook of Experimental Pharmacology* **191:** 111-136.

Birnby DA, Link EM, Vowels JJ, Tian H, Colacurcio PL, Thomas JH (2000). A Transmembrane Guanylyl Cyclase (DAF-11) and Hsp90 (DAF-21) Regulate a Common Set of Chemosensory Behaviors in Caenorhabditis elegans. *Genetics* **155**(1)**:** 85-104.

Bock A, Annibale P, Konrad C, Hannawacker A, Anton SE, Maiellaro I*, et al.* (2020). Optical Mapping of cAMP Signaling at the Nanometer Scale. *Cell* **182**(6)**:** 1519-1530 e1517.

Boulin T, Etchberger JF, Hobert O (2006). Reporter gene fusions *The C. elegans Research Community, WormBook***:** 1-23.

Boulin T, Gielen M, Richmond JE, Williams DC, Paoletti P, Bessereau JL (2008). Eight genes are required for functional reconstitution of the Caenorhabditis elegans levamisole-sensitive acetylcholine receptor. *Proc Natl Acad Sci U S A* **105**(47)**:** 18590-18595.

Boyden ES, Zhang F, Bamberg E, Nagel G, Deisseroth K (2005). Millisecond-timescale, genetically targeted optical control of neural activity. *Nature neuroscience* **8**(9)**:** 1263–1268.

Bradley J, Frings S, Yau K-W, Reed R (2001). Nomenclature for Ion Channel Subunits. *Science* **294**(5549)**:** 2095-2096.

Bradley J, Li J, Davidson N, Lester HA, Zinn K (1994). Heteromeric olfactory cyclic nucleotide-gated channels a subunit that confers increased sensitivity to cAMP. *Proc. Nati. Acad. Sci.* **91:** 8890-8894,.

Braiman M, Mathies R (1980). Resonance Raman evidence for an all-trans to 13-cis isomerization in the proton-pumping cycle of bacteriorhodopsin. *Biochemistry* **19:** 5421-5428.

Brenner S (1974). The genetics of Caenorhabditis elegans. *Genetics***:** 71–94.

Brescia M, Zaccolo M (2016). Modulation of Compartmentalised Cyclic Nucleotide Signalling via Local Inhibition of Phosphodiesterase Activity. *International journal of molecular sciences* **17**(10).

Brown RL, Snow SD, Haley TL (1998). Movement of gating machinery during the activation of rod cyclic nucleotide-gated channels. *Biophysical journal* **75:** 825-833.

Cesca F, Baldelli P, Valtorta F, Benfenati F (2010). The synapsins: key actors of synapse function and plasticity. *Progress in neurobiology* **91**(4)**:** 313-348.

Chalfie M, Tu Y, Euskirchen G, Ward WW, Prasher DC (1994). Green fluorescent protein as a marker for gene expression. *Science (New York, N.Y.)* **263**(5148)**:** 802-805.

Charlie NK, Schade MA, Thomure AM, Miller KG (2006). Presynaptic UNC-31 (CAPS) is required to activate the G alpha(s) pathway of the Caenorhabditis elegans synaptic signaling network. *Genetics* **172**(2)**:** 943-961.

Chen X, Zaro JL, Shen WC (2013). Fusion protein linkers: property, design and functionality. *Advanced drug delivery reviews* **65**(10)**:** 1357-1369.

Cho S-W, Cho J-H, Song H-O, Park C-S (2005). Identification and Characterization of a Putative Cyclic Nucleotide-gated Channel, CNG-1, in C. elegans. *Molecules and Cells* **19:** 149-154.

Cho SW, Choi KY, Park CS (2004). A new putative cyclic nucleotide-gated channel gene, cng-3, is critical for thermotolerance in Caenorhabditis elegans. *Biochem Biophys Res Commun* **325**(2)**:** 525-531.

Chow BY, Han X, Dobry AS, Qian X, Chuong AS, Li M*, et al.* (2010). High-performance genetically targetable optical neural silencing by light-driven proton pumps. *Nature* **463**(7277)**:** 98–102.

Clayton GM, Silverman WR, Heginbotham L, Morais-Cabral JH (2004). Structural basis of ligand activation in a cyclic nucleotide regulated potassium channel. *Cell* **119**(5)**:** 615-627.

Collins KM, Koelle MR (2013). Postsynaptic ERG potassium channels limit muscle excitability to allow distinct egg-laying behavior states in Caenorhabditis elegans. *The Journal of neuroscience : the official journal of the Society for Neuroscience* **33**(2)**:** 761-775.

Compton SJ, Jones CG (1985). Mechanism of dye response and interference in the Bradford protein assay. *Analytical Biochemistry* **151:** 396-374.

Consortium TCeS (1998). Genome sequence of the nematode C. elegans: a platform for investigating biology. *Science* **282**.

Conti M, Beavo J (2007). Biochemistry and physiology of cyclic nucleotide phosphodiesterases: essential components in cyclic nucleotide signaling. *Annual review of biochemistry* **76:** 481-511.

Cooper DM, Tabbasum VG (2014). Adenylate cyclase-centred microdomains. *Biochem J* **462**(2)**:** 199-213.

Corsi AK, Wightman B, Chalfie M (2015). A Transparent window into biology: A primer on Caenorhabditis elegans *The C. elegans Research Community, WormBook***:** 387-407.

Craven KB, Zagotta WN (2006). CNG and HCN channels: two peas, one pod. *Annual review of physiology* **68:** 375-401.

Cui J, Kagan A, Qin D, Mathew J, Melman YF, McDonald TV (2001). Analysis of the cyclic nucleotide binding domain of the HERG potassium channel and interactions with KCNE2. *J Biol Chem* **276**(20)**:** 17244-17251.

Cui J, Melman Y, Palma E, Fishman GI, McDonald TV (2000). Cyclic AMP regulates the HERG K(+) channel by dual pathways. *Curr Biol.* **1**(10)**:** 671-674.

Culetto E, Baylis HA, Richmond JE, Kones AK, Fleming JT, Squire MD*, et al.* (2004). The Caenorhabditis elegans unc-63 gene encodes a levamisole-sensitive nicotinic acetylcholine receptor alpha subunit. *Journal of Biological Chemistry* **279**(41)**:** 42476-42483.

Dawydow A, Gueta R, Ljaschenko D, Ullrich S, Hermann M, Ehmann N*, et al.* (2014). Channelrhodopsin-2–XXL, a powerful optogenetic tool for low-light applications. *PNAS* **11**(38)**:** 13972–13977.

de Bono M, Maricq AV (2005). Neuronal substrates of complex behaviors in C. elegans. *Ann. Rev. Neurosci.* **28:** 451-501.

de Rooji J, Zwartkruis FJT, Verheijen MHG, Cool RH, Nijman SMB, Wittinghofer A*, et al.* (1998). Epac is a Rap1 guanine-nucleotide-exchange factor directly activated by cyclic AMP. *Nature* **396:** 474-477.

Deisseroth K (2015). Optogenetics 10 years of microbial opsins in neuroscience. *Nature neuroscience* **18:** 1213–1225.

Dhallan RS, Yau K-W, Schrader KA, Reed R (1990). Primary structure and functional expression of a cyclic nucleotide-activated channel from olfactory neurons. *Nature* **347:** 184-187.

Diester I, Kaufman MT, Mogri M, Pashaie R, Goo W, Yizhar O*, et al.* (2011). An optogenetic toolbox designed for primates. *Nat Neurosci* **14**(3)**:** 387-397.

Dittman JS, Kaplan JM (2008). Behavioral impact of neurotransmitter-activated G-protein-coupled receptors: muscarinic and GABAB receptors regulate Caenorhabditis elegans locomotion. *The Journal of neuroscience : the official journal of the Society for Neuroscience* **28**(28)**:** 7104-7112.

Dixon SJ, Alexander M, Fernandes R, Ricker N, Roy PJ (2006). FGF negatively regulates muscle membrane extension in Caenorhabditis elegans. *Development* **133**(7)**:** 1263-1275.

Dixon SJ, Roy PJ (2005). Muscle arm development in Caenorhabditis elegans. *Development* **132**(13)**:** 3079-3092.

Dominguez N, van Weering JRT, Borges R, Toonen RFG, Verhage M (2018). Dense-core vesicle biogenesis and exocytosis in neurons lacking chromogranins A and B. *J Neurochem* **144**(3)**:** 241-254.

Dong X, Liu OW, Howell AS, Shen K (2013). An extracellular adhesion molecule complex patterns dendritic branching and morphogenesis. *Cell* **155**(2)**:** 296-307.

Edwards SL, Charlie NK, Milfort MC, Brown BS, Gravlin CN, Knecht JE*, et al.* (2008). A novel molecular solution for ultraviolet light detection in Caenorhabditis elegans. *PLoS biology* **6**(8)**:** e198.

El-Gaby M, Zhang Y, Wolf K, Schwiening CJ, Paulsen O, Shipton OA (2016). Archaerhodopsin Selectively and Reversibly Silences Synaptic Transmission through Altered pH. *Cell reports* **16**(8)**:** 2259-2268.

Erbguth K, Prigge M, Schneider F, Hegemann P, Gottschalk A (2012). Bimodal activation of different neuron classes with the spectrally red-shifted channelrhodopsin chimera C1V1 in Caenorhabditis elegans. *PloS one* **7**(10)**:** e46827.

Ernst OP, Lodowski DT, Elstner M, Hegemann P, Brown LS, Kandori H (2014). Microbial and animal rhodopsins: structures, functions, and molecular mechanisms. *Chemical reviews* **114**(1)**:** 126-163.

Etzl S, Lindner R, Nelson MD, Winkler A (2018). Structure-guided design and functional characterization of an artificial red light-regulated guanylate/adenylate cyclase for optogenetic applications. *The Journal of biological chemistry* **293**(23)**:** 9078–9089.

Fang-Yen C, Alkema MJ, Samuel ADT (2015). Illuminating neural circuits and behaviour in Caenorhabditis elegans with optogenetics. *Philosophical Transactions of the Royal Society B: Biological Sciences* **370**(1677)**:** 20140212.

Feldbauer K, Zimmermann D, Pintschovius V, Spitz J, Bamann C, Bamberg E (2009). Channelrhodopsin-2 is a leaky proton pump. *Proc Natl Acad Sci U S A* **106**(30)**:** 12317-12322.

Ferkey DM, Sengupta P, L'Etoile ND (2021). Chemosensory signal transduction in Caenorhabditis elegans. *Genetics* **217**(3).

Fesenko EE, Kolesnikov SS, Lyubarsky AL (1985). Induction by cyclic GMP of cationic conductance in plasma membrane of retinal rod outer segment. *Nature* **313:** 310–313.

Fielenbach N, Antebi A (2008). C. elegans dauer formation and the molecular basis of plasticity. *Genes Dev* **22**(16)**:** 2149-2165.

Fire A, Xu S, Montgomery MK, Kostas SA, Driver SE, Mello CC (1998). Potent and specific genetic interference by double-stranded RNA in Caenorhabditis elegans. *Nature* **391**(6669)**:** 806-811.

Fischer P, Mukherjee S, Peter E, Broser M, Bartl F, Hegemann P (2021). The inner mechanics of rhodopsin guanylyl cyclase during cGMP-formation revealed by real-time FTIR spectroscopy. *eLife* **10**.

Fleming JT, Squire MD, Barnes TM, Tornoe C, Matsuda K, Ahnn J*, et al.* (1997). Caenorhabditis elegans levamisole resistance genes lev-1, unc-29, and unc-38 encode functional nicotinic acetylcholine receptor subunits. *The Journal of Neuroscience* **17**(15)**:** 5843–5857.

Flynn GE, Black KD, Islas LD, Sankaran B, Zagotta WN (2007). Structure and rearrangements in the carboxy-terminal region of SpIH channels. *Structure* **15**(6)**:** 671-682.

Flynn GE, Johnson JP, Zagotta WN (2001). Cyclic nucleotide-gated channels shedding light on the opening of a channel pore. *Nature Reviews* **2:** 643-652.

Francis MM, Evans SP, Jensen M, Madsen DM, Mancuso J, Norman KR*, et al.* (2005). The Ror receptor tyrosine kinase CAM-1 is required for ACR-16-mediated synaptic transmission at the C. elegans neuromuscular junction. *Neuron* **46**(4)**:** 581-594.

Fraser AG, Kamath RS, Zipperlen P, Martinez-Campos M, Sohrmann M, Ahringer J (2000). Functional genomic analysis of C. elegans chromosome I by systematic RNA interference. *Nature* **408**(6810)**:** 325-330.

Froese A, Breher SS, Waldeyer C, Schindler RF, Nikolaev VO, Rinne S*, et al.* (2012). Popeye domain containing proteins are essential for stress-mediated modulation of cardiac pacemaking in mice. *The Journal of clinical investigation* **122**(3)**:** 1119-1130.

Gao L, Zhao J, Ardiel E, Hall Q, Nurrish S, Kaplan JM (2022). Shank promotes action potential repolarization by recruiting BK channels to calcium microdomains. *eLife* **11**.

Gao S, Nagpal J, Schneider MW, Kozjak-Pavlovic V, Nagel G, Gottschalk A (2015). Optogenetic manipulation of cGMP in cells and animals by the tightly light-regulated guanylyl-cyclase opsin CyclOp. *Nature communications* **6:** 8046.

Gao S, Zhen M (2011). Action potentials drive body wall muscle contractions in Caenorhabditis elegans. *Proc Natl Acad Sci U S A* **108**(6)**:** 2557-2562.

Garcia RL, Sternberg PW (2003). Caenorhabditis elegans UNC-103 ERG-Like Potassium Channel Regulates Contractile Behaviors of Sex Muscles in Males before and during Mating. *The Journal of Neuroscience* **23**(7)**:** 2696 –2705.

Gasser C, Taiber S, Yeh CM, Wittig CH, Hegemann P, Ryu S*, et al.* (2014). Engineering of a red-light-activated human cAMP/cGMP-specific phosphodiesterase. *Proc Natl Acad Sci U S A* **111**(24)**:** 8803-8808.

Gerlt JA, Coderre JA, Wolin MS (1980). Mechanism of the adenylate cyclase reaction. Stereochemistry of the reaction catalyzed by the enzyme from Brevibacterium liquefaciens. *Journal of Biological Chemistry* **255**(2)**:** 331-334.

Gomelsky M, Hoff WD (2011). Light helps bacteria make important lifestyle decisions. *Trends in microbiology* **19**(9)**:** 441-448.

Gomelsky M, Klug G (2002). BLUF: a novel FAD-binding domain involved in sensory transduction in microorganisms. *Trends in Biochemical Sciences* **27:** 497-500.

Gordon SE, Downing-Park J, Tam B, Zimmerman AL (1995). Diacylglycerol analogs inhibit the rod cGMP-gated channel by a phosphorylation-independent mechanism. *Biophysical journal* **69:** 409-417.

Gottschalk A, Almedom RB, Schedletzky T, Anderson SD, Yates III JR, Schafer WR (2005). Identification and characterization of novel nicotinic receptor-associated proteins in Caenorhabditis elegans. *The EMBO Journal* **24:** 2566–2578.

Goujon M, McWilliam H, Li W, Valentin F, Squizzato S, Paern J*, et al.* (2010). A new bioinformatics analysis tools framework at EMBL-EBI. *Nucleic acids research* **38**(Web Server issue)**:** W695-699.

Govorunova EG, Sineshchekov OA, Janz R, Liu X, Spudich JL (2015). Natural light-gated anion channels: A family of microbial rhodopsins for advanced optogenetics. *Science* **349**(6248)**:** 647-650.

Govorunova EG, Sineshchekov OA, Li H, Janz R, Spudich JL (2013). Characterization of a highly efficient blue-shifted channelrhodopsin from the marine alga Platymonas subcordiformis. *J Biol Chem* **288**(41)**:** 29911-29922.

Govorunova EG, Sineshchekov OA, Li H, Spudich JL (2017). Microbial Rhodopsins: Diversity, Mechanisms, and Optogenetic Applications. *Annual review of biochemistry* **86:** 845-872.

Gradinaru V, Thompson KR, Deisseroth K (2008). eNpHR: a Natronomonas halorhodopsin enhanced for optogenetic applications. *Brain cell biology* **36**(1-4)**:** 129-139.

Grant AO (2009). Cardiac ion channels. *Circulation. Arrhythmia and electrophysiology* **2**(2)**:** 185-194.

Grant BD, Sato M (2006). Intracellular trafficking. *The C. elegans Research Community, WormBook***:** 1-9.

Gray J, Lissmann HW (1964). The Locomotion of Nematodes. *Journal of Experimental Biology* **41**(1)**:** 135-154.

Gunaydin LA, Yizhar O, Berndt A, Sohal VS, Deisseroth K, Hegemann P (2010). Ultrafast optogenetic control. *Nat Neurosci* **13**(3)**:** 387-392.

Gutman GA, Chandy KG, Adelman JP, Aiyar J, Bayliss DA, Clapham DE*, et al.* (2003). International Union of Pharmacology. XLI. Compendium of voltage-gated ion channels: potassium channels. *Pharmacol Rev* **55**(4)**:** 583-586.

Hager HA, Roberts RJ, Cross EE, Proux-Gillardeaux V, Bader DM (2010). Identification of a novel Bves function regulation of vesicular transport. *The EMBO Journal* **29**(3)**:** 532–545.

Hammarlund M, Hobert O, Miller DM, 3rd, Sestan N (2018). The CeNGEN Project: The Complete Gene Expression Map of an Entire Nervous System. In: *Neuron* Vol. 99, 2018/08/10 edn, pp 430-433.

Han X, Boyden ES (2007). Multiple-color optical activation, silencing, and desynchronization of neural activity, with single-spike temporal resolution. *PloS one* **2**(3)**:** e299.

Han X, Chow BY, Zhou H, Klapoetke NC, Chuong A, Rajimehr R*, et al.* (2011). A high-light sensitivity optical neural silencer: development and application to optogenetic control of non-human primate cortex. *Frontiers in systems neuroscience* **5:** 18.

Haupts U, Tittor J, Oesterhelt D (1999). CLOSING IN ON BACTERIORHODOPSIN Progress in Understanding the Molecule. *Annu. Rev. Biophys. Biomol. Struct.* **28:** 367–399.

He Y, Karpen J (2001). Probing the interactions between cAMP and cGMP in cyclic nucleotide-gated channels using covalently tethered ligands. *Biochemistry* **40:** 286-295.

Heine S, Michalakis S, Kallenborn-Gerhardt W, Lu R, Lim HY, Weiland J*, et al.* (2011). CNGA3: a target of spinal nitric oxide/cGMP signaling and modulator of inflammatory pain hypersensitivity. *The Journal of neuroscience : the official journal of the Society for Neuroscience* **31**(31)**:** 11184-11192.

Henss T, Nagpal J, Gao S, Scheib U, Pieragnolo A, Hirschhauser A*, et al.* (2021). Optogenetic tools for manipulation of cyclic nucleotides functionally coupled to cyclic nucleotide-gated channels. *British journal of pharmacology*.

Herzfeld J, Lansing JC (2002). Magnetic Resonance Studies of the Bacteriorhodopsin Pump Cycle. *Annual Review of Biophysics and Biomolecular Structure* **31**(1)**:** 73-95.

Hibino H, Inanobe A, Furutani K, Murukami S, Findlay I, Kurachi Y (2010). Inwardly Rectifying Potassium Channels: Their Structure, Function, and Physiological Roles. *Physiol Rev* **90:** 291–366.

Hodgkin J, Horvitz HR, Brenner S (1979). Nondisjunction Mutants of the Nematode Caenorhabditis Elegans. *Genetics* **91:** 67-94.

Hoff WD, Jung KH, Spudich JL (1997). MOLECULAR MECHANISM OF PHOTOSIGNALING BY ARCHAEAL SENSORY RHODOPSINS. *Annual Review of Biophysics and Biomolecular Structure* **26:** 223-258.

Hu PJ (2007). Dauer. *WormBook : the online review of C. elegans biology***:** 1-19.

Hu Z, Pym EC, Babu K, Vashlishan Murray AB, Kaplan JM (2011). A neuropeptide-mediated stretch response links muscle contraction to changes in neurotransmitter release. *Neuron* **71**(1)**:** 92-102.

Huala E, Oeller PW, Liscum E, Han IS, Larsen E, Briggs WR (1997). Arabidopsis NPH1: a protein kinase with a putative redox-sensing domain. *Science (New York, N.Y.)* **278:** 2120-2123.

Husson SJ, Liewald JF, Schultheis C, Stirman JN, Lu H, Gottschalk A (2012). Microbial light-activatable proton pumps as neuronal inhibitors to functionally dissect neuronal networks in C. elegans. *PloS one* **7**(7)**:** e40937.

Ihara K, Umemura T, Katagiri I, Kitajima-Ihara T, Sugiyama Y, Kimura Y*, et al.* (1999). Evolution of the archaeal rhodopsins evolution rate changes by gene duplication and functional differentiation. *J. Mol. Biol.* **285:** 163-174.

Inoue K, Ono H, Abe-Yoshizumi R, Yoshizawa S, Ito H, Kogure K*, et al.* (2013). A light-driven sodium ion pump in marine bacteria. *Nat Commun* **4:** 1678.

Inoue T, Heo WD, Grimley JS, Wandless TJ, Meyer T (2005). An inducible translocation strategy to rapidly activate and inhibit small GTPase signaling pathways. *Nat Methods* **2**(6)**:** 415-418.

Iseki M, Matsunaga S, Murakami A, Ohno K, Shiga K, Yoshida K*, et al.* (2002). A blue-light-activated adenylyl cyclase mediates photoavoidance in Euglena gracilis. *nature* **415:** 1047-1051.

Jahne S, Rizzoli SO, Helm MS (2015). The structure and function of presynaptic endosomes. *Experimental cell research* **335**(2)**:** 172-179.

James ZM, Borst AJ, Haitin Y, Frenz B, DiMaio F, Zagotta WN*, et al.* (2017). CryoEM structure of a prokaryotic cyclic nucleotide-gated ion channel. *PNAS* **114**(17)**:** 4430–4435.

Jarrell TA, Wang Y, Bloniarz AE, Brittin CA, Xu M, Thomson JN*, et al.* (2012). The Connectome of a Decision-Making Neural Network. *Science (New York, N.Y.)* **337**(6093)**:** 437-444.

Jeremic D, Sanchez-Rodriguez I, Jimenez-Diaz L, Navarro-Lopez JD (2021). Therapeutic potential of targeting G protein-gated inwardly rectifying potassium (GIRK) channels in the central nervous system. *Pharmacology & therapeutics* **223:** 107808.

Jorgensen EM (2005). Gaba. *WormBook : the online review of C. elegans biology***:** 1-13.

Jospin M, Jacquemond V, Mariol MC, Segalat L, Allard B (2002). The L-type voltage-dependent Ca2+ channel EGL-19 controls body wall muscle function in Caenorhabditis elegans. *J Cell Biol* **159**(2)**:** 337-348.

Jospin M, Qi YB, Stawicki TM, Boulin T, Schuske KR, Horvitz HR*, et al.* (2009). A neuronal acetylcholine receptor regulates the balance of muscle excitation and inhibition in Caenorhabditis elegans. *PLoS Biol* **7**(12)**:** e1000265.

Kamath RS, Martinez-Campos M, Zipperlen P, Fraser AG, Ahringer J (2001). Effectiveness of specific RNA-mediated interference through ingested double-stranded RNA in Caenorhabditis elegans. *Genome Biology* **2**(1)**:** research0002.0001–0002.0010.

Kato HE, Inoue K, Abe-Yoshizumi R, Kato Y, Ono H, Konno M*, et al.* (2015). Structural basis for Na(+) transport mechanism by a light-driven Na(+) pump. *Nature* **521**(7550)**:** 48-53.

Kaupp UB, Niidome T, Tanabe T, Terada S, Bönigk W, Stühmer W*, et al.* (1989). Primary structure and functional expression from complementary DNA of the rod photoreceptor cyclic GMP-gated channel. *Nature* **342:** 762-766.

Kaupp UB, Seifert R (2002). Cyclic nucleotide-gated ion channels. *Physiol Rev* **82:** 769-824.

Kawasaki H, Springett GM, Mochizuki N, Toki S, Nakaya M, *et al.* (1998). A Family of cAMP-Binding Proteins That Directly Activate Rap1. *Science (New York, N.Y.)* **282**(5397)**:** 2275-2279.

Kelley CA, Cram EJ (2019). Regulation of Actin Dynamics in the C. elegans Somatic Gonad. *Journal of developmental biology* **7**(1).

Kennis JT, Mathes T (2013). Molecular eyes: proteins that transform light into biological information. *Interface focus* **3**(5)**:** 20130005.

Kesters D, Brams M, Nys M, Wijckmans E, Spurny R, Voets T, *et al.* (2015). Structure of the SthK carboxy-terminal region reveals a gating mechanism for cyclic nucleotide-modulated ion channels. *PLoS One* **10**(1)**:** e0116369.

Kim D, Park S, Mahadevan L, Shin JH (2011). The shallow turn of a worm. *J Exp Biol* **214**(Pt 9)**:** 1554-1559.

Kim JM, Hwa J, Garriga P, Reeves P, J., Rai Bhandary UL, Khorana HG (2005). Light-Driven Activation of β2-Adrenergic Receptor Signaling by a Chimeric Rhodopsin Containing the β2-Adrenergic Receptor Cytoplasmic Loops. *Biochemistry* **44:** 2284-2292.

Kim T, Folcher M, Doaud-El Baba M, Fussenegger M (2015). A synthetic erectile optogenetic stimulator enabling blue-light-inducible penile erection. *Angewandte Chemie* **54**(20)**:** 5933-5938.

Kimble J, Hirsh D (1979). The postembryonic cell lineages of the hermaphrodite and male gonads in Caenorhabditis elegans. *Developmental Biology* **70:** 396-417.

Kittelmann M, Liewald JF, Hegermann J, Schultheis C, Brauner M, Steuer Costa W, *et al.* (2013). In vivo synaptic recovery following optogenetic hyperstimulation. *Proc Natl Acad Sci U S A* **110**(32)**:** E3007-3016.

Klapoetke NC, Murata Y, Kim SS, Pulver SR, Birdsey-Benson A, Cho YK, *et al.* (2014). Independent optical excitation of distinct neural populations. *Nature methods* **11**(3)**:** 338–346.

Klare JP, Bordignon E, Engelhard M, Steinhoff H-J (2004). Sensory rhodopsin II and bacteriorhodopsin Light activated helix F movement. *Photochem. Photobiol. Sci.* **3:** 543-547.

Klare JP, Chizhov I, Engelhard M (2008). Microbial Rhodopsins: Scaffolds for Ion Pumps, Channels, and Sensors. *Results Probl Cell Differ* **45**.

Kleinlogel S, Feldbauer K, Dempski RE, Fotis H, Wood PG, Bamann C*, et al.* (2011). Ultra light-sensitive and fast neuronal activation with the Ca(2)+-permeable channelrhodopsin CatCh. *Nat Neurosci* **14**(4)**:** 513-518.

Knöpfel T, Lin MZ, Levskaya A, Tian L, Lin JY, Boyden ES (2010). Toward the Second Generation of Optogenetic Tools. *The Journal of Neuroscience* **30:** 14998–15004.

Komatsu H, Jin Y-H, L'Etoile N, Mori I, Bargmann CI, Akaike N*, et al.* (1999). Functional reconstitution of a heteromeric cyclic nucleotide-gated channel of Caenorhabditis elegans in cultured cells. *Brain Research* **821:** 160–168.

Komatsu H, Mori I, Rhee J-S, Akaike N, Ohshima Y (1996). Mutations in a Cyclic Nucleotide–Gated Channel Lead to Abnormal Thermosensation and Chemosensation in C. elegans. *Neuron* **4:** 707–718.

Kononenko NL, Haucke V (2015). Molecular mechanisms of presynaptic membrane retrieval and synaptic vesicle reformation. *Neuron* **85**(3)**:** 484-496.

Kort R, Hoff WD, Van West M, Kroon AR, Hoffer SM, Vlieg KH*, et al.* (1996). The xanthopsins: a new family of eubacterial blue-light photoreceptors. *The EMBO Journal* **15:** 3209–3218.

Kowal J, Biyani N, Chami M, Scherer S, Rzepiela AJ, Baumgartner P*, et al.* (2018). High-Resolution Cryoelectron Microscopy Structure of the Cyclic Nucleotide-Modulated Potassium Channel MloK1 in a Lipid Bilayer. *Structure* **26**(1)**:** 20-27 e23.

Laemmli UK (1970). Cleavage of Structural Proteins during the Assembly of the Head of Bacteriophage T4. *Nature* **227:** 680-685.

Lancet D (1986). Vertebrate Olfactory Reception. *Ann. Rev. Neurosci.* **9:** 329-355.

Lanyi JK (2004). Bacteriorhodopsin. *Annual review of physiology* **66:** 665-688.

Lee RC, Felnbaum RL, Ambros V (1993). The C. elegans heterochronic gene lin-4 encodes small RNAs with antisense complementarity to lin-14. *Cell* **75:** 843-854.

Lee RYN, Lobel L, Hengartner M, Horvitz HR, Avery L (1997). Mutations in the α1 subunit of an L-type voltage-activated Ca2+ channel cause myotonia in Caenorhabditis elegans. *The EMBO Journal* **16**(20)**:** 6066–6076.

Levitzki A (1988). From Epinephrine to Cyclic AMP. *Science (New York, N.Y.)* **241**(4867)**:** 800-806.

Li C, Kim K (2014). Family of FLP Peptides in Caenorhabditis elegans and Related Nematodes. *Frontiers in endocrinology* **5:** 150.

Li C, Kim K (2008). Neuropeptides. *WormBook : the online review of C. elegans biology***:** 1-36.

Li M, Zhou X, Wang S, Michailidis I, Gong Y, Su D*, et al.* (2017). Structure of a eukaryotic cyclic-nucleotide-gated channel. *Nature* **542**(7639)**:** 60-65.

Li W, Feng Z, Sternberg PW, Xu XZ (2006). A C. elegans stretch receptor neuron revealed by a mechanosensitive TRP channel homologue. *Nature* **440**(7084)**:** 684-687.

Li X, Gutierrez DV, Hanson MG, Han J, Mark MD, Chiel H*, et al.* (2005). Fast noninvasive activation and inhibition of neural and network activity by vertebrate rhodopsin and green algae channelrhodopsin. *Proc Natl Acad Sci U S A* **102**(49)**:** 17816-17821.

Liewald JF, Brauner M, Stephens GJ, Bouhours M, Schultheis C, Zhen M*, et al.* (2008). Optogenetic analysis of synaptic function. *Nature methods* **5**(10)**:** 895–902.

Lin JY, Knutsen PM, Muller A, Kleinfeld D, Tsien RY (2013). ReaChR: a red-shifted variant of channelrhodopsin enables deep transcranial optogenetic excitation. *Nat Neurosci* **16**(10)**:** 1499-1508.

Lin JY, Lin MZ, Steinbach P, Tsien RY (2009). Characterization of engineered channelrhodopsin variants with improved properties and kinetics. *Biophysical journal* **96**(5)**:** 1803-1814.

Lin YF, Jan YN, Jan LY (2000). Regulation of ATP-sensitive potassium channel function by protein kinase A-mediated phosphorylation in transfected HEK293 cells. *EMBO Journal* **19**(5)**:** 942-955.

Linder JU (2005). Substrate selection by class III adenylyl cyclases and guanylyl cyclases. *IUBMB life* **57**(12)**:** 797–803.

Liu F, Xiao Y, Ji XL, Zhang KQ, Zou CG (2017). The cAMP-PKA pathway-mediated fat mobilization is required for cold tolerance in C. elegans. *Scientific reports* **7**(1)**:** 638.

Liu P, Ge Q, Chen B, Salkoff L, Kotlikoff MI, Wang ZW (2011). Genetic dissection of ion currents underlying all-or-none action potentials in C. elegans body-wall muscle cells. *The Journal of physiology* **589**(Pt 1)**:** 101-117.

Liu Q, Sinnen BL, Boxer EE, Schneider MW, Grybko MJ, Buchta WC*, et al.* (2019). A Photoactivatable Botulinum Neurotoxin for Inducible Control of Neurotransmission. *Neuron* **101**(5)**:** 863-875.

Loewi O (1921). Über humorale übertragbarkeit der Herznervenwirkung. *Pflüger's Archiv für die gesamte Physiologie des Menschen und der Tiere* **189:** 239–242.

Lorenz R, Bertinetti D, Herberg FW (2017a). cAMP-Dependent Protein Kinase and cGMP-Dependent Protein Kinase as Cyclic Nucleotide Effectors. *Handbook of experimental pharmacology* **238:** 105-122.

Lorenz R, Moon EW, Kim JJ, Schmidt SH, Sankaran B, Pavlidis IV*, et al.* (2017b). Mutations of PKA cyclic nucleotide-binding domains reveal novel aspects of cyclic nucleotide selectivity. *Biochem J* **474**(14)**:** 2389-2403.

Lozier RH, Bogomolni RA, Stoeckenius W (1975). Bacteriorhodopsin a light-driven proton pump in Halobacterium Halobium. *Biophysical journal* **15:** 955-962.

Mahn M, Prigge M, Ron S, Levy R, Yizhar O (2016). Biophysical constraints of optogenetic inhibition at presynaptic terminals. *Nature neuroscience* **19**(4)**:** 554–556.

Man D, Wang W, Sabehi G, Aravind L, Post AF, Massana R*, et al.* (2003). Diversification and spectral tuning in marine proteorhodopsins. *The EMBO Journal* **22**(8)**:** 1725±1731.

Maryon EB, Coronado R, Anderson P (1996). unc-68 encodes a ryanodine receptor involved in regulating C. elegans body-wall muscle contraction. *The Journal of Cell Biology* **134:** 885-893.

Masuda S, Bauer CE (2002). AppA is a blue light photoreceptor that antirepresses photosynthesis gene expression in Rhodobacter sphaeroides. *Cell* **110:** 613–623.

Mathies RA, Lin SW, Ames JB, Pollard WT (1991). From Femtoseconds to Biology Mechanism of Bacteriorhodopsin's Light-Driven Proton Pump. *Annu. Rev. Biophys . Biop/zys. Chern* **20:** 491-518.

McKay DB, Steitz T (1981). Structure of catabolite gene activator protein at 2.9 Å resolution suggests binding to left-handed B-DNA. *Nature* **290:** 744-749.

Mello CC, Kramer JM, Stinchcomb D, Ambros V (1991). Efficient gene transfer in C.elegans: extrachromosomal maintenance and integration of transforming sequences. *The EMBO Journal* **10**(12)**:** 3959-3970.

Menegon A, Bonanomi D, Albertinazzi C, Lotti F, Ferrari G, Kao HT*, et al.* (2006). Protein kinase A-mediated synapsin I phosphorylation is a central modulator of Ca2+-dependent synaptic activity. *The Journal of neuroscience : the official journal of the Society for Neuroscience* **26**(45)**:** 11670-11681.

Merril CR, Goldman D, Sedman SA, Ebert MH (1981). Ultrasensitive Stain for Proteins in Polyacrylamide Gels Shows Regional Variation in Cerebrospinal Fluid Proteins. *Science* **211:** 1437-1438.

Mukherjee S, Hegemann P, Broser M (2019). Enzymerhodopsins: novel photoregulated catalysts for optogenetics. *Current opinion in structural biology* **57:** 118-126.

Musheshe N, Schmidt M, Zaccolo M (2018). cAMP: From Long-Range Second Messenger to Nanodomain Signalling. *Trends in pharmacological sciences* **39**(2)**:** 209-222.

Nache V, Kusch J, Hagen V, Benndorf K (2006). Gating of cyclic nucleotide-gated (CNGA1) channels by cGMP jumps and depolarizing voltage steps. *Biophysical journal* **90**(9)**:** 3146-3154.

Nagahama T, Suzuki T, Yoshikawa S, Iseki M (2007). Functional transplant of photoactivated adenylyl cyclase (PAC) into Aplysia sensory neurons. *Neuroscience research* **59**(1)**:** 81-88.

Nagel G, Brauner M, Liewald JF, Adeishvili N, Bamberg E, Gottschalk A (2005). Light activation of channelrhodopsin-2 in excitable cells of Caenorhabditis elegans triggers rapid behavioral responses. *Current biology : CB* **15**(24)**:** 2279–2284.

Nagel G, Ollig D, Fuhrmann M, Kateriya S, Musti AM, Bamberg E*, et al.* (2002). Channelrhodopsin-1: A Light-Gated Proton Channel in Green Algae. *Science* **296**(5577)**:** 2395-2398.

Nagel G, Szellas T, Huhn W, Kateriya S, Adeishvili N, Berthold P*, et al.* (2003). Channelrhodopsin-2, a directly light-gated cation-selective membrane channel. *PNAS* **100:** 13940–13945.

Nagpal J (2016). Development and implementation of novel optogenetic tools in the nematode Caenorhabditis elegans. *Dissertation. Universitätsbibliothek Johann Christian Senckenberg, Frankfurt am Main.***:** 1-200.

Nakai J, Ohkura M, Imoto K (2001). A high signal-to-noise Ca2+ probe composed of a single green fluorescent protein. *Nature* **19:** 137–141.

Nakanishi K (1991). Why 11-cis-Retinal? *AMER. ZOOL.* **31:** 479-489.

Nelson LS, Rosoff ML, Li C (1998). Disruption of a Neuropeptide Gene, flp-1, Causes Multiple Behavioral Defects in Caenorhabditis elegans. *Science (New York, N.Y.)* **281**(5383)**:** 1686 - 1690.

Nelson MT, Quayle JM (1995). Physiological roles and properties of potassium channels in arterial smooth muscle. *Am J Physiol* **268:** C799-822.

Nimigean CM, Shane T, Miller C (2004). A cyclic nucleotide modulated prokaryotic K+ channel. *J Gen Physiol* **124**(3)**:** 203-210.

O'Halloran DM, Altshuler-Keylin S, Zhang X-D, He C, Morales-Phan C, Yu Y*, et al.* (2017). Contribution of the cyclic nucleotide gated channel subunit, CNG-3, to olfactory plasticity in Caenorhabditis elegans. *Scientific reports* **7**(1).

Ohya S, Asakura K, Muraki K, Watanabe M, Imaizumi Y (2002). Molecular and functional characterization of ERG, KCNQ, and KCNE subtypes in rat stomach smooth muscle. *Am J Physiol Gastrointest Liver Physiol* **282:** G277–G287.

Oikonomou G, Shaham S (2011). The glia of Caenorhabditis elegans. *Glia* **59**(9)**:** 1253-1263.

Oranth A, Schultheis C, Tolstenkov O, Erbguth K, Nagpal J, Hain D*, et al.* (2018). Food Sensation Modulates Locomotion by Dopamine and Neuropeptide Signaling in a Distributed Neuronal Network. *Neuron* **100**(6)**:** 1414-1428 e1410.

Osler ME, Chang MS, Bader DM (2005). Bves modulates epithelial integrity through an interaction at the tight junction. *Journal of Cell Science* **118**(20)**:** 4667-4678.

Pages F, Ildefonse M, Ragno M, Crouzy S, Bennett N (2000). Coexpression of alpha and beta subunits of the rod cyclic GMP-gated channel restores native sensitivity to cyclic AMP: role of D604/N1201. *Biophysical journal* **78:** 1227–1239.

Palczewski K (2006). G protein-coupled receptor rhodopsin. *Annual review of biochemistry* **75:** 743–767.

Park J, Meisel JD, Kim DH (2020). Immediate activation of chemosensory neuron gene expression by bacterial metabolites is selectively induced by distinct cyclic GMP-dependent pathways in Caenorhabditis elegans. *PLoS genetics* **16**(8)**:** e1008505.

Park SY, Tame JRH (2017). Seeing the light with BLUF proteins. *Biophysical reviews* **9**(2)**:** 169-176.

Park YS, Hur EM, Choi BH, Kwak E, Jun DJ, Park SJ*, et al.* (2006). Involvement of protein kinase C-epsilon in activity-dependent potentiation of large dense-core vesicle exocytosis in chromaffin cells. *The Journal of neuroscience : the official journal of the Society for Neuroscience* **26**(35)**:** 8999-9005.

Penzkofer A, Scheib U, Hegemann P, Stehfest K (2017). Absorption and emission spectroscopic investigation of thermal dynamics and photo-dynamics of the rhodopsin domain of the rhodopsin-guanylyl cyclase from the aquatic fungus Blastocladiella emersonii. *BAOJ Physics* **2**(1).

Petersen CI, McFarland TR, Stepanovic SZ, Yang P, Reiner DJ, Hayashi K*, et al.* (2004). In vivo identification of genes that modify ether-a-go-go-related gene activity in Caenorhabditis elegans may also affect human cardiac arrhythmia. *Proc Natl Acad Sci U S A* **101**(32)**:** 11773-11778.

Pifferi S, Boccaccio A, Menini A (2006). Cyclic nucleotide-gated ion channels in sensory transduction. *FEBS Letters* **580**(12)**:** 2853-2859.

Prigge M, Schneider F, Tsunoda SP, Shilyansky C, Wietek J, Deisseroth K*, et al.* (2012). Color-tuned channelrhodopsins for multiwavelength optogenetics. *The Journal of biological chemistry* **287**(38)**:** 31804–31812.

Proks P, Antcliff JF, Lippiat J, Gloyn AL, Hattersley AT, Ashcroft FM (2004). Molecular basis of Kir6.2 mutations associated with neonatal diabetes or neonatal diabetes plus neurological features. *Proc Natl Acad Sci U S A* **101**(50)**:** 17539-17544.

Puig O, Caspary F, Rigaut G, Rutz B, Bouveret E, Bragado-Nilsson E*, et al.* (2001). The tandem affinity purification (TAP) method: a general procedure of protein complex purification. *Methods* **24**(3)**:** 218-229.

Quail, P. H. (1998). The phytochrome family: dissection of functional roles and signalling pathways among family members. *Philos Trans R Soc Lond B Biol Sci* **353:** 1399–1403.

Quinn KV, Giblin JP, Tinker A (2004). Multisite phosphorylation mechanism for protein kinase A activation of the smooth muscle ATP-sensitive K+ channel. *Circulation research* **94**(10)**:** 1359-1366.

Rahmani A, Chew YL (2021). Investigating the molecular mechanisms of learning and memory using Caenorhabditis elegans. *J Neurochem* **159**(3)**:** 417-451.

Raizen DM, Zimmerman JE, Maycock MH, Ta UD, You YJ, Sundaram MV*, et al.* (2008). Lethargus is a Caenorhabditis elegans sleep-like state. *Nature* **451**(7178)**:** 569-572.

Rajasethupathy P, Sankaran S, Marshel JH, Kim CK, Ferenczi E, Lee SY*, et al.* (2015). Projections from neocortex mediate top-down control of memory retrieval. *Nature* **526**(7575)**:** 653-659.

Rand JB (2007). Acetylcholine. *The C. elegans Research Community, WormBook***:** 1-21.

Rehmann H, Wittinghofer A, Bos JL (2007). Capturing cyclic nucleotides in action: snapshots from crystallographic studies. *Nature reviews. Molecular cell biology* **8**(1)**:** 63-73.

Reiner DJ, Weinshenker D, Thomas JH (1995). Analysis of dominant mutations affecting muscle excitation in Caenorhabditis elegans. *Genetics* **141:** 961-976.

Reiner DJ, Weinshenker D, Tian H, Thomas JH, Nishiwaki K, Miwa J*, et al.* (2006). Behavioral genetics of caenorhabditis elegans unc-103-encoded erg-like K(+) channel. *Journal of neurogenetics* **20**(1-2)**:** 41-66.

Rheinberger J, Gao X, Schmidpeter PAM, Nimigean CM (2018). Ligand discrimination and gating in cyclic nucleotide-gated ion channels from apo and partial agonist-bound cryo-EM structures. *eLife* **7**.

Richmond JE, Jorgensen EM (1999). One GABA and two acetylcholine receptors function at the C. elegans neuromuscular junction. *Nature neuroscience* **2:** 791–797.

Rigaut G, Shevchenko A, Rutz B, Wilm M, Mann M, Séraphin B (1999). A generic protein purification method for protein complex characterization and proteome exploration. *Nature Biotechnology*(17)**:** 1030–1032.

Rizzoli SO (2014). Synaptic vesicle recycling: steps and principles. *EMBO J* **33**(8)**:** 788-822.

Rodbell M, Birnbaumer L, Pohl SL, Krans HM (1971). The glucagon-sensitive adenyl cyclase system in plasma membranes of rat liver. V. An obligatory role of guanylnucleotides in glucagon action. *Journal of Biological Chemistry* **246**(6)**:** 1877-1882.

Rosenbaum T, Gordon SE (2002). Dissecting intersubunit contacts in cyclic nucleotide-gated ion channels. *Neuron,* **33:** 703–713.

Ross EM, Howlett AC, Ferguson KM, Gilman AG (1978). Reconstitution of hormone-sensitive adenylate cyclase activity with resolved components of the enzyme. *Journal of Biological Chemistry* **253**(18)**:** 6401-6412.

Rost BR, Schneider-Warme F, Schmitz D, Hegemann P (2017). Optogenetic Tools for Subcellular Applications in Neuroscience. *Neuron* **96**(3)**:** 572-603.

Rupnik M, Kreft M, Sikdar SK, Grilc S, Romih R, Zupancic G*, et al.* (2000). Rapid regulated dense-core vesicle exocytosis requires the CAPS protein. *Proc Natl Acad Sci U S A* **97**(10)**:** 5627-5632.

Russo AF (2017). Overview of Neuropeptides: Awakening the Senses? *Headache* **57 Suppl 2:** 37-46.

Ryu M-H, Kang I-H, Nelson MD, Jensen TM, Lyuksyutova AI, Siltberg-Liberles J*, et al.* (2014). Engineering adenylate cyclases regulated by near-infrared window light. *Proceedings of the National Academy of Sciences of the United States of America* **111**(28)**:** 10167–10172.

Ryu M-H, Moskvin OV, Siltberg-Liberles J, Gomelsky M (2010). Natural and engineered photoactivated nucleotidyl cyclases for optogenetic applications. *The Journal of biological chemistry* **285**(53)**:** 41501–41508.

Salkoff L, Wei AD, Baban B, Butler A, Fawcett G, Ferreira G*, et al.* (2005). Potassium channels in C. elegans. *WormBook : the online review of C. elegans biology***:** 1-15.

Schafer WR (2002). Genetic analysis of nicotinic signaling in worms and flies. *Journal of neurobiology* **53**(4)**:** 535-541.

Scheib U, Broser M, Constantin OM, Yang S, Gao S, Mukherjee S*, et al.* (2018). Rhodopsin-cyclases for photocontrol of cGMP/cAMP and 2.3 A structure of the adenylyl cyclase domain. *Nat Commun* **9**(1)**:** 2046.

Scheib U, Stehfest K, Gee CE, Korschen HG, Fudim R, Oertner TG*, et al.* (2015). The rhodopsin-guanylyl cyclase of the aquatic fungus Blastocladiella emersonii enables fast optical control of cGMP signaling. *Sci Signal* **8**(389)**:** rs8.

Schmidpeter PAM, Gao X, Uphadyay V, Rheinberger J, Nimigean CM (2018). Ligand binding and activation properties of the purified bacterial cyclic nucleotide-gated channel SthK. *J Gen Physiol* **150**(6)**:** 821-834.

Schneider F, Gradmann D, Hegemann P (2013). Ion selectivity and competition in channelrhodopsins. *Biophysical journal* **105**(1)**:** 91-100.

Schneider F, Grimm C, Hegemann P (2015). Biophysics of Channelrhodopsin. *Annual review of biophysics* **44:** 167-186.

Schröder-Lang S, Schwärzel M, Seifert R, Strünker T, Kateriya S, Looser J*, et al.* (2007). Fast manipulation of cellular cAMP level by light in vivo. *Nature methods* **4**(1)**:** 39–42.

Schroll C, Riemensperger T, Bucher D, Ehmer J, Voller T, Erbguth K*, et al.* (2006). Light-induced activation of distinct modulatory neurons triggers appetitive or aversive learning in Drosophila larvae. *Curr Biol* **16**(17)**:** 1741-1747.

Schultheis C, Liewald JF, Bamberg E, Nagel G, Gottschalk A (2011). Optogenetic long-term manipulation of behavior and animal development. *PloS one* **6**(4)**:** e18766.

Schuske K, Beg AA, Jorgensen EM (2004). The GABA nervous system in C. elegans. *Trends in neurosciences* **27**(7)**:** 407-414.

Schwarz EM (2005). Genomic classification of protein-coding gene families. *The C. elegans Research Community, WormBook***:** 1-23.

Selbie LA, Hill SJ (1998). G protein-coupled-receptor cross-talk the fine-tuning of multiple receptor-signalling pathways. *Trends in pharmacological sciences* **19:** 87-93.

Shapiro MS, Zagotta WN (2000). Structural Basis for Ligand Selectivity of Heteromeric Olfactory Cyclic Nucleotide-Gated Channels. *Biophysical journal* **78:** 2307–2320.

Shcherbakova DM, Shemetov AA, Kaberniuk AA, Verkhusha VV (2015). Natural photoreceptors as a source of fluorescent proteins, biosensors, and optogenetic tools. *Annual review of biochemistry* **84:** 519-550.

Shi YP, Thouta S, Claydon TW (2020). Modulation of hERG K(+) Channel Deactivation by Voltage Sensor Relaxation. *Frontiers in pharmacology* **11:** 139.

Shoeb F, Malykhina AP, Akbarali HI (2003). Cloning and functional characterization of the smooth muscle ether-a-go-go-related gene K+ channel. Potential role of a conserved amino acid substitution in the S4 region. *J Biol Chem* **278**(4)**:** 2503-2514.

Shu L, Zhang W, Su G, Zhang J, Liu C, Xu J (2013). Modulation of HERG K+ channels by chronic exposure to activators and inhibitors of PKA and PKC: actions independent of PKA and PKC phosphorylation. *Cellular physiology and biochemistry : international journal of experimental cellular physiology, biochemistry, and pharmacology* **32**(6)**:** 1830-1844.

Sieburth D, Madison JM, Kaplan JM (2006). PKC-1 regulates secretion of neuropeptides. *Nature neuroscience* **10**(1)**:** 49-57.

Sievers F, Wilm A, Dineen D, Gibson TJ, Karplus K, Li W*, et al.* (2011). Fast, scalable generation of high-quality protein multiple sequence alignments using Clustal Omega. *Molecular systems biology* **7:** 539.

Siksou L, Rostaing P, Lechaire JP, Boudier T, Ohtsuka T, Fejtova A*, et al.* (2007). Three-dimensional architecture of presynaptic terminal cytomatrix. *The Journal of neuroscience : the official journal of the Society for Neuroscience* **27**(26)**:** 6868-6877.

Sineshchekov OA, Govorunova EG, Li H, Spudich JL (2015). Gating mechanisms of a natural anion channelrhodopsin. *PNAS* **112**(46)**:** 14236 – 14241.

Sineshchekov OA, Li H, Govorunova EG, Spudich JL (2016). Photochemical reaction cycle transitions during anion channelrhodopsin gating. *Proc Natl Acad Sci U S A* **113**(14)**:** E1993-2000.

Sinha SC, Sprang SR (2006). Structures, mechanism, regulation and evolution of class III nucleotidyl cyclases. *Reviews of physiology, biochemistry and pharmacology* **157:** 105-140.

Smith HK, Luo L, O´Halloran D, Guo D, Huang X-Y, Samuel ADT*, et al.* (2013). Defining Specificity Determinants of cGMP Mediated Gustatory Sensory Transduction in Caenorhabditis elegans. *Genetics* **194:** 885–901.

Soppa J (1994). Two hypotheses--one answer. Sequence comparison does not support an evolutionary link between halobacterial retinal proteins including bacteriorhodopsin and eukaryotic G-protein-coupled receptors. *FEBS Letters* **342:** 7-11.

Spudich JL (2006). The multitalented microbial sensory rhodopsins. *Trends in microbiology* **14**(11)**:** 480-487.

Spudich JL, Yang C-S, Kwang-Hwan J, Spudich EN (2000). Retinylidene protein structures and functions from archaea to humans. *Annu. Rev. Cell Dev. Biol.* **16:** 365–392.

Stawicki TM, Takayanagi-Kiya S, Zhou K, Jin Y (2013). Neuropeptides function in a homeostatic manner to modulate excitation-inhibition imbalance in C. elegans. *PLoS genetics* **9**(5)**:** e1003472.

Steegborn C (2014). Structure, mechanism, and regulation of soluble adenylyl cyclases - similarities and differences to transmembrane adenylyl cyclases. *Biochimica et biophysica acta* **1842**(12 Pt B)**:** 2535-2547.

Steegborn C, Litvin TN, Levin LR, Buck J, Wu H (2005). Bicarbonate activation of adenylyl cyclase via promotion of catalytic active site closure and metal recruitment. *Nature structural & molecular biology* **12**(1)**:** 32-37.

Stepanovic SZ, Potet F, Petersen CI, Smith JA, Meiler J, Balser JR*, et al.* (2009). The evolutionarily conserved residue A653 plays a key role in HERG channel closing. *The Journal of physiology* **587**(Pt 11)**:** 2555-2566.

Steuer Costa W, Van der Auwera P, Glock C, Liewald JF, Bach M, Schuler C*, et al.* (2019). A GABAergic and peptidergic sleep neuron as a locomotion stop neuron with compartmentalized Ca2+ dynamics. *Nat Commun* **10**(1)**:** 4095.

Steuer Costa W, Yu S-C, Liewald JF, Gottschalk A (2017). Fast cAMP Modulation of Neurotransmission via Neuropeptide Signals and Vesicle Loading. *Current biology : CB* **27**(4)**:** 495–507.

Stierl M, Stumpf P, Udwari D, Gueta R, Hagedorn R, Losi A*, et al.* (2011). Light modulation of cellular cAMP by a small bacterial photoactivated adenylyl cyclase, bPAC, of the soil bacterium Beggiatoa. *The Journal of biological chemistry* **286**(2)**:** 1181–1188.

Stigloher C, Zhan H, Zhen M, Richmond J, Bessereau JL (2011). The presynaptic dense projection of the Caenorhabditis elegans cholinergic neuromuscular junction localizes synaptic vesicles at the active zone through SYD-2/liprin and UNC-10/RIM-dependent interactions. *The Journal of neuroscience : the official journal of the Society for Neuroscience* **31**(12)**:** 4388-4396.

Stirman JN, Crane MM, Husson SJ, Wabnig S, Schultheis C, Gottschalk A*, et al.* (2011). Real-time multimodal optical control of neurons and muscles in freely behaving Caenorhabditis elegans. *Nature methods* **8**(2)**:** 153–158.

Stretton AO (1976). Anatomy and development of the somatic musculature of the nematode Ascaris. *J Exp Biol* **3:** 773-788.

Su Y, Dostmann WRG, Herberg FW, Durick K, Xuong NH, Ten Eyck L*, et al.* (1995). Regulatory Subunit Of Protein Kinase A: Structure of Deletion Mutant with cAMP Binding Domains. *Science* **269**(5225)**:** 807-813.

Sulston J, Brenner S (1975). Dopaminergic neurons in the nematode Caenorhabditis elegans. *Journal of comparative neurobiology* **163:** 215-226.

Sulston J, Horvitz HR (1977). Post-embryonic cell lineages of the nematode, Caenorhabditis elegans. *Developmental Biology* **56:** 110-156.

Sulston J, Schierenberg E, White JG, Thomas JN (1983). The embryonic cell lineage of the nematode Caenorhabditis elegans. *Developmental Biology* **100:** 64-119.

Sunahara RK, Beuve A, Tesmer JJG, Sprang SR, Garbers DL, Gilman AG (1998). Exchange of Substrate and Inhibitor Specificities between Adenylyl and Guanylyl Cyclases. *The Journal of biological chemistry* **273:** 16332–16338.

Sutherland EW, Rall TW (1958). Fractionation and characterization of a cyclic adenine ribonucleotide formed by tissue particles. *Journal of Biological Chemistry* **232:** 1077-1091.

Swierczek NA, Giles AC, Rankin CH, Kerr RA (2011). High-throughput behavioral analysis in C. elegans. *Nat Methods* **8**(7)**:** 592-598.

Tanwar M, Sharma K, Moar P, Kateriya S (2018). Biochemical Characterization of the Engineered Soluble Photoactivated Guanylate Cyclases from Microbes Expands Optogenetic Tools. *Applied biochemistry and biotechnology* **185**(4)**:** 1014–1028.

Taylor SS, Zhang P, Steichen JM, Keshwani MM, Kornev AP (2013). PKA: lessons learned after twenty years. *Biochimica et biophysica acta* **1834**(7)**:** 1271-1278.

Tesmer JJG, Sunahara RK, Johnson RA, Gosselin G, Gilman AG, Sprang SR (1999). Two-Metal-Ion Catalysis in Adenylyl Cyclase. *Science* **285**(5428)**:** 756-760.

Thomas D, Zhang W, Karle CA, Kathofer S, Schols W, Kubler W*, et al.* (1999). Deletion of protein kinase A phosphorylation sites in the HERG potassium channel inhibits activation shift by protein kinase A. *J Biol Chem* **274**(39)**:** 27457-27462.

Tibbs GR, Liu DT, Leypold BG, Siegelbaum SA (1998). A state-independent interaction between ligand and a conserved arginine residue in cyclic nucleotide-gated channels reveals a functional polarity of the cyclic nucleotide binding site. *J Biol Chem* **273**(8)**:** 4497-4505.

Tolstenkov O, Van der Auwera P, Steuer Costa W, Bazhanova O, Gemeinhardt TM, Bergs ACF*, et al.* (2018). Functionally asymmetric motor neurons contribute to coordinating locomotion of Caenorhabditis elegans. *eLife* **7**.

Toplak Z, Hendrickx LA, Abdelaziz R, Shi X, Peigneur S, Tomasic T*, et al.* (2022). Overcoming challenges of HERG potassium channel liability through rational design: Eag1 inhibitors for cancer treatment. *Medicinal research reviews* **42**(1)**:** 183-226.

Touroutine D, Fox RM, Von Stetina SE, Burdina A, Miller DM, 3rd, Richmond JE (2005). acr-16 encodes an essential subunit of the levamisole-resistant nicotinic

receptor at the Caenorhabditis elegans neuromuscular junction. *J Biol Chem* **280**(29)**:** 27013-27021.

Towbin H, Staehelin T, Gordon J (1979). Electrophoretic transfer of proteins from polyacrylamide gels to nitrocellulose sheets procedure and some applications. *Proceedings of the National Academy of Sciences* **76:** 4350-4354.

Towers PR, Edwards B, Richmond JE, Sattelle DB (2005). The Caenorhabditis elegans lev-8 gene encodes a novel type of nicotinic acetylcholine receptor alpha subunit. *J Neurochem* **93**(1)**:** 1-9.

Trieu MM, Devine EL, Lamarche LB, Ammerman AE, Greco JA, Birge RR*, et al.* (2017). Expression, purification, and spectral tuning of RhoGC, a retinylidene/guanylyl cyclase fusion protein and optogenetics tool from the aquatic fungus Blastocladiella emersonii. *J Biol Chem* **292**(25)**:** 10379-10389.

Tsvetanova NG, von Zastrow M (2014). Spatial encoding of cyclic AMP signaling specificity by GPCR endocytosis. *Nature Chemical Biology* **10:** 1061–1065.

van de Bospoort R, Farina M, Schmitz SK, de Jong A, de Wit H, Verhage M*, et al.* (2012). Munc13 controls the location and efficiency of dense-core vesicle release in neurons. *J Cell Biol* **199**(6)**:** 883-891.

van der Horst MA, Hellingwerf KJ (2004). Photoreceptor Proteins, “Star Actors of Modern Times”: A Review of the Functional Dynamics in the Structure of Representative Members of Six Different Photoreceptor Families. *Acc. Chem. Res* **37:** 13-20.

Vandenberg J, Perry M, Perrin M, Mann S, Ke Y, Hill A (2012). hERG K+ CHANNELS: STRUCTURE, FUNCTION, AND CLINICAL SIGNIFICANCE. *Physiol Rev* **92:** 1393–1478.

Varnum MD, Black KD, Zagotta WN (1995). Molecular mechanism for ligand discrimination of cyclic nucleotide-gated channels. *Neuron* **15:** 619-625.

Varnum MD, Dai G (2015). Cyclic nucleotide–gated channels. *Handbook of Ion Channels*.

Varo G, Brown LS, Sasaki J, Kandori H, Maeda A, Needleman R*, et al.* (1995). Light-driven chloride ion transport by halorhodopsin from Natronobacterium pharaonis. 1. The photochemical cycle. *Biochemistry* **34:** 14490- 14499.

Vella MC, Slack FJ (2005). C. elegans microRNAs. *The C. elegans Research Community, WormBook***:** 1-9.

Von Stetina SE, Treinin M, Miller DM (2005). The Motor Circuit. **69:** 125-167.

Waggoner L, Hardaker L, S G, Schafer WR (2000). Effect of a neuropeptide gene on behavioral states in Caenorhabditis elegans egg-laying. *Genetics* **154**(3)**:** 1181-1192.

Walsh JD, Boivin O, Barr MM (2020). What about the males? the C. elegans sexually dimorphic nervous system and a CRISPR-based tool to study males in a hermaphroditic species. *Journal of neurogenetics* **34**(3-4)**:** 323-334.

Wang H, Webster P, Chen L, Fisher AL (2019). Cell-autonomous and non-autonomous roles of daf-16 in muscle function and mitochondrial capacity in aging C. elegans. *Aging* **11**(8)**:** 2295-2311.

Warmke J, Ganetzky B (1994). A family of potassium channel genes related to eag in Drosophila and mammals. *Proc Natl Acad Sci U S A* **8:** 3438-3442.

Watanabe S, Trimbuch T, Camacho-Perez M, Rost BR, Brokowski B, Sohl-Kielczynski B*, et al.* (2014). Clathrin regenerates synaptic vesicles from endosomes. *Nature* **515**(7526)**:** 228-233.

Weber IT, Shabb JB, Corbin JD (1989). Predicted structures of the cGMP binding domains of the cGMP-dependent protein kinase a key alanine,threonine difference in evolutionary divergence of cAMP and cGMP binding sites. *Biochemistry* **28**(14)**:** 6122–6127.

Weinshenker D, Wei A, Salkoff L, Thomas JH (1999). Block of an ether-a-go-go-Like K+ Channel by Imipramine Rescues egl-2 Excitation Defects inCaenorhabditis elegans. *Journal of Neuroscience* **19**(22)**:** 9831-9840.

Weissenberger S, Schultheis C, Liewald JF, Erbguth K, Nagel G, Gottschalk A (2011). PACα--an optogenetic tool for in vivo manipulation of cellular cAMP levels, neurotransmitter release, and behavior in Caenorhabditis elegans. *Journal of neurochemistry* **116**(4)**:** 616–625.

White JG (2013). Getting into the mind of a worm—a personal view. *The C. elegans Research Community, WormBook***:** 1-10.

White JG, Southgate E, Thomson JN, Brenner S (1986). The structure of the nervous system of the nematode Caenorhabditis elegans. *Philos Trans R Soc Lond B* **314:** 1-340.

Wicher D, Schafer R, Bauernfeind R, Stensmyr MC, Heller R, Heinemann SH*, et al.* (2008). Drosophila odorant receptors are both ligand-gated and cyclic-nucleotide-activated cation channels. *Nature* **452**(7190)**:** 1007-1011.

Wiegert JS, Oertner TG (2016). How (not) to silence long-range projections with light. *Nature neuroscience* **19:** 527–528.

Wietek J, Beltramo R, Scanziani M, Hegemann P, Oertner TG, Wiegert JS (2015). An improved chloride-conducting channelrhodopsin for light-induced inhibition of neuronal activity in vivo. *Scientific reports* **5:** 14807.

Wietek J, Broser M, Krause BS, Hegemann P (2016). Identification of a Natural Green Light Absorbing Chloride Conducting Channelrhodopsin from Proteomonas sulcata. *J Biol Chem* **291**(8)**:** 4121-4127.

Wietek J, Wiegert JS, Adeishvili N, Schneider F, Watanabe H, Tsunoda SP*, et al.* (2014). Conversion of channelrhodopsin into a light-gated chloride channel. *Science (New York, N.Y.)* **344**(6182)**:** 409–412.

Wightman B, Ha I, Ruvkun G (1993). Posttranscriptional regulation of the heterochronic gene lin-14 by lin-4 mediates temporal pattern formation in C. elegans. *Cell* **75**(855-862).

Wilkinson WJ, Benjamin AR, De Proost I, Orogo-Wenn MC, Yamazaki Y, Staub O*, et al.* (2011). Alveolar epithelial CNGA1 channels mediate cGMP-stimulated, amiloride-insensitive, lung liquid absorption. *Pflugers Archiv : European journal of physiology* **462**(2)**:** 267-279.

Willoughby D, Cooper MF (2007). Organization and Ca2+ regulation of adenylyl cyclases in cAMP microdomains. *Physiol Rev* **87:** 965–1010.

Wojtyniak M, Brear AG, O'Halloran DM, Sengupta P (2013). Cell- and subunit-specific mechanisms of CNG channel ciliary trafficking and localization in C. elegans. *J Cell Sci* **126**(Pt 19)**:** 4381-4395.

Woldemariam S, Nagpal J, Hill T, Li J, Schneider MW, Shankar R*, et al.* (2019). Using a Robust and Sensitive GFP-Based cGMP Sensor for Real-Time Imaging in Intact Caenorhabditis elegans. *Genetics* **213**(1)**:** 59-77.

Wong MY, Zhou C, Shakiryanova D, Lloyd TE, Deitcher DL, Levitan ES (2012). Neuropeptide delivery to synapses by long-range vesicle circulation and sporadic capture. *Cell* **148**(5)**:** 1029-1038.

Wood W (1988). The nematode C. elegans. *Cold Spring Harbor Monograph Series* (17).

Yang S, Constantin OM, Sachidanandan D, Hofmann H, Kunz TC, Kozjak-Pavlovic V*, et al.* (2021). PACmn for improved optogenetic control of intracellular cAMP. *BMC biology* **19**(1)**:** 227.

Yizhar O, Fenno LE, Davidson TJ, Mogri M, Deisseroth K (2011). Optogenetics in neural systems. *Neuron* **71**(1)**:** 9–34.

Young EC, Krougliak N (2004). Distinct structural determinants of efficacy and sensitivity in the ligand-binding domain of cyclic nucleotide-gated channels. *J Biol Chem* **279**(5)**:** 3553-3562.

Yu B, Wang X, Wei S, Fu T, Dzakah EE, Waqas A*, et al.* (2017). Convergent Transcriptional Programs Regulate cAMP Levels in C. elegans GABAergic Motor Neurons. *Developmental cell* **43**(2)**:** 212-226 e217.

Yu SC, Liewald JF, Shao J, Steuer Costa W, Gottschalk A (2021). Synapsin Is Required for Dense Core Vesicle Capture and cAMP-Dependent Neuropeptide Release. *The Journal of neuroscience : the official journal of the Society for Neuroscience* **41**(19)**:** 4187-4201.

Zagotta WN (1996). Structure and function of cyclic nucleotide-gated channels. *Ann. Rev. Neurosci.* **19:** 253-263.

Zagotta WN, Olivier NB, Black KD, Young EC, Olson R, Gouaux E (2003). Structural basis for modulation and agonist specificity of HCN pacemaker channels. *Nature* **425**(6954)**:** 200-205.

Zarkower D (2006). Somatic sex determination. *The C. elegans Research Community, WormBook***:** 1-12.

Zhang F, Vierock J, Yizhar O, Fenno LE, Tsunoda S, Kianianmomeni A*, et al.* (2011). The microbial opsin family of optogenetic tools. *Cell* **147**(7)**:** 1446-1457.

Zhang F, Wang L-P, Brauner M, Liewald JF, Kay K, Watzke N*, et al.* (2007a). Multimodal fast optical interrogation of neural circuitry. *Nature* **446**(7136)**:** 633–639.

Zhang G, Liu Y, Ruoho AE, Hurley JH (1997). Structure of the adenylyl cyclase catalytic core. *Nature* **386:** 247-253.

Zhang YP, Oertner TG (2007b). Optical induction of synaptic plasticity using a light-sensitive channel. *Nat Methods* **4**(2)**:** 139-141.

Zhen M, Samuel AD (2015). C. elegans locomotion: small circuits, complex functions. *Current opinion in neurobiology* **33:** 117-126.

Zhou L, Olivier NB, Yao H, Young EC, Siegelbaum SA (2004). A conserved tripeptide in CNG and HCN channels regulates ligand gating by controlling C-terminal oligomerization. *Neuron* **44**(5)**:** 823-834.

Zhou L, Siegelbaum SA (2007). Gating of HCN channels by cyclic nucleotides: residue contacts that underlie ligand binding, selectivity, and efficacy. *Structure* **15**(6)**:** 655-670.

Zong X, Zucker H, Hofmann F, Biel M (1998). Three amino acids in the C-linker are major determinants of gating in cyclic nucleotide-gated channels. *The EMBO Journal* **17**(2)**:** 353-362.

6. Appendix

6.1. Sequence Alignments

6.1.1. Sequence alignment of PKA regulatory subunit RIα and PKG Iβ and the *C. elegans* ion channels TAX-4, CNG-1, CNG-2, CNG-3, CHE-6, EGL-2 and UNC-103

To identify ion channels comprising a cAMP binding domain and to examine the nucleotide binding pockets of the channels, a sequence alignment of PKA´s regulatory subunit Riα (PDB entry 1NE6) and PKG Iβ (PDB ID 4KU7) was performed with the *C. elegans* genome (Figure 88). The regulatory subunit of PKA was selected for sequence alignment because its cAMP-binding domain is one of the best studied binding domain among cAMP effectors (Berman *et al.*, 2005; Lorenz *et al.*, 2017a; Lorenz *et al.*, 2017b).

```
PKA          ------------------------------------------------------------ 0
PKG          ------------------------------------------------------------ 0
tax-4        ------------------------------------------------------------ 0
CNG-1        ------------------------------------------------------------ 0
CNG-2        MFSSFNFEDPPPS----------EVPRKVQRKDRSVRYLRALSAKNQERTANEHSSVDVA 50
CNG-3        ------------------------------------------------------------ 0
CHE-6        ------------------------------------------------------------ 0
EGL-2        ------MPVGKRGLVAPQNTFLENVIRRCNNADTSFILANAQVVDYPIVYCNDGFSKLVG 54
UNC-103      ------MPRRPPLL------RLAPVP-EDEEDDEVFF-EPADK--------NDDKQ---- 34


PKA          ------------------------------------------------------------ 0
PKG          ------------------------------------------------------------ 0
tax-4        --------------MSTAEPAP-------------------------DPTNPSTSGL 18
CNG-1        ------------------------------------------------------------M 1
CNG-2        VTQASLSVPRPGILRLPSSDPGE-------------------------EDPQPSTSSI 83
CNG-3        ------------------------------------------------------------ 0
CHE-6        ------------------------------------------------------------ 0
EGL-2        YTRAEI-MQKPCSLAFMHGEHGEVGSLQKMQEALENARTEQAEIGLCKKNKTPIWLLVHL 113
UNC-103      --------------RFLPK--QSRGSSRFVSEDVLNNSDDEEENKRCHLVSSSHASLRSL 78


PKA          ------------------------------------------------------------ 0
PKG          ------------------------------------------------------------ 0
tax-4        APTTN-----------------------------------------------GIGSPP 29
CNG-1        AENVS-----------------------------------------------TTSSAR 12
CNG-2        PHRPSKWATVREKSPQIIGGHA-KEVTFQERHHKLDLNKSRSTSKNRRKSAQNGGAEDPG 142
CNG-3        ------------------------------------------------------------ 0
CHE-6        ------------------------------------------------------------ 0
EGL-2        APIKNH------KDAVVLYLCQFKDIT-----------------PLKQPLDDENNKGLSR 150
UNC-103      SPCPSL------QSSSSIGGCGGGGMV-----------------GG----GGGGGAGGSS 111


PKA          ------------------------------------------------------------ 0
PKG          ------------------------------------------------------------ 0
tax-4        PTASAATKFS----------ILTKFLRRK-NQVHTTTAQQNEFMQKYMPNGNSNAVQPAA 87
CNG-1        RETFGGIVFRIY--------ALRGWMQRAQKRLHLFR-----------KND--VDIE--- 48
CNG-2        QKSFSDVVKTAM--------MLRTWISAMEHDERES----------------EPDRDATT 178
CNG-3        -------------------------MSTH-----SA---------QKLPNLHERKRRMS- 20
CHE-6        -------------------------MSSAEVSDSES----------------LLDIDISQ 19
EGL-2        ILQIARIAK-----------SKQQFNQIETKDLHKS-----------------PGNTSSN 182
UNC-103      TRRNAAIASTSSTTSSAAGRRASAFVRRMSM-AIPT----------------LSADPVP 153


PKA          ------------------------------------------------------------ 0
PKG          ------------------------------------------------------------ 0
tax-4        TGGQPASSDGGSAIEVPPPKESY----------AVRIRKYLANYTQDPSTDNFYYWTCVV 128
CNG-1        -----------TNFREALREEQE----------DDEKSSGFMSFTVDEHSNTFYLWTGLV 87
CNG-2        TNAEITAADDRSILPSPPIFQQRQTGFTQIKDILTDKCRKLYYFYVTENSTFFYYWTAII 238
CNG-3        -----KKPDDDDLIPQHFEYENQYEKW------RAANPRIEYDFSVDESGYIYWIWTFFV 69
CHE-6        Y--EV--VEKYLEDEELESFDIYPSGWTICKDILHDSFHRLLYFYVPFNSKYYYIWSFFV 75
EGL-2        FNQV--MNLGG---DMLPQYRQETPKTSPHI--------------ILHYSSFKTIWDWSI 223
UNC-103      FSAV--LSLGA---DVLPEYKLQPTRIHHCT--------------IVHYSPFKAVWDWII 194


PKA          ------------------------------------------------------------ 0
PKG          ------------------------------------------------------------ 0
tax-4        TVAYIYNLLFVIARQVFNDLIGPSSQSLCRFYNGTLNSTTQVECTYNMLTNMKEMPTYSQ 188
CNG-1        SLVALHPLVFTAL-SVFQDVH--------PF---------------------------- 109
CNG-2        SIGILYNMFAMVI-FIFDDVH---------------------------------------- 258
CNG-3        VCGCLYNIIVLSV-LAFENIR---------------------------------------- 89
CHE-6        SFGVMYNMFAMVI-FIFADIK---------------------------------------- 95
EGL-2        LALTFYTAFMVPFNIAFKNSL-------RPFYLIS------------------------- 251
UNC-103      LLLVIYTAVFTPYVAAFLLRE-------L-----Q------------------------- 217
```

```
PKA          ------------------------------------------------------------ 0
PKG          ------------------------------------------------------------ 0
tax-4        YPDLGWSKYWHFRMLWVFFDLLMDCVYLIDTFLNYRMGYMDQGL----VVREAEKVTKAY 244
CNG-1        ------------LRNTGPLNLLLDLVNILDLIAHTRIEYVENGV----AVKNLSKLMHHR 153
CNG-2        ---------FGYFNQWLYVNLFFDFCFLLDCLVGSRMTFVSEGN----EVSQTDKMFKNY 305
CNG-3        ---------YAYIEKILPINIAFDTVFLFDIILRSMLSFYEDGV----LITSFSETWRHY 136
CHE-6        ---------TQYFWNWIFLNVMFDMVFIVDIFVQSRLTYLHEGE----EVKNTKKLRKNY 142
EGL-2        ----SRENPGGGIDSVALMDSIVDVIFFADILLNFHTTFVGPGG---EVVIEPSVIRQNY 304
UNC-103      ----DTAKKSRFTEPLEIVDLIVDIMFIVDIIINFRTTYVNENDEACQVVSDPGKIATHY 273

PKA          ------------------------------------------------------------ 0
PKG          ------------------------------------------------------------ 0
tax-4        W-QSKQYRIDGISLIPLDYILGWPIPYI----NWRGLPILRLNRLIRYKRVRNCLERTET 346
CNG-1        L-KSTFFILDVIAVVPAESLHIFGDSF-----FW-----SRINRLTKCYRLFDFSTQTDT 252
CNG-2        R-QSRRCKLDLLCLAPADFYLFIDTKA----------SLVRAIRLVKAYRLYEFIMLTQR 404
CNG-3        V-HSFYFAIDLLAIFPFDYLLIRKTSA----------AFCRLNRFLKIYRIANFIAQSYG 244
CHE-6        FFQKLKVANDIFCLLPLDFLLFFDDSM----------SLVRTIRIVKVIRLMDFVQRTQQ 242
EGL-2        F--KSWFLIDLLSCLPYDIFYMFKRDDERIGSLFSALKVVRLLRLGRVARKLD------- 409
UNC-103      F--KGWFIIDMVAAVPFDLLLVSTNSDE-TTTLIGLLKTARLLRLVRVARKLD------- 371

PKA          ------------------------------------------------------------ 0
PKG          ------------------------------------------------------------ 0
tax-4        RSSMPNAFRVVVVVWYIVIIIHWNACLYFWISEW------IGL----G---TDAWVYGHL 346
CNG-1        RTTSPHAFGLFKLIFICVVIFHWNGCLYFYISKV------YNY----TTARLEHWIFSYD 252
CNG-2        RTDFPHFMKILFLTSSCAILFHWNACVYFLFSLY------QGL----TEDDPNAFGFSYY 404
CNG-3        KLTQ-VTISLSKIFTACFLLFHVNACVFYIISVNSDTSSWDGVNATFDDDEYLPWPYTPE 244
CHE-6        QTTFPRAFKIILLAVSCIVLFHWNACLYFLFSLY------EGI----TEESQTEFGFSYY 242
EGL-2        NYLEYGAATLLLLLCAYVIVAHWLACVWFWIGDSEVRLKMDNL------ALPDGWLWKLS 409
UNC-103      RYSEYGAAVLLLLMATFALIAHWLACIWYAIGSAELSHK------------EYTWLHQLS 371

PKA          -------RRRRGAISAEVYTEEDAA----SYVRKVIPKDYKTM---------------AA 34
PKG          ------------------------------------------------------------ 0
tax-4        N--K------------------------QSLPD----------------------DITDT 358
CNG-1        KIINPILATCVTDIPNHRDFCDTDDLLITHLPENEVQFTVTDYMTTWEN--KTTTIKFAN 310
CNG-2        KVFDPRFSICDALYDQDCYYPEDTE-VL-DI-RDERPHYMEDMYKFWDK--KFNILQIGN 459
CNG-3        KITDAYFVGCDGRTD--CYNPY-------FYYDEAREDHLVELYHFWRTDNRTHIYNFSQ 295
CHE-6        KVFEPVFPTCQAYYDENCWFGEDIDHTL-DL-DDVRDSYKKEMAEYWKD--KHYRWTTGN 298
EGL-2        N-------------------------------DLRQHYNIPL------SNKTTLVGGPS 431
UNC-103      K-------------------------------QLAQPYTS--------TNGTIPTGGPT 391

PKA          LAKAIEKNVLFSHLD--------------DNERSDIFDAMFPVSFIAGETVIQQGDEGDN 80
PKG          ------------------------------------------------------------ 0
tax-4        LLRRYVYSFYWSTLILTTIGEVPSPVRN-IEYAFVTLDLMCGVLIFAT----IVGNVGSM 413
CNG-1        FFRQYALSFYWSALTLVTLGEQPSPCTT-FQNAFEIGDTLLGLVIFAV----IVGDVGNM 365
CNG-2        FSREYSMTIYWSSLTITKCGQQPWPSKS-SQNSLEIFDTLIGVLVFAT----IIGGVGSV 514
CNG-3        FTKEYTLSMYWSAMTMTTLGEQPAPNTS-LQNAFEIVNTLAGLLLFAV----IMGSIGDL 350
CHE-6        FSREYSMSIYWSALTITTCGQQPWPSTS-SQNSLEVFDTLIGVLVFAT----IIGSVGSV 353
EGL-2        RTSAYISSLYYTMSCMSTVGFGNIASNTDNEKIFGVCMMIISALLYAA----IFGHMTTI 487
UNC-103      LKSRYVTSLYFTLSTITSIGFGNVSATTDSEKIFTIIMMILGSLMYAS----VFGNVSAI 447

PKA          FYVIDQGEMDVYVNNEWATSVGEGGSFGELALIYGTPRAATVKA-KTNVKLWGIDR---- 135
PKG          ------------------------------------------------------------ 0
tax-4        ISNMS------AARTEFQNKMDGIKQYMELR---KVSKQLEIRVIKWFDYLWTNKQSL-S 463
CNG-1        VVAIN------LRKSEFENVLDGCKRFMVYR---KVPNLLRKKAVEYFAYVWAHGGAQVD 416
CNG-2        VTQMS------QNVNDFREMMDGIKFYMKYR---GVQSAIQDRVLNCFLYLNSHNQLY-D 564
CNG-3        VANAN------AVKTFWQTLMDGLKQYMTYR---NLNERLQTKVLKYCEYEMAEETIM-K 400
CHE-6        VTQMS------QTVNEFRQMMDGIKFYMKYR---EVNSAIQERALSCFMYLMAHNQLD-D 403
EGL-2        IQQMT------SSTVRYHEMISNVREFIKLQ---EIPKELAERVMDYVVSTWAMTKGI-D 537
UNC-103      IQRLY------SGTARYHTEMSRLREFIRFH---QIPNPLRQRLEEYFQHAWSYTNGI-D 497
```

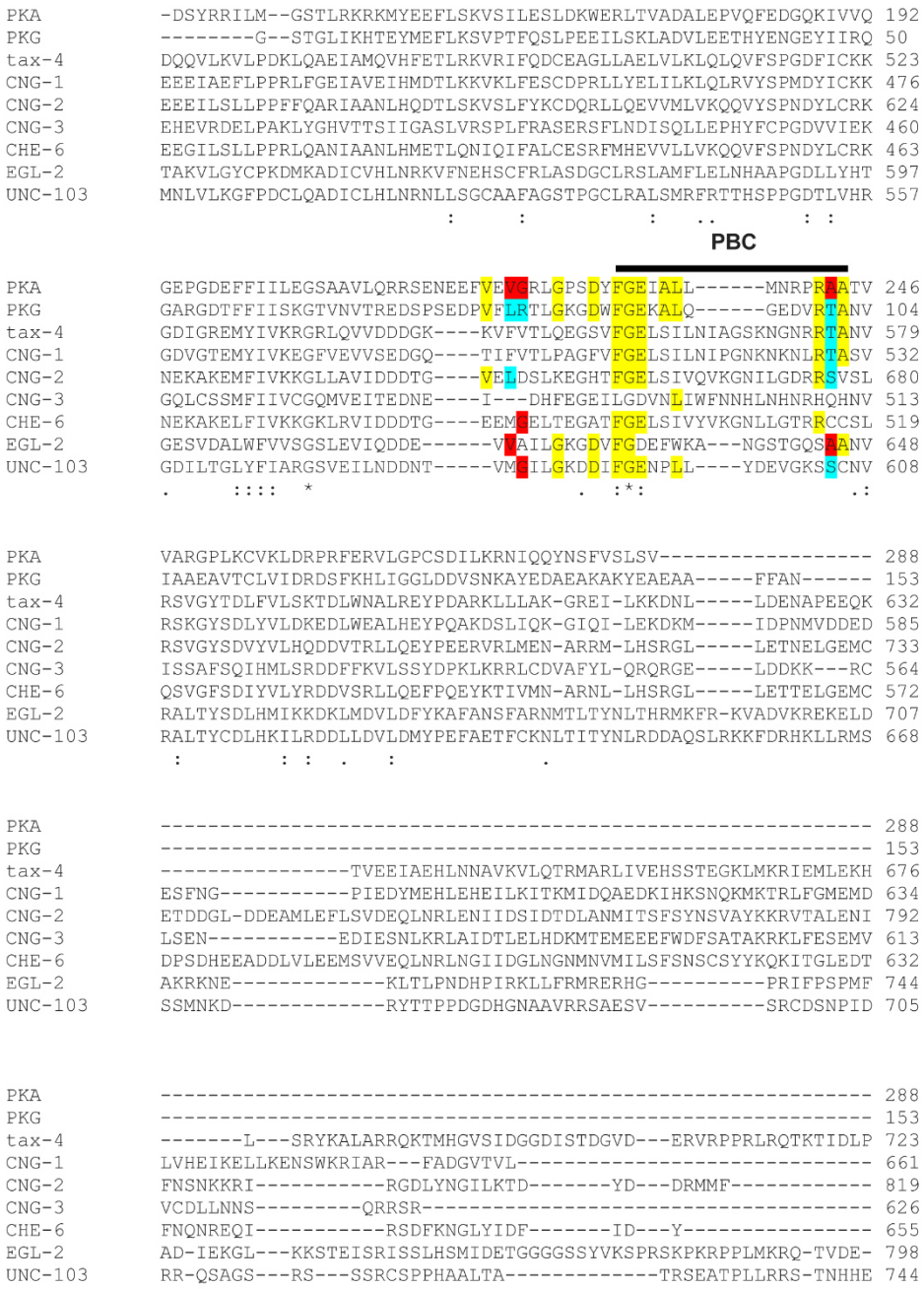
PBC

```
PKA          ------------------------------------------------------------ 288
PKG          ------------------------------------------------------------ 153
tax-4        ----------------------------------TGTESESLLK---------------- 733
CNG-1        ------------------------------------------------------------ 661
CNG-2        ------------------------------------------------------------ 819
CNG-3        ------------------------------------------------------------ 626
CHE-6        ------------------------------------------------------------ 655
EGL-2        --DALSRTSWGMDK----------------------KDREWSSLSNIKT-EMKSKFDII 832
UNC-103      EDDALFDDIRAFARGNTVTMSPTVAGNSVSPTTAIHNDGIHSQQLSDRSDDYEERRANMF 804


PKA          ------------------------------------------------------------ 288
PKG          ------------------------------------------------------------ 153
tax-4        ------------------------------------------------------------ 733
CNG-1        ------------------------------------------------------------ 661
CNG-2        ------------------------------------------------------------ 819
CNG-3        ------------------------------------------------------------ 626
CHE-6        ------------------------------------------------------------ 655
EGL-2        GERLTIIEQI--------NSRL----A-LLERVLIGNNGGANTPSTMPVG------SFSA 873
UNC-103      GRRLESIESQMERMQNKFNSDMETLIKLVKEQSIIRNNGSSNEEPNARYRPNNYISSAIR 864


PKA          ------------------------------------------------------------ 288
PKG          ------------------------------------------------------------ 153
tax-4        ------------------------------------------------------------ 733
CNG-1        ------------------------------------------------------------ 661
CNG-2        ------------------------------------------------------------ 819
CNG-3        ------------------------------------------------------------ 626
CHE-6        ------------------------------------------------------------ 655
EGL-2        LNESGNRLTLDAAPVARSVSWSEQHQPHWQRTSTVPPLRELEAGEWEPPIREPTPNPSTS 933
UNC-103      LPNGGGGGVVDEMRVS-----------------------RLSSHEPPT----PTQETD 895


PKA          ----------------------- 288
PKG          ----------------------- 153
tax-4        ----------------------- 733
CNG-1        ----------------------- 661
CNG-2        ----------------------- 819
CNG-3        ----------------------- 626
CHE-6        ----------------------- 655
EGL-2        SSRVPHIQIDEDGEARPPTRTRI 956
UNC-103      --TIL------------------ 898
```

Figure 88: Sequence alignment of PKA regulatory subunit RIα and PKG Iβ and the C. elegans ion channels TAX-4, CNG-1, CNG-2, CNG-3, CHE-6, EGL-2 and UNC-103. *The phosphate-binding cassette (PBC), which interacts with the sugar-phosphate part of cAMP, is highlighted by a black bar. Conserved residues near and within the PBC are illustrated in yellow (Berman et al., 2005; Lorenz et al., 2017a; Lorenz et al., 2017b). Key residues mediating cAMP or cGMP specificity are highlighted in red or cyan, respectively (Lorenz et al., 2017b; Weber et al., 1989). In general, conserved residues are represented as asterisks (*) and semiconserved residues as semicolons (:) and dots (.). Sequences were aligned using Clustal Omega (Goujon et al., 2010; Sievers et al., 2011). PKA Riα from Bos taurus (PDB ID 1RGS) and PKG Iβ from Homo sapiens (PDB ID 4KU7) were used for alignment.*

6.1.2. Sequence alignment of the potassium channels hERG and Eag and the *C. elegans* channels EGL-2 and UNC-103

To examine the potential domain architecture and ion selectivity of UNC-103 and EGL-2, the amino acid sequences were aligned against the potassium channels hERG from *Homo sapiens* (UniProtKB ID Q12809) and Eag from *Drosophila melanogaster* (UniProtKB ID M9PHT2) (Figure 89).

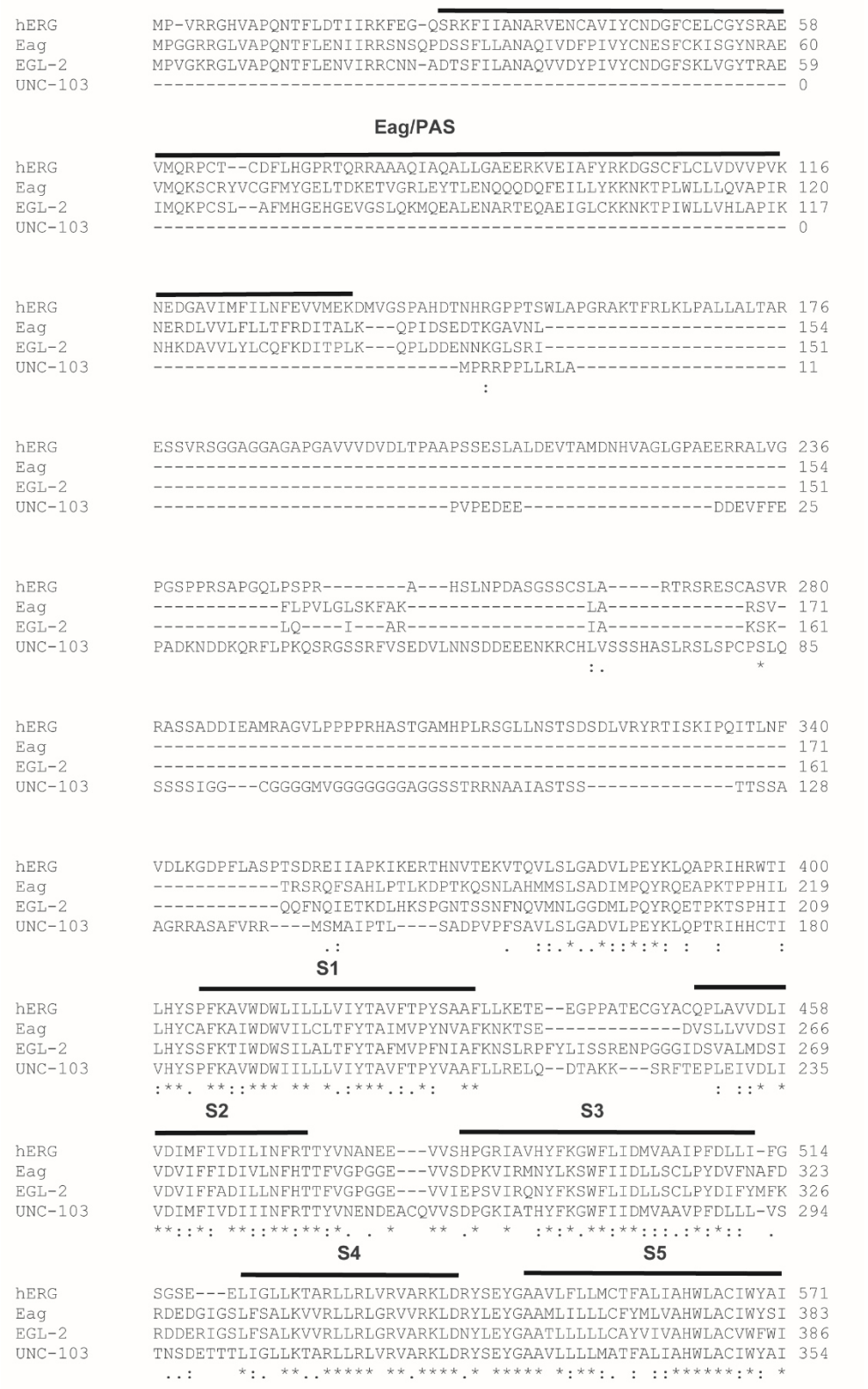
Eag/PAS
S1
S2
S3
S4
S5

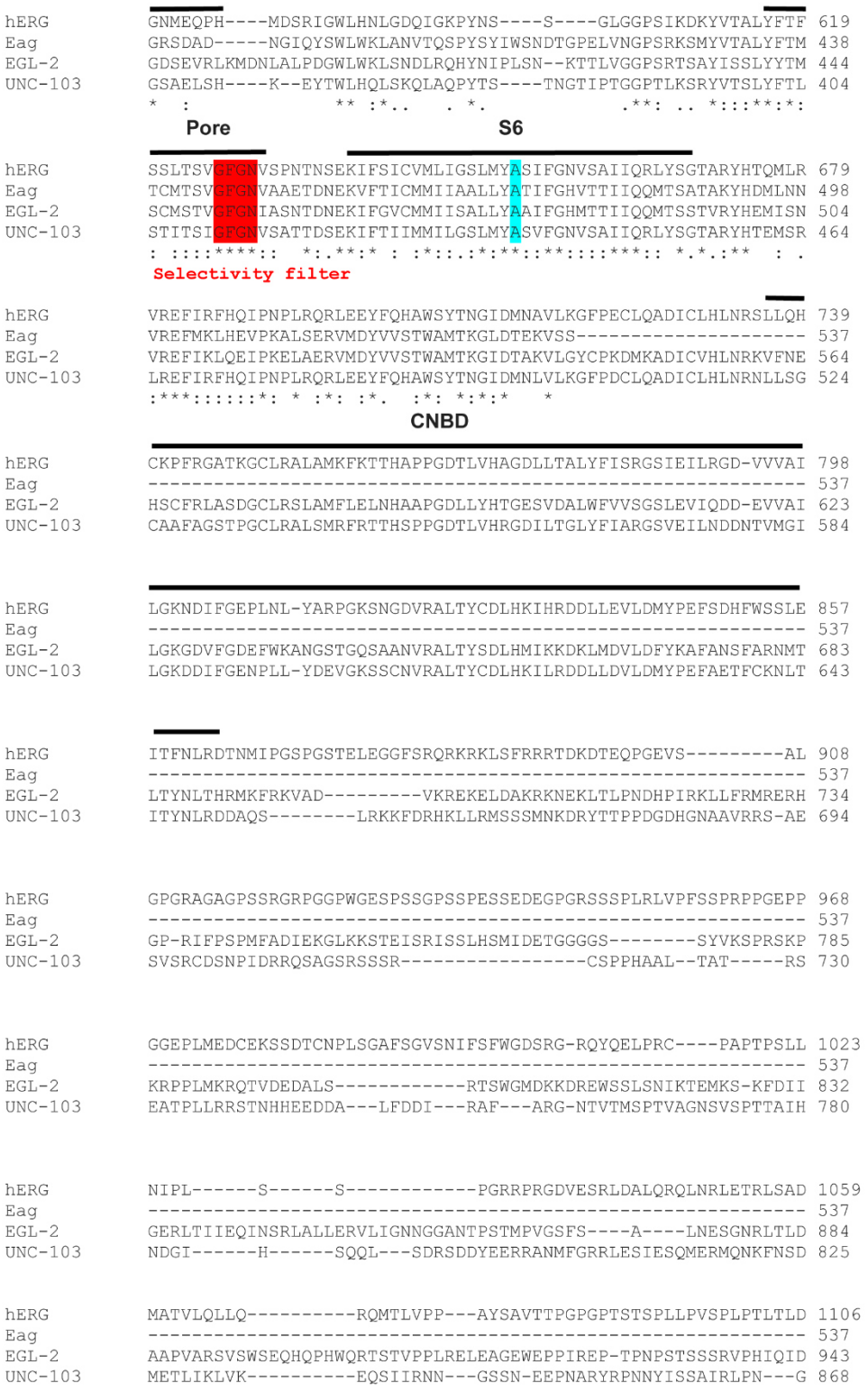
Pore
S6
Selectivity filter
CNBD

```
hERG        SLSQVSQFMACEELPPGAPELPQEGPTRRLSLPGQLGALTSQPLHRHGSDPGS 1159
Eag         -------------------------------------------------- 537
EGL-2       EDGEA------------RPPTRTR-----I---------------------- 956
UNC-103     GGGGVVDEMRVSRLSSHEPPTPTQETDTIL---------------------- 898
```

Figure 89: Sequence alignment of the potassium channels hERG and Eag and the C. elegans ion channels EGL-2 and UNC-103. *The intracellular Per-Arnt-Sim (PAS) domain, the transmembrane helices S1-S6, the pore helix (pore), and the intracellular cyclic nucleotide-binding domain (CNBD) are indicated via a black bar above the sequence (Barros et al., 2020). The potassium selectivity filter GFGN is highlighted in red (Toplak et al., 2022). The conserved alanine residue in segment 6 is highlighted in cyan. Mutating this residue to threonine caused an increased conductance (Gain-of-function) (Reiner et al., 2006). Conserved residues are represented as asterisks (*) and semiconserved residues as semicolons (:) and dots (.). Sequences were aligned using Clustal Omega (Goujon et al., 2010; Sievers et al., 2011). hERG (human eag-related gene) from* Homo sapiens *(UniProtKB ID Q12809) and Eag (ether-à-go-go) from* Drosophila melanogaster *(UniProtKB ID M9PHT2) were used for alignment.*

6.1.3. Sequence alignment of the cation channel CNGA1 and the *C. elegans* ion channels TAX-4, CNG-1, CNG-2, CNG-3 and CHE-6

To examine the potential domain architecture and ion selectivity of CNG-1, CNG-2, CNG-3 and CHE-6, the amino acid sequences were aligned against the cation channels Cyclic nucleotide-gated channel alpha 1 (CNGA1) from *Bos taurus* (UniProtKB ID Q00194) and TAX-4 (Figure 90).

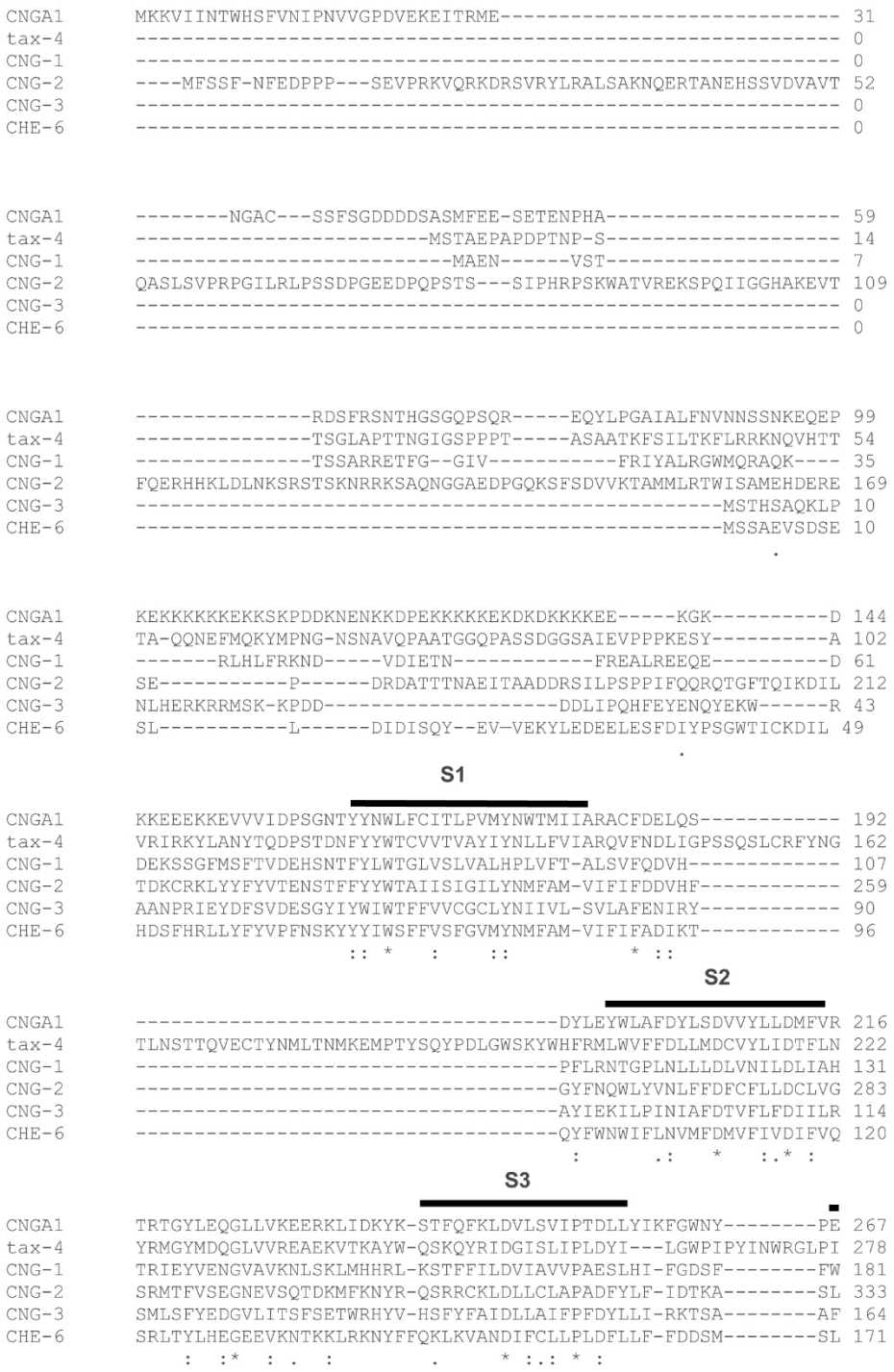
CNGA1 MKKVIINTWHSFVNIPNVVGPDVEKEITRME 31
tax-4 0
CNG-1 0
CNG-2 ----MFSSF-NFEDPPP---SEVPRKVQRKDRSVRYLRALSAKNQERTANEHSSVDVAVT 52
CNG-3 0
CHE-6 0
CNGA1 --------NGAC---SSFSGDDDDSASMFEE-SETENPHA 59
tax-4 ----------MSTAEPAPDPTNP-S 14
CNG-1 ----------MAEN------VST 7
CNG-2 QASLSVPRPGILRLPSSDPGEEDPQPSTS---SIPHRPSKWATVREKSPQIIGGHAKEVT 109
CNG-3 0
CHE-6 0
CNGA1 ---------------RDSFRSNTHGSGQPSQR-----EQYLPGAIALFNVNNSSNKEQEP 99
tax-4 ---------------TSGLAPTTNGIGSPPPT-----ASAATKFSILTKFLRRKNQVHTT 54
CNG-1 ---------------TSSARRETFG--GIV----------FRIYALRGWMQRAQK---- 35
CNG-2 FQERHHKLDLNKSRSTSKNRRKSAQNGGAEDPGQKSFSDVVKTAMMLRTWISAMEHDERE 169
CNG-3 ----------MSTHSAQKLP 10
CHE-6 ----------MSSAEVSDSE 10
CNGA1 KEKKKKKKEKKSKPDDKNENKKDPEKKKKKEKDKDKKKKEE-----KGK----------D 144
tax-4 TA-QQNEFMQKYMPNG-NSNAVQPAATGGQPASSDGGSAIEVPPPKESY----------A 102
CNG-1 -------RLHLFRKND-----VDIETN----------FREALREEQE----------D 61
CNG-2 SE----------P------DRDATTTNAEITAADDRSILPSPPIFQQRQTGFTQIKDIL 212
CNG-3 NLHERKRRMSK-KPDD--------------------DDLIPQHFEYENQYEKW------R 43
CHE-6 SL----------L------DIDISQY--EV-VEKYLEDEELESFDIYPSGWTICKDIL 49
S1
CNGA1 KKEEEKKEVVVIDPSGNTYYNWLFCITLPVMYNWTMIIARACFDELQS---------- 192
tax-4 VRIRKYLANYTQDPSTDNFYYWTCVVTVAYIYNLLFVIARQVFNDLIGPSSQSLCRFYNG 162
CNG-1 DEKSSGFMSFTVDEHSNTFYLWTGLVSLVALHPLVFT-ALSVFQDVH---------- 107
CNG-2 TDKCRKLYYFYVTENSTFFYYWTAIISIGILYNMFAM-VIFIFDDVHF---------- 259
CNG-3 AANPRIEYDFSVDESGYIYWIWTFFVVCGCLYNIIVL-SVLAFENIRY---------- 90
CHE-6 HDSFHRLLYFYVPFNSKYYYIWSFFVSFGVMYNMFAM-VIFIFADIKT---------- 96
S2
CNGA1 ----------DYLEYWLAFDYLSDVVYLLDMFVR 216
tax-4 TLNSTTQVECTYNMLTNMKEMPTYSQYPDLGWSKYWHFRMLWVFFDLLMDCVYLIDTFLN 222
CNG-1 ----------PFLRNTGPLNLLLDLVNILDLIAH 131
CNG-2 ----------GYFNQWLYVNLFFDFCFLLDCLVG 283
CNG-3 ----------AYIEKILPINIAFDTVFLFDIILR 114
CHE-6 ----------QYFWNWIFLNVMFDMVFIVDIFVQ 120
S3
CNGA1 TRTGYLEQGLLVKEERKLIDKYK-STFQFKLDVLSVIPTDLLYIKFGWNY--------PE 267
tax-4 YRMGYMDQGLVVREAEKVTKAYW-QSKQYRIDGISLIPLDYI---LGWPIPYINWRGLPI 278
CNG-1 TRIEYVENGVAVKNLSKLMHHRL-KSTFFILDVIAVVPAESLHI-FGDSF--------FW 181
CNG-2 SRMTFVSEGNEVSQTDKMFKNYR-QSRRCKLDLLCLAPADFYLF-IDTKA--------SL 333
CNG-3 SMLSFYEDGVLITSFSETWRHYV-HSFYFAIDLLAIFPFDYLLI-RKTSA--------AF 164
CHE-6 SRLTYLHEGEEVKNTKKLRKNYFFQKLKVANDIFCLLPLDFLLF-FDDSM--------SL 171

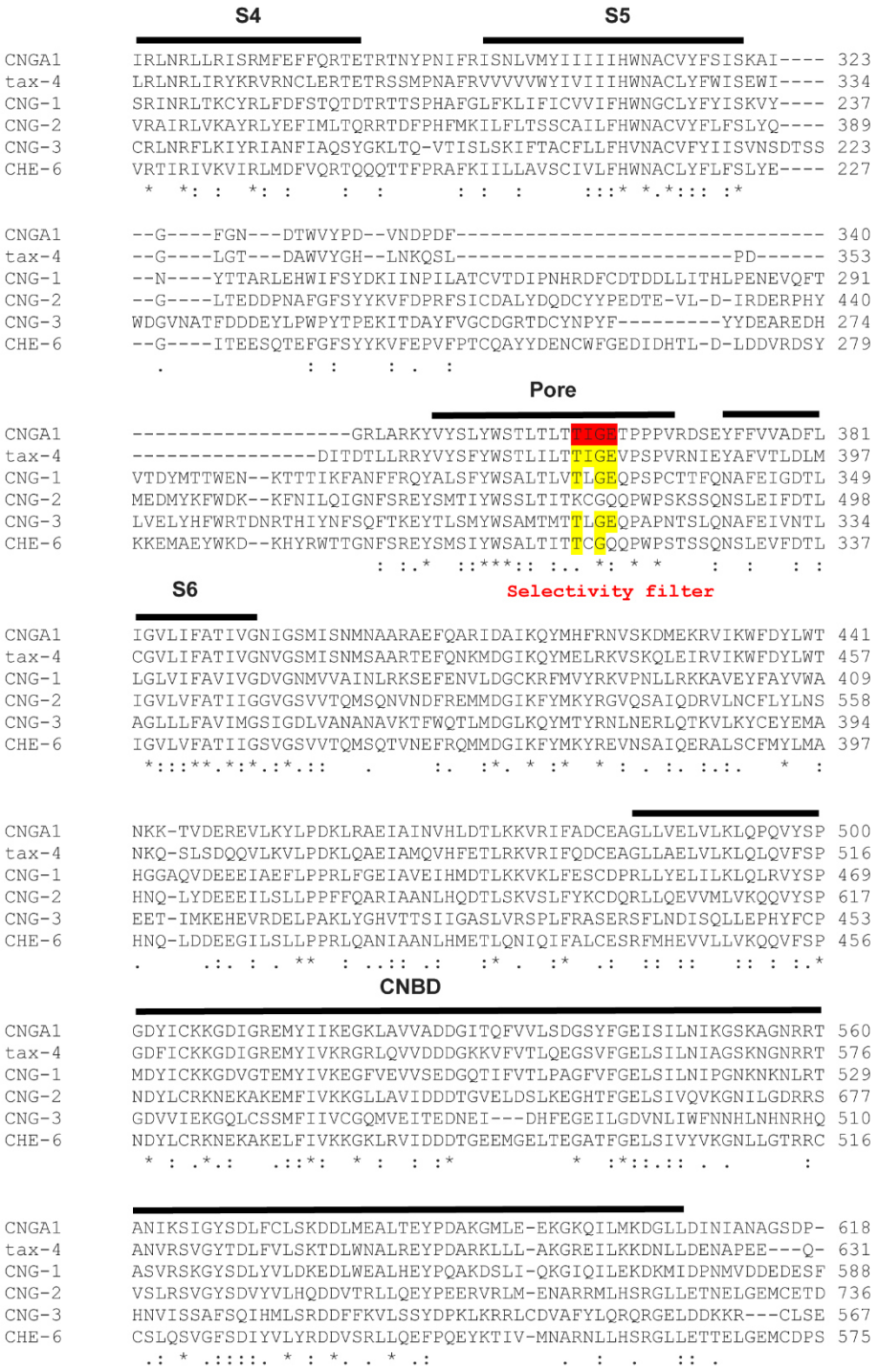
S4
S5
Pore
S6
Selectivity filter
CNBD

```
CNGA1      -K-----------DLEEKVTRMESSVDLLQTRFARILAEYESMQQKLKQRLTKVEKFLKP 666
tax-4      -K-----------TVEEIAEHLNNAVKVLQTRMARLIVEHSSTEGKLMKRIEMLEKHLSR 679
CNG-1      NG-----------PIEDYMEHLEHEILKITKMIDQAEDKIHKSNQKMKTRLFGMEMDLVH 637
CNG-2      DGL-DDEAMLEFLSVDEQLNRLENIIDSIDTDLANMITSFSYNSVAYKKRVTALENIFNS 795
CNG-3      N-----------EDIESNLKRLAIDTLELHDKMTEMEEEFWDFSATAKRKLFESEMVVCD 616
CHE-6      DHEEADDLVLEEMSVVEQLNRLNGIIDGLNGNMNVMILSFSNSCSYYKQKITGLEDTFNQ 635
                        : .   ::      :   :     .          ::   *  .

CNGA1      -LIDTE--------FSAIEGSGTESGPTDS------------TQD--------------- 690
tax-4      -YKALA------RRQKTMHGVSIDGGDISTDGVDERVRPPRLRQTKTIDLPTGTESESLL 732
CNG-1      EIKELLKENSWKRIARFADGVTVL---------------------------------- 661
CNG-2      NKKRIR--------GDLYNGILKTD-------YDDRMMF-------------------- 819
CNG-3      LLNNSQ------RRSR-------------------------------------------- 626
CHE-6      NREQIR--------SDFKNGLYIDF-------IDY------------------------ 655

CNGA1      -
tax-4      K
CNG-1      -
CNG-2      -
CNG-3      -
CHE-6      -
```

Figure 90: Sequence alignment of the cation channel CNGA1 and the C. elegans ion channels TAX-4, CNG-1, CNG-2, CNG-3 and CHE-6. *The transmembrane helices S1-S6, the pore helix (pore), and the intracellular cyclic nucleotide-binding domain (CNBD) are indicated via a black bar above the sequence (Komatsu et al., 1996). The selectivity filter motif TIGE is highlighted in red (Toplak et al., 2022). Conserved residues within this motif are depicted in yellow. In general, conserved residues are represented as asterisks (*) and semiconserved residues as semicolons (:) and dots (.). Sequences were aligned using Clustal Omega (Goujon et al., 2010; Sievers et al., 2011). Cyclic nucleotide-gated channel alpha 1 (CNGA1) from Bos taurus (UniProtKB ID Q00194) was used for alignment.*

6.2. Investigation of cAMP evoked muscle relaxation in channel loss of function background

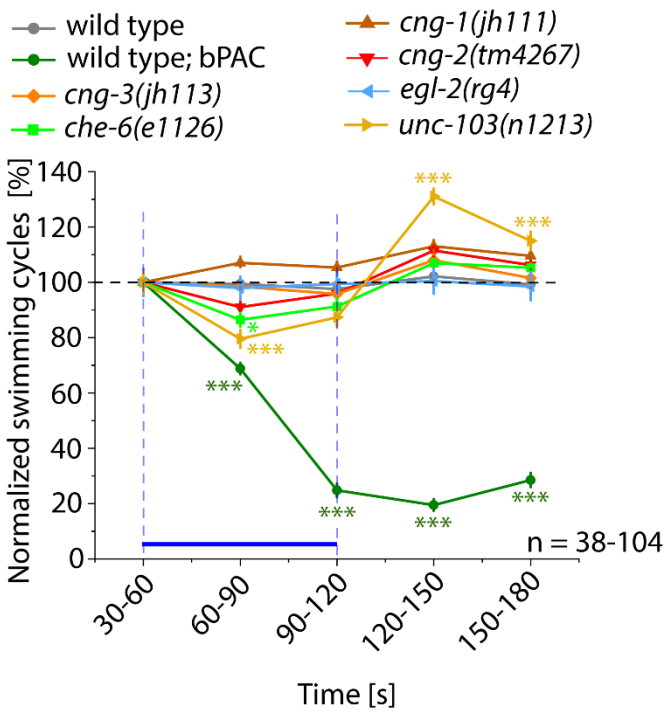

Figure 91: Influence of light application on channel loss of function mutant backgrounds. *A) Mean normalized swimming cycles ±SEM of cng-1(jh111), cng-2(tm4267), cng-3(jh113), che-6(e1126), egl-2(rg4), unc-103(n1213), wild type animals, and of wild type animals expressing bPAC in body wall muscle cells. Swimming cycles were calculated 60 s before, 60 s during, and 60 s after light exposure (0.9 mW/mm^2; 470 nm), and normalized to the mean swimming frequencies 30 s before the light stimulus. n = number of animals. Statistically significant differences to wild type animals were calculated using two-way ANOVA with Bonferroni correction (*p ≤ 0.05 and ***p ≤ 0.001).*

6.3. The cardiac action potential and its fundamental membrane currents

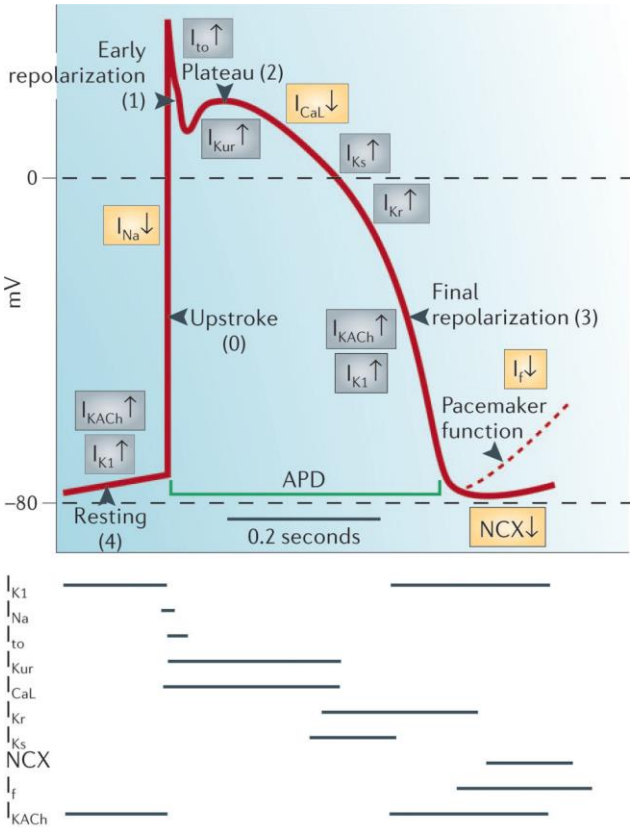

Figure 92: The cardiac action potential and its fundamental membrane currents. *The action potential is divided into 5 phases: Resting phase (4), depolarization (0), early repolarization (1), plateau phase (2), and final repolarization (3). Illustrated are the responsible membrane currents of each phase. The duration of the cardiac action potential is approximately 200 ms. NCX, sodium-calcium exchanger; ADP, Action potential duration. Image adapted from (Grant, 2009).*

6.4. Characterization of membrane-anchored bacterial photoactivatable adenylyl cyclases in body wall muscle cells

Aiming on the implementation of a membrane-anchored optogenetic tool for cAMP generation in *C. elegans*, the bacterial soluble photoactivatable adenylyl cyclases bPAC and biPAC were N-terminally fused with a 2xLyn11, endoplasmic reticulum export signal and YFP sequence. The Lyn sequence comprises the 11 N-terminal amino acids (aa) of Lyn kinase (MGCIKSKGKDS, Lyn11), which includes myristoylation and palmitoylation sites for targeting soluble proteins to the plasma membrane, and the sequence has been used for targeting proteins to the plasma membrane in mammalian cells and *Xenopus* oocytes (Inoue *et al.*, 2005; Tsvetanova *et al.*, 2014; Yang *et al.*, 2021). The photoactivatable adenylyl cyclases were

expressed with an N-terminal YFP to reduce cAMP production under dark conditions. To further decrease the dark activity, bPAC was modified by the mutation F198Y. Recently, the construct 2xLyn-Venus-bPAC(F198Y), also termed as PACmn (plasma membrane-anchored PAC), was characterized in *Xenopus* oocytes and hippocampal neurons, whereas no detectable dark activity was observed, and whose activity increased >4000-fold in light. However, the measured light turnover was about 50-fold lower compared to Venus-bPAC(wt) (Yang *et al.*, 2021). biPAC is a new photoactivatable adenylyl cyclase and was used because it showed lower dark activity compared to bPAC (S. Gao, University of Würzburg, personal communication). For simplicity, the 2xLyn11- endoplasmic reticulum export signal sequence is abbreviated as lipid-anchor (la). The plasmids la-YFP-bPAC, la-YFP-bPAC[F198Y] and la-YFP-biPAC were a gift from G. Nagel (University of Würzburg). To characterize the membrane-anchored photoactivatable adenylyl cyclases after membrane-targeting and optogenetic cAMP production in *C. elegans*, the coding sequences were subcloned into a vector containing the *myo-3* promoter to achieve their expression in body wall muscle cells. For investigation of the subcellular localization, 30 ng/µl la-YFP-bPAC were injected into the genetic background *lite-1(ce314)* and analysed via fluorescence microscopy. Here, la-YFP-bPAC depicted a clustered appearance along the muscle membrane (Figure 93 A). To assess the membrane-anchored photoactivatable adenylyl cyclases after optogenetic cAMP production, 15 ng/µl plasmid DNA of la-YFP-bPAC[F198Y] or la-YFP-biPAC were injected into the strain ZX2393 (*pmyo-3::SthK::SL2::GFP; pmyo-2::mCherry*) and characterized via swimming behaviour analysis. Here, co-expression of SthK and either la-YFP-biPAC or la-YFP-bPAC[F198Y] showed reduced basal swimming frequencies compared to animals, only expressing SthK (Figure 93 B). For both two component optogenetic systems, no obvious light evoked reduction of the swimming rates was detected. To further evaluate la-YFP-bPAC[F198Y] after optogenetic cAMP generation, 15 ng/µl of la-YFP-bPAC[F198Y] were injected into the strain ZX1741 (*pmyo-3::tax-2::GFP, pmyo-3::tax-4::GFP, pmyo-2::mCherry*) and body length measurements were performed. In this context, no light triggered reduction of the body length of animals, co-expressing TAX-2/-4 and la-YFP-bPAC[F198Y] was detected (Figure 93 D, E). In conclusion, the membrane-anchored photoactivatable adenylyl cyclases did not show detectable light-dependent cAMP production, which

could be due to membrane targeting failure or a low amount of light-induced cAMP production.

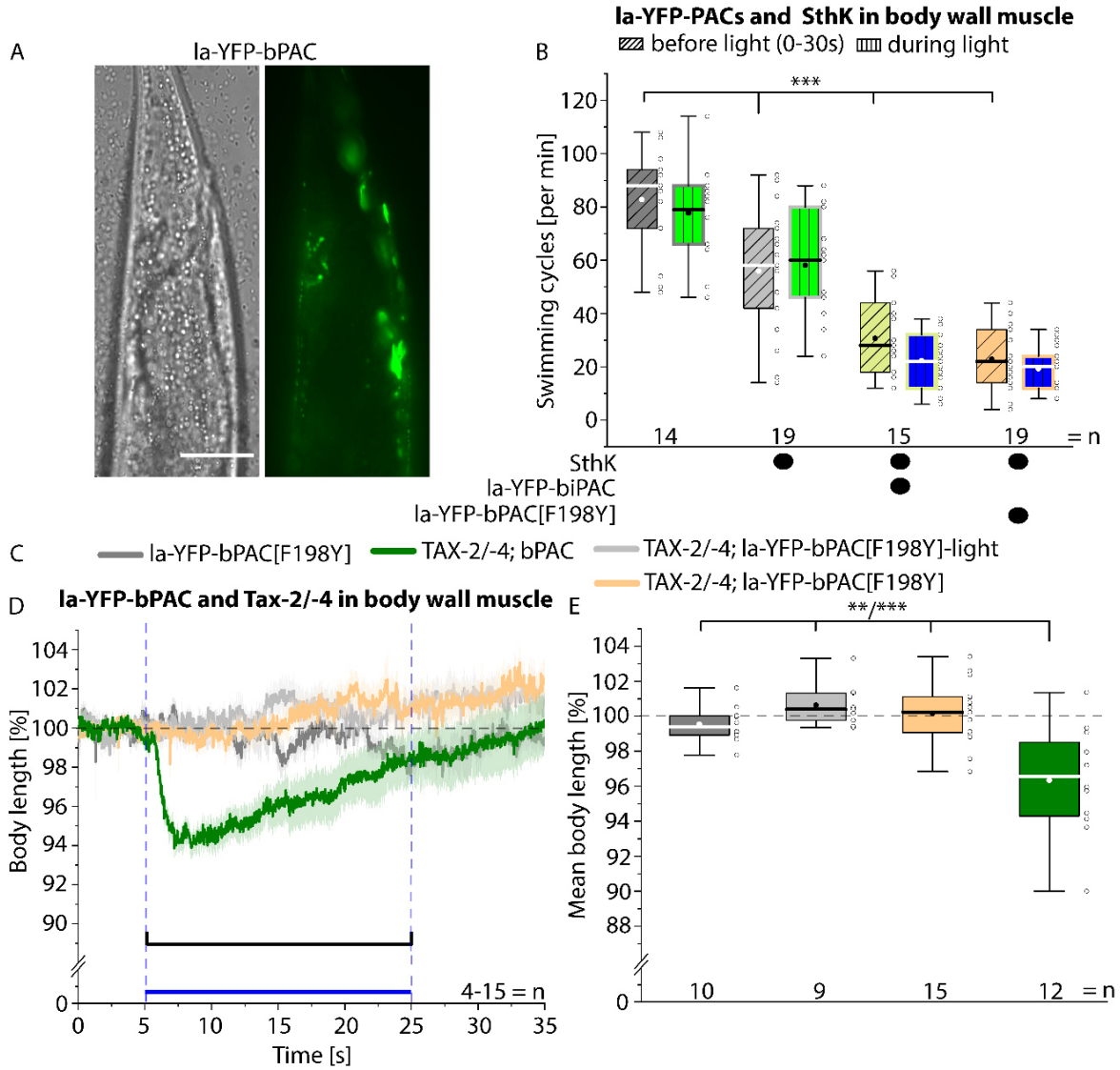

Figure 93: Characterization of membrane-anchored bacterial photoactivatable adenylyl cyclases in C. elegans muscle cells. *A) Fluorescence (right) and DIC bright field image (left) of an animal, expressing la-YFP-bPAC in body wall muscle cells using the myo-3 promoter. B) Swimming* behaviour *analysis of animals, expressing only SthK, or co-expressing SthK and either la-YFP-biPAC or la-YFP-bPAC[F198Y] in body wall muscle cells, and the genetic background lite-1(ce314), before and during 30 s light application (0.5 mW/mm², 470; 1 mW/mm², 535 nm). C)* Colour *code for the* analysed *strains in D and E. D) Body length measurements ±SEM of animals, only expressing la-YFP-bPAC[F198Y], or co-expressing TAX-2/-4 and either la-YFP-bPAC[F198Y] or bPAC. Blue bar indicates the period of illumination (0.9 mW/mm²; 470 nm). E) Quantification of the mean normalized body lengths for the indicated time period during light (5 – 25 s). In B and E, the interquartile range (IQR), median (–), mean values (●), individual measurements (o), and whiskers (1.5 * IQR) are depicted. n = number of animals. Statistically significant differences were determined using B) two-way ANOVA with Bonferroni correction or E) one-way ANOVA with Bonferroni correction (**p ≤ 0.01 and ***p ≤ 0.001).*

6.5. Characterization of SthK and mPAC in cholinergic neurons

Since animals co-expressing SthK and bPAC in cholinergic neurons showed a strong reduction of the basal swimming frequency due to a pre-activation of SthK by bPAC`s dark activity, an attempt to improve the system was to co-express SthK with the photoactivatable adenylyl cyclase from the cyanobacterium *Microcoleus chthonoplastes* (mPAC). To this end, two strains were generated that differ in the expression level of mPAC (3 and 30 ng/µl). To assess the two component optogenetic system after a possible pre-activation of SthK and its potential to hyperpolarize *C. elegans* cholinergic neurons, swimming behaviour analysis were executed. Here, no reduction of the basal swimming rate was measured for the strain expressing a low level of mPAC. However, increasing the expression level of mPAC caused a decrease of the basal swimming rate of the animals. No light evoked reduction of the swimming frequency was observed for animals, expressing SthK and mPAC, independently of the expression level of mPAC (Figure 94). In conclusion, the two component optogenetic system consisting of SthK and mPAC depicted no detectable light dependent hyperpolarization of *C. elegans* cholinergic neurons.

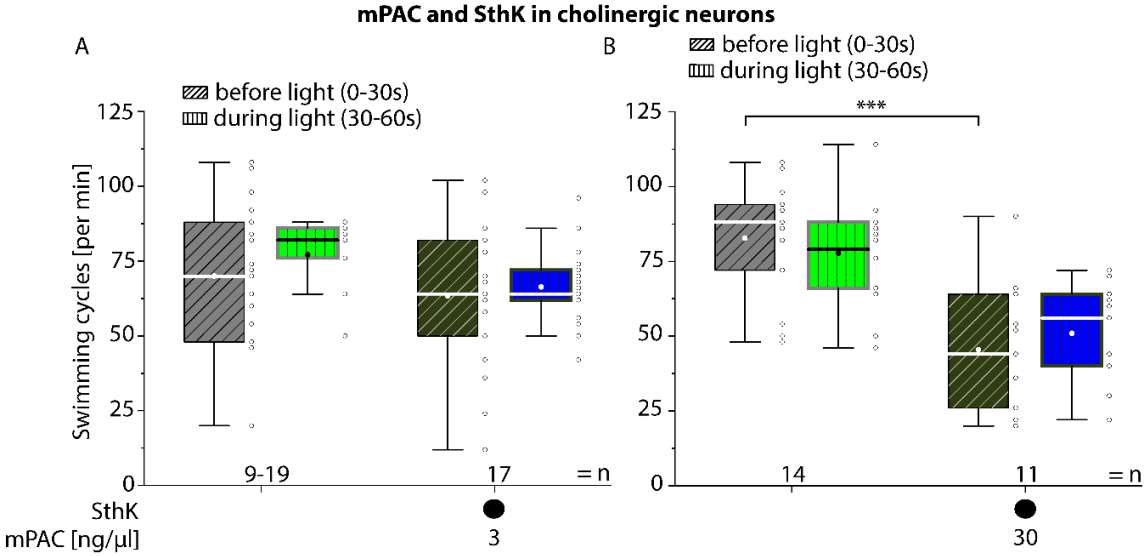

Figure 94: Application of mPAC and SthK in cholinergic neurons. *A, B) Swimming* behaviour *of animals, co-expressing SthK and mPAC in cholinergic neurons, and the genetic background lite-1(ce314), before and during 30 s light application (0.5 mW/mm², 470; 1 mW/mm², 535 nm). Transgenic strains were generated using different amounts of mPAC plasmid DNA (indicated by ng/µl). The interquartile range (IQR), median (–), mean values (●), individual measurements (o), and whiskers (1.5 * IQR) are depicted. n = number of animals. Statistically significant differences were determined using two-way ANOVA with Bonferroni correction (***p ≤ 0.001).*

6.6. Investigation of the chimeric protein SthK-YFP-bPAC in body wall muscle cells

Another attempt to improve the SthK; bPAC system was to express both proteins as chimeric protein (SthK-YFP-bPAC). In this context, the dark activity of bPAC should be reduced due to steric hindrance. Further, SthK was modified by the mutation T378V and N-terminally shortened by 12 aa to 428 aa to reduce the affinity of the channel for cAMP (Georg Nagel, University of Würzburg, personal communication). All modifications aimed on generating an optogenetic tool for the manipulation of K^+-currents that is not activated under dark conditions. The modifications and the generation of the chimeric construct were performed by Shiquiang Gao and Georg Nagel (University of Würzburg), who provided the plasmid. To investigate the expression and subcellular localization of the chimeric protein in *C. elegans* muscle cells, N. Ho injected 100 ng/µl plasmid DNA into the genetic background *lite-1(ce314)* and analysed the expression via fluorescence microscopy. Here, the chimeric protein depicted a clustered appearance along the muscle membrane (Figure 95 B). To characterize the ability of the chimeric protein to hyperpolarize the muscle cells, I have injected 1 ng/µl plasmid DNA into *lite-1(ce314)* animals and assessed by body length measurements its functionality. Illumination of animals, expressing SthK-YFP-bPAC depicted an increase of the body length of about 1 % during light application, that was not significantly different compared to the genetic background *lite-1(ce314)* (Figure 95 C-D). To further investigate the chimeric protein, I have executed swimming behaviour analysis. Animals, expressing SthK-YFP-bPAC showed comparable basal swimming rates as the genetic background *lite-1(ce314)*. However, no light evoked reduction of the swimming frequency was measured (Figure 95 G). For that reason, N. Ho performed body length measurements and swimming behaviour analysis of the strain with an increased expression level of the chimeric protein. The body length measurement was further modified by extending the duration of light application to increase the amount of optogenetic cAMP production. Illumination of animals, expressing SthK-YFP-bPAC showed a body length increase of about 1 % during and after light (Figure 95 E-F). However, no light dependent reduction of the swimming frequency was detected for animals, expressing the chimeric protein (Figure 95 H). In sum, the system was able to slightly hyperpolarize *C. elegans* muscle cells, at high expression levels.

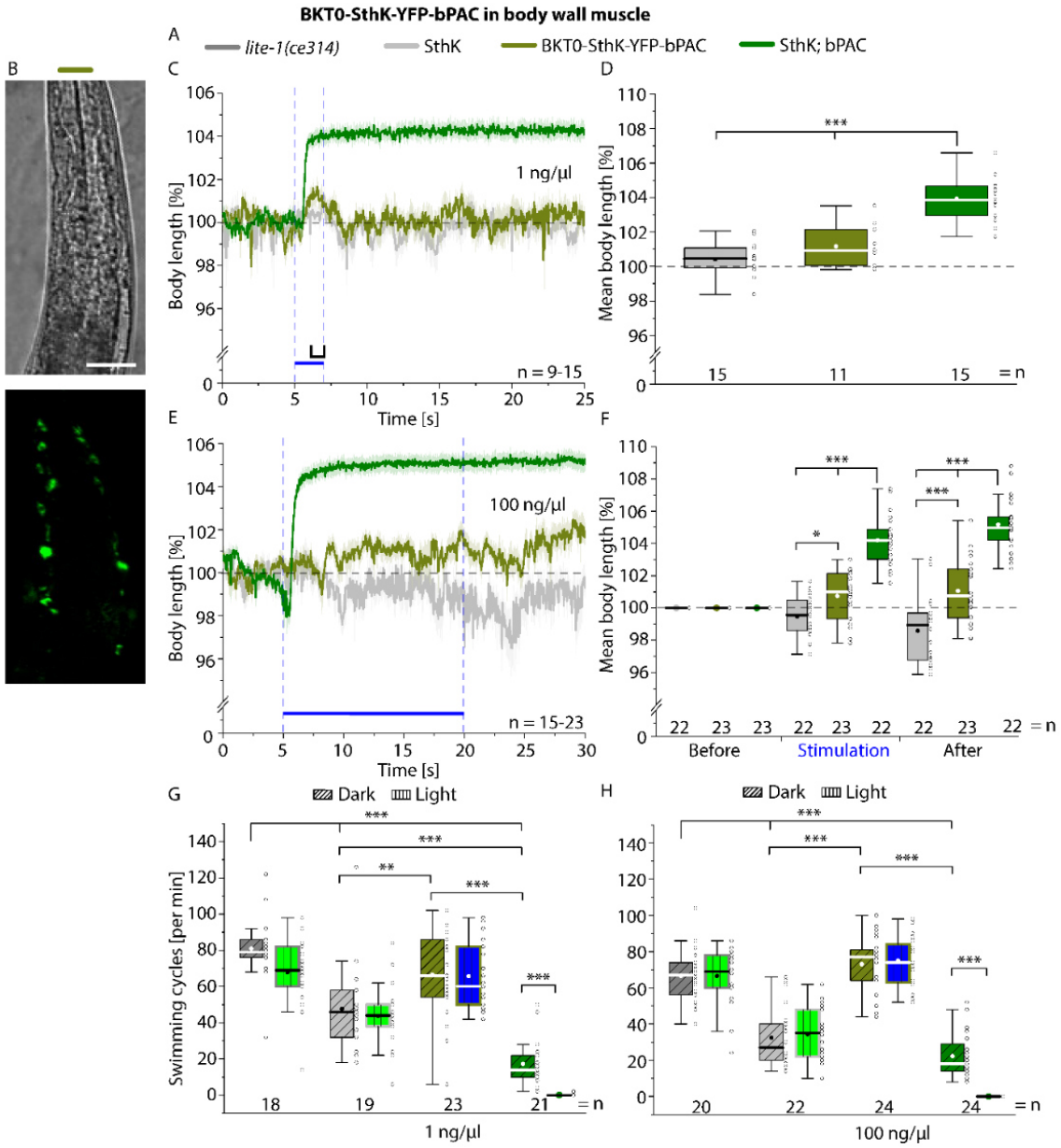

Figure 95: Application of SthK-YFP-bPAC in C. elegans muscle cells. *A)* Colour *code for the* analysed *strains in B-H). B) Fluorescence (bottom) and DIC bright field image (top) of an animal, expressing SthK-YFP-bPAC in body wall muscle cells using the myo-3 promoter. Scale bar = 20 µm C, E) Body length measurements ±SEM of animals, only expressing SthK, or co-expressing SthK and SthK-YFP-bPAC in body wall muscle cells. Transgenic SthK-YFP-bPAC strains were generated using C) 1 ng/µl and E) 100 ng/µl. Blue bar indicates the period of illumination (0.9 mW/mm^2; 470 nm). D, F) Quantification of the mean normalized body lengths for the indicated time periods D) during light (6 – 7 s), and F) before (0 – 5 s), during (5 – 20 s) and after light (20 – 30 s). G, H) Swimming* behaviour *analysis of animals, only expressing SthK or SthK-YFP-bPAC, co-expressing SthK and bPAC, and the genetic background lite-1(ce314), before and during 30 s light application (0.5 mW/mm^2, 470; 1 mW/mm^2, 535 nm). In D, F, G, and H, the interquartile range (IQR), median (–), mean values (●), individual measurements (o), and whiskers (1.5 * IQR) are depicted. n = number of animals. Statistically significant differences were determined using D, F) one-way ANOVA with Bonferroni correction or G, H) two-way ANOVA with Bonferroni correction (*p ≤ 0.05, **p ≤ 0.01 and ***p ≤ 0.001). Fluorescence and DIC brightfield images, body length measurements in E and the quantification in F, and swimming* behaviour *analysis in H were performed and analysed by Napyin Ho.*

6.7. Characterization of PaaC+7 and SthK in body wall muscle cells

To implement a two component optogenetic system for the manipulation of K^+-currents, another approach was to combine the synthetic phytochrome-linked cyclase PaaC+7 with SthK. We reasoned that application of blue light sensing proteins is accompanied by several problems, i.e. a low penetration depth and high energy of blue light that could damage tissue upon extended light exposure. Thus, these aspects are representing challenges for their application in higher animals, thus a red-light activated system may be more tolerable and applicable. To achieve expression of PaaC+7 in body wall muscle cells, N. Ho subcloned the coding sequence into a vector containing the *myo-3* promoter and analysed the expression of PaaC+7 via fluorescence microscopy. Here, PaaC+7 and the mCherry fluorescence reporter are expressed from bicistronic mRNAs, and fluorescence was observed at the outer wall of the animal (Figure 96 B). Next, N. Ho. generated strains co-expressing SthK and PaaC+7 in body wall muscle cells via microinjection, and he analysed the functionality of the system by performing swimming behaviour analysis and body length measurements. In regard of swimming behaviour analysis, animals expressing PaaC+7 showed comparable basal swimming rates as the genetic background *lite-1(ce314)*, which was not influenced by additional biliverdin supplementation. However, animals co-expressing SthK and PaaC+7 depicted reduced basal swimming frequencies compared to animals expressing PaaC+7 only and the genetic background. Illumination of animals, co-expressing SthK and Paac+7 exhibited a slightly reduced swimming frequency, though no significant difference was determined (Figure 96 C). To further investigate the ability of the system to hyperpolarize *C. elegans* muscle cells, N. Ho performed body length measurements. However, no light evoked increase of the body length was observed for animals, co-expressing SthK and PaaC+7 (Figure 96 F, G). In conclusion, the two component optogenetic system SthK and PaaC+7 depicted no obvious light dependent muscle hyperpolarization.

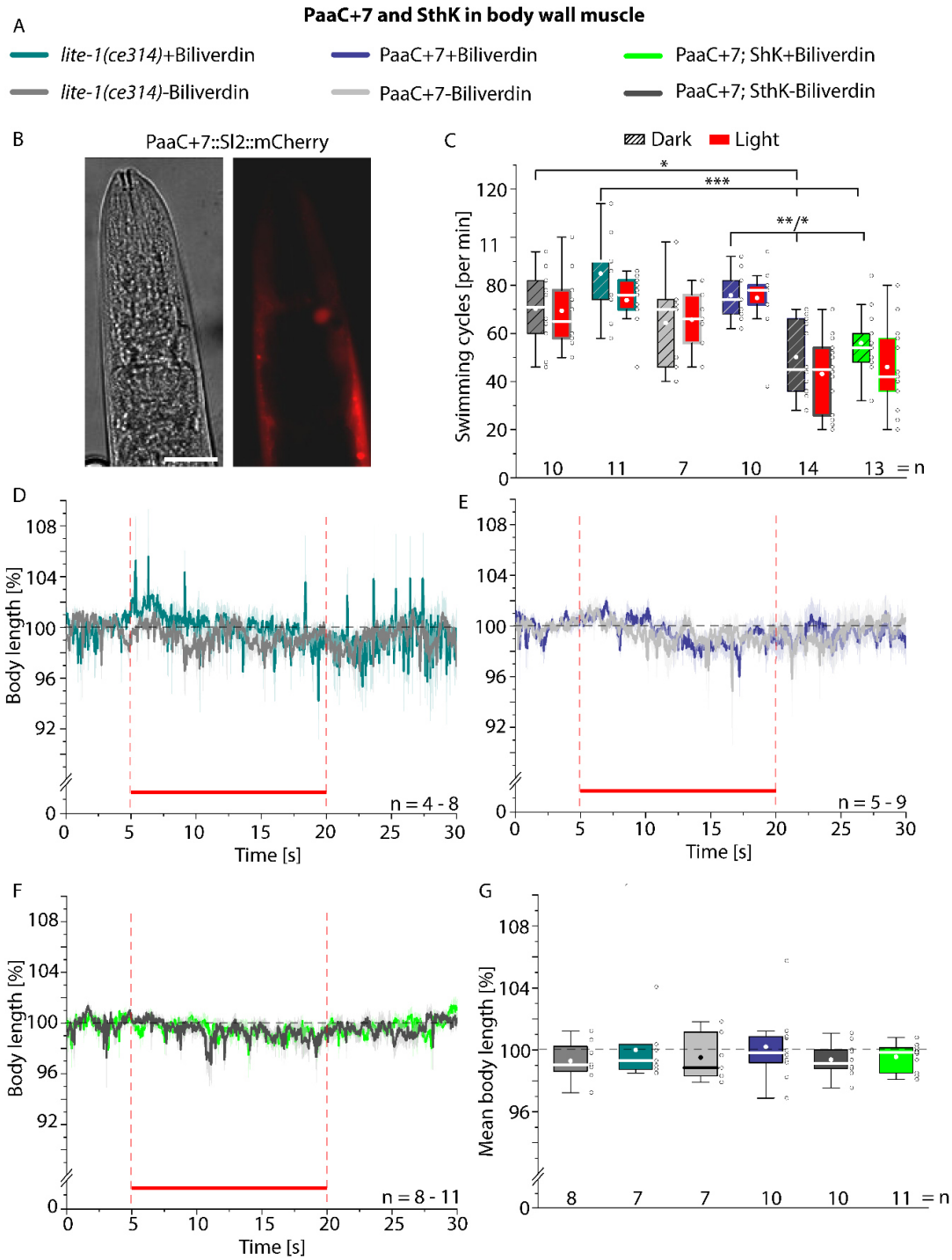

Figure 96: Application of the synthetic phytochrome-linked cyclase PaaC+7 and SthK in C. elegans muscle cells. *A)* Colour *code for the* analysed *strains in B-G). B) Fluorescence (right) and DIC bright field image (left) of an animal, expressing PaaC+7::SI2::mCherry in body wall muscle cells using the myo-3 promoter. Scale bar = 20 µm. C) Swimming* behaviour *analysis of animals, expressing only SthK or PaaC+7, or co-expressing SthK and PaaC+7 in body wall muscle cells, and the genetic background lite-1(ce314) before and during 30 s light application (0.16 – 0.3 mW/mm², 675 nm). Animals were raised with (+) or without (-) biliverdin. D-F) Body length measurements ±SEM of D) the genetic background lite-1(ce314), and animals E) only expressing PaaC+7 or F) co-expressing SthK and PaaC+7. Red bars indicate the period of illumination (0.16 – 0.3 mW/mm²; 675 nm). Animals were supplemented with (+) or without (-) 1 mM biliverdin. G) Quantification of the mean normalized body lengths during light application (5 – 20 s). In C and G, the interquartile range (IQR), median (–), mean values (●), individual measurements (o), and whiskers (1.5 * IQR) are depicted. n = number of animals. Statistically significant differences were determined using two-way ANOVA with Bonferroni correction (*p ≤ 0.05, **p ≤ 0.01 and ***p ≤ 0.001). Fluorescence and DIC*

brightfield images, body length measurements and swimming behaviour analysis were performed and analysed by Napyin Ho.

6.8. Synthetic retinal analogue support BeCyclOp function

To change the functional and spectral properties of BeCyclOp and to generate an optogenetic tool that could be activated in the red spectral range, the BeCyclOp apoprotein was combined with synthetic retinal analogues as chromophore (Figure 97). In this context, light activation of rhodopsins is based on the absorption spectrum of their attached chromophore, which depends on the molecular environment inside the protein. For these experiments, synthetic retinal analogues used in (AzimiHashemi *et al.*, 2014) were applied.

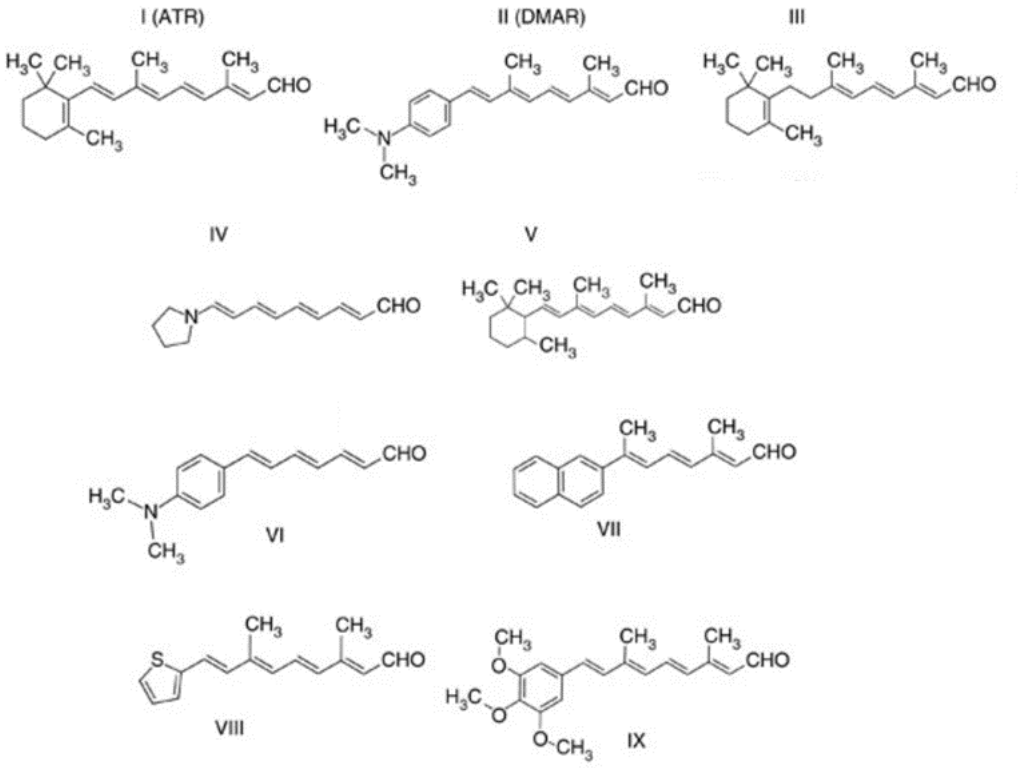

Figure 97: Chemical structures of the synthetic retinal analogues applied for spectral tuning of BeCyclOp. *Image adapted from (AzimiHashemi et al., 2014).*

To investigate the retinal analogues after their ability to support BeCyclOp function, body length measurements with green light (0.9 mW/mm^2; 535 nm) and the established BeCyclOp; TAX-2/-4 expressing strain (ZX1742; Gao et al., 2015) were conducted. Here, light evoked body length reductions were observed for animals,

raised with the analogues II, V, VII, VIII and IX. In contrast to this, no light dependent body length decrease was detected for the analogues IV and VI (Figure 98). In sum, the synthetic retinal analogues II, V, VII, VIII and IX support BeCyclOp function.

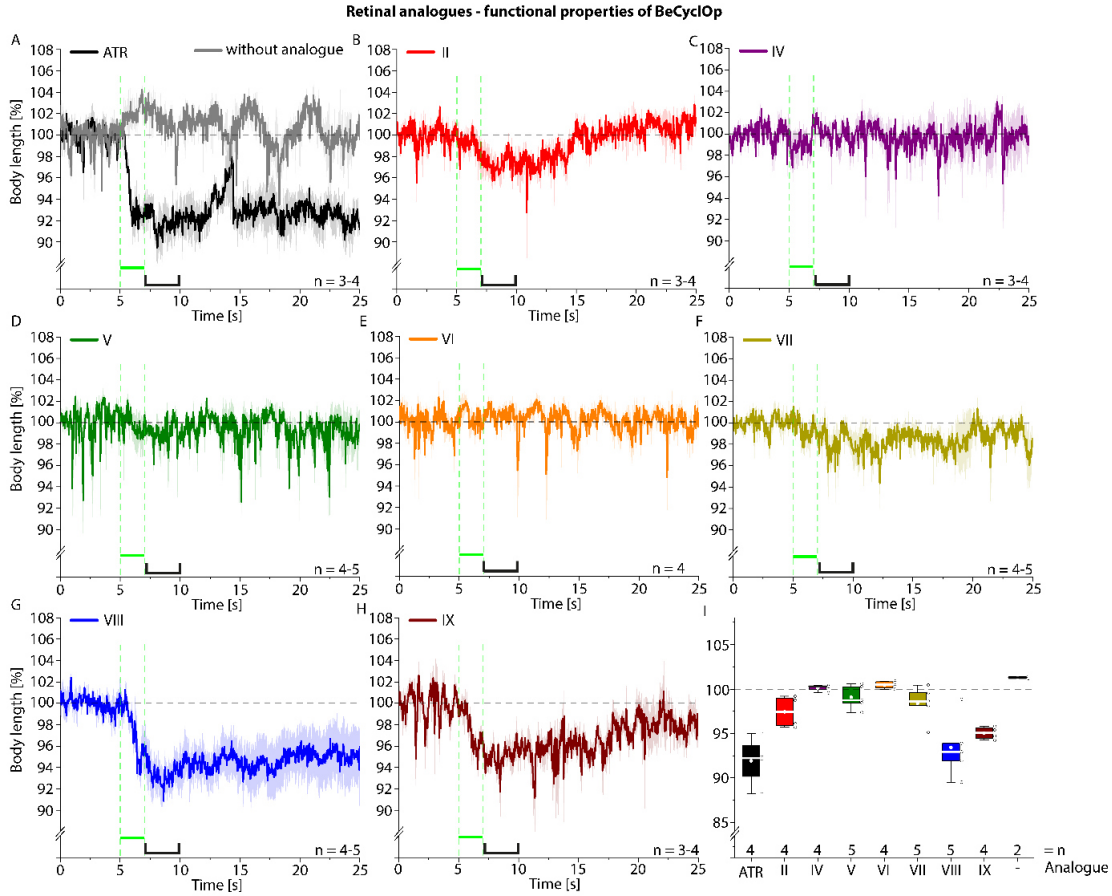

Figure 98: Investigation of BeCyclOp functionality using synthetic retinal analogues. *Body length measurements ±SEM of animals, co-expressing BeCyclOp and TAX-2/-4 in body wall muscle cells, supplemented with A) ATR, B) analogue II, C) analogue IV, D) analogue V, E) analogue VII, F) analogue VII, G) analogue VIII, and H) analogue IX. Animals were raised on 200 µM analogue, respectively. Green bar indicates the period of illumination (0.9 mW/mm^2; 535 nm). I) Quantification of the mean normalized body lengths for the indicated time period (7 – 10 s). The interquartile range (IQR), median (–), mean values (●), individual measurements (o), and whiskers (1.5 * IQR) are depicted. n = number of animals. N (independent measurements per Graph) = 1.*

6.9. Spectral tuning of BeCyclOp using synthetic retinal analogue

Aiming on the spectral tuning of BeCyclOp, body length measurements of BeCyclOp TAX-2/-4 expressing animals at different wavelengths (434, 470, 535, 580 and 615 nm) were performed. For this experiment, only the synthetic retinal analogues II, V, VII, VIII and IX were utilized, that support BeCyclOp functionality. As controls, body length measurements of animals, cultivated with and without ATR were executed. For ATR, illumination of animals co-expressing BeCyclOp and TAX-2/-4 evoked similar

body length reductions of about 8 – 9 %, independently of the applied wavelength (Figure 99 B, C). However, the spectrum did not resemble the known absorption spectrum of BeCyclOp, which could be due to too high applied light intensity (Gao *et al.*, 2015; Scheib *et al.*, 2015). For analogue II, the maximal reduction of the body length was measured at 535 nm (~3 %), whereas comparable reductions of about 2 % were detected at 470, 580 and 615 nm. No light dependent effect was observed at 434 nm (Figure 99 D, E). In case of analogue V, strong light triggered body reductions were determined at 434 nm (~5 %) and 470 nm (~10 %). No obvious body length changes were detected for the wavelengths 535, 580 and 615 nm (Figure 99 F, G). For analogue VII, maximal light induced body length decrease was measured at 470 nm (~4 %), and slight reductions at 434 and 535 nm (1 – 2 %), and no obvious effect at 580 and 615 nm (Figure 99 H, I). For analogue VIII, illumination of the animals reduced the body length maximal at 434 nm (~8 %), which decayed to about 4 % with increasing wavelength (Figure 99 J, K). In case of analogue IX, minor body length changes were observed at the wavelengths 434 and 615 nm (~1 %), whereas the strongest body length reduction was measured at 470 nm (~7 %) (Figure 99 L, M).

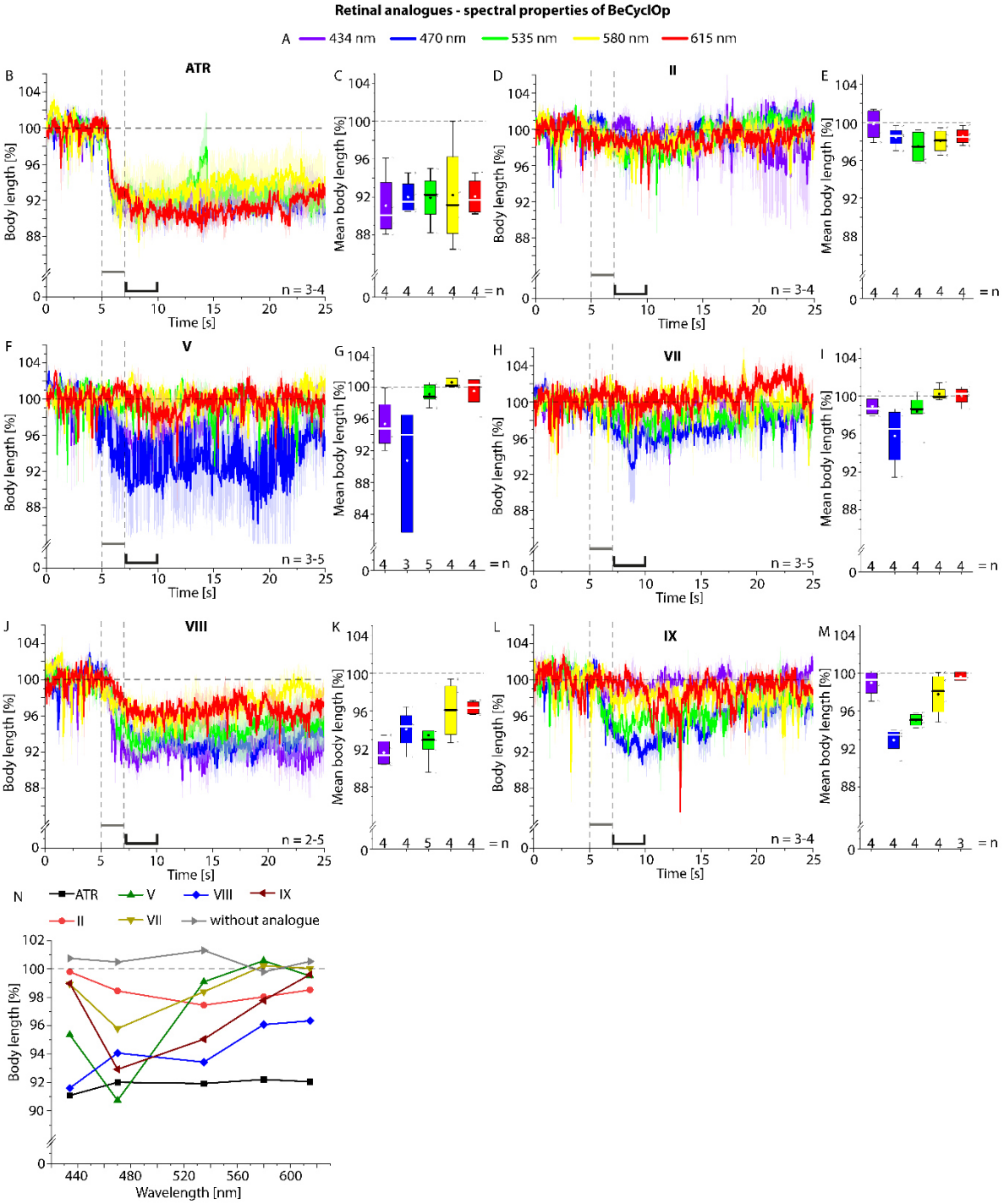

Figure 99: Spectral tuning of BeCyclOp using synthetic retinal analogues. *A)* Colour *code for the applied wavelengths (434, 470, 535, 580 and 615 nm) in B – M. Body length measurements ±SEM of animals, co-expressing BeCyclOp and TAX-2/-4 in body wall muscle cells, supplemented with B) ATR, D) analogue II, F) analogue V, H) analogue VII, J) analogue VIII, and L) analogue IX. Animals were raised on 200 µM analogue, respectively. Gray bars indicate the period of illumination (0.9 mW/mm^2; 434, 470, 535, 580 and 615 nm). C, E, G, I, K, M) Quantification of the mean normalized body lengths for the indicated time period (7 – 10 s). The interquartile range (IQR), median (–), mean values (●), individual measurements (o), and whiskers (1.5 * IQR) are depicted. n = number of animals. N) Action spectra of photostimulated body length changes in animals, co-expressing BeCyclOp and TAX-2/-4, supplemented with the retinal analogue II, V, VII, VIII, IX and with ATR, and control animals cultivated without chromophore. Shown are the mean normalized body lengths for the time period (7 – 10 s). N (independent measurements per Graph) = 1.*

6.10. Expression and subcellular localization of BeCyclOp fragments in *C. elegans* muscle cells

To investigate the subcellular targeting of the individual BeCyclOp domains in *C. elegans* muscle cells, the BeCyclOp fragments TM1-7, TM0-7, TM0-7-coiled-coil, TM0-7-coiled-coil-guanylyl cyclase, N-terminus-TM0-7-coiled-coil, N-terminus-TM0-7, coiled-coil-guanylyl cyclase, guanylyl cyclase, N-terminus-TM0 and TM6-7-coiled-coil-guanylyl cyclase were subcloned into a vector containing the *myo-3* promoter (Figure 100). The fragments were C-terminally fused to the mCherry fluorescence reporter, and the strains were analysed using fluorescence microscopy. With exception of the guanylyl cyclase domain, all fragments depicted a clustered appearance along the muscle membrane, which differ in their extent of clustering (Figure 101).

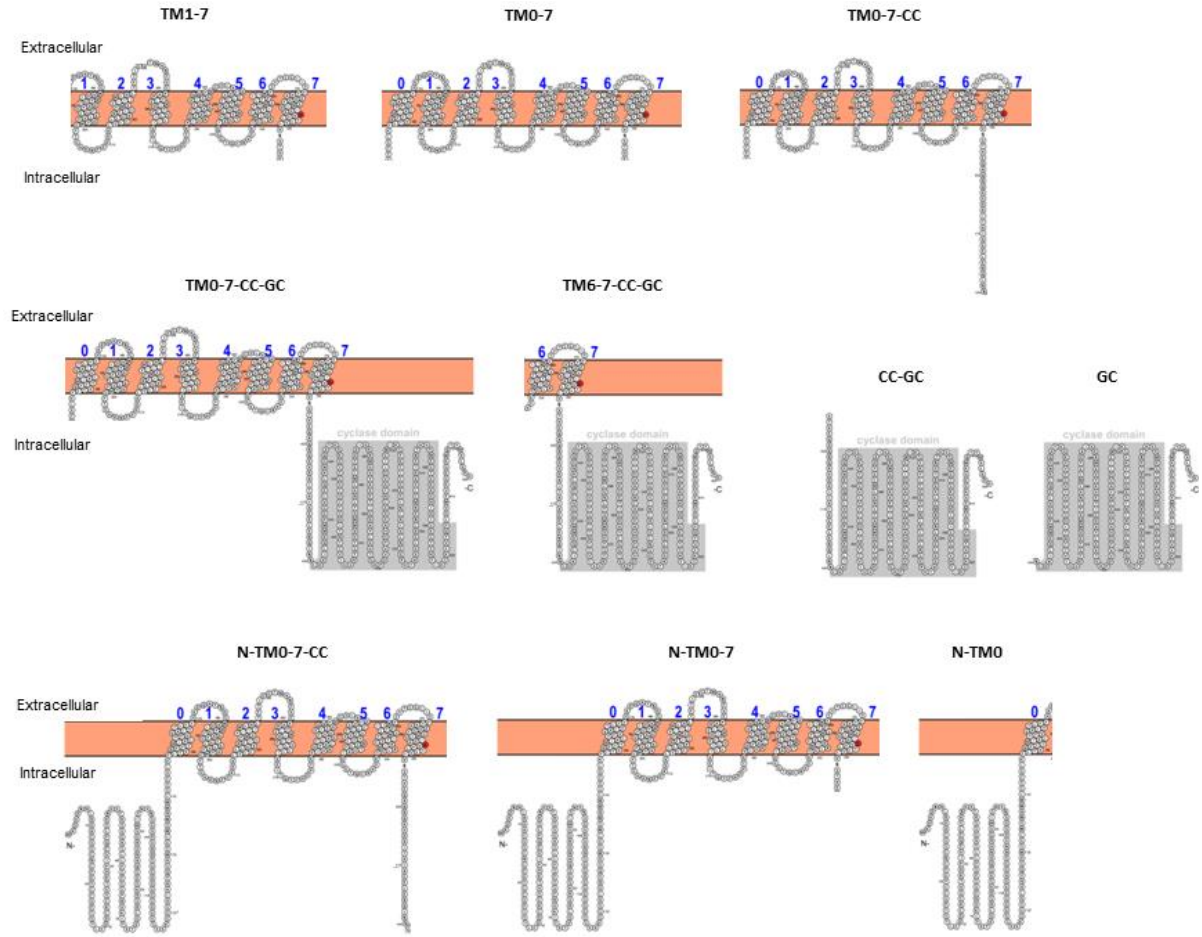

Figure 100: Schematic overview of BeCyclOp fragments designed for this thesis. *The following BeCyclOp fragments were created: TM1-7 (aa171-399), TM0-7 (aa139-399), TM0-7-CC (aa139-442), TM0-7-CC-GC (aa139-626), N-TM0-7-CC (aa1-442), N-TM0-7 (aa1-399), CC-GC (aa397-626), GC (aa442-626), N-TM0 (aa1-178) and TM6-7-CC-GC (aa230-626). Abbreviations: CC, Coiled-coil domain; GC, Guanylyl cyclase; N, N-Terminus; TM, transmembrane helix. Image adapted and modified from (Gao et al., 2015).*

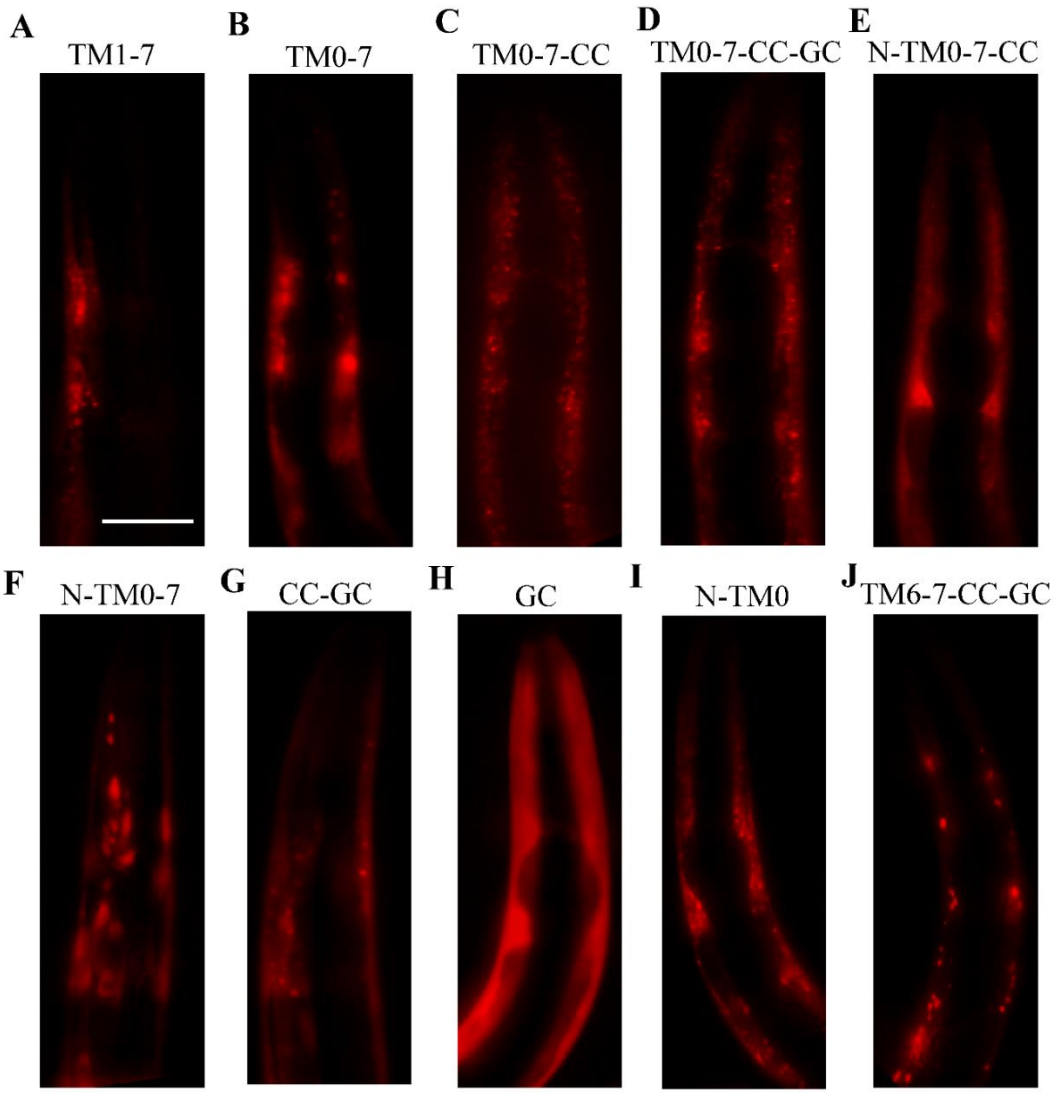

Figure 101: Expression and subcellular localization of BeCyclOp fragments in C. elegans body wall muscle cells. *Fluorescence images of animals, expressing the BeCyclOp fragments A) TM1-7 (aa171-399), B) TM0-7 (aa139-399), C) TM0-7-CC (aa139-442), D) TM0-7-CC-GC (aa139-626), E) N-TM0-7-CC (aa1-442), F) N-TM0-7 (aa1-399), G) CC-GC (aa397-626), H) GC (aa442-626), I) N-TM0 (aa1-178) and TM6-7-CC-GC (aa230-626) in body wall muscle cells. BeCyclOp fragments were fused C-terminally to the mCherry fluorescence reporter. Scale bar = 50 µm. Abbreviations: aa, amino acid; TM, transmembrane helix; CC, Coiled-Coil domain; N, N-terminus; GC, guanylyl cyclase.*

To examine the functionality of the individual BeCyclOp domains in body wall muscle cells, the fragments were subcloned into a vector containing the myo-3 promoter and the SL2 trans-splicing sequence to express the BeCyclOp fragments and the fluorescent reporter as separate proteins and thus to prevent an impact on the functionality of the domains. Strains expressing individual BeCyclOp fragments, co-expressing BeCyclOp fragments, or co-expressing BeCyclOp fragments and the TAX-2/-4 channel in body wall muscle cells are summarized in table 10.

6.11. Investigation of a functional impact of BeCyclOp N-termini on guanylyl cyclase activity

Recently, Gao et al., 2015 showed that a truncated version of BeCyclOp, lacking the first 90 amino acids, exhibited a higher dark activity and a lower light-evoked cGMP generation. Thus, it was expected that the BeCyclOp N-terminus participates in tight regulation of guanylyl cyclase activity. To shed light on a possible impact of the BeCyclOp N-terminus on guanylyl cyclase function, and to characterize the guanylyl cyclase domain with respect to its basal activity, the BeCyclOp fragments aa1-146 and aa397-626 were subcloned into a vector containing the *myo-3* promoter. Subsequently, strains were generated that only express the guanylyl cyclase domain, or co-express the guanylyl cyclase and the N-terminal domain, or co-express the TAX-2/-4 CNGC and either the guanylyl cyclase domain or the guanylyl cyclase and N-terminal domain. To analyse the guanylyl cyclase activity under basal conditions and a possible regulation of its activity due to an interaction with the N-terminus, swimming behaviour analysis were performed. Here, animals only expressing the guanylyl cyclase domain exhibited a decreased swimming rate compared to the genetic background *lite-1(ce314)*, that is comparable to the swimming rate of animals, co-expressing the guanylyl cyclase domain and the N-terminus, and animals that co-express TAX-2/-4 and the guanylyl cyclase domain. Animals, co-expressing TAX-2/-4, the guanylyl cyclase and N-terminal domains, showed a tendency for a further reduced swimming rate (Figure 102).

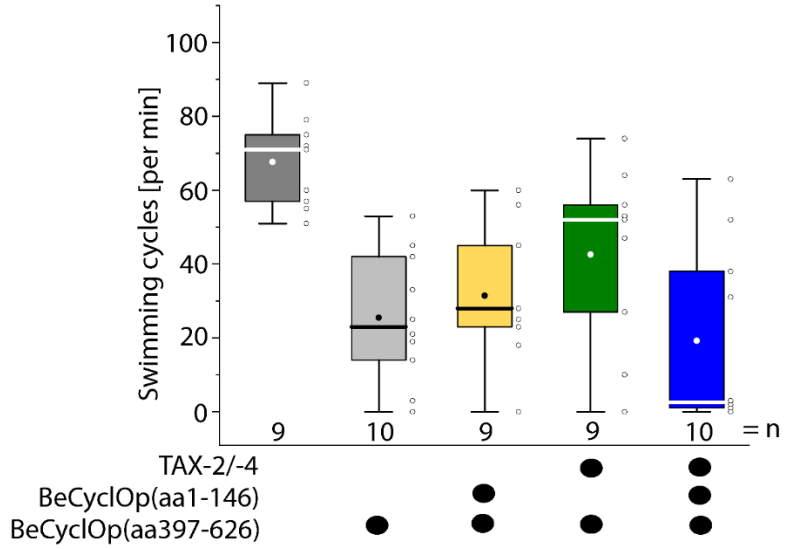

Figure 102: Characterization of a functional impact of BeCyclOp N-termini on guanylyl cyclase activity. *Basal swimming frequencies of animals, only expressing TAX-2/-4 or BeCyclOp(aa397-626), or co-expressing BeCyclOp(aa1-146) and BeCyclOp(aa397-626), or TAX-2/-4 and BeCyclOp(aa397-626), or TAX-2/-4, BeCyclOp(aa1-146) and BeCyclOp(aa397-626) in body wall muscle cells. The interquartile range (IQR), median (–), mean values (●), individual measurements (o), and whiskers (1.5 * IQR) are depicted. n = number of animals. N (independent measurements per Graph) = 1. Abbreviations: aa, amino acid.*

6.12. Abbreviations

6.12.1. Units and prefixes

°C	degree Celsius	**M**	molar
f	femto	**min**	minute
g	gram/earth`s gravitational force	**n**	nano
h	hour	**rpm**	Revolutions per minute
J	Joule	**s**	second
L	liter	**S**	Siemens
µ	micro	**U**	Unit
m	milli/meter	**V**	Volt

6.12.2. Acronyms

ACR	anion channel rhodopsin	**iChloC**	improved ChloC
AA	amino acid	**IQR**	interquartile range

APS	ammonium persulfate	**Kr2**	*Krokinobacter eikastus* rhodopsin 2
Arch	archaerhodopsin-3	**la**	lipid-anchor
ArchT	archaerhodopsin from the Halorubrum strain TP009	**LB**	Lysogeny broth
ATP	adenosine triphosphate	**LDAO**	N,N-Dimethyldodecylamine N-oxide
ATR	all-trans retinal	**LOV**	light-oxygen-voltage
BeCyclOp	*Blastocladiella emersonii* guanylyl cyclase rhodopsin	**mPAC**	*Microcoleus chthonoplastes* photoactivatable adenylyl cyclase
BLUF	blue light-sensors that use flavine adenine dinucleotide	**NEB**	New England Biolabs
BR	bacteriorhodopsin	**NGM**	Nematode growth medium
BSA	Bovine serum albumin	**NpHR**	*Natronomonas pharaonis* halorhodopsin
CaCyclOp	*Catenaria anguillulae* guanylyl cyclase opsin	**NTP**	nucleoside triphosphate
C. elegans	*Caenorhabditis elegans*	**OG**	Octylglucoside
cAMP	3`,5`-cyclic adenosine monophosphate	**OTG**	Octylthioglucoside
cGMP	3`,5`-cyclic guanosine monophosphate	**PA-BoNT**	photoactivatable botulinum neurotoxin
cNMP	cyclic nucleoside-3`,5`-monophosphate	**PACmn**	plasma membrane-anchored photoactivatable adenylyl cyclase
CAPS	calcium-activated protein for secretion	**PAP**	Peroxidase-Anti-Peroxidase
CatCh	ChR2-L132C	**PAS**	Per-Arnt-Sim

CBP	calmodulin binding peptide	**PBC**	phosphate-binding cassette
CFP	cyan fluorescent protein	**PCR**	polymerase chain reaction
CGC	Caenorhabditis Genetics Center	**PDE**	phosphodiesterase
ChETA	ChR2-E123T	**PEG**	Polyethylen glycol
ChETA$_{TC}$	ChR2-E123T/T159C	**PKA**	protein kinase A
ChR	channelrhodopsin	**PKC**	protein kinase C
ChR2	channelrhodopsin-2	**PKG**	protein kinase G
Chronos	channelrhodopsin from *Stigeoclonium helveticum*	**PMSF**	Phenylmethane sulfonyl fluoride
CMC	critical micelle concentration	**POPDC**	popeye domain-containing
CNBD	cyclic nucleotide-binding domain	**PsChR**	channelrhodopsin from *Platymonias subcordiformus*
CNG	cyclic nucleotide-gated	**ProtA**	*Staphylococcus aureus* protein A
CNGC	cyclic nucleotide-gated channel	**PVDF**	polyvinylidene fluoride
CyclOp	guanylyl cyclase rhodopsins	**RFP**	red fluorescent protein
DChR1	channelrhodopsin from Dunaliella salina	**RhGC**	rhodopsin guanylyl cyclases
DDM	Dodecylmaltoside	**RhoPDE**	rhodopsin phosphodiesterases
DIC	Differential interference contrast	**RSB**	Retinal Schiff base
DM	Decylmaltoside	**RT**	room temperature
DMAR	Dimethylamino-retinal	**SDS**	Sodium dodecyl sulfate
DMSO	Dimethyl sulfoxide	**SDS-PAGE**	Sodium dodecyl sulfate polyacrylamide gel electrophoresis
dNTP	deoxyribonucleoside triphosphate	**SEWLB**	Single egg/worm lysis buffer

DTT	Dithiotreitol	**SFO**	step-function opsins
E. coli	*Escherichia coli*	**Soc**	Super Optimal broth with Catabolite repression
Eag	ether-à-go-go	**SthK**	*Spirochaeta thermophila* cAMP-gated K^+ channel
EDTA	Ethylene-diamine-tetra-acetic acid	**TAE**	TRIS acetate EDTA
EGTA	ethylene glycol-bis(β-aminoethyl ether)-N,N,N′,N′-tetraacetic acid	**TAME**	Nα-p-Tosyl-L-arginine methyl ester hydrochloride
EPAC	exchange protein directly activated by cAMP	**TAP**	Tandem affinity purification
FAD	flavin adenine dinucleotide	**TBS**	Tris-buffered saline
FMN	flavin mononucleotide	**TBS-T**	Tris-buffered saline with Tween-20 (TBS-T)
GABA	γ-amino butyric acid	**TCA**	Trichloroacetic acid
GEF	guanine nucleotide exchange factor	**TEMED**	Tetramethylethylenediamine
GFP	green fluorescent protein	**TEV**	Tobacco etch virus
GirK	G-protein-gated inwardly rectifying potassium channel	**TM**	transmembrane
GPCR	G-protein-coupled receptors	**TRIS**	Tris-(hydroxymethyl)-aminomethane
HCN	hyperpolarization-activated cyclic nucleotide-gated	**TsChR**	ChR from Tetraselmis striata
hERG	human ether-a-go-go-related gene	**Tween-20**	Polyethylene glycol sorbitan monolaurate

HKR	histidine kinase rhodopsins	**vAChT**	vesicular acetylcholine transporter
IBMX	3-isobutyl-1-methylxanthine		

6.13. List of figures

6.12. List of tables

6.13. Figure and table contribution

The authors' contributions are listed in table 25. Unless otherwise stated, the author's contribution consists only of the image that was adapted. In addition, contributions from colleagues are listed.

Table 24: List of figures and author.

Figure/Name	Page	Author
Figure 1: Overview of particular sensory photoreceptor classes and their associated chromophores and primary photochemical reactions	3	Shcherbakova DM, Shemetov AA, Kaberniuk AA, Verkhusha VV (2015). Natural photoreceptors as a source of fluorescent proteins, biosensors, and optogenetic tools. *Annual review of biochemistry* **84:** 519-550
Figure 2: Schematic representation of the architecture of rhodopsins	5	Ernst OP, Lodowski DT, Elstner M, Hegemann P, Brown LS, Kandori H (2014). Microbial and animal rhodopsins: structures, functions, and molecular mechanisms. *Chemical reviews* **114**(1)**:** 126-163
Figure 3: Overview of the photocycle of microbial rhodopsins	6	Ernst OP, Lodowski DT, Elstner M, Hegemann P, Brown LS, Kandori H (2014). Microbial and animal rhodopsins: structures, functions, and molecular mechanisms. *Chemical reviews* **114**(1)**:** 126-163
Figure 4: Schematic illustration of the CyclOp domain architecture and proposed model for light-induced activation of the guanylyl cyclase domain of CyclOps	8	Fischer P, Mukherjee S, Peter E, Broser M, Bartl F, Hegemann P (2021). The inner mechanics of rhodopsin guanylyl cyclase during cGMP-formation revealed by real-time FTIR spectroscopy. *eLife* **10**
Figure 5: Schematic overview of the conserved photochemically active residues of microbial rhodopsins and the Ca rhodopsin photocycle	9	Mukherjee S, Hegemann P, Broser M (2019). Enzymerhodopsins: novel photoregulated catalysts for optogenetics. *Current opinion in structural biology* **57:** 118-126 & Scheib U, Broser M, Constantin OM, Yang S, Gao S, Mukherjee S*, et al.* (2018). Rhodopsin-cyclases for photocontrol of cGMP/cAMP and 2.3 A structure of the adenylyl cyclase domain. *Nat Commun* **9**(1)**:** 2046, modified by Thilo Henß

Figure/Name	Page	Author
Figure 6: Schematic overview of the nucleotide binding pocket of class III cyclases and the structure of the CaCyclOp adenylyl cyclase domain	11	Mukherjee S, Hegemann P, Broser M (2019). Enzymerhodopsins: novel photoregulated catalysts for optogenetics. *Current opinion in structural biology* **57:** 118-126, modified by Thilo Henß
Figure 7: Overview of microbial rhodopsins acting as optogenetic actuators	12	Rost BR, Schneider-Warme F, Schmitz D, Hegemann P (2017). Optogenetic Tools for Subcellular Applications in Neuroscience. *Neuron* **96**(3)**:** 572-603, modified by Thilo Henß
Figure 8: Schematic overview of BLUF proteins and light induced signal transduction	16	Kennis JT, Mathes T (2013). Molecular eyes: proteins that transform light into biological information. *Interface focus* **3**(5)**:** 20130005 & Park SY, Tame JRH (2017). Seeing the light with BLUF proteins. *Biophysical reviews* **9**(2)**:** 169-176, modified by Thilo Henß
Figure 9: Schematic overview of CNGC domain structure	18	Rheinberger J, Gao X, Schmidpeter PAM, Nimigean CM (2018). Ligand discrimination and gating in cyclic nucleotide-gated ion channels from apo and partial agonist-bound cryo-EM structures. *eLife* **7**, modified by Thilo Henß
Figure 10: Proposed gating mechanism of CNGCs	21	Rheinberger J, Gao X, Schmidpeter PAM, Nimigean CM (2018). Ligand discrimination and gating in cyclic nucleotide-gated ion channels from apo and partial agonist-bound cryo-EM structures. *eLife* **7**, modified by Thilo Henß
Figure 11: Schematic illustration of the cAMP signalling pathways	23	Musheshe N, Schmidt M, Zaccolo M (2018). cAMP: From Long-Range Second Messenger to Nanodomain Signalling. *Trends in pharmacological sciences* **39**(2)**:** 209-222.
Figure 12: C. elegans anatomy	26	Altun ZF, Hall DH (2009a). Introduction. *WormAtlas*
Figure 13: C. elegans life cycle at 22 °C	27	Altun ZF, Hall DH (2009a). Introduction. *WormAtlas*
Figure 14: Schematic overview of C. elegans body wall muscle organization	28	Altun ZF, Hall DH (2009b). Muscle system, introduction. *WormAtlas*.
Figure 15: Illustration of the C. elegans nervous system	30	Fang-Yen C, Alkema MJ, Samuel ADT (2015). Illuminating neural circuits and behaviour in Caenorhabditis elegans with optogenetics. *Philosophical Transactions of the Royal Society B: Biological Sciences* **370**(1677)**:** 20140212.
Figure 16: Schematic overview of the C. elegans motor circuit	34	Zhen M, Samuel AD (2015). C. elegans locomotion: small circuits, complex functions. *Current opinion in neurobiology* **33:** 117-126.

Figure/Name	Page	Author
Figure 17: Schematic overview of cAMP modulation of cholinergic neurotransmission via neuropeptide signalling and synaptic vesicle loading	36	Steuer Costa W, Yu S-C, Liewald JF, Gottschalk A (2017). Fast cAMP Modulation of Neurotransmission via Neuropeptide Signals and Vesicle Loading. *Current biology : CB* **27**(4)**:** 495–507, modified by Thilo Henß
Figure 18: Optogenetic activation of cholinergic motor neurons via bPAC has profound effects on locomotion behaviour	37	Steuer Costa W, Yu S-C, Liewald JF, Gottschalk A (2017). Fast cAMP Modulation of Neurotransmission via Neuropeptide Signals and Vesicle Loading. *Current biology : CB* **27**(4)**:** 495–507, modified by Thilo Henß
Figure 19: Evaluation of novel and engineered de- and hyperpolarizers in C. elegans	39	Bergs A, Schultheis C, Fischer E, Tsunoda SP, Erbguth K, Husson SJ*, et al.* (2018). Rhodopsin optogenetic toolbox v2.0 for light-sensitive excitation and inhibition in Caenorhabditis elegans. *PloS one* **13**(2)**:** e0191802.
Figure 20: Photoactivatable guanylyl cyclases vary in cGMP production rate and magnitude, enabling different amplitudes and ON-kinetics for cell depolarization by coupling to TAX-2/-4 in body wall muscle cells	108	Henss T, Nagpal J, Gao S, Scheib U, Pieragnolo A, Hirschhauser A*, et al.* (2021). Optogenetic tools for manipulation of cyclic nucleotides functionally coupled to cyclic nucleotide-gated channels. *British journal of pharmacology*.
Figure 21: Photoactivatable guanylyl cyclases are saturated at light conditions of ≥ 0.2 mW/mm2 in body wall muscle cells	109	Henss T, Nagpal J, Gao S, Scheib U, Pieragnolo A, Hirschhauser A*, et al.* (2021). Optogenetic tools for manipulation of cyclic nucleotides functionally coupled to cyclic nucleotide-gated channels. *British journal of pharmacology*.
Figure 22: BeCyclOp shows the highest, and bPGC the lowest mRNA levels in body wall muscle cells	110	Henss T, Nagpal J, Gao S, Scheib U, Pieragnolo A, Hirschhauser A*, et al.* (2021). Optogenetic tools for manipulation of cyclic nucleotides functionally coupled to cyclic nucleotide-gated channels. *British journal of pharmacology*.
Figure 23: BeCyclOp(A-2x) and bPAC evoke comparably increased swimming cycles, however the effect induced by bPAC decayed faster in cholinergic neurons	112	Henss T, Nagpal J, Gao S, Scheib U, Pieragnolo A, Hirschhauser A*, et al.* (2021). Optogenetic tools for manipulation of cyclic nucleotides functionally coupled to cyclic nucleotide-gated channels. *British journal of pharmacology*.

Figure/Name	Page	Author
Figure 24: YFP-CaCyclOp(A-2x) triggers the highest increase in swimming frequency during 30 s light application in cholinergic neurons	113	Henss T, Nagpal J, Gao S, Scheib U, Pieragnolo A, Hirschhauser A*, et al.* (2021). Optogenetic tools for manipulation of cyclic nucleotides functionally coupled to cyclic nucleotide-gated channels. *British journal of pharmacology*.
Figure 25: bPAC enhanced swimming rate maximizes at 0.2 mW/mm2, and drops at 0.4 mW/mm2 in cholinergic neurons	114	Henss T, Nagpal J, Gao S, Scheib U, Pieragnolo A, Hirschhauser A*, et al.* (2021). Optogenetic tools for manipulation of cyclic nucleotides functionally coupled to cyclic nucleotide-gated channels. *British journal of pharmacology*.
Figure 26: YFP-BeCyclOp(A-2x) increased swimming behaviour saturates at light conditions of 0.1 mW/mm2 in cholinergic neurons	114	Henss T, Nagpal J, Gao S, Scheib U, Pieragnolo A, Hirschhauser A*, et al.* (2021). Optogenetic tools for manipulation of cyclic nucleotides functionally coupled to cyclic nucleotide-gated channels. *British journal of pharmacology*.
Figure 27: Photoactivatable nucleotidyl cyclases expression in cholinergic neurons reduce basal swimming rate (excluded from CaCyclOp(A-2x))	115	Henss T, Nagpal J, Gao S, Scheib U, Pieragnolo A, Hirschhauser A*, et al.* (2021). Optogenetic tools for manipulation of cyclic nucleotides functionally coupled to cyclic nucleotide-gated channels. *British journal of pharmacology*.
Figure 28: BeCyclOp(A-2x) and bPAC evoke comparably enhanced crawling speeds, however the effect induced by bPAC decayed faster in cholinergic neurons	117	Henss T, Nagpal J, Gao S, Scheib U, Pieragnolo A, Hirschhauser A*, et al.* (2021). Optogenetic tools for manipulation of cyclic nucleotides functionally coupled to cyclic nucleotide-gated channels. *British journal of pharmacology*.
Figure 29: YFP-CyclOp(A-2x)s raise crawling speeds nearly comparably strong as bPAC and BeCyclOp(A-2x) in cholinergic neurons	118	Henss T, Nagpal J, Gao S, Scheib U, Pieragnolo A, Hirschhauser A*, et al.* (2021). Optogenetic tools for manipulation of cyclic nucleotides functionally coupled to cyclic nucleotide-gated channels. *British journal of pharmacology*.
Figure 30: Only BeCyclOp(A-2x) expression in cholinergic neurons reduces basal crawling speed,	119	Henss T, Nagpal J, Gao S, Scheib U, Pieragnolo A, Hirschhauser A*, et al.* (2021). Optogenetic tools for manipulation of cyclic nucleotides functionally coupled to cyclic nucleotide-gated channels. *British journal of pharmacology*.

Figure/Name	Page	Author
independent of ATR addition		
Figure 31: In contrast to bPAC, BeCyclOp(A-2x) photoactivation in cholinergic neurons evokes no change in the mean bending angles	120	Henss T, Nagpal J, Gao S, Scheib U, Pieragnolo A, Hirschhauser A*, et al.* (2021). Optogenetic tools for manipulation of cyclic nucleotides functionally coupled to cyclic nucleotide-gated channels. *British journal of pharmacology*.
Figure 32: YFP-CyclOp(a-2x)s light stimulation in cholinergic neurons produce no obvious change in the mean bending angles	121	Henss T, Nagpal J, Gao S, Scheib U, Pieragnolo A, Hirschhauser A*, et al.* (2021). Optogenetic tools for manipulation of cyclic nucleotides functionally coupled to cyclic nucleotide-gated channels. *British journal of pharmacology*.
Figure 33: Photo stimulation of BeCyclOp(A-2x) in cholinergic neurons slightly decreases the body length, though not reaching the extend triggered by bPAC	122	Henss T, Nagpal J, Gao S, Scheib U, Pieragnolo A, Hirschhauser A*, et al.* (2021). Optogenetic tools for manipulation of cyclic nucleotides functionally coupled to cyclic nucleotide-gated channels. *British journal of pharmacology*.
Figure 34: YFP-CyclOp(A-2x)s photoactivation in cholinergic neurons produce no obvious reduction in body length	123	Henss T, Nagpal J, Gao S, Scheib U, Pieragnolo A, Hirschhauser A*, et al.* (2021). Optogenetic tools for manipulation of cyclic nucleotides functionally coupled to cyclic nucleotide-gated channels. *British journal of pharmacology*.
Figure 35: Membrane-bound photoactivatable adenylyl cyclases are expressed at much lower levels than bPAC in cholinergic neurons	124	Henss T, Nagpal J, Gao S, Scheib U, Pieragnolo A, Hirschhauser A*, et al.* (2021). Optogenetic tools for manipulation of cyclic nucleotides functionally coupled to cyclic nucleotide-gated channels. *British journal of pharmacology*.
Figure 36: Membrane-bound photoactivatable adenylyl cyclases and TAX-2/-4 CNGC depict different efficiencies and kinetics for cell depolarization in body wall muscle cells	126	Henss T, Nagpal J, Gao S, Scheib U, Pieragnolo A, Hirschhauser A*, et al.* (2021). Optogenetic tools for manipulation of cyclic nucleotides functionally coupled to cyclic nucleotide-gated channels. *British journal of pharmacology*.
Figure 37: bPAC stimulation evokes stronger body	127	Henss T, Nagpal J, Gao S, Scheib U, Pieragnolo A, Hirschhauser A*, et al.* (2021). Optogenetic tools for manipulation of cyclic

Figure/Name	Page	Author
contraction than BeCyclOp(A-2x), indicating higher overall cAMP generation in body wall muscle cells		nucleotides functionally coupled to cyclic nucleotide-gated channels. *British journal of pharmacology*.
Figure 38: BeCyclOp(A-2x), BeCyclOp(A-3x) and bPAC depict the highest mRNA levels, whereas YFP-CyclOp(A-2x)s shows about half or intermediate expression levels in body wall muscle cells	128	Henss T, Nagpal J, Gao S, Scheib U, Pieragnolo A, Hirschhauser A*, et al.* (2021). Optogenetic tools for manipulation of cyclic nucleotides functionally coupled to cyclic nucleotide-gated channels. *British journal of pharmacology*.
Figure 39: Membrane-bound photoactivatable adenylyl cyclases generate (and accumulate) cAMP at high levels *in vivo*, with high specificity	129	Henss T, Nagpal J, Gao S, Scheib U, Pieragnolo A, Hirschhauser A*, et al.* (2021). Optogenetic tools for manipulation of cyclic nucleotides functionally coupled to cyclic nucleotide-gated channels. *British journal of pharmacology*.
Figure 40: Under conditions matching the light conditions of behavioural experiments, bPAC produced ca. 4x more cAMP than YFP-BeCyclOp(A-2x)	130	Henss T, Nagpal J, Gao S, Scheib U, Pieragnolo A, Hirschhauser A*, et al.* (2021). Optogenetic tools for manipulation of cyclic nucleotides functionally coupled to cyclic nucleotide-gated channels. *British journal of pharmacology*.
Figure 41: Expression pattern of BeCNG1::YFP BeCyclOp::SL2::mCherry using the myo-3 promoter	132	Henss T, Nagpal J, Gao S, Scheib U, Pieragnolo A, Hirschhauser A*, et al.* (2021). Optogenetic tools for manipulation of cyclic nucleotides functionally coupled to cyclic nucleotide-gated channels. *British journal of pharmacology*.
Figure 42: BeCyclOp and BeCNG1 trigger moderate, but long-lasting hyperpolarization of body wall muscle cells	133	Henss T, Nagpal J, Gao S, Scheib U, Pieragnolo A, Hirschhauser A*, et al.* (2021). Optogenetic tools for manipulation of cyclic nucleotides functionally coupled to cyclic nucleotide-gated channels. *British journal of pharmacology*.
Figure 43: Expression pattern of SthK::mCherry using the myo-3 promoter	134	Henss T, Nagpal J, Gao S, Scheib U, Pieragnolo A, Hirschhauser A*, et al.* (2021). Optogenetic tools for manipulation of cyclic nucleotides functionally coupled to cyclic nucleotide-gated channels. *British journal of pharmacology*.
Figure 44: bPAC and SthK light stimulation in body wall muscle cells	135	Henss T, Nagpal J, Gao S, Scheib U, Pieragnolo A, Hirschhauser A*, et al.* (2021). Optogenetic tools for manipulation of cyclic

Figure/Name	Page	Author
provoke fast and robust muscle hyperpolarization		nucleotides functionally coupled to cyclic nucleotide-gated channels. *British journal of pharmacology*.
Figure 45: bPAC and SthK evoked muscle elongation lasted up to 10 min	136	Henss T, Nagpal J, Gao S, Scheib U, Pieragnolo A, Hirschhauser A*, et al.* (2021). Optogenetic tools for manipulation of cyclic nucleotides functionally coupled to cyclic nucleotide-gated channels. *British journal of pharmacology*.
Figure 46: SthK pre-activation by intrinsic cAMP and increased cAMP level due to bPACs dark activity reduce basal swimming rate, and illumination of SthK; bPAC evoked a complete arrest of the swimming behaviour	137	Henss T, Nagpal J, Gao S, Scheib U, Pieragnolo A, Hirschhauser A*, et al.* (2021). Optogenetic tools for manipulation of cyclic nucleotides functionally coupled to cyclic nucleotide-gated channels. *British journal of pharmacology*.
Figure 47: Expression pattern of SthK::mCherry using the unc-17 promoter	138	Henss T, Nagpal J, Gao S, Scheib U, Pieragnolo A, Hirschhauser A*, et al.* (2021). Optogenetic tools for manipulation of cyclic nucleotides functionally coupled to cyclic nucleotide-gated channels. *British journal of pharmacology*.
Figure 48: Pre-activation of SthK reduces basal swimming frequencies, and photo activation of SthK and bPAC provoke a nearly complete arrest of the swimming behaviour	139	Henss T, Nagpal J, Gao S, Scheib U, Pieragnolo A, Hirschhauser A*, et al.* (2021). Optogenetic tools for manipulation of cyclic nucleotides functionally coupled to cyclic nucleotide-gated channels. *British journal of pharmacology*.
Figure 49: bPAC and SthK evoked arrest of swimming behaviour last up to 90 – 150 s	149	Henss T, Nagpal J, Gao S, Scheib U, Pieragnolo A, Hirschhauser A*, et al.* (2021). Optogenetic tools for manipulation of cyclic nucleotides functionally coupled to cyclic nucleotide-gated channels. *British journal of pharmacology*.
Figure 50: BeCyclOp(A-3x) and SthK induce a strong muscle hyperpolarization	142	Henss T, Nagpal J, Gao S, Scheib U, Pieragnolo A, Hirschhauser A*, et al.* (2021). Optogenetic tools for manipulation of cyclic nucleotides functionally coupled to cyclic nucleotide-gated channels. *British journal of pharmacology*.
Figure 51: Co-expression of BeCyclOp(A-3x) causes no further pre-	143	Henss T, Nagpal J, Gao S, Scheib U, Pieragnolo A, Hirschhauser A*, et al.* (2021). Optogenetic tools for manipulation of cyclic

Figure/Name	Page	Author
activation of SthK, and light stimulation strongly reduce the swimming rate		nucleotides functionally coupled to cyclic nucleotide-gated channels. *British journal of pharmacology*.
Figure 52: Membrane-bound photoactivatable adenylyl cyclase and SthK co-expression in cholinergic neurons reduce basal swimming rate, and illumination triggered a robust decrease of the swimming cycles, increasing again after turning off light	144	Henss T, Nagpal J, Gao S, Scheib U, Pieragnolo A, Hirschhauser A*, et al.* (2021). Optogenetic tools for manipulation of cyclic nucleotides functionally coupled to cyclic nucleotide-gated channels. *British journal of pharmacology*.
Figure 53: Titration of YFP-BeCyclOp(A-2x) and SthK expression levels did not optimize the system	145	Henss T, Nagpal J, Gao S, Scheib U, Pieragnolo A, Hirschhauser A*, et al.* (2021). Optogenetic tools for manipulation of cyclic nucleotides functionally coupled to cyclic nucleotide-gated channels. *British journal of pharmacology*.
Figure 54: Triton X-100 achieves highest amount of solubilized BeCyclOp	147	Thilo Henß, ImageJ and OriginLab software
Figure 55: IgG-Agarose precipitates BeCyclOp::TAP out of LDAO and OG solubilizates	148	Thilo Henß, Software Image J
Figure 56: Calmodulin-agarose precipitates BeCyclOp::TAP out of Triton X-100, LDAO, OG and DDM solubilizates	149	Thilo Henß, Software Image J
Figure 57: Tandem affinity precipitation test depicts no signal for BeCyclOp::TAP	150	Thilo Henß, Software Image J
Figure 58: TEV cleavage test shows successful cleavage of the TAP-tag through the TEV protease	151	Thilo Henß, Software Image J
Figure 59: Confirmation of BeCyclOp::TAP expression after integration in C. elegans genome	152	Thilo Henß, Software Image J

Figure/Name	Page	Author
Figure 60: Tandem affinity purification exhibits strong signal of BeCyclOp::TAP in IgG-agarose flow through	153	Thilo Henß, Software Image J
Figure 61: Addition of dialysis step strongly reduced BeCyclOp::TAP content in IgG-Agarose flow through	154	Thilo Henß, Software Image J
Figure 62: BeCyclOp::TAP precipitates after dialysis	155	Thilo Henß, Software Image J
Figure 63: BeCyclOp Concatamer is expressed in C. elegans muscle cells	156	Thilo Henß, Software Image J
Figure 64: BeCyclOp concatamer is functional, though not reaching the same level of activity as the BeCyclOp monomer	157	Thilo Henß, Software OriginLab
Figure 65: Confirmation of BeCyclOp concatamer expression after integration in C. elegans genome	158	Thilo Henß, Software Image J
Figure 66: Tandem affinity purification depicts cleavage of BeCyclOp concatamer into BeCyclOp monomers	159	Thilo Henß, Software Image J
Figure 67: Increase of protease inhibitor concentration successfully inhibit BeCyclOp concatamer cleavage into monomers	160	Thilo Henß, Software Image J
Figure 68: bPAC and BeCyclOp(A-2x) activation increase the body length by 1 – 2 %	162	Thilo Henß, Software OriginLab
Figure 69: bPAC stimulation strongly reduces the swimming frequency	163	Thilo Henß, Software OriginLab; Alessia Pieragnolo performed behavioural recordings and data analysis
Figure 70: Influence of optogenetic cAMP	165	S. Zhou BSc Thesis

Figure/Name	Page	Author
generation through bPAC on the body length in channel loss of function lite-1(ce314) background		
Figure 71: Influence of optogenetic cAMP generation through bPAC on the swimming rate in channel loss of function lite-1(ce314) background	165	S. Zhou BSc Thesis
Figure 72: Optogenetic cAMP generation by bPAC evokes muscle elongation in lite-1(ce314) unc-103(n1213) background	167	Thilo Henß, Software OriginLab
Figure 73: bPAC activation in body wall muscle cells causes no obvious increase of the body length under these experimental conditions, but strongly decreased the swimming cycles in wild type animals	168	Thilo Henß, Software OriginLab
Figure 74: Optogenetic cAMP generation through bPAC evokes muscle relaxation in wild type animals	169	Thilo Henß, Software OriginLab
Figure 75: Optogenetic cAMP generation triggers muscle relaxation in cng-1(jh111) mutant background	170	Thilo Henß, Software OriginLab
Figure 76: bPAC stimulation in cng-2(tm4267) background reduces the swimming rate	171	Thilo Henß, Software OriginLab
Figure 77: Optogenetic cAMP production evokes muscle hyperpolarization in cng-3(jh113) background	172	Thilo Henß, Software OriginLab

Figure/Name	Page	Author
Figure 78: bPAC activation in che-6(e1126) background reduces the swimming frequency	173	Thilo Henß, Software OriginLab
Figure 79: cAMP production by bPAC evokes muscle relaxation in egl-2(rg4) background	174	Thilo Henß, Software OriginLab
Figure 80: bPAC stimulation in unc-103(n1213) decreases the swimming rate	175	Thilo Henß, Software OriginLab
Figure 81: Most channel loss of function strains exhibit reduced basal swimming rates	176	Thilo Henß, Software OriginLab
Figure 82: Optogenetic cAMP production reduced swimming frequency in all mutant strains	177	Thilo Henß, Software OriginLab
Figure 83: Evaluation of photoactivatable guanylyl cyclases characterized in this thesis	182	Henss T, Nagpal J, Gao S, Scheib U, Pieragnolo A, Hirschhauser A*, et al.* (2021). Optogenetic tools for manipulation of cyclic nucleotides functionally coupled to cyclic nucleotide-gated channels. *British journal of pharmacology*, modified by Thilo Henß
Figure 84: Evaluation of photoactivatable adenylyl cyclases characterized in this thesis	187	Henss T, Nagpal J, Gao S, Scheib U, Pieragnolo A, Hirschhauser A*, et al.* (2021). Optogenetic tools for manipulation of cyclic nucleotides functionally coupled to cyclic nucleotide-gated channels. *British journal of pharmacology*, modified by Thilo Henß
Figure 85: Evaluation of depolarizing multicomponent optogenetic tools characterized in this thesis	189	Henss T, Nagpal J, Gao S, Scheib U, Pieragnolo A, Hirschhauser A*, et al.* (2021). Optogenetic tools for manipulation of cyclic nucleotides functionally coupled to cyclic nucleotide-gated channels. *British journal of pharmacology*, modified by Thilo Henß
Figure 86: Evaluation of hyperpolarizing two-component optogenetic tools characterized in this thesis	194	Henss T, Nagpal J, Gao S, Scheib U, Pieragnolo A, Hirschhauser A*, et al.* (2021). Optogenetic tools for manipulation of cyclic nucleotides functionally coupled to cyclic nucleotide-gated channels. *British journal of pharmacology*, modified by Thilo Henß
Figure 87: Proposed model for the physiological function of	207	Thilo Henß

Figure/Name	Page	Author
UNC-103 in body wall muscle cells		
Figure 88: Sequence alignment of PKA regulatory subunit RIα and PKG Iβ and the C. elegans ion channels TAX-4, CNG-1, CNG-2, CNG-3, CHE-6, EGL-2 and UNC-103	246	Thilo Henß, Software Clustal Omega
Figure 89: Sequence alignment of the potassium channels hERG and Eag and the C. elegans ion channels EGL-2 and UNC-103	249	Thilo Henß, Software Clustal Omega
Figure 90: Sequence alignment of the cation channel CNGA1 and the C. elegans ion channels TAX-4, CNG-1, CNG-2, CNG-3 and CHE-6	252	Thilo Henß, Software Clustal Omega
Figure 91: Influence of light application on channel loss of function mutant backgrounds	253	Thilo Henß, Software OriginLab
Figure 92: The cardiac action potential and its fundamental membrane currents	254	Grant AO (2009). Cardiac ion channels. *Circulation. Arrhythmia and electrophysiology* **2**(2)**:** 185-194.
Figure 93: Characterization of membrane-anchored bacterial photoactivatable adenylyl cyclases in C. elegans muscle cells	256	Thilo Henß, Software OriginLab
Figure 94: Application of mPAC and SthK in cholinergic neurons	267	Thilo Henß, Software OriginLab
Figure 95: Application of SthK-YFP-bPAC in C. elegans muscle cells	259	B, E, F, H = N. Ho BSc Thesis C, D, G = Thilo Henß, Software OriginLab
Figure 96: Application of the synthetic phytochrome-linked cyclase PaaC+7 and SthK in C. elegans muscle cells	261	N. Ho BSc Thesis

Figure/Name	Page	Author
Figure 97: Chemical structures of the synthetic retinal analogues applied for spectral tuning of BeCyclOp	262	AzimiHashemi N, Erbguth K, Vogt A, Riemensperger T, Rauch E, Woodmansee D*, et al.* (2014). Synthetic retinal analogues modify the spectral and kinetic characteristics of microbial rhodopsin optogenetic tools. *Nat Commun* **5:** 5810
Figure 98: Investigation of BeCyclOp functionality using synthetic retinal analogues	263	Thilo Henß, Software OriginLab
Figure 99: Spectral tuning of BeCyclOp using synthetic retinal analogues	265	Thilo Henß, Software OriginLab
Figure 100: Schematic overview of BeCyclOp fragments designed for this thesis	267	Gao S, Nagpal J, Schneider MW, Kozjak-Pavlovic V, Nagel G, Gottschalk A (2015). Optogenetic manipulation of cGMP in cells and animals by the tightly light-regulated guanylyl-cyclase opsin CyclOp. *Nature communications* **6:** 8046, adapted and modified by Thilo Henß
Figure 101: Expression and subcellular localization of BeCyclOp fragments in C. elegans body wall muscle cells	268	Thilo Henß, Software Image J
Figure 102: Characterization of a functional impact of BeCyclOp N-termini on guanylyl cyclase activity	270	Thilo Henß, Software OriginLab

Table 25: List of tables and author.

Table/Name	Page	Author
Table 1: Used chemical substances	42	Thilo Henß
Table 2: Used devices and equipment	45	Thilo Henß
Table 3: Used buffer and media	47	Thilo Henß
Table 4: Used kits and beads	51	Thilo Henß
Table 5: Used enzymes	52	Thilo Henß
Table 6: Used antibodies	53	Thilo Henß
Table 7: Used oligonucleotides	53	Thilo Henß
Table 8: Used plasmids	57	Thilo Henß
Table 9: Used organisms	60	Thilo Henß
Table 10: Used C. elegans strains	60	Thilo Henß
Table 11: Used consumables	70	Thilo Henß
Table 12: Used software	71	Thilo Henß